



UNIVERSIDAD
POLITECNICA
DE VALENCIA



UNIVERSIDAD POLITÉCNICA DE VALENCIA
Departamento de Física Aplicada

**On the control of propagating acoustic
waves in sonic crystals:
analytical, numerical and optimization
techniques**

Tesis doctoral presentada por
D. Vicent Romero García

Dirigida por los Doctores
Juan Vicente Sánchez Pérez
Luis Miguel Garcia Raffi

València, Noviembre, 2010

AGRADECIMIENTOS

Esta Tesis doctoral es el fiel reflejo del cariño, apoyo, confianza y generosidad de un conjunto de personas que, sin ellas, estoy firmamente convencido, jamás hubiera llegado a ver la luz.

En primer lugar me gustaría agradecer a mis directores, al Dr. Juan Vicente Sánchez-Pérez y al Dr. Lluís Miquel Garcia-Raffi, todo lo que han hecho por mí durante estos años. Gracias a ellos he tenido la oportunidad de introducirme en el camino científico y aprender muchísima física. No sólo han sido mis directores de tesis, sino que se han convertido en verdaderos compañeros y amigos con los que he compartido muchos momentos buenos y malos. Qué bien lo hemos pasado con la *bicicleta* y, sobre todo, durante discusiones científicas en los congresos, en la cámara anecoica, en los despachos, en el bar... Muchas gracias.

Durante estos años he tenido la oportunidad de conocer magníficas personalidades que me han hecho muy fácil la tarea y, sobre todo, me han hecho ver que la ciencia no está reñida con las buenas personas. En primer lugar me gustaría acordarme de todo el trabajo que mi amigo Elies Fuster aportó a este proyecto. Gracias a él surgió todo esto. En segundo lugar, me gustaría agradecer el apoyo del Dr. Víctor J. Sánchez-Morcillo, del Dr. Hermelando Estellés y del Dr. Francisco Belmar. Han demostrado ser unos gradísimos profesionales y sobre todo buenos compañeros. Entre ellos, me gustaría mostrar mi agradecimiento a mi vecino de despacho, al Dr. Hermelando Estellés. La alegría que desborda todas las mañanas me ha hecho muy llevadero el trabajo, y en los momentos en los que no ha estado, lo he echado muchísimo de menos. Me alegro mucho de tu regreso. Finalmente me gustaría agradecer el apoyo del Dr. Enrique Alfonso Sánchez Pérez, del Dr. Enrique Berjano Zanón, del Dr. Francisco Meseguer, de la Dra. Macarena Trujillo, del Dr. Jose Calabuig, de la Dra. Constanza Rubio y de Sergio Castiñeira.

No podía ser de otra manera, esta Tesis la he dedicado a mis padres, Vicente y Maribel. Nunca podré agradecer ni devolverles todo lo que han hecho por mí. La vida me dio la tremenda suerte de tenerlos como padres, y para mí es un orgullo decir que ellos son mis padres y que siempre han depositado su confianza en mí. Va por vosotros! Muchas gracias!!

Me gustaría también agradecer el apoyo que siempre me han mostrado mi tía Carmen y mis primos M^a Carmen y Vicente Martí. Siempre han estado dispuestos a aconsejarme y apoyarme en mis decisiones. En estos años la vida se ha llevado a mi tío Pepe que tanto me ha querido. Me gustaría desde aquí agradecerle todo su cariño y recordar, con mucho afecto, las bromas que me hacía que, de alguna forma, me han servido para estar más despierto.

Gracias a la música he tenido la suerte de conocer a la persona que me apoya en todo momento, que me ofrece su cariño y que me complementa en todos los sentidos. Maria me lo ha dado siempre todo y nunca ha dejado de confiar en mí. Ella ha hecho que vea la vida de otra forma, con más alegría e ilusión, y sobre todo me ha dejado formar parte de su vida. Ella es responsable de este trabajo hasta un punto que dudo mucho que ella misma sea capaz de imaginar. “Moltes gràcies!!”

Mención especial quisiera dar a la familia Falcó Frígols al completo, y en especial a Marina, a Ramón, a Jose, a M^a Nieves. Muchas gracias por dejarme formar parte de vuestro día a día, y por el respeto y cariño que me ofrecéis.

Mis amigos han sido un apoyo fundamental durante estos años. Me gustaría en especial agradecer la amistad que siempre me ha brindado Sergio Iborra y, ahora también, Sabina. El apoyo que he recibido de Carlos Martínez (“el señor Ministro”) y mis compañeros de la banda. La generosidad de Carlos y May, sin la cual no hubiera podido poner fin a la Tesis.

Para finalizar quisiera también mostrar mi agradecimiento al Ministerio de Educación y Ciencia, al Instituto de Ciencia de Materiales de Madrid (Consejo superior de investigaciones científicas, CSIC), al Departamento de Física Aplicada de la Universidad Politécnica de Valencia, al Centro de Tecnologías Físicas: A.M.A., así como a la University of Salford y a la Open University. Especialmente me gustaría agradecer a D. Ángel Martín Zarza y a Dña. Pilar Capilla su invaluable ayuda en la gestión; al Dr. Jorge Curiel por su apoyo en la gestión de la docencia; a la Dra. Olga Umnova y al Prof. Keith Attenborough por su cordialidad durante mi estancia en U.K.; a los compañeros de la University of Salford que me acogieron con los brazos abiertos, en especial al Dr. Anton Krynkin, al Dr. Diego Turo, al Dr. Rodolfo Venegas y al Dr. Konstantinos Dadiotis.

A mis padres, infinitamente agradecido
y orgulloso de ellos.

To my parents, infinitely grateful
and proud of them.

Los sonidos domesticados decían
mucho más de lo que decían
(originaban círculos concéntricos
-como la piedra arrojada al agua-
que se multiplicaban, se expandían,
se atenuaban hasta regresar a la lisura y el sosiego):
y todos percibían su esencia misteriosa
que no sabían descifrar.

José Hierro.
Cuaderno de Nueva York

The sounds, once familiar, meant
much more than they had meant
(they started concentric circles
-like a stone thrown into the water-
that multiplied, expanded,
grew weak until returning to smoothness and serenity):
and everyone sensed their mysterious essence
that they couldn't decipher.

José Hierro.
New York Notebook

RESUM DE LA TESI DOCTORAL

Control de la propagació d'ones acústiques en cristalls de so: tècniques analítiques, numèriques i d'optimització

per

D. Vicent Romero García

Departament de Física Aplicada
Universitat Politècnica de València, Novembre 2010

El control de les propietats acústiques dels cristalls de so (CS) necessita de l'estudi de la distribució dels dispersors en la pròpia estructura i de les propietats acústiques intrínseques dels dispersors. En aquest treball es presenta un estudi exhaustiu de les propietats de CS amb diferents distribucions, així com l'estudi de la millora de les propietats acústiques de CS constituïts per diversos dispersors amb propietats absorbents i/o ressonant. Aquests dos procediments, tant independentment com conjuntament, introduïxen possibilitats reals per al control de la propagació d'ones acústiques a través dels CS.

Des del punt de vista teòric, les propietats de la propagació d'ones acústiques a través de estructures periòdiques i quasiperiòdiques s'han analitzat amb els mètodes de la dispersió múltiple, de l'expansió d'ones planes i dels elements finits. En aquest treball es presenta una novedosa extensió del mètode de l'expansió d'ones planes amb la qual es poden obtenir les relacions complexes de dispersió per als CS. Aquesta tècnica complementa la informació obtinguda amb els mètodes clàssics i permet conèixer el comportament evanescent dels modes a l'interior de les bandes de propagació prohibida del CS així com dels modes localitzats al voltant de possibles defectes puntuals en CS.

La necessitat de mesures acurades de les propietats acústiques dels CS ha provocat el desenvolupament d'un novedós sistema tridimensional que sincronitza el moviment del receptor i l'adquisició de senyals temporals. Els resultats experimentals obtinguts mostren una gran similitud amb els resultats

teòrics.

L'actuació conjunta de distribucions de dispersors optimitzades i de les propietats intrínseques d'aquestos, s'aplica per a la generació d'un dispositiu que presenta un rang ample de freqüències atenuades. Aquestos sistemes es presenten com una alternativa a barreres acústiques tradicionals on es pot controlar el pas d'ones al seu través.

Els resultats mostrats ajuden a entendre correctament el funcionament del CS per a la localització de so i per al guiat i per al filtratge d'ones acústiques.

RESUMEN DE LA TESIS DOCTORAL

Control de la propagación de ondas acústicas en cristales de sonido: técnicas analíticas, numéricas y de optimización

por

D. Vicent Romero García

Departamento de Física Aplicada
Universidad Politécnica de Valencia, Noviembre 2010

El control de las propiedades acústicas de los cristales de sonido (CS) necesita del estudio de la distribución de dispersores en la propia estructura y de las propiedades acústicas intrínsecas de dichos dispersores. En este trabajo se presenta un estudio exhaustivo de diferentes distribuciones, así como el estudio de la mejora de las propiedades acústicas de CS constituidos por dispersores con propiedades absorbentes y/o resonantes. Estos dos procedimientos, tanto independientemente como conjuntamente, introducen posibilidades reales para el control de la propagación de ondas acústicas a través de los CS.

Desde el punto de vista teórico, la propagación de ondas a través de estructuras periódicas y quasiperiódicas se ha analizado mediante los métodos de la dispersión múltiple, de la expansión en ondas planas y de los elementos finitos. En este trabajo se presenta una novedosa extensión del método de la expansión en ondas planas que permite obtener las relaciones complejas de dispersión para los CS. Esta técnica complementa la información obtenida por los métodos clásicos y permite conocer el comportamiento evanescente de los modos en el interior de las bandas de propagación prohibida del CS, así como de los modos localizados alrededor de posibles defectos puntuales en CS.

La necesidad de medidas precisas de las propiedades acústicas de los CS ha provocado el desarrollo de un novedoso sistema tridimensional que sincroniza el movimiento del receptor y la adquisición de señales temporales. Los resul-

tados experimentales obtenidos en este trabajo muestran una gran similitud con los resultados teóricos.

La actuación conjunta de distribuciones de dispersores optimizadas y de las propiedades intrínsecas de éstos, se aplica para la generación de dispositivos que presentan un rango amplio de frecuencias atenuadas. Estos sistemas se presentan como una alternativa a las barreras acústicas tradicionales donde se puede controlar el paso de ondas a su través.

Los resultados ayudan a entender correctamente el funcionamiento de los CS para la localización de sonido, y para el guiado y filtrado de ondas acústicas.

ABSTRACT OF THE DOCTORAL THESIS

On the control of propagating acoustic waves in sonic crystals: analytical, numerical and optimization techniques

by

D. Vicent Romero García

Applied Physics Department

Polytechnic University of Valencia, November 2010

The control of the acoustical properties of the sonic crystals (SC) needs the study of both the distribution of the scatterers in the structure and the intrinsic acoustical properties of the scatterers. In this work an exhaustive analysis of the distribution of the scatterers as well as the improvement of the acoustical properties of the SC made of scatterers with absorbent and/or resonant properties is presented. Both procedures, working together or independently, provide real possibilities to control the propagation of acoustic waves through SC.

From the theoretical point of view, the wave propagation through periodic and quasiperiodic structures has been analysed by means of the multiple scattering theory, the plane wave expansion and the finite elements method. A novel extension of the plane wave expansion allowing the complex relation dispersion for SC is presented in this work. This technique complements the provided information using the classical methods and it allows us to analyse the evanescent behaviour of the modes inside of the band gaps as well as the evanescent behaviour of localized modes around the point defects in SC.

The necessity of accurate measurements of the acoustical properties of the SC has motivated the development of a novel three-dimensional acquisition system that synchronises the motion of the receiver and acquisition of the temporal signals. A good agreement between the theoretical and experimental data is shown in this work.

The joint work between the optimized structures of scatterers and the intrinsic properties of the scatterers themselves is applied to generate devices that present wide ranges of attenuated frequencies. These systems are presented as an alternative to the classic acoustic barrier where the propagation of waves through SC can be controlled.

The results help to correctly understand the behaviour of SC for the localization of sound and for the design of both wave guides and acoustic filters.

Contents

1	Sculptures as acoustic filters	1
1.1	Control of sound propagation in sonic crystals	4
1.2	Object and motivation of the work	9
1.3	Overview of the work	13
1.3.1	Bibliographic notes	16
2	Fundamentals of periodic systems	17
2.1	Periodic systems	18
2.1.1	Geometric properties	18
2.1.2	Wave propagation	21
2.1.2.1	Band gaps	25
2.1.2.2	Defects, localization and waveguides	32
2.1.3	Sonic crystals, the acoustic periodic system	36
2.2	Parameters and symbols	37
3	Theoretical models and numerical techniques	41
3.1	Multiple scattering theory	42
3.1.1	Two-dimensional scattering by circular cylinders	43
3.1.1.1	Incidence of a plane wave	44
3.1.1.2	Incidence of a cylindrical wave	50
3.2	Plane wave expansion	56
3.2.1	$\omega(k)$ method	57
3.2.2	$k(\omega)$ method: extended plane wave expansion	60
3.2.3	Supercell approximation	64
3.2.3.1	Complete arrays	65
3.2.3.2	Arrays with defects	66

CONTENTS

3.3	Finite elements method	67
3.3.1	Bounded problem: eigenvalue problem	67
3.3.2	Unbounded problem: scattering problem	71
3.3.2.1	Radiation boundary conditions	72
3.3.2.2	Perfectly matched layers	74
4	Optimization: genetic algorithms	77
4.1	Optimizing sonic crystals	78
4.2	Evolutionary algorithms: genetic algorithms	80
4.2.1	Fundamentals	80
4.2.2	Coding	81
4.2.3	Cost functions	84
4.2.3.1	Simple genetic algorithm	85
4.2.3.2	Multi-objective problems	86
4.2.4	Operators	88
4.2.5	Termination test	90
4.3	Multi-objective optimization	91
4.3.1	Pareto front	91
4.3.2	Epsilon-variable multi-objective genetic algorithms . .	93
4.3.2.1	ϵ -dominance	95
4.3.2.2	ϵ -Pareto front	96
4.3.3	Parallelization	100
5	Experimental setup	103
5.1	Anechoic chamber	104
5.2	Acquisition system	107
5.2.1	Non robotized system	107
5.2.1.1	Sound source	108
5.2.2	3DReAMS	108
5.2.2.1	Robotized system and control of motion .	108
5.2.2.2	Acquisition hardware	111
5.2.2.3	Sound source	112
5.3	Microphones and accelerometers	112
5.3.1	Microphone	112
5.3.2	Accelerometer	114

5.4	Scatterers	114
6	Low number of vacancies: point defects in sonic crystals	117
6.1	Point defects in sonic crystal	118
6.1.1	Localized modes	119
6.1.2	Evanescent behaviour	122
6.2	N-point defects in sonic crystals	127
6.2.1	Double point defect	130
6.2.1.1	Localization	132
6.2.1.2	Symmetry of vibrational patterns	135
6.2.1.3	Evanescent decay	137
6.3	Discussion	140
7	High number of vacancies. Optimization	143
7.1	Quasi ordered structures (QOS)	145
7.2	Simple genetic algorithm optimization	146
7.3	Multi-objective optimization	149
7.3.1	Starting conditions. Strategies in the creation of holes .	150
7.3.2	Characterization of the QOS	151
7.3.3	Improving the attenuation capabilities with QOS . . .	152
7.3.3.1	Initial test: Improvement of the preliminary QOS	153
7.3.3.2	Symmetries in the generation of vacancies	156
7.3.4	Improving focusing capabilities with QOS	160
7.4	Dependence on the searching path	163
7.4.1	Procedure 1	163
7.4.2	Procedure 2	166
7.5	General rules for creating vacancies in sonic crystals	170
7.5.0.1	Experimental evidence	175
7.6	Discussion	177
8	Improving the acoustic properties of the scatterers	181
8.1	Balloons as resonant scatterers in sonic crystals	183
8.1.1	Results	184
8.2	Split ring resonators in sonic crystals	187
8.2.1	Design of single resonators	188

CONTENTS

8.2.2	Eigenvalue problem: band structures of SC made of SRR	190
8.2.3	Scattering problem of finite SC made of SRR	191
8.2.3.1	Dependence on the number of rows and on the incidence direction	194
8.3	Elastic U-profile scatterers	196
8.3.1	Motivating results	196
8.3.2	Phenomenological analysis	197
8.3.2.1	Elastic resonances	197
8.3.2.2	Cavity resonances	201
8.3.3	Acoustic-structure interaction	202
8.3.3.1	FEM model	202
8.3.4	Numerical results	204
8.3.4.1	Scattering problem	204
8.3.4.2	Eigenvalue problem	208
8.3.5	Experimental results	208
8.3.5.1	Single scatterer	209
8.3.5.2	Periodic array	211
8.3.6	Discussion: locally resonant acoustic metamaterial	213
8.4	Towards superscatterers for attenuation devices based on SC	219
9	Engineering and design of Sonic Crystals	221
9.1	Targeted attenuation band creation using mixed sonic crystals including resonant and rigid scatterers	222
9.2	Design of a sonic crystal acoustic barrier	225
9.2.1	Combining absorption, resonances and multiple scattering	226
9.2.1.1	Scattering of a SCAB made of absorbent SRR	228
9.2.1.2	Dependence of the IL on the number of rows and on the incidence direction	231
10	Concluding remarks	233
10.1	Conclusions	233
10.1.1	Defects in sonic crystals	233

10.1.2	Intrinsic properties of the scatterers	237
10.1.3	Combining physical phenomena	239
10.2	Future work	240
A	Appendix: Addition theorems	243
B	Appendix: Computational time multiple scattering theory	247
C	Appendix: multiple scattering of arrays of cylinders covered with absorbing material	249
C.1	Numerical test	252
D	Appendix: Vibration of an elastic beam	255
E	Publications	257
E.1	International Journals	257
E.2	International meetings	259
E.3	Invited Conferences	261
E.4	Awards	261
E.5	Patents	262
	Abbreviations	263
	Symbols	264
	List of Figures	267
	List of Tables	283
	Bibliography	283

CONTENTS

1

Sculptures as acoustic filters

In the late 80's Yablonovitch [[Yablonovitch87](#)] and John [[John87](#)] simultaneously triggered the primary emphasis in periodic systems due to the interesting propagation properties of the electromagnetic waves inside of them. Their proposal consisted of using a periodic distribution of dielectric scatterers embedded in a host medium with different dielectric properties. These periodic systems exhibit ranges of frequencies related to the periodicity of the structure where there is no wave propagation. By analogy with the electronic band gap in semiconductor crystals, these ranges of frequency were called band gaps (BG) and these periodic structures were called photonic crystals. For a brief review of photonic band structures see reference [[Yablonovitch88](#)].

Yablonovitch [[Yablonovitch87](#)] showed that the spontaneous emissions by atoms is not necessarily a fixed and immutable property of the coupling between the matter and space, and it could be controlled by modifying the properties of the radiation field using photonic crystals. Several works have developed new methodologies to observe the inhibition of this radiative decay [[Martorell90](#), [Yablonovitch93](#), [Boroditsky99](#), [Englund05](#)]. On the other hand, John pointed out [[John87](#)] that carefully prepared three-dimensional dielectric superlattices with moderate disorder could provide the key to the predictable and systematic observation of strong localization of photons in non dissipative materials with an everywhere real positive dielectric constant. Subsequent works have been developed to analyse localization in photonic crystals [[Genack91](#), [Ling92](#), [John88](#), [John91](#), [Yablonovitch91](#), [Meade91](#), [Wiersma97](#),

CHAPTER 1. SCULPTURES AS ACOUSTIC FILTERS

[Schwartz07](#)].

From a fundamental point of view, both effects appear due to the existence of the BG and this fact was exploited in the subsequent years to explore the prominent phenomena emerging from the physics of photonic crystals. The ability to manipulate the propagation properties of electromagnetic radiation have produced a number of practical applications such as modifying the spontaneous emission rate of emitters [[Englund05](#), [Boroditsky99](#)], slowing down the group velocity of light [[Altug05a](#), [Vlasov05](#)], designing highly efficient nanoscale lasers [[Altug05b](#)], enhancing surface mounted microwave antennas [[Brown93](#)], sharp bend radius waveguides [[Meade94](#)], efficient radiation sources [[Altug06](#)], sensors [[Elkady06](#)], and optical computer chips [[Chutinan03](#)].



Figure 1.1: Kinematic sculpture by Eusebio Sempere placed at the Juan March Foundation in Madrid.

A few years after, at the beginning of the 90's, an increasing interest in the comparable process of acoustic wave propagation in periodic arrays appeared. Motivated by the results of the photonic crystals, several theoretical works started the analysis of periodic arrays made of isotropic solids embedded in an elastic background which was also isotropic [[Ruffa92](#), [Sigalas92](#), [Sigalas93](#),

[Kushwaha93](#), [Kushwaha94](#), [Sigalas94](#)]. By analogy with the photonic case, these periodic arrangements present BG, defined here as: frequency ranges where vibrations, sound and phonons were forbidden. Analogously they were called phononic crystals (PC).

Depending on the distribution of the periodic solid elastic composites one can obtain one-dimensional (1D), two-dimensional (2D) or three-dimensional (3D) PC. In each of these PC one can observe different combinations of transversal, longitudinal or mixed waves. However a drastic simplification arises in the case of fluids, which permits only longitudinal waves. It is said that if one of the elastic materials in the PC is a fluid medium, then PC are called sonic crystals (SC). Several studies discuss the similarities and differences between these periodic systems [[Sigalas94](#), [Economou93](#)].

The measurements of the sound attenuation by a sculpture, by Eusebio Sempere, exhibited at the Juan March Foundation in Madrid (see [Figure 1.1](#)), constituted the first experimental evidence of the presence of BG in a SC [[Martinez95](#)]. The work of Martínez-Sala *et al.* [[Martinez95](#)] experimentally showed that the repetition of cylinder rods with a strong modulation (2D), inhibited the sound transmission for certain frequency ranges related to this modulation, just as photonic crystals do with light. Immediate theoretical predictions [[Kushwaha97](#), [Sanchez98](#)] and experimental results [[Robertson98](#)] were motivated by these experimental results in order to explain the propagation properties of this sculpture that could filter noise.

Since these acoustical properties were measured in that minimalist sculpture, a great research interest, both experimental and theoretical, have been emphasized on the existence of complete elastic/acoustic BG, opening possibilities to interesting applications such as elastic/acoustic filters, noise control, improvements in the design of transducers, as well as for the study of pure physics phenomena such as localization of waves. In the next Section, a review of the art state of the control of sound by periodic structures is presented, showing the most relevant bibliography used in the this work.

1.1 Control of sound propagation in sonic crystals

The study of acoustic wave propagation in periodic binary composites shows that BG can exist under specific conditions concerned mainly in the density and velocity contrast of the components of the composite, the volume fraction of one of the two components, the lattice structure and the topology [Kushwaha94, Sanchez98]. The presence of BG in SC is due to the well-known Bragg's scattering which represents a complex interplay between the wave velocity and density ratios of the composite materials, and their spatial arrangement. The emphasis in the acoustical properties of SC for frequencies high enough to distinguish the inner structure of the array marks the initial steps in the research on SC. A great research interest in the existence of spectral gaps in PC made of several materials, shapes and distribution of scatterers were witnessed in the 90's [Kushwaha96, Kushwaha97, Sigalas96, Vasseur97, Wang90].

Robertson *et al.* showed that photonic crystals present allowed states depending on the symmetry with respect to the incidence wave. In the acoustic counterpart, Sánchez-Pérez *et al.* [Sanchez98] showed that the excited modes inside the SC not only depends on the scatterers and the volume occupied by them, but also on the relationship between the incident wave and the field pattern of the mode to be excited. If the incident wave presents the proper symmetry to excite the mode, a propagating mode is excited. Otherwise the mode cannot propagate and the propagating band is called deaf band.

In the electromagnetic counterpart, it was observed that by locally breaking the periodicity of photonic crystals [Bayindir00] or creating impurities in a semiconductor [Yablonoitch91] it is possible to highly localize and guide modes within the BG. Motivated by these results an intense analysis of the localized modes in PC began with the work of Sigalas in 1997 [Sigalas97, Sigalas98]. These properties make the system a potential candidate for the design of elastic or acoustic waveguides or filters. Nowadays the analysis of the SC with point defect is still a hot topic in the relevant literature of this field [Tanaka07, Vasseur08, Zhao09, Wu09a, Wu09b, Romero10a].

1.1. CONTROL OF SOUND PROPAGATION IN SONIC CRYSTALS

In 1961 Suzuki discovered that some alkali halide can be doped with divalent cations to produce a new ionic compound with periodically distributed vacancies and lattice parameter roughly twice the original one [Suzuki61]. The compound was called the Suzuki phase and it retained properties of the initial compound and new properties arose as a consequence of the translational symmetry imposed by the vacancies. Years later, Anderson and Giapis [Anderson98] observed larger BG in PC by adding elements with different sizes inside the unit cell of square and honeycomb lattices and, as such, introducing a periodical distribution of vacancies in the PC. Motivated by these works, the same symmetry reductions were used to increase the BG in SC [Caballero99, Caballero01]: SC consisting of a rectangular lattice of vacancies embedded in a triangular array of sound scatterers in air present BG for sound transmission at frequencies related to the symmetry imposed by the vacancies and, at the same time, attenuation bands of the underlying triangular lattice still remain in the attenuation spectra at higher frequencies.

In 2002 the interest in the study of SC at wavelengths below the first BG started, i.e., in the frequencies where the wavelength is very large in comparison with the lattice constant. In this case the wave sees the media as if it were homogeneous [Cervera02]. The fact that a periodic distribution of cylindrical solid scatterers in air constitutes a system in which the sound travels at subsonic velocity was used by Cervera *et al.* to construct two refractive devices: a Fabry-Perot interferometer and a convergent lens. From this work, a controversy arose about the minimum size of the sample in which the refractive effects dominate over the diffractive ones [Garcia03, Hakansson05, Garcia05]. Moreover, additional theoretical works predicted the focusing effect of refractive devices [Kuo04, Hu05], showing that SC lenses must present low acoustic impedance contrast between the SC and the medium; otherwise acoustic waves will be mostly reflected. Then, the converging lens can be either convex or concave depending on whether the sound speed in the SC is smaller or greater than that in the medium.

The properties of the SC in the range of frequencies above the first BG, where the wavelengths are much lesser than the lattice constant in SC, were used by Yang *et al.* [Yang04] to introduce the negative refractive index in the field of the PC. The authors claim that the relationship between the phase velocity and

the wave vector in the second band suggests that both novel focusing and large negative refraction phenomena may occur. The work showed both theoretically and experimentally how a dramatic variation in wave propagation with both frequency and propagation direction led to novel focusing phenomena associated with large negative refraction.

On the other hand, several developments to obtain focalization with a slab of SC for frequencies below the first BG were made. The phenomenon of the negative refraction in SC was also observed in the range of frequencies below the first BG, having a strong dependence on the frequency and on the incident angles [Feng05]. However, as Hakansson *et al.* [Hakansson04] showed, it is possible to design acoustical devices to focus the sound at a predetermined focal distance without negative refraction. The presented methodology was an approach to the problem based on a stochastic search algorithm, especially a Genetic Algorithm in conjunction with the multiple scattering theory. Both acoustical [Hakansson05b] and optical [Hakansson05c] devices, as well as acoustic [Hakansson06] or optical [Hakanson05a] wavelength demultiplexers have been applications obtained using this optimization technique.

Propagation of waves through periodic system are mainly characterized by dispersion, but there is a fascinating effect, originally named self-collimation in which a beam propagates in the periodic system without apparent diffraction keeping its original size. This phenomenon has been experimentally demonstrated to date for different frequency ranges of electromagnetic waves, in particular in the optical [Rakich06] and microwave [Lu06] regimes. In the acoustic counterpart recent works have observed the subdiffractive propagation of sonic waves in phononic (or sonic) crystals [Perez07, Espinosa07]. It has come out that the spatial periodicity can affect not only temporal dispersion, but also the spatial one. Such subdiffractive sonic beams are supported by crystals with perfect symmetry, and do not require the presence of defects. The phenomenon is independent of the spatial scale and consequently it must be observable in other (e.g. audible) regimes, as well as in the 3D case.

The theoretical results of Veselago in 1968, in which the simultaneously negative permittivity and permeability were predicted to give a negative refractive index to the inhomogeneous medium, became a reality once Pendry *et al.*

1.1. CONTROL OF SOUND PROPAGATION IN SONIC CRYSTALS

[Pendry96, Pendry99] proposed materials which would have effectively negative permittivity and permeability. In the acoustic counterpart, simultaneously to the development of the refractive devices, the pioneering work of Liu *et al.* [Liu00a] provided the first numerical evidence of localized resonant structures for elastic waves in 3D arrays of coated spheres, and introduced the acoustic analogue of the electromagnetic metamaterials. Subsequently, several works proposed different kinds of scatterers to achieve locally resonant acoustic materials with negative properties: cylinders with split ring cross-section as building blocks [Movchan04], Helmholtz resonators [Hu05, Fang06] or C-shaped resonators [Guenneau07]. Similar double negative material was proposed by Li and Chan [Li05].

Electromagnetic metamaterials are structured at subwavelength lengthscales, typically one tenth of the wavelength, and it is possible to regard them as homogeneous and describe their response with dispersing effective medium parameters. The homogenization theories applied to determine the effective parameters of PC have become a topic of increasing interest in the last four years since Torrent *et al.* [Torrent06a] homogenized a SC using a methodology based on multiple scattering theory. This technique was used to design a broadband gradient index 2D sonic lens producing sound focusing with high intensity [Torrent07]. This technique could be used to achieve an acoustic metamaterial for cloaking acoustic waves.

Several theoretical methods were used for the analysis of the wave propagation through periodic media in all the aforementioned works. The initial works of the theoretical analysis of sound wave propagation in SC used plane wave expansion (PWE) [Sigalas93, Kushwaha93, Kushwaha94]. Making use of the periodicity of the system, one can expand the physical properties of the inhomogeneous media in Fourier series and, using the Bloch theorem, the wave Equation is transformed in a set of linear, homogeneous equations that constitutes an eigenvalue problem. Then, propagation properties of SC can be obtained. On the other hand, variational methods have also been used to calculate the acoustic dispersion relation in SC [Sanchez98, Rubio99].

The multiple scattering theory (transfer matrix methods), developed in the beginning of the 20th century by Závıška [Zaviska13] as a method of describing

the scattering of waves in finite arrays in 2D acoustic fields was applied to analyse the scattering of sound in finite arrays of scatterers by Sigalas and Economou in 1996 [Sigalas96]. A few years later the method was extended and improved by Chen and Ye [Chen01] and several modifications were used in the relevant literature of SC [Hakansson04, Umnova06].

Previous analytical methods work properly when the geometries of the scatterers are defined well and their radiation pattern can be characterized by well-known functions. Moreover, there is a variety of PC, specially for a composite of elastic media with large acoustic mismatch, for which the conventional PWE cannot be applied. Thus more efficient methods are necessary to characterize the propagation properties of PC. The first alternative was proposed by García-Pablos *et al.* [Garcia00], for using the finite-difference time domain (FDTD) method. The FDTD method is a popular numerical scheme for the solution of many problems in electromagnetics. Moreover FDTD method enables study of finite systems and to simulate the experiments in the same way as they are carried out.

From the experimental point of view the BG of SC were observed by means of several methods. The pioneering work of Martínez-Sala *et al.* [Martinez95] shows the measurement of the sound attenuation spectra observing the corresponding attenuation peaks in the proper frequencies depending on the incident direction of the wave. In other works, BG were characterized measuring the phase delay [Rubio99]. It was observed that the phase delay presents a linear dependence on frequency with a positive slope when the sound is transmitted inside the structure through a propagation mode, but it presents both a negative slope and an erratic behaviour for frequencies inside the BG. On the other hand, BG have also been analysed by studying the reflectance properties of SC observing full standing wave for the frequencies inside the BG [Sanchis01].

1.2 Object and motivation of the work

One of the main practical applications of SC is the design of attenuation devices, like for example, acoustic barriers made of periodic arrays of scatterers. The seminal work of Sánchez-Pérez *et al.* [Sanchez02] showed that these structures produce fairly good sound attenuation values, able to acoustically compete with conventional acoustic barriers, presenting some important advantages: they are very light and easy to built, and they allow the control of sound propagation properties by changing the characteristics of the lattice or the scatterers. However, further investigations are needed in order to improve the attenuation properties.

Recent works of Umnova *et al.* [Umnova06], Martínez-Sala *et al.* [Martinez06] and Romero *et al.* [Romero06] started the improvement of the attenuation properties of the array of scatterers, and the application of SC as the acoustic barrier has received increasing interest in the recent years.

The main object of this work deals with longitudinal waves propagating in 2D distribution of infinitely long scatterers of different cross sections and showing different acoustical properties. Using the possibility for control of the wave propagation by both the distribution of the scatterers and the intrinsic acoustical properties of the scatterers, several structures and scatterers are presented in this work in order to improve the acoustical properties of the whole structure. In this work almost all the structures have been analysed both experimentally and theoretically. This work was motivated by the results previously obtained by several authors in recent years.

In the following Sections we show the goals of this work as well as their relation to the references which are the main motivations of this work.

Studying the evanescent modes and point defects in sonic crystals

The abstract concept of SC involves infinite periodic replications of a base in

the space, producing an infinite system. The BG produced by these systems are understood as ranges of frequencies where any vibrational mode inside the crystal can be excited [Kushwaha94]. However in finite systems the situation is different. Joannopoulos *et al.* [joannopoulos08] introduced for the first time an interpretation of the behaviour of waves inside the BG in terms of evanescent modes. These modes cannot be excited in infinite systems because they do not satisfy the translational symmetry.

On the other hand, the only way to observe this evanescent behaviour in infinite systems is by means of the locally breaking of the translational symmetry of the SC. Point defects, as for example removing one scatterer, locally break the periodicity of the system and introduce localized modes within the BG inside the point defect. These modes are localized because the defect is surrounded by complete crystal and they have evanescent behaviour inside the periodic system. The generation of N_p vacancies (N_p being much lower than the total number of scatterers of the structure N_{cyl}) in periodic systems introduces a rich amount of physics phenomena: from the localized modes in point defects [Sigalas97] to the splitting of localized frequencies in multi-point defects [Li05] or to the application for the generation of waveguides [Sigalas98] or high precision acoustic filters [Khelif03, Khelif04, Vasseur08].

To the best of our knowledge, the physical consequences of point defects in SC have always been explained theoretically in terms of infinite periodic systems. However, in real situations, one can only work with finite systems and the theoretical physical properties of the system can only be approximated in some cases using the finite systems: the bigger the system the more approximated the properties predicted by the theoretical methods of infinite systems are. Thus the evanescent behaviour of modes in the BG or of the localized modes has hardly been taken into account.

The aforementioned arguments motivated an extension of the plane wave expansion [Kushwaha94] in order to analyse the evanescent behaviour of both modes in the BG in complete systems and localized modes in point defects. In this work we extend the plane wave expansion to analyse both complete systems and systems with N-point defects. The several physical effects appearing in the transition from one point defect to N-point defects in SC are

analysed in this work in terms of their evanescent behaviour. The description and the theoretical model have been richly complemented by very recent works devoted to the complex dispersion relation of SC [[Sainidou05](#), [Hsue05](#), [Sainidou06](#), [Laude09](#)]

Optimizing the scattering process in sonic crystals

One of the main motivations of this work comes from the works of Caballero *et al.* [[Caballero99](#), [Caballero01](#)] in which the Suzuki phase is used to introduce new attenuation bands in periodic systems. It is interesting that lattices of vacancies embedded in a SC can be used as a mechanism of sound control in these materials. On the other hand, another important motivation is the methodology presented by Hakansson *et al.* [[Hakansson04](#)] based on genetic algorithms to improve the scattering process inside the array of rigid scatterers in order to focalize sound in a predetermined point. Basically, Hakansson *et al.* looked for a distribution of vacancies that optimizes the scattering problem to accomplish some objectives.

In contrast with SC with point defects where $N_p \ll N_{cyl}$, for the cases of the Suzuki phase and optimized devices using genetic algorithms, $N_p \sim N_{cyl}$. In this last case, if the N_p defects present a periodicity (Suzuki phase) one can predict the physical effects of this array of vacancies using their periodicity, however if the N_p vacancies are produced without periodicity only the solution of the scattering problem can provide information about the response of the structure. One also can use statistical parameters based on the distribution of the vacancies to explain the physical behaviour of the structure.

Thus the immediate question is: Is the Suzuki phase the best distribution of vacancies to add new attenuation bands? In this work this question is analysed using an improved optimization algorithm based also on genetic algorithms, considering a multi-objective problem and as such several properties can be simultaneously improved by creating vacancies. We analyse the dependence of the improvement of the acoustical properties on the symmetry of generation of vacancies, therefore several symmetries for the distribution of vacancies in

the SC have been analysed, obtaining some general rules for the optimization of the attenuation properties by removing scatterers of the structure.

Designing scatterers with additional acoustical properties for their use as building blocks of sonic crystals

The pioneering work of Liu *et al.* [Liu00] not only paves the way towards the analogous acoustic metamaterial, but it proposes a new way to introduce additional stop bands in the propagation properties of the periodic systems making use of the resonant properties of the scatterers. The additional stop bands are determined by the intrinsic structure of the scatterers, and the depth of the sound attenuation bands increases proportionally with the number and density of local resonators. Moreover the resonant frequencies can be tuned by varying their size and geometry. Interesting works in the range of the audible frequencies were presented by Hirsekorn [Hirsekorn04a, Hirsekorn04b].

In recent years not only scatterers with resonant properties have been designed for their use in SC, but scatterers with absorbent materials have also been analysed by Umnova *et al.* [Umnova06]. The authors observed that the absorbent covering reduces the variation of transmission loss with frequency due to the stop/pass band structure observed with an array of rigid cylinders with similar overall radius and improves the overall attenuation in the higher frequency range.

Motivated by the previous works, the possibility of designing simple models of locally resonant absorbent materials made of ordinary, conventional material and, in some cases recyclable materials, is analysed in this work. The periodic systems made of these materials could efficiently be used to build attenuation devices. Using the absorbent properties of the scatterers it should be possible to introduce a high overall attenuation, meaning that, a threshold of attenuation. On the other hand, the resonant properties of the scatterers could be used to introduce attenuation peaks in regions of frequency where the attenuation produced by the distribution of absorbent scatterers is deficient. Thus, scatterers with absorbent and/or resonant properties could introduce a new

design possibilities.

Combining scattering, resonances and absorption in sonic crystals

As it can be seen, one can improve the acoustical properties of SC using two different mechanisms. One is the generation of a distribution of vacancies and the other one is the inclusion of scatterers with additional properties. But, can we use both methodologies together, in such a way the inclusion of the scatterers with acoustical additional properties in the distribution of vacancies can act simultaneously without interfering between the properties of the individual scatterers? If the answer is affirmative, this mechanism could be used to combine several effects in the same periodic system. The question is also analysed in this work.

1.3 Overview of the work

A concise description of the organization of the contents in this work is shown in this Section. The document has been split in 10 Chapters and 4 Appendixes.

Chapter 2 is devoted to the fundamentals of periodic systems showing their main properties. The nomenclature and some important parameters used through the work are briefly shown.

Chapter 3 introduces the theoretical methods used in this work for the analysis of the wave propagation through SC: multiple scattering theory (MST), plane wave expansion (PWE), extended plane wave expansion (EPWE) and finite element methods (FEM). MST, especially the 2D scattering by circular cylinders, is shown. The explicit matrix formulation, useful to programme codes like, for example, MATLAB, is described considering both plane and cylindrical incident waves. We have described the main characteristics of PWE for the calculation of the dispersion relation $\omega(\vec{k})$ of SC. The extensions

to consider the inverse complex problem $k(\omega)$ and the supercell approximation for studying arrays with defects constitutes a fundamental point in this Chapter. Finally in this Chapter, we show the description of FEM to calculate the dispersion relation and the scattering problem of SC made of scatterers with irregular cross-sections or with different materials in this Chapter. Note that through Chapter 3 we present several comparisons between the results obtained using each theoretical method.

The optimization algorithm used in this work is shown in Chapter 4. It shows the fundamentals of genetic algorithms (GA) and how the genetic operators produce the distribution of vacancies in the SC. The Chapter describes both the simple Genetic Algorithm (only one objective function is optimized) and the multi-objective problem (several objective functions are simultaneously optimized). Finally a procedure to reduce the computational time of the optimization process is shown explaining a methodology of parallelization.

The experimental measurements are fundamental in this work. The most of the theoretical results of this works have been experimentally tested. The experimental setup is shown in Chapter 5. During the development of this work two different experimental setup were used. Both are described and a detailed description of the sound sources, the microphones and the accelerometers is also given. All the scatterers and the SC experimentally used are detailed in the last part of the Chapter.

In Chapters 6 and 7 we analyse the creation of vacancies in SC. We distinguish between two different situations: (i) low number of vacancies with respect to the total number of cylinders ($N_p \ll N_{cyl}$), where one can use periodicity of the crystal and the locally breaking periodicity to explain the behaviour of the system (localization, symmetry of the vibrational patters, splitting in frequencies,...). And (ii) High number of vacancies and, as such, the number of vacancies in the same order as the number of cylinders in the structure ($N_p \sim N_{cyl}$).

In Chapter 6 we show the transition from a single point defect to N-point defects in the SC. Using MST, PWE, FEM and particularly EPWE we show a complete picture of the physical phenomenon of both the evanescent behaviour of modes inside the BG in complete SC and the localization of sound

in N-point defects, showing the localization of the evanescent behaviour of the localized modes and the splitting in frequencies for multi-point defects. These properties of SC with point defects have been complemented with novel theoretical and very accurate experimental description of their evanescent behaviour.

On the other hand, random defect creation is shown in Chapter 7. Here, we present the results of the optimization of SC by removing scatterers for both attenuation and focalization devices, generating the Quasi-Ordered Structures (QOS). We define some parameters based on the optimization process and on the geometry of the QOS that can help to characterize of these devices. We also describe the dependence of the optimization process on the symmetry of the generation of vacancies. From the results of the optimization, we show a list of general rules to create vacancies in SC in order to improve their attenuation properties. These rules were experimentally tested in good agreement with the predictions.

The use of scatterers with acoustical properties added as building blocks of SC is shown in Chapter 8. Several proposals of scatterers with elastic or cavity resonance properties are presented in order to improve the attenuation properties of the SC below the first BG. A brief discussion, motivated by the homogenization theories in the electromagnetic field, on the effective parameters of a SC made of a kind of elastic-acoustic resonance is also presented.

Chapter 9 analyses several engineering aspects of SC. In this Chapter one can find the answer to the previous question: can we include scatterers with acoustical additional properties in the distribution of vacancies of the optimized structures without destroying both effects? Finally a proposal of SC combining absorption, resonances and multiple scattering is shown as a good alternative to the classical acoustic barriers.

Finally Chapter 10 summarizes the work, showing the most important conclusions and introducing the possibilities for a future work.

1.3.1 Bibliographic notes

The references of this work are mainly research articles or books. In order to differentiate them we have used the following nomenclature: articles are referenced writing the name of the first author in capitals; books are referenced typing the name of the first author in lowercases.

2

Fundamentals of periodic systems

Propagation of waves inside periodic structures has received increasing attention in the last years [[Martinez95](#), [Yablonovitch89](#), [John87](#), [Economou93](#)]. Since extraordinary phenomena were observed in a periodic sculpture in 1995 [[Martinez95](#)], the enthusiasm for these systems appears due to their applications in several branches of science and technology [[Yang04](#), [Sanchez02](#), [Soukoulis06a](#)].

In a medium with many several scatterers, waves will be scattered by each scatterer, and then the scattered waves can be scattered again by other scatterers. This process is repeated to establish an infinite iterative pattern forming a multiple scattering process. If the scatterers are placed periodically in the space, the multiple scattering process leads to some interesting physical properties, leading to several applications: Waveguides [[Kafesaki00](#)], lenses [[Kuo04](#)], filters [[Sanchez98](#)], multiplexors [[Hakansson06](#)], ... among others applications in optics, electromagnetism and acoustics.

The fundamentals of wave propagation in periodic systems are presented in this Chapter. We pay special attention to the two-dimensional periodic systems, because they are the subject of this work. The Chapter is based on the references [[kittel04](#), [joannopoulos08](#), [kosevich05](#), [soukoulis93](#), [soukoulis01](#), [brillouin46](#)].

2.1 Periodic systems

2.1.1 Geometric properties

The infinite periodic distribution of a *base* constitutes a periodic system. The sites where the base are placed are called lattice. A particular lattice \vec{R} in \mathbb{R}^n is defined in such a way the periodic system is equally observed from any point of the lattice, this means that, the system is invariant under translations and, sometimes, under rotations. Using group theory it has been proved that there is a unique one-dimensional (1D) periodic system, five two-dimensional (2D) and fourteen three-dimensional (3D) different lattices.

The concept of periodic system is a mathematical abstraction that implies the existence of an infinite structure or an infinite medium. However, in nature one cannot find infinite systems, but some examples may mimic the periodic systems. For instance, crystalline structures can be studied as periodic media using periodic boundary conditions if the crystal accomplishes some approximations. For example the size of the crystalline structure should be much smaller than the wavelength of the wave used to explore the crystal. In Figure 2.1 one can see some examples of real systems that can be considered periodic. 1D periodic systems present the periodicity only in one direction; in 2D, the periodicity appears in two directions being homogeneous in the third dimension; finally, a 3D periodic system presents its periodicity in the three dimensions of the space. In Figure 2.1 examples of the three types of periodicity are shown.

Considering that \vec{a}_i are the vectors defining the lattice \vec{R} in \mathbb{R}^n with $i = 1, \dots, n$, thus \vec{R} could be defined as:

$$\vec{R} = \left\{ \sum_{i=1}^n v_i \vec{a}_i \right\}, \quad (2.1)$$

where $v_i \in \mathbb{Z}$. The parallelepiped defined by the vectors \vec{a}_i forms the well known *primitive cell*, which is a particular kind of *unit cell*. The translation of the unit cell following the vectors \vec{a}_i in the space produces the lattice of the

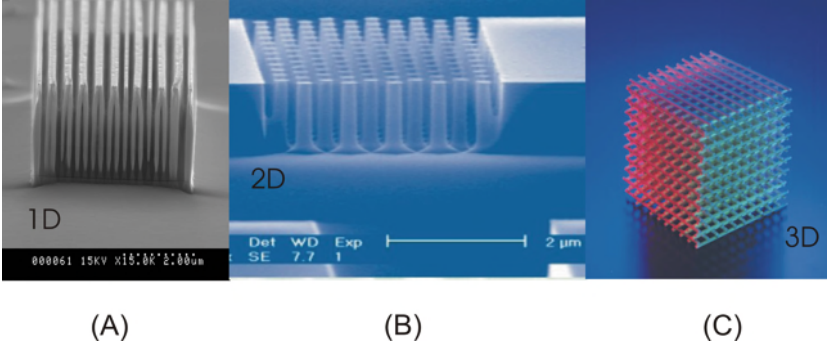


Figure 2.1: Examples of periodic systems: (A) 1D, (B) 2D and (C) 3D. The Figures correspond to Photonic crystals.

periodic system. As the periodic replication is done in the direct space, the lattice \vec{R} is called the lattice of the direct space, or direct lattice.

Associated with the direct lattice, the reciprocal lattice is defined and it may be used for better understanding of the physical properties of these systems. The vectors of the primitive cell in the reciprocal lattice are defined from the vectors of the direct lattice via the following expression

$$\vec{b}_i = 2\pi \frac{\epsilon_{ijk} \vec{a}_j \times \vec{a}_k}{\vec{a}_1 \cdot (\vec{a}_2 \times \vec{a}_3)}, \quad (2.2)$$

where ϵ_{ijk} is the completely anti-symmetric Levi Civita symbol. Both the vectors of the direct and the reciprocal arrays satisfy a relationship of orthogonality: $\vec{a}_i \cdot \vec{b}_j = 2\pi \delta_{ij}$. Any linear combination $\vec{k} = \left\{ \sum_{i=1}^n \mu_i \vec{b}_i \right\}$ with $\mu_i \in \mathbb{Z}$, reaches a point of the reciprocal lattice.

The five periodic lattices that can be constructed in the case of 2D ($n = 2$)¹ have been shown in Figure 2.2A: Oblique, square, triangular, rectangular and centered. Among all of these arrays, both the square and the triangular arrays are the most important for this work.

The lattices are usually characterized by the well known *lattice constant*, a ,

¹more information about these kind of lattice and the usual nomenclature can be found in the reference [kittel04]

CHAPTER 2. FUNDAMENTALS OF PERIODIC SYSTEMS

that, in the case of both triangular and square lattices, corresponds with one of the vectors of the base \vec{R} , $a = |\vec{a}_i|$. The lattice constant is crucial in such periodic systems because it defines the relationship between the geometrical properties of the lattice and one of the most important physical property related to the propagation features of such systems, the *Band Gaps*, defined in the Section 2.1.2.

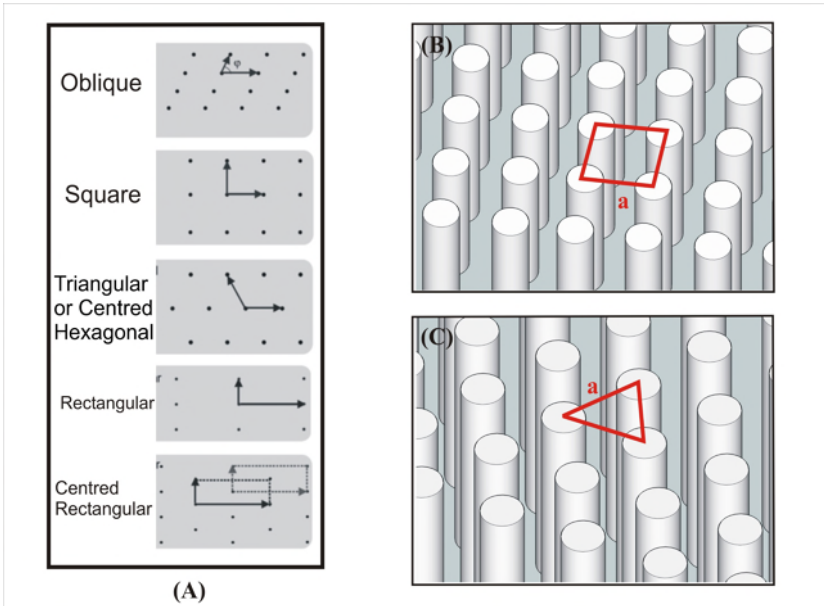


Figure 2.2: 2D periodic systems. (A) 2D lattices. (B) Square lattice. (C) Triangular lattice (also called hexagonal lattice).

Once the lattice constant and the size of the scatterers are known, one can define the *filling fraction* (ff) as a geometrical parameter that, in the same way as the lattice constant, presents a direct relationship with the physical properties of the system. The ff is defined as the ratio between the volume occupied by the scatterers and the total volume occupied by the unit cell. If cylindrical scatterers with radius r_0 are considered, the ff 's for both the

square and triangular lattices are respectively,

$$f_{square} = \frac{\pi r_0^2}{a^2}, \quad (2.3)$$

$$f_{triangular} = \frac{2\pi r_0^2}{\sqrt{3}a^2}. \quad (2.4)$$

2.1.2 Wave propagation

The Schrödinger equation in quantum mechanics, the Maxwell equations in electromagnetism, the vectorial equation of Navier for elasticity and the wave equation in acoustics present the same type of solution when they are solved for periodic system. Bloch's theorem² affirms that the solutions of the equations in such periodic systems present the same periodicity as the structure except in phase [kittel04]. This means that, the discrete periodicity of the lattice produces a solution of the problem which is a function presenting the same periodicity as the lattice, $\psi_{\vec{k}}(\vec{r})$, multiplied by a plane wave, $e^{i\vec{k}\vec{r}}$, where \vec{k} is the so-called the Bloch vector. Thus, the solution, $\Theta_{\vec{k}}(\vec{r})$, provided by the Bloch theorem for scalar waves in periodic media is³

$$\Theta_{\vec{k}}(\vec{r}) = e^{i\vec{k}\vec{r}}\psi_{\vec{k}}(\vec{r}). \quad (2.5)$$

It is possible to make an explanation of this solution with a simple image: a plane wave, as it would appear in the free space, but modulated by a function with the same periodicity as the lattice. It is said that $\psi_{\vec{k}}$ is a Bloch state and \vec{k} represents the Bloch vector.

The state of Bloch, for all the vectors of the direct lattice \vec{R} , accomplishes

$$\Psi_{\vec{k}}(\vec{r}) = \psi_{\vec{k}}(\vec{r} + \vec{R}). \quad (2.6)$$

²In solid-state it is known as Bloch theorem, but in Mechanics it is known as Floquet theorem. For this reason, in some references it is called Floquet-Bloch theorem. Here it is called Bloch theorem.

³In this thesis we are interested in the propagation of acoustic waves through periodic systems, where the medium only supports scalar waves (longitudinal). From here on we adopt the notation for scalar waves

CHAPTER 2. FUNDAMENTALS OF PERIODIC SYSTEMS

Thus, the field in each unit cell of the direct space presents the same distribution. This property has an important consequence on the solution of the problem: By applying the proper boundary condition we can solve the problem only in a unique unit cell in the direct space.

On the other hand, vectors \vec{k} that have to be considered to solve the problem are also constrained. It should be noted that the state of Bloch for a vector \vec{k} is the same as the vector $\vec{k} + \vec{G}$ if \vec{G} is a vector of the reciprocal lattice [kittel04]. If we take into account that the vector \vec{k} gives the phase shift between the unit cells, then if \vec{k} is incremented in a vector of the reciprocal lattice \vec{G} , the phase shift is incremented in $\vec{R} \cdot \vec{G} = 2m\pi$, m being an integer. Thus, there is no phase shift and there are redundant values of vector \vec{k} . In the same way as solutions are constrained in a unit cell in the direct lattice, in the reciprocal lattice it is said that the calculation is constrained to the *first Brillouin zone*. The first Brillouin zone is a uniquely defined primitive cell in reciprocal space. The boundaries of this cell are given by planes related to points in the reciprocal lattice [kittel04].

To interpret the solution of the scalar wave equation in a periodic medium, the wave equation in an acoustic medium with harmonic temporal dependence of type $e^{i\omega t}$ is considered:

$$\nabla^2 p(x, y, z) + \frac{\omega^2}{c^2} p(x, y, z) = 0, \quad (2.7)$$

where, $p(x, y, z)$ is the acoustic pressure, c is the sound velocity and ω is the angular frequency of the wave. The solution of this equation in the free field, considered as isotropic and homogeneous medium is the type of $e^{i\vec{k}\vec{x}}$, where $|\vec{k}| = \omega/c$ is the absolute value of the wave vector of the wave in free field and depends on the frequency with a linear relationship.

In the case of solving the equation in a periodic medium, the Bloch theorem indicates the solution. The governing equation of the process is the wave Equation 2.7 solved considering the periodic Bloch boundary conditions, which means that

$$\nabla^2 p_k(\vec{r}) + \left(\frac{\omega(\vec{k})}{c} \right)^2 p_k(\vec{r}) = 0, \quad (2.8)$$

with the Bloch boundary condition,

$$p_k(\vec{r} + \vec{R}) = p_k(\vec{r})e^{i\vec{k}\vec{R}}. \quad (2.9)$$

where the vector \vec{k} takes values in the first Brillouin zone. The Equation 2.8 is solved in the space occupied by a unit cell. In this case, the vector \vec{k} can be interpreted as an indicator of the propagating mode (band). Actually, \vec{k} is the wave vector inside the periodic media. Then the dispersion relation $\omega(\vec{k})$ could be different than in the free field.

The solution of the eigenvalue problem, defined by equations 2.8 and 2.9, gives an infinite discrete number of eigenvalues $\omega(\vec{k})$ for each value of \vec{k} , and they represent the frequencies of the possible modes supported by the unit cell. These frequencies are discretely separated, and we can mark them with the *band index* n ; then, each band is a continuous function $\omega_n(\vec{k})$. The representation of ω versus k for a given n , is a continuous function that represents the dispersion relation of the band n . Thus, band structures can be seen as a group of continuous functions discretely separated, that represents the dispersion relation of the medium.

In Figure 2.3 one can see the band structures for a square lattice of rigid cylinders with radius $r = 0.07$ m and lattice constant $a = 0.15$ m, which represents a filling fraction $ff \simeq 68.4\%$. We represent the frequency versus the Bloch vector scanning the borders of the first irreducible Brillouin zone shown in the inset. Each colored line represents a band of allowed states, that can be excited with a wave with the corresponding frequency represented in the vertical axis.

The calculation of the band structures of a periodic system is extensively analysed in the bibliography [Meade92, joannopoulos08]. In Chapter 3 of this work, we briefly present some of the most used methods plane wave expansion (PWE) [Kushwaha94] and finite element methods (FEM) [ihlenburg98]. There are other methods, like for example the finite difference time domain (FDTD) [Sigalas00], for the calculation of the band structures.

Due to the periodicity of the considered system, the band structures show several interesting properties. One of them is the presence of the Band Gaps

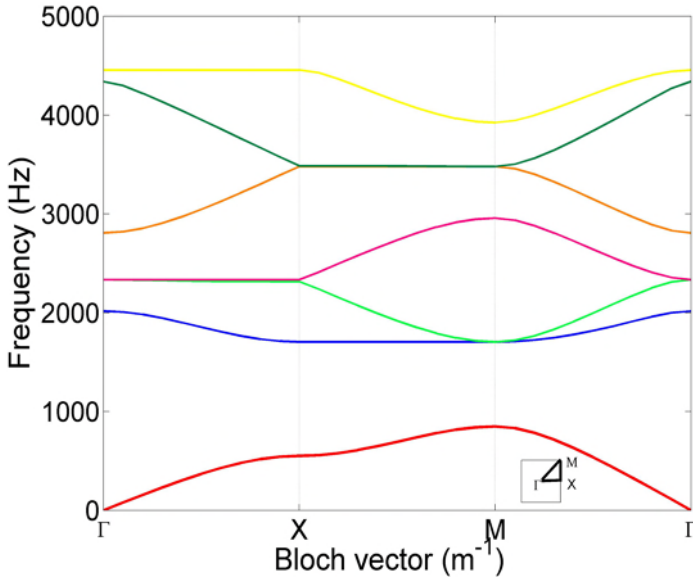


Figure 2.3: Band Structure of a square lattice of rigid cylinders with radius $r = 0.07$ m and lattice constant $a = 0.15$ m. $ff \simeq 68.4\%$

(BG), ranges of frequencies where sound propagation through the periodic system is not allowed. The BG are necessary for some important applications of these structures such as filters for trapping or guiding waves. On the other hand, as we will see later, the generation of point defects in crystals breaks the symmetry of the lattice and produces localized states, defined as modes that are localized around the point defect and presenting an evanescent behaviour inside the system. These properties open the door for applications as high precision filters or wave guides.

Apart from these properties, other interesting effects can appear in periodic systems. For example surface waves or negative refraction (left handed materials), that can be used to focalize the wave in a point behind the structure.

In the next Section the concepts of the BG and the localized states will be briefly explained. The Chapter is based on [joannopoulos08, soukoulis93, soukoulis01].

2.1.2.1 Band gaps

In order to understand how the periodic system influences the propagation of waves, several periodic structures with different configurations are considered. First, the weak interaction between the wave and the periodic lattice considering infinitesimal scatterers is analysed. After increasing the size of the scatterers, one can observe the effect of the periodicity over the propagation properties of the wave. Also the dispersion relation of waves by 2D periodic structures is presented. Similar analysis is done in [joannopoulos08] for 1D periodic systems.

We consider a square lattice of infinitesimal scatterers. The behaviour of waves, propagating in such periodic system should be very close to a wave propagating in a free field, which dispersion relation is $\omega = c|\vec{k}|$. Then, the band structures will consist in linear relations between ω and k . To show this, the band structure of rigid scatterers with very small radius ($r = 0.0001$ m) placed in square array has been calculated. The periodicity used in all of the calculations of this Section is $a = 0.15$ m.⁴ Figure 2.4A represents the band structures calculated using plane wave expansion (introduced in Chapter 3). One can observe in Figure 2.4A the lineal behaviour of the band structure for this periodic system. Each band represents a propagating mode, and it can be observed that, in this case, all of them are connected, therefore all frequencies are propagated through the structure. Moreover the linear behaviour of the bands shows that the medium can be considered as quasi free space propagation.

An increase in the radius of the scatterers, for instance, to $r = 0.03$ m, has now been considered. The band structure corresponding to this new configuration is shown in Figure 2.4B. The results are similar to the ones obtained for the lattice with small scatterers but now some discontinuities appear in points X and M . These discontinuities are called pseudogaps. For the filling fraction analysed in this case only the pseudogap at ΓX direction can be observed in the band structures. Regarding the ΓM direction, theory predicts the existence

⁴We could perform the calculations with non dimensional parameters based only on the filling fraction, but we use dimensional parameters for the easy understanding of the results.

of two bands in the range of frequencies near point M (second and third bands in Figure 2.4B) that would produce the transmission of waves. However, the existence of the *deaf bands* [Sanchez98] could produce a pseudogap at ΓM direction. Transmission bands can become deaf bands depending on the kind of incidence of the waves. The pressure field pattern of the eigenmodes at point M for the second (blue line) and third band (green line) presents determined symmetries that can be excited by the correct incident wave with the appropriate symmetry [Sanchez98]. For example, the mode of the second band presents the proper symmetry to be excited by an incident plane wave travelling along the ΓM directions, however the pressure field of the mode of the third band in point M has the planes of equal phase along the perpendicular direction and consequently cannot be excited by such a wave. Then, in this case, the third band (green line) can be called deaf band and a pseudogap appears in the ΓM direction.

Thus, in each main direction of symmetry⁵ of the periodic structure, ΓX and ΓM , one could observe a pseudogap. The upper and lower bounds of the pseudogaps in each direction of symmetry are marked with black arrows in Figure 2.4B. Between these boundaries of the pseudogap, there is no frequency that excites a propagating mode inside the structure in the ΓX direction.

The pseudogaps for the square lattice appear at points $\vec{k}_{\Gamma X} = (\pi/a, 0)$ and $\vec{k}_{\Gamma M} = (\pi/a, \pi/a)$, which define the limits of the irreducible Brillouin zone. From these points and with the relation $|\vec{k}| = \frac{2\pi\nu}{c_{host}}$, one can obtain approximate values for the frequencies of the pseudogaps:

$$\nu_{\Gamma X} = \frac{c_{host}}{2a} \quad (2.10)$$

$$\nu_{\Gamma M} = \frac{c_{host}}{\sqrt{2}a} \quad (2.11)$$

where c_{host} is the sound velocity in the host medium⁶.

We consider now scatterers with bigger radius than in the previous periodic

⁵borders of the irreducible first Brillouin zone [kittel04].

⁶In the case of triangular lattice, the points where the discontinuities appear are: $\vec{k}_{\Gamma X} = (\pi/a, 0)$ y $\vec{k}_{\Gamma J} = (\pi/a, \frac{\pi}{\sqrt{3}a})$. Thus, the Bragg's frequencies are $\nu_{\Gamma X} = \frac{c_{host}}{2a}$ and $\nu_{\Gamma J} = \frac{c_{host}}{\sqrt{3}a}$.

structures, $r = 0.07$ m. The transmission bands obtained are represented in Figure 2.4C. One can observe that the pseudogaps in each main direction of symmetry present some intervals of frequencies in common, meaning that, the pseudogaps are coupled forming the so-called BG (or full BG). The green area in Figure 2.4C shows the BG of an square lattice with $a = 0.15$ m and $ff = 0.68$. Inside the BG no propagating modes are excited in the crystal. By increasing the radius of the scatterers, the filling fraction also increases and the pseudogaps become wider. Then the coupling between the pseudogaps in each main direction can create a BG.

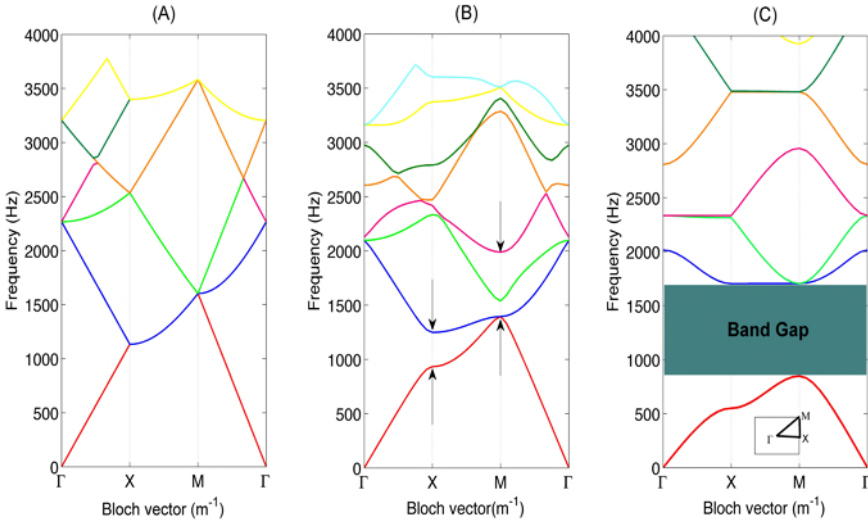


Figure 2.4: Band Structure of rigid cylinders. (A) Square lattice with infinitesimal radius and lattice constant $a = 0.15$ m in air. (B) Square lattice with $r = 0.03$ m and lattice constant $a = 0.15$ m. (C) Square lattice with $r = 0.07$ m and lattice constant $a = 0.15$ m.

We note that the transmission bands are curved for frequencies close to the BG, this means that, these frequencies present a stronger dispersion. There is a useful representation for analysing such effect, the isofrequency contours. They represent the lines of equal frequencies of one transmission band of the dispersion relation, $\omega(k_z, k_{norm})$, with $k_{norm} = (k_x, k_y)$, inside the first Brillouin zone. The diffraction in SC is ruled by the dispersion relation and is due to the

dephasing of the waves during propagation. The group velocity of the wave is determined by the gradient of the frequency in k -space, $v_g = \nabla_k \omega(k)$. As a consequence, for a given time and space frequency component, the power propagates along the perpendicular direction of the spatial dispersion curves or isofrequency surfaces $k_z = f(\omega(k_{norm}))$. During a finite propagation distance l , the phase accumulated is $\phi = k_z(k_{norm})l$. In geometrical terms, the spatial dispersion curve is characterized by its curvature at each point, resulting in a corresponding diffracting broadening of the beam. References [Perez07, Espinosa07] explain the relationship between the way of dispersion and the curvature of the isofrequency curves.

In Figure 2.5, the equifrequency contours of the first band of each periodic system represented in the Figure 2.4 are shown. Here, one can see how the curvature of the band changes in the region close to the borders of the first Brillouin zone as the filling fraction increases. Circular equispaced contours represent linear dispersion relationship.

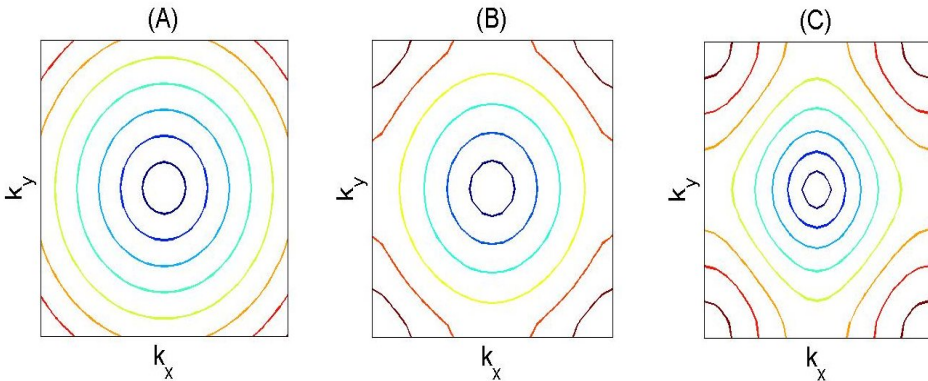


Figure 2.5: Isofrequency surfaces of the first transmission band for the square lattice with lattice constant $a = 0.15$ m and (A) infinitesimal radius, (B) $r = 0.03$ m and (C) $r = 0.07$ m

Up to now, the creation of the BG in periodic media has been analysed, but what happens when a wave with a frequency ω impinges the periodic system? We consider that the frequency ω is outside the BG (or pseudogap in a determined direction of symmetry), then this frequency can excite a propagating

mode, characterized by k , related to ω by the band structures corresponding with the transmission band. In this case, the wave can travel through the crystal. However, if the frequency ω is inside the BG, the situation is absolutely different and there is no excited k that allows the propagation of the wave through the periodic system. Then the existence of BG is indicated by the absence of bands in determined ranges of frequencies. In the next lines, we describe briefly this last case.

As we have seen the BG is ranged between the first ($n = 1$) and the second ($n = 2$) bands. By expansion of the second band in powers of k around the edge $k = \pi/a$, Joannopoulos *et al.* [joannopoulos08] explain the BG as ranges of frequencies where modes are characterized by complex wave vectors. Expanding the second band of the Figure 2.4C (blue line):

$$\Delta\omega = \omega(k) - \omega\left(\frac{\pi}{a}\right) \simeq \alpha\left(k - \frac{\pi}{a}\right)^2 = \alpha(\Delta k)^2 \quad (2.12)$$

For frequencies above the upper bound of the BG, Δk is purely real because $\Delta\omega > 0$, then the wave is in the second band and a propagating mode exists. However, for frequencies below the upper bound of the BG, which are frequencies in the BG, $\Delta\omega < 0$, and then, Δk is purely imaginary. Then, the modes inside the BG are characterized by complex Bloch vectors, $k + i\kappa$. Moreover, the imaginary part of the wave number for frequencies inside the BG grows for values of frequency closer to the center of the BG and disappears at the edges of the BG. From Equation 2.5 we can observe that a complex value of the Bloch vector, \vec{k} , introduces a negative exponent because of the imaginary part of \vec{k} and the modes present evanescent behaviour. This indicates that the rate of decay is bigger for frequencies closer to the center of the BG. In such situation, the modes inside the BG exponentially decay when they penetrate a crystal.

Some recent techniques, like the extended plane wave expansion (EPWE) [Hsue05, Laude09, Romero10b], presented in Chapter 3, allow the analysis of the imaginary part of the band structures. Using EPWE method the relation $k(\omega)$ is obtained with k being probably complex and without any restriction of periodicity. In Figure 2.6 we represent the real and the imaginary band structures for a periodic system with square lattice $a = 0.15$ m and cylindrical

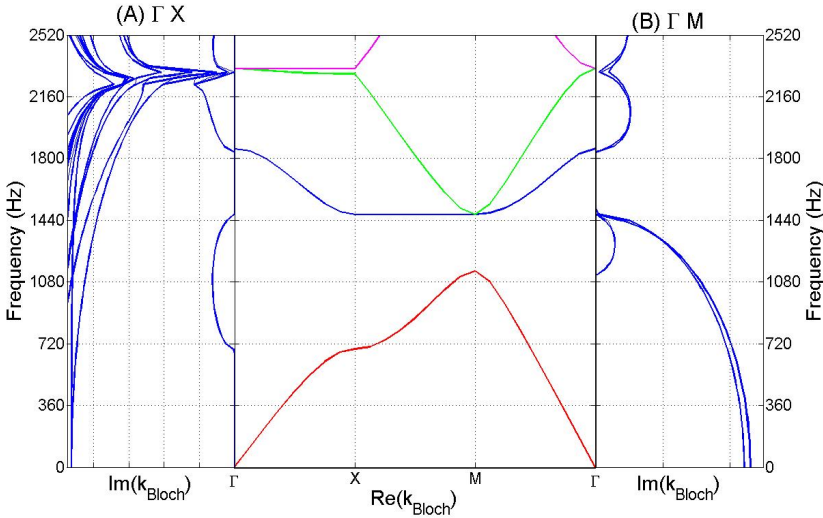


Figure 2.6: Complex band structures for a SC with square lattice with lattice constant $a = 0.15$ m and cylindrical scatterers with radius $r = 0.06$ m

scatterers with radius $r = 0.06$ m. In this Figure, one can see that modes inside the BG present complex wave vectors. In Figure 2.6 one can observe in ΓX and in ΓM directions that the imaginary part of the wave number for frequencies inside the BG grows with values of frequency closer to the center of the BG, and disappears at the edges of the BG, i. e., the rate of decay is bigger for frequencies closer to the center of the BG, as it was predicted by Joannopoulos *et al.* [joannopoulos08]. Also it can be observed that imaginary part of the wave vector connects propagating bands, conserving the overall number of modes.

This evanescent behaviour of the modes inside the BG has also been recently measured in [Romero10a]. In Figure 2.7 we have presented novel experimental measurements of the absolute value of the pressure inside SC for propagating and evanescent modes. The inset of the Figure 2.7 shows the measured points in steps of 1 cm placed between two rows of cylinders inside the SC made of rigid cylinders with square periodicity, $a = 0.22$ m. Connected blue squares represent the absolute value of the pressure for a frequency outside the BG, 442 Hz. This frequency represents a propagating mode inside the

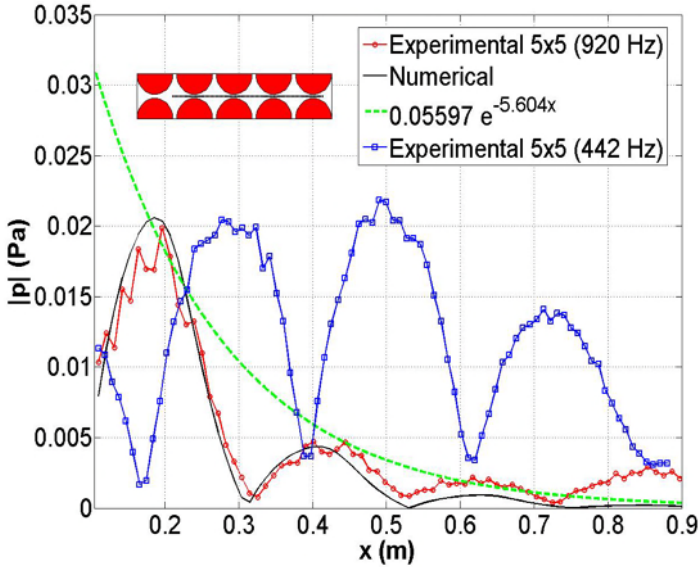


Figure 2.7: Absolute value of the pressure inside SC in the positions between two rows. Blue squares represent these values for a frequency outside of the BG, 442 Hz. Red circles represent these values for a frequency inside the BG, 920 Hz. The green line represents a decay exponential fit to the evanescent mode inside the BG. The black continuous line represents the absolute values of the pressure obtained using the Finite Element Methods.

SC. Connected red circles represent the absolute value of the pressure for a frequency inside the BG, 920 Hz. In this case last case, the pressure decays all along inside the SC because the mode is inside the BG and it presents evanescent behaviour.

In contrast with the propagating mode (connected blue squares), the evanescent mode (connected red squares) is practically killed at the end of the crystal, but there is still a small value of the pressure coming out. This characteristic of the evanescent behaviour in finite SC has been measured recently by Wu *et al.* [Wu09a, Wu09b] in a SC with a point defect.

The evanescent modes cannot be excited in perfect (infinite) crystals because

these modes do not satisfy the translational symmetry. However it is possible to use them to explain intuitively the physics of the modes inside the BG. On the other hand, in the real world there are no infinite crystals, thus the modes inside the BG present evanescent behaviour.

2.1.2.2 Defects, localization and waveguides

Defects

Any distortion or violation of the regularity in a periodic system can be considered as a defect. Defects in periodic systems directly affect their physical properties, in such a way that the distortion of this physical property depends on the dimension of the defect.

A point defect is defined as a distortion of the system in a volume similar to the volume occupied by a unit cell. The most common point defects are:

- *Interstitial Scatterers*: Scatterers occupying a place between the equilibrium sites in the lattice.
- *Vacancies*: Sites of the lattice where no scatterer exists.
- *Interstitial Defects*: Scatterers with different material placed at interstitial sites of the lattice.
- *Substitutional Defects*: Scatterers with different material placed at the sites of the lattice.

In Figure 2.8, one can see the 2D representation of the previous point defects.

In this Section the physical properties of periodic systems with point defects are briefly introduced. The defects are created by removing cylinders, this means that, they are vacancies in the crystal. In the proximity of a vacancy, the periodicity of the array is completely broken, and also new physical properties appear when point defects are created, for instance localized modes.

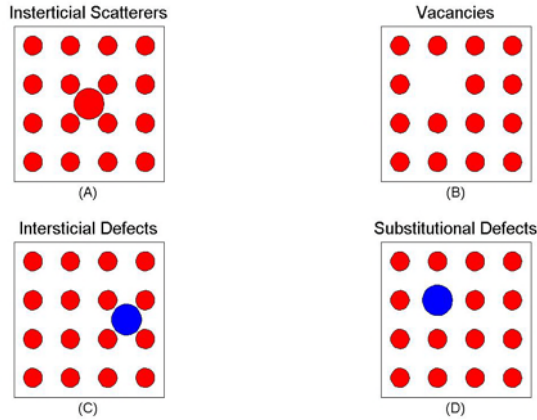


Figure 2.8: Point defects in 2D periodic systems. (A) Scatterer in an interstitial position. (B) Vacancy by removing a scatterer. (C) Scatterer of different material placed in an interstitial position. (D) Scatterer of different material placed in a position of the periodic system.

Localization

One important property of periodic structures is the emergence of localized modes within the BG when a point defect is introduced [Sigalas97, Li05]. The creation of a vacancy in a periodic system generates a cavity surrounded by a periodic medium. Thus, waves with frequency in the BG corresponding to this periodicity, could be localized in the cavity because its borders act as perfect mirrors for these frequencies. This is the reason that these modes are called *localized modes*. When a wave goes into the cavity, a part of the wave is transmitted to the periodic medium and the other one is reflected back by the borders of the cavity. The transmitted wave presents an exponential decay caused by their evanescent behaviour, however the back reflected wave contributes to the localized mode.

On the other hand the finite size of the cavity is a constraint of the problem that introduces a quantization of the allowed modes. The allowed frequencies for the localized modes correspond to the intersection between the eigenfre-

quencies of the cavity and the frequencies of the BG.

Figure 2.9 shows the acoustic field inside a vacancy created in a square lattice with the same properties as the ones analysed in Figure 2.3. The incident wave, from the left side of the structure, presents a frequency inside the BG, 1340Hz. One can observe that the wave does not propagate through the crystal, but it is localized in the cavity. We can also show the variation of the pressure sound level inside the cavity, showing a maximum at the localized frequency. The results have been obtained using the Finite Element Methods (FEM).

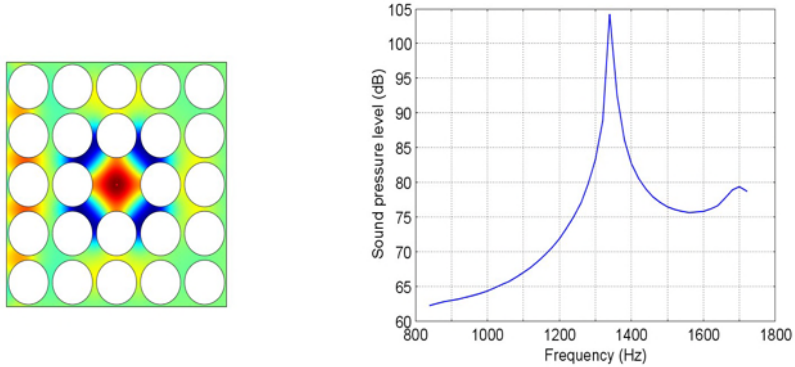


Figure 2.9: Localization for a localization frequency of 1340 Hz. Left panel: Pressure field inside the vacancy in a square lattice with $a = 0.15\text{m}$ and $r = 0.075\text{m}$. Right panel: Sound pressure spectrum calculated in the center of the cavity. Results obtained using the Finite Element Method.

A technique widely used in the literature to obtain the effect of the creation of point defects in crystals is the supercell approximation in PWE [Sigalas98, Wu01, Zhao09]. This approximation only gives information about the propagation of the localized modes in point defects. In these cases when periodicity is broken or when SC have finite size, evanescent modes inside the periodic system may appear. Localized modes or modes inside the BG are characterized by their evanescent behaviour [joannopoulos08, Engelen09, Romero10a, Romero10b]. Then, a more accurate analysis is needed to characterize the properties of the modes inside the periodic system. An extended analysis of the properties of point defects in acoustic periodic systems will be presented

in Chapter 6.

Waveguides

The location and width of acoustic BG result from a large contrast in the value of the acoustic constants in SC. Therefore, there is a great deal of interest in developing periodic systems-based waveguides where one can confine and efficiently guide waves around sharp corners, which is not feasible with classical waveguides. Guiding waves without losses in straight waveguides using two-dimensional crystals was studied theoretically by several groups [[Kafesaki00](#), [Khelif03](#), [Khelif02](#)].

One can design a waveguide creating extended linear defects in a periodic system, for instance, by removing a row of scatterers in the original system. Grafting other defects (for example, a side branch or stub) along an extended waveguide permits some frequency selectivity in the form of zero transmission in the primary transmission spectrum of the perfect guide.

In a waveguide, one generates a corridor dividing the original periodic system into two identical periodic systems, in such a way, the waves with frequency inside the BG of both periodic media can propagate through this wave guide. In [Figure 2.10](#) an example of waveguide is shown. In the periodic medium with square lattice with $a = 0.15$ m, we have generated a line of defects or waveguide where the wave with frequency inside the BG, $\nu = 1260$ Hz, can propagate in the corridor and cross the crystal with two different paths.

An example of waveguide can be observed in [Figure 2.10](#). A corridor generated by a line of defects is decoupled into two corridors generating two different paths for the outgoing wave. By means of this procedure, we can divide an incident beam into two different beams with the same frequency. Moreover, the outgoing waves present very low dispersion in frequency. Several applications based on waveguides in periodic system have been developed in the literature [[Hakansson06](#)].

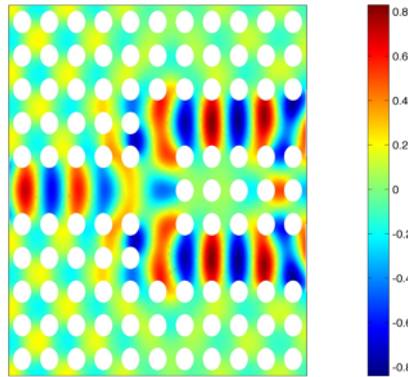


Figure 2.10: Waveguides. Guided wave with frequency $\nu = 1260$ Hz, inside a lattice square with lattice constant $a = 0.15$ m and $r = 0.05$ m.

2.1.3 Sonic crystals, the acoustic periodic system

Up to now, an overview on the propagation of scalar waves in periodic heterogeneous materials has been presented. This Section introduces the concept of Sonic Crystals as the periodic media for the propagation of acoustic waves.

Artificial materials made with different dielectric properties were analysed in the 80's. The pioneering works of Yablonovitch *et al.* and John *et al.* [Yablonovitch87, John87] observed the existence of prohibited frequencies related to the periodicity of the medium. Because of the similarity of the properties of the crystalline structure and these periodic media, they were called Photonic Crystals. After that, in the early 90's, the Phononic Crystals (PC) appeared, which are periodic compositions of several materials with different elastic properties. These systems presented analogue properties to the Photonic Crystals but for elastic waves. Especially, when one of the composites is a fluid, the system is usually called Sonic Crystal (SC), which are the systems studied in this work.

The propagation of the elastic waves in an elastic material is determined by

the vectorial equation of Navier,

$$\rho \frac{\partial^2 u^i}{\partial t^2} = \frac{\partial}{\partial x_i} \left[\lambda \frac{\partial u^l}{\partial x_l} \right] + \frac{\partial}{\partial x_l} \left\{ \mu \left(\frac{\partial u^i}{\partial x_l} + \frac{\partial u^l}{\partial x_i} \right) \right\} \quad (2.13)$$

where $i, l = x, y, z$, u^i is the i -th component of the displacement vector and λ and μ are the Lamé coefficients; ρ is the density of the material. The Lamé coefficients can be related to the propagating velocities of the wave in the elastic media as, $\lambda = \rho c_l^2 - 2\rho c_t^2$ and $\mu = \rho c_t^2$, where c_l and c_t are the longitudinal and transversal sound velocities respectively. With that in mind, the equation of Navier (2.13) can be rewritten in the following form,

$$\rho \frac{\partial^2 u^i}{\partial t^2} = \vec{\nabla} \left[\rho c_l^2 \vec{\nabla} u^i \right] + \rho c_t^2 \vec{\nabla} \frac{\partial \vec{u}}{\partial x_i} + \frac{\partial}{\partial x_i} \left\{ (\rho c_l^2 - 2\rho c_t^2) \vec{\nabla} \vec{u} \right\}. \quad (2.14)$$

In the particular case of a fluid, where the transversal modes are not allowed, it is accomplished that $\mu = \rho c_t = 0$, thus the Equation 2.14, follows the following expression

$$\rho \frac{\partial^2 u^i}{\partial t^2} = \frac{\partial}{\partial x_i} \left\{ (\rho c_l^2) \vec{\nabla} \vec{u} \right\}. \quad (2.15)$$

Taking into account that the acoustic pressure can be related to the displacement of the particles \vec{u} as $p = -\rho c_l \vec{\nabla} \vec{u}$, the Equation 2.15 has the form of the acoustic wave equation shown in 2.7 considering harmonic temporal dependence. We note that, indeed, the governing equations of the propagation of waves in a SC are a particular case of the corresponding case of PC⁷.

2.2 Parameters and symbols

The interest of the SC has been focused in last years on increasing their acoustical focalization [Hakansson05b] and attenuation properties [Liu00a,

⁷We notice that when a longitudinal wave impinges a SC, the transversal modes are localized only in the elastic medium [Einspruch60]

Umnova06]. Throughout this work several parameters to quantitatively measure the improvement of the properties of SC have been used. In this Section are some of these parameters like the insertion loss, the attenuation area, the fraction of vacancies and the asymmetry. These parameters will help us to characterize the acoustical properties of the SC.

As we have previously mentioned, in this work we study the optimization of the acoustical properties of SC by creating vacancies in the system. The goal is to produce systems with improved attenuation and focalization capabilities with respect to the complete SC. Thus, some parameters based on the optimization process are also necessary to classify the optimized structures. However these parameters need the explanation of some properties of the optimization technique, therefore they will be presented in Chapter 4.

The physical and structural parameters used in this work are as follows:

Insertion loss (IL) This parameter is defined as the difference between the sound level recorded at the same point with and without the sample. The effectiveness of a road traffic noise barrier is measured by the insertion loss.

$$IL(dB) = 20 \log\left(\frac{P_{direct}}{P_{interferred}}\right) \quad (2.16)$$

Area of spectrum (AS) This parameter is obtained from the frequency response produced by the distribution of scatterers. It is defined as the area enclosed between the positive spectrum and the 0dB threshold in the selected frequency range. If the AS is measured from the attenuation spectra, the parameter is called Attenuation Area, AA, and if it is obtained from the Pressure level Spectra, it is called Focusing Area, FA.

An increasing in the value of these parameters implies an improvement in the attenuation or focalization properties of the system. AA parameter has been used in several works [Romero06, Herrero09, Romero09] in order to measure the attenuation capability of a distribution of scatterers and FA has been also used [Romero09] for characterize the focalization capability. In Figure 2.11 one can observe an example of the AA

in the range of frequencies from 2100 Hz to 4800 Hz in an IL spectrum.

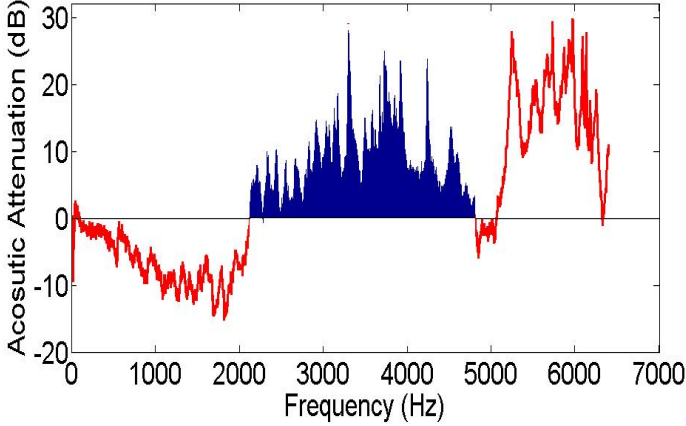


Figure 2.11: Attenuation Area (AA). The attenuation area is plotted in blue between the frequencies 2100 and 4800 Hz.

Fraction of vacancies (F_v) This structural parameter gives information on the number of vacancies in a structure. We define the F_v as the fraction between the number of vacancies and the total number of cylinders in the structure:

$$F_v = \frac{N_p}{N} \quad (2.17)$$

where N_p is the number of vacancies and N is the total number of scatterers in the complete structure. F_v is ranged in the interval $[0, 1]$.

Asymmetry (A) This parameter gives information on the distribution of the vacancies in the structure, taking into account the asymmetry of each vacancy with respect to the symmetry axis of the structure. We define this parameter as,

$$A = \frac{A_x + A_y}{2} \quad (2.18)$$

CHAPTER 2. FUNDAMENTALS OF PERIODIC SYSTEMS

where A_i with $(i = x, y)$ represents the Asymmetry with respect to the axis i , which is defined as

$$A = \frac{\sum_{j=1}^N N \gamma_A (b_j - b'_j)}{2N_p}. \quad (2.19)$$

b_j and b'_j can have the values 1 or 0 depending on the existence or not of the scatterer in position j , or in the symmetric position j' , with respect to the symmetry axis of the structure. N_v again represents the number of vacancies. The parameters b and b' are binary vectors with a dimension equal to the total number of scatterers N . Then, we have defined the distribution of symmetry γ_A as

$$\gamma_A(x) = \begin{cases} 1 & \text{if } x \neq 0 \\ 0 & \text{if } x = 0 \end{cases} \quad (2.20)$$

With the previous definitions, A belongs to the interval $[0, 1]$.

3

Theoretical models and numerical techniques

Interaction of waves with obstacles is a hot topic in many branches of science. Wave propagation inside periodic media has especially been analysed in many branches of science and technology as, for example, solid-state physics [[korringa47](#), [kohn54](#), [ashcroft76](#)], water waves [[Linton90](#)], electromagnetic waves [[Twersky51](#), [Wang93](#)], acoustics [[Zaviska13](#), [Twersky51](#), [Sigalas00](#), [Chen01](#), [martin06](#)], elastic media [[Kafesaki99](#), [Liu00](#), [Psarobas00](#), [Mei03](#)] and seismology [[Tregoures02](#), [Wu88](#), [Shang88](#)]. A wide range of mathematical techniques are now available for the solution of problems involving the interaction of waves with scatterers inside these crystals. This Chapter draws together the methods used in this work: multiple scattering theory (MST); plane wave expansion (PWE) and extended plane wave expansion (EPWE) are also presented using the supercell approximation; and finite element method (FEM). The cylindrical symmetry of the scatterers is analysed in this Chapter as it allows an easy analytical nomenclature and due to the interest in the 2D SC analysis.

3.1 Multiple scattering theory

MST has a long history. In 1913, Závíska [Zaviska13] described the method for the scattering of finite arrays in 2D acoustic fields, which Ignatowsky applied in 1914 to the case of normal incidence on an infinite row of cylinders [Ignatowsky14]. After that, extensions of the work to the oblique incidence were studied [Twersky62, Guenneau04].

Multiple scattering can be understood as an interaction of wave fields with two or more obstacles. The classical multiple scattering problem of sound waves by rigid cylinders is presented briefly in this Section. MST solves the problem taking into account that the field scattered from one obstacle induces further scattered fields from all the other obstacles, which induces further scattered fields from all the other obstacles, and so on. This characterizes MST as a self-consistent method, being applicable to randomly or periodically-spaced cylinders.

We consider N disjoint obstacles. Given an incident wave on them, the problem is to calculate the scattered waves. The total field can be expressed as

$$p = p_{inc} + \sum_{j=1}^N p_{sc}^j, \quad (3.1)$$

where p_{inc} is the given incident field and p_{sc}^j is the field scattered by the j -th scatterer. Then the incident field over the n -th cylinder in the presence of the other $N - 1$ is

$$p_n = p_{inc} + \sum_{j=1, j \neq n}^N p_{sc}^j. \quad (3.2)$$

Considering that the problem is linear, it should be possible to write,

$$p_{inc}^j = T_j p_j \quad (3.3)$$

where T_j is an operator relating to the field incident on the j -th cylinder, p_j ,

and the field scattered by the j -th scatterer, p_{sc}^j . Then,

$$p_n = p_{inc} + \sum_{j=1, j \neq n}^N T_j p_j, \quad (3.4)$$

or, equivalently,

$$p_n = T_n \left(p_{inc} + \sum_{j=1, j \neq n}^N p_{sc}^j \right). \quad (3.5)$$

Solving Equation (3.4) for p_n or (3.5) for p_{sc}^j , $n = 1, 2, \dots, N$ the total field then would be given by

$$p = p_{inc} + \sum_{j=1}^N T_j p_j, \quad (3.6)$$

The simplicity of previous equations is misleading because the operator T_j is not clearly defined and it is not specified where previous equations are required to hold in space. In the next section we show the method of separation of variables together with an appropriate addition theorem to study the acoustic scattering produced by two or more cylindrical obstacles. Plane and cylindrical incident waves will be considered. The exact method was used by Zaviška in 1913 [Zaviska13], and it leads to an infinite system of simultaneous algebraic equations.

3.1.1 Two-dimensional scattering by circular cylinders

We consider N straight cylinders located at $\vec{r}_i = (r_i, \theta_i)$ of radius a_i with $i = 1, 2, \dots, N$ to form either a regular lattice or a random array perpendicular to the $x - y$ plane. The cylinders are parallel to the z -axis, then since the boundary conditions and the geometry do not change with z , the problem can be reduced to two uncoupled problems for the scalar Helmholtz equation. The final wave reaches a receiver located at \vec{r}_r and, as we have seen in a previous Section, it is formed by the sum of the direct wave from the source and

the scattered waves from all the cylinders (see Equation 3.4). The problem is to solve the previous self-consistent method, satisfying some boundary conditions on the surfaces of the cylinders and a radiation condition at infinity. Such a scattering problem can be exactly formulated in cylindrical coordinates.

Solutions for the scattering of waves by cylindrical objects can be expressed in terms of two important functions: $H_n(kr)e^{in\theta}$ and $J_n(kr)e^{in\theta}$, Hankel and Bessel function of n -order and first kind respectively. Both are solutions of the Helmholtz equation for the planar problem. The first one satisfies the radiation condition at infinity and is singular at the origin of coordinates. The second one is regular in the origin of coordinates. Thus the first one could be used to represent outgoing cylindrical waves whereas the second one could express regular cylindrical waves.

The incident wave over 2D system of scatterers can be considered either plane wave from the infinity or cylindrical wave (spherical wave in 3D) from a line source. Both cases are considered in the next Sections. Assumption of time harmonic dependence has been considered in the subsequent calculations.

3.1.1.1 Incidence of a plane wave

A plane wave incoming from the negative values of x can be expressed with respect to the origin of the cartesian coordinates by an exponential $e^{i\vec{k}\vec{x}}$, where \vec{k} and $\vec{r} = \vec{x}$ are the wave vector ($k = 2\pi/\lambda$; λ wavelength of the wave) and the position respectively. As mentioned earlier, the scattering problem of N cylindrical obstacles is solved by means of cylindrical coordinates for simplicity. It is possible to express the plane wave as an expansion of Bessel functions of the first kind centered at the origin of coordinates,

$$p_{inc} = \sum_{q=-\infty}^{q=+\infty} A_q J_q(kr) e^{iq\theta} \quad (3.7)$$

where A_q are the coefficients that determine the incident wave. For plane waves, one can show that $A_q = i^q$ [Sanchis01].

The scattered field from the j -th scatterer can be expressed with respect to the

3.1. MULTIPLE SCATTERING THEORY

origin of coordinates of the j -th cylinder using n -th order Hankel functions of first kind as

$$p_{sc}^j = \sum_{q=-\infty}^{q=+\infty} A_{jq} H_q(kr_j) e^{iq\theta_j} \quad (3.8)$$

where

$$r_j = \sqrt{(x-x_j)^2 + (y-y_j)^2} \quad (3.9)$$

$$\theta_j = \arcsin\left[\frac{(y-y_j)}{r_j}\right]. \quad (3.10)$$

Figure 3.1 shows the schematic view of the coordinate systems centered in each cylinder.

The total incident wave over the j -th cylinder can be computed with Equation 3.2. However all the terms of this equation must be expressed in the same origin of coordinates. To do so, the addition theorems of the Bessel and Hankel functions are necessary. In the Appendix A some important addition theorems for the case of cylindrical coordinates are shown.

Using Graf's additional theorem for $J_q(kr)e^{iq\theta}$, the incident wave can be expressed in the coordinates of the l -th cylinder as follows,

$$p_{inc} = \sum_{s=-\infty}^{s=+\infty} S_{ls} J_s(kr_l) e^{is\theta_l} \quad (3.11)$$

where

$$S_{ls} = \sum_{q=-\infty}^{q=+\infty} A_q e^{i(s-q)\theta_l} J_{q-s}(kr_l). \quad (3.12)$$

Analogously, we can express the scattered wave by the j -th cylinder in the coordinates centered at l -th cylinder, using Graf's theorem for $H_m^{(1)}(kr)e^{im\theta}$. Thus,

$$p_{sc}^{lj} = \sum_{s=-\infty}^{s=\infty} C_{ljs} J_s(kr_l) e^{is\theta_l}, \quad (3.13)$$

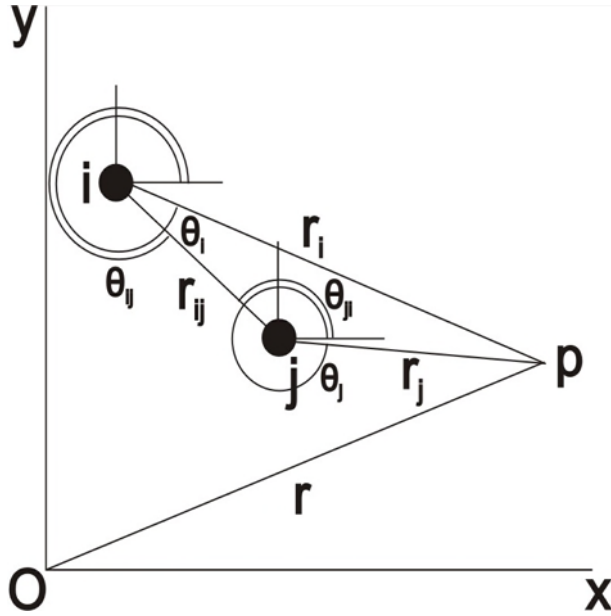


Figure 3.1: Notation used for the addition theorems.

where,

$$C_{ljs} = \sum_{q=-\infty}^{q=\infty} A_{jq} e^{i(q-s)\theta_{lj}} H_{s-q}(kr_{lj}). \quad (3.14)$$

On the other hand, the total incident pressure over the l -th cylinder can be expressed in terms of a expansion of Bessel functions:

$$p^l = \sum_{s=-\infty}^{s=+\infty} B_{ls} J_s(kr_l) e^{is\theta_l}. \quad (3.15)$$

Thus, introducing Equations (3.11), (3.13) and (3.15) in Equation (3.2), we obtain

$$B_{ls} = S_{ls} + \sum_{j=1}^N \sum_{q=-\infty}^{q=\infty} A_{jq} \alpha_{ljsq} \quad (3.16)$$

where

$$\alpha_{ljsq} = (1 - \delta_{lj})e^{i(q-s)\theta_{lj}}H_{s-q}(kr_{lj}). \quad (3.17)$$

In Equation (3.16) the coefficients S_{ls} are known (see Equation 3.12) and they are determined by the incident wave¹. However A_{jq} and B_{ls} are unknown and they are related by the boundary conditions of the problem. The matrix that relates these two unknown parameters is the so-called scattering matrix, or T-matrix.

The boundary conditions consider that both the pressure and the normal velocity are continuous across the interface between the scatterer and the surrounding medium. Thus, for the case of the j -th cylinder, the boundary conditions are written,

$$p_{ext}|_{\partial\Omega_j} = p_{int}|_{\partial\Omega_j} \quad (3.18)$$

$$\frac{1}{\rho} \frac{\partial p_{ext}}{\partial n}|_{\partial\Omega_j} = \frac{1}{\rho_j} \frac{\partial p_{int}}{\partial n}|_{\partial\Omega_j} \quad (3.19)$$

where $\partial\Omega_j$ is the boundary of the j -th scatterer, ρ is the density of the surrounding medium and ρ_j is the density of the j -th scatterer. In the case of rigid scatterers embedded in air, the periodic system presents a large acoustic mismatch ($\rho_{cyl} \gg \rho_{air}$), and it is possible to consider Neumann boundary condition in the walls of the j -th cylinder,

$$\frac{\partial p_{ext}}{\partial n}|_{\partial\Omega_j} = \frac{\partial(p^l + p_{sc}^l)}{\partial n}|_{\partial\Omega_j} = 0 \quad (3.20)$$

where p_{sc}^l is the scattered wave by the l -th cylinder,

$$p_{sc}^l = \sum_{q=-\infty}^{q=+\infty} A_{lq}H_q(kr_l)e^{iq\theta_l}. \quad (3.21)$$

Finally, substituting Equations (3.15) and (3.21) in (3.20),

$$A_{ls} = t_{ls}B_{ls}, \quad (3.22)$$

¹We note that for an incident plane wave, $A_q = i^q$, so that, Equation 3.12 is absolutely defined for a determined structure of scatterers

with²

$$t_{ls} = \frac{J_{s+1}(ka_l) - J_{s-1}(ka_l)}{H_{s-1}(ka_l) - H_{s+1}(ka_l)}. \quad (3.23)$$

Then, multiplying both terms of Equation 3.16 by the coefficients t_{ls} ,

$$A_{ls} - \sum_{j=1}^N \sum_{q=-\infty}^{q=\infty} t_{js} A_{jq} \alpha_{ljsq} = t_{ls} S_{ls}, \quad (3.24)$$

which is an infinite system of linear equations that can be solved by truncation. The subindexes q and s take values from $-M$ to M , the system is reduced to $2M + 1$ equations and Equation 3.24 can be expressed in terms of products of matrices. This formulation will be presented in the next Section (3.1.1.2) as the formalism for the incident cylindrical wave is analogous to the case presented here. Thus, the pressure in a point (x, y) can be expressed by

$$p(x, y) = p_{inc} + \sum_{l=1}^N \sum_{s=-\infty}^{s=\infty} A_{ls} H_{ls}(kr_l) e^{(is\theta_l)}, \quad (3.25)$$

where the solution of the problem is the coefficients A_{ls}

The previous equation is valid for any configuration of the cylinders. This means that, it works for situations in which the cylinders can be placed either randomly or periodically.

By representing the Equation (3.22) in products of matrices, then,

$$A_l = T_l B_l \quad (3.26)$$

where the T-matrix of the problem is

$$T_{lss'} = \frac{J_{s+1}(ka_l) - J_{s-1}(ka_l)}{H_{s-1}(ka_l) - H_{s+1}(ka_l)} \delta_{ss'}, \quad (3.27)$$

where $\delta_{ss'}$ is the Kronecker's delta. We note that the T-matrix of the problem of rigid cylinders is square and diagonal.

²using $\frac{dK(f(z))}{dz} = \frac{1}{2} \frac{df}{dz} (K_{s-1}(f(z)) - K_{s+1}(f(z)))$ where K can represent the Bessel ($J(f(z))$) or Hankel ($H(f(z))$) functions.

3.1. MULTIPLE SCATTERING THEORY

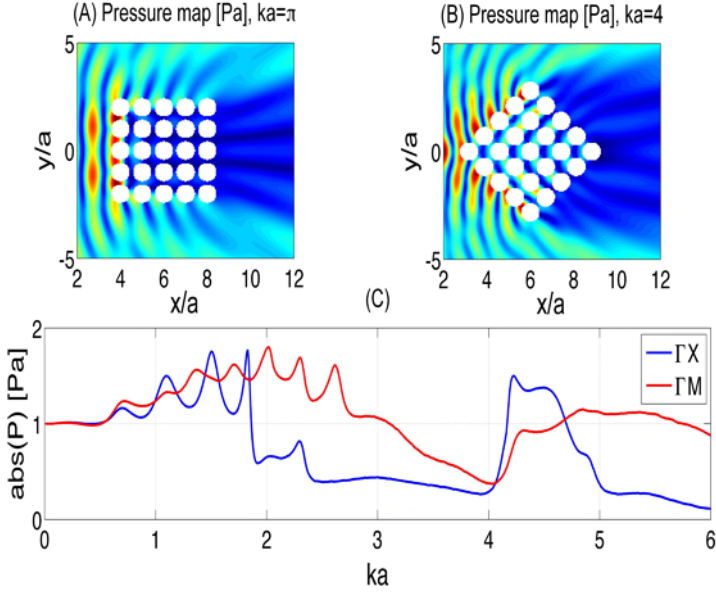


Figure 3.2: Maps and spectra of absolute values of pressure calculated using MST for a plane wave impinging on the crystal. (A) Acoustic field produced by the scattering of waves in a SC with square lattice in the ΓX direction for the frequency inside the pseudogap at $ka = \pi$. (B) Acoustic field produced by the scattering and the incidence waves in a SC with square lattice in the ΓM direction for the frequency inside the pseudogap at $ka = 4$. (C) Spectra for the ΓX (blue line) and ΓM (red line) direction, calculated at the point $(x/a, y/a) = (11, 5)$.

An example of the results obtained using this methodology for calculating pressure field is shown in Figure 3.2. This Figure represents two maps for the absolute values of pressure due to the incidence of a plane wave over a $5a \times 5a$ square array of rigid cylinders. In the left panel, one can observe the 0° incidence of the plane wave over the array, whereas the right panel represents the 45° incidence. Two different frequencies inside the BG have been used for the simulation, $ka = \pi$ (0°) and $ka = 4$ (45°). One can observe the low pressure values behind the array.

3.1.1.2 Incidence of a cylindrical wave

In this case, an acoustic source transmitting monochromatic waves is placed at point \vec{r}_s , some distance from the system of scatterers. For simplicity without compromising generality, the acoustic source can be approximated as a line source located at origin, i. e., $\vec{r}_s = \vec{0}$. The acoustic wave equation with such a source follows the following expression:

$$\left(\vec{\nabla}^2 + k^2\right) p(\vec{r}) = -4\pi\delta^2(\vec{r}), \quad (3.28)$$

where $k = \omega/c$ and δ^2 is the 2-dimensional delta-function. In cylindrical coordinates, the solution is

$$p(\vec{r}) = i\pi H_0(kr), \quad (3.29)$$

where H_0 is the zero-*th* order Hankel function of the first kind. The solution represents a line source located at origin.

Considering the presence of the N cylinders placed at \vec{r}_i , the scattered wave from the j -th cylinder can be expressed as

$$p_{sc}^j = \sum_{n=-\infty}^{\infty} i\pi A_{jn} H_n(kr_j) e^{in\theta_j} \quad (3.30)$$

where H_n is the n -th order Hankel function of the first kind, A_{jn} are the coefficients to be determined, and θ_j is the azimuthal angle of the vector r_j relative to the positive x axis (see Figure 3.1).

In order to separate the governing equations into modes, we can express the total incident wave as:

$$p_{inc}^i = \sum_{n=-\infty}^{\infty} B_{in} J_n(kr_i) e^{in\theta_i}. \quad (3.31)$$

For determining the matrix relation (T-matrix) between B_{in} and A_{jn} , it is necessary to express p_{sc}^j and p_{inc} , for each $j \neq i$, respect to the origin centered at the i -th scatterer. Following the same procedure than in the previous section,

3.1. MULTIPLE SCATTERING THEORY

we use the Graf's additional theorem for $H_m(kr)e^{im\theta}$ (see Appendix A), for representing the p_{sc}^j in the form

$$P_{sc}^j = \sum_{n=-\infty}^{\infty} C_{jin} J_n(kr_i) e^{im\theta_i}, \quad (3.32)$$

where

$$C_{jin} = \sum_{l=-\infty}^{\infty} i\pi A_{jl} H_{l-j}(kr_{ij}) e^{i(l-n)\theta_{ij}}. \quad (3.33)$$

On the other hand, using again the Graf's theorem, the incident pressure can be expressed as,

$$P_{inc} = \sum_{l=-\infty}^{\infty} S_{il} J_l(kr_i) e^{il\theta_i}, \quad (3.34)$$

where

$$S_{il} = i\pi H_{-l}(kr_i) e^{-il\theta_i}. \quad (3.35)$$

At this stage, the S_{il} is known, but both B_{in} and A_{jl} are unknown. Boundary conditions will provide another equation relating them together. In the previous Section we used the Neumann's boundary conditions as we were interested in rigid scatterers. Now, in this Section we will consider the general boundary condition, this means that to say, the continuity of both the pressure and the normal velocity across the interface between a scatterer and the surrounding medium. After that, considering the big contrast between both the densities and sound velocities, it will be possible to reproduce the results of rigid scatterers. In this Section we use constant values of densities and velocities, however it is possible to introduce, for instance, frequency dependent density or velocity. Tournat *et al.* [Tournat04] introduced scatterers with a mesoscopic scale much larger than the microscopic scale in a porous medium as host material, in such a way that the propagation can be described by the multiple scattering by the scatterers (at the mesoscale) taking place in a homogenized porous absorbing medium described by the an homogenized theory of porous materials. Few years later, Umnova *et al.* [Umnova06] analysed

CHAPTER 3. THEORETICAL MODELS AND NUMERICAL TECHNIQUES

the multiple scattering of sound wave by combined scatterers of rigid cores and an absorbent covering in air. Appendix C shows the applications of the methodology shown in this Section but with absorbent boundary conditions.

The boundary conditions in the j -th rigid cylinder follows the following equations,

$$p_{ext}|_{\partial\Omega_j} = p_{int}|_{\partial\Omega_j} \quad (3.36)$$

$$\frac{1}{\rho} \frac{\partial p_{ext}}{\partial n}|_{\partial\Omega_j} = \frac{1}{\rho_j} \frac{\partial p_{int}}{\partial n}|_{\partial\Omega_j} \quad (3.37)$$

where $\partial\Omega_j$ is the boundary of the j -th scatterer, ρ is the density of the surrounding medium and ρ_j is the density of the j -th scatterer.

In order to apply the previous boundary conditions, we consider that the pressure field inside the i -th cylinder can be represented by

$$P_{int}^i = \sum_{n=-\infty}^{\infty} D_{in} J_n(k_{1i} r_i) e^{in\theta_i}, \quad (3.38)$$

where k_{1i} is the wave number inside the i -th cylinder.

Using the boundary conditions and the expressions of the incident, scattered and interior wave we can obtain the following relation,

$$B_{in} = i\pi \Gamma_{in} A_{in}, \quad (3.39)$$

where

$$\Gamma_{in} = \frac{H_n(ka_i) J_n'(ka_i/h_i) - g_i h_i H_n'(ka_i) J_n(ka_i/h)}{g_i h_i J_n'(ka_i) J_n(ka_i/h_i) - J_n(ka_i) J_n'(ka_i/h_i)}. \quad (3.40)$$

Here a_i is the radius of the i -th cylinder (in this work the radius of the scatterers take the same value for all the cylinders, $a_i = a$), $g_i = \rho_1^i / \rho$ is the density ratio, and $h_i = k/k_1^i = c_1^i / c$ is the sound speed ratio for the i -th cylinder. Then with the previous expression, it is possible to relate the coefficients B_{in} to the A_{jn} . To do this, it is necessary to define the following values:

$$T_{in} = S_{in} / i\pi, \quad (3.41)$$

$$G_{ijln} = H_{l-n}(kr_{ij}) e^{i(l-n)\theta_{rij}} \quad i \neq j. \quad (3.42)$$

Then,

$$\Gamma_{in}A_{in} - \sum_{j=1, j \neq i}^N \sum_{l=-\infty}^{\infty} G_{ijln}A_{jl} = T_{in} \quad (3.43)$$

is a infinite system of equations that can be used to determine A_{ni} if it is properly truncated. The equations are completely analogous to the Equation 3.24. Then, if the subindexes q and s take values from $-M$ to M , both systems are reduced to $2M + 1$ equations that can be expressed in matrix formulation as follows:

$$(\Gamma - G)A = T, \quad (3.44)$$

then the vector of coefficients A can be obtained as

$$A = (\Gamma - G)^{-1}T, \quad (3.45)$$

where the subindex -1 indicates the inverse of the matrix. The matrices Γ , G and the vectors A and T are represented by:

$$\Gamma = \begin{pmatrix} \Gamma_1 & 0 & \dots & 0 \\ 0 & \Gamma_2 & \dots & 0 \\ \vdots & \vdots & \ddots & \vdots \\ 0 & \dots & \dots & \Gamma_N \end{pmatrix}, \quad (3.46)$$

where N is the number of cylinders of the structure and

$$\Gamma_i = \begin{pmatrix} \Gamma_{i,-M} & 0 & \dots & 0 \\ 0 & \Gamma_{i,-M+1} & \dots & 0 \\ \vdots & \vdots & \ddots & \vdots \\ 0 & \dots & \dots & \Gamma_{i,M} \end{pmatrix}; \quad (3.47)$$

$$G = \begin{pmatrix} 0 & \dots & 0 & G_{-M,-M}^{1,2} & \dots & G_{M,-M}^{1,2} & \dots & \dots & G_{-M,-M}^{1,N} & \dots & G_{M,-M}^{1,N} \\ \vdots & \ddots & \dots & \vdots & \ddots & \vdots & \dots & \dots & G_{-M,-M}^{1,N} & \ddots & G_{M,-M}^{1,N} \\ 0 & \dots & 0 & G_{-M,M}^{1,2} & \dots & G_{M,M}^{1,2} & \dots & \dots & G_{-M,M}^{1,N} & \dots & G_{M,M}^{1,N} \\ G_{-M,-M}^{2,1} & \dots & G_{M,-M}^{2,1} & 0 & \dots & 0 & \dots & \dots & G_{-M,-M}^{2,N} & \dots & G_{M,-M}^{2,N} \\ \vdots & \ddots & \vdots & \vdots & \ddots & \vdots & \dots & \dots & G_{-M,-M}^{2,N} & \ddots & G_{M,-M}^{2,N} \\ G_{-M,M}^{2,1} & \dots & G_{M,M}^{2,1} & 0 & \dots & 0 & \dots & \dots & G_{-M,M}^{2,N} & \dots & G_{M,M}^{2,N} \\ \vdots & \vdots \\ \vdots & \vdots \\ G_{-M,-M}^{N,1} & \dots & G_{M,-M}^{N,1} & \dots & \dots & \dots & \dots & \dots & 0 & \dots & 0 \\ \vdots & \ddots & \vdots & \dots & \dots & \dots & \dots & \dots & \vdots & \ddots & \vdots \\ G_{-M,M}^{N,1} & \dots & G_{M,M}^{N,1} & \dots & \dots & \dots & \dots & \dots & 0 & \dots & 0 \end{pmatrix}; \quad (3.48)$$

and

$$A = \begin{pmatrix} A_{1,-M} \\ \vdots \\ A_{1,M} \\ A_{2,-M} \\ \vdots \\ A_{2,M} \\ \vdots \\ \vdots \\ A_{N,-M} \\ \vdots \\ A_{N,M} \end{pmatrix}, T = \begin{pmatrix} T_{1,-M} \\ \vdots \\ T_{1,M} \\ T_{2,-M} \\ \vdots \\ T_{2,M} \\ \vdots \\ \vdots \\ T_{N,-M} \\ \vdots \\ T_{N,M} \end{pmatrix}, \quad (3.49)$$

where the values of the components of the previous matrices are given by Equations 3.40, 3.41 and 3.42. We note that the size of the matrices Γ and G is $N(2M + 1) \times N(2M + 1)$ while the vectors T and A present a length equal to $N(2M + 1)$.

Once the infinite system of equations to obtain the coefficients A_{in} is solved, the total wave at any point is

$$p(\vec{r}) = i\pi H_0(kr) + \sum_{i=1}^N \sum_{n=-\infty}^{\infty} i\pi A_{in} H_n(kr_i) e^{in\theta_i}. \quad (3.50)$$

3.1. MULTIPLE SCATTERING THEORY

We note that an inclusion of the lowest order in multiple scattering may be sufficient for certain situations and that the above derivation is valid for any configuration of the cylinders.

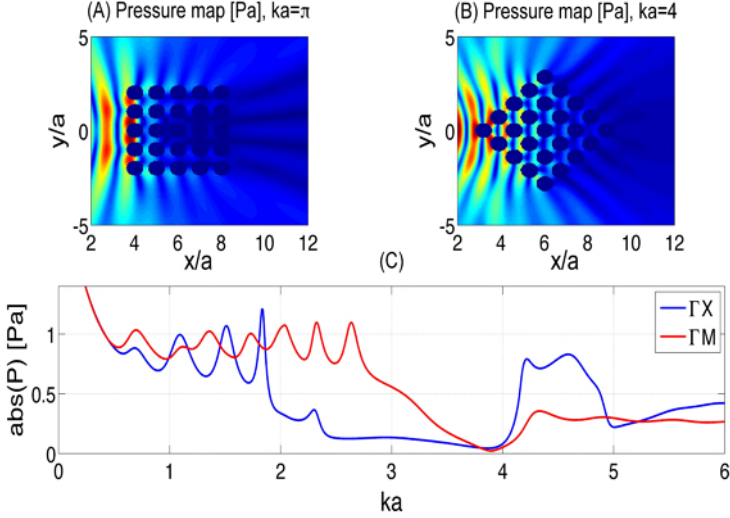


Figure 3.3: Maps and spectra calculated using MST for a cylindrical wave impinging a $5a \times 5a$ square array of rigid cylinders with a filling fraction $ff = 50\%$. (A) map for a frequency $ka = \pi$ inside the pseudogap at ΓX direction. (B) map for a frequency $ka = 4$ inside the pseudogap at ΓM direction. (C) Blue line (Red line) represents the spectrum for the ΓX (ΓM) direction measured at the point $(x/a, y/a) = (11, 0)$ from the source location.

Figures 3.3A and 3.3B show the maps produced by the acoustic scattering of a square array of cylinders for the two main directions of symmetry (0 and 45 degrees), with size $5a \times 5a$ and filling fraction $ff = 50\%$. Compared with the maps shown in Figure 3.2 it can be concluded that the differences between a cylindrical source and a plane wave are not significant. Figure 3.3C also represents the acoustic spectra for the two main directions of symmetry measured at point $(x, y) = (11a, 0a)$ from the source location. We can observe the ranges of inhibition in both directions (pseudogaps). The transmission outside these ranges can vary significantly as the number of scatterers or the shape of the array changes. The oscillatory behaviour for frequencies below

$ka = 3$ is caused by external shape of the crystal. They may appear or not, depending on the arrangement of the array. But the inhibition behaviour remains quantitatively the same for both directions. Such a stable inhibition range is a clear indicator for the stop band. This will be further confirmed by the band structure calculation given below.

3.2 Plane wave expansion

By analogy to electron waves in a crystal, waves transmission inside periodic systems should be described using the bands theory. This idea was first introduced in 1987 [Yablonovitch87, John87] . Then, the concepts of Bloch waves, dispersion relations, Brillouin zones, ... can be applied to the case of all kind of periodic systems: photonic, phononic and sonic crystals.

Plane wave expansion (PWE) uses the periodicity of the system and the Bloch theorem to solve the wave equation, obtaining a simple eigenvalue problem relating to the wave vector and the frequency of the incident wave. Such kind of models have been used in the literature to analyse periodic systems, from photonic to sonic crystals [Yablonovitch89, Meade92, Economou93, Kushwaha94]. Depending on the eigenequation obtained, the problem can be solved for both the real or the imaginary part of the wave vector, \vec{k} . Real part is related to the propagation of the mode inside the system, and imaginary part is related to the decaying of the mode through the crystal. Traditionally, it has been only solved for the real part, and the terminology PWE refers to the solution of the $\omega(\vec{k})$ problem. The extension to solve the imaginary band structures, appears when one solve the inverse problem $k(\omega)$. This methodology is known as extended plane wave expansion (EPWE). In this Section both methodologies are shown, as well as the extension to the supercell approximation, which is used mainly for the analysis of the periodic systems with defects.

3.2.1 $\omega(k)$ method

Propagation of sound is described by the equation

$$\frac{1}{\rho c^2} \frac{\partial^2 p}{\partial t^2} = \nabla \cdot \left(\frac{1}{\rho} \nabla p \right) \quad (3.51)$$

where c is the sound velocity, ρ is the density of the medium and p is the pressure.

In this Section a system composed of an array of straight, infinite cylinders made of an isotropic solid A , embedded in an acoustic isotropic background B has been considered. There is translational invariance in the direction z parallel to the cylinders and the system has 2D periodicity in the transverse plane. By using this periodicity, it is possible to expand the properties of the medium in Fourier series,

$$\sigma = \frac{1}{\rho(\vec{r})} = \sum_{\vec{G}} \sigma_{\vec{k}}(\vec{G}) e^{i\vec{G}\vec{r}}, \quad (3.52)$$

$$\eta = \frac{1}{B(\vec{r})} = \sum_{\vec{G}} \eta_{\vec{k}}(\vec{G}) e^{i\vec{G}\vec{r}}, \quad (3.53)$$

where \vec{G} is the 2D reciprocal-lattice vector and $B(\vec{r}) = \rho(\vec{r})c(\vec{r})^2$ is the bulk modulus. For the pressure p can be obtained by applying the Bloch theorem and harmonic temporal dependence,

$$p(\vec{r}, t) = e^{i(\vec{k}\vec{r} - \omega t)} \sum_{\vec{G}} p_{\vec{k}}(\vec{G}) e^{i\vec{G}\vec{r}}. \quad (3.54)$$

It is easy to show that [Kushwaha94]

$$\alpha(\vec{G}) = \begin{cases} \beta_A f f + \beta_B (1 - f f) & \text{if } \vec{G} = \vec{0} \\ (\beta_A - \beta_B) F(\vec{G}) & \text{if } \vec{G} \neq \vec{0} \end{cases} \quad (3.55)$$

where $\beta = (\sigma, \eta)$, and $F(\vec{G})$ is the structure factor. For circular cross section of radius r , the structure factor is

$$F(\vec{G}) = \frac{1}{A_{uc}} \int_{A_{cyl}} e^{-i\vec{G}\vec{r}} d\vec{r} = \frac{2ff}{Gr} J_1(Gr). \quad (3.56)$$

CHAPTER 3. THEORETICAL MODELS AND NUMERICAL TECHNIQUES

A_{uc} is the area of the unit cell, A_{cyl} is the area of the considered cylinder and J_1 is the Bessel function of the first kind of order 1. ff is the filling fraction defined in the previous Chapter.

Using Equations (3.52), (3.53), (3.54) and (8.6) we obtain [Kushwaha94]

$$\sum_{\vec{G}'} \left((\vec{k} + \vec{G}) \sigma_k(\vec{G} - \vec{G}') (\vec{k} + \vec{G}') - \omega^2 \eta_{\vec{k}}(\vec{G} - \vec{G}') \right) p_{\vec{k}}(\vec{G}') = 0. \quad (3.57)$$

For \vec{G} taking all the possible values, Equation (3.57) constitutes a set of linear, homogeneous equations for the eigenvectors $p_{\vec{k}}(\vec{G})$ and the eigenfrequencies $\omega(\vec{k})$.

Equation (3.57) can be expressed by the following matrix formulation

$$\sum_{i=1}^3 \Gamma_i \Sigma \Gamma_i P = \omega^2 \Omega P, \quad (3.58)$$

where $i=1,2,3$. The matrices Γ_i , Σ and Ω are defined as

$$(\Gamma_i)_{mn} = \delta_{mn} (k_i + G_i^m). \quad (3.59)$$

The explicit matrix formulation is shown as follow:

$$\Gamma_i = \begin{pmatrix} k_i + G_i & 0 & \dots & 0 \\ 0 & k_i + G_i & \dots & 0 \\ \vdots & \vdots & \ddots & \vdots \\ 0 & \dots & \dots & k_i + G_i \end{pmatrix}, \quad (3.60)$$

$$\Sigma = \begin{pmatrix} \sigma(\vec{G}_1 - \vec{G}_1) & \dots & \sigma(\vec{G}_1 - \vec{G}_{N \times N}) \\ \vdots & \ddots & \vdots \\ \sigma(\vec{G}_{N \times N} - \vec{G}_1) & \dots & \sigma(\vec{G}_{N \times N} - \vec{G}_{N \times N}) \end{pmatrix}, \quad (3.61)$$

3.2. PLANE WAVE EXPANSION

$$\Omega = \begin{pmatrix} \eta(\vec{G}_1 - \vec{G}_1) & \dots & \eta(\vec{G}_1 - \vec{G}_{N \times N}) \\ \vdots & \ddots & \vdots \\ \eta(\vec{G}_{N \times N} - \vec{G}_1) & \dots & \eta(\vec{G}_{N \times N} - \vec{G}_{N \times N}) \end{pmatrix}, \quad (3.62)$$

$$P = \begin{pmatrix} P(\vec{G}_1) \\ \vdots \\ P(\vec{G}_{N \times N}) \end{pmatrix}, \quad (3.63)$$

where $\vec{G} = (G_1, G_2, G_3) = (2\pi m/a_1, 2\pi n/a_2, 0)$. If $m = n = (-M, \dots, M)$, the size of the previous matrices is $N \times N = (2M + 1) \times (2M + 1)$.

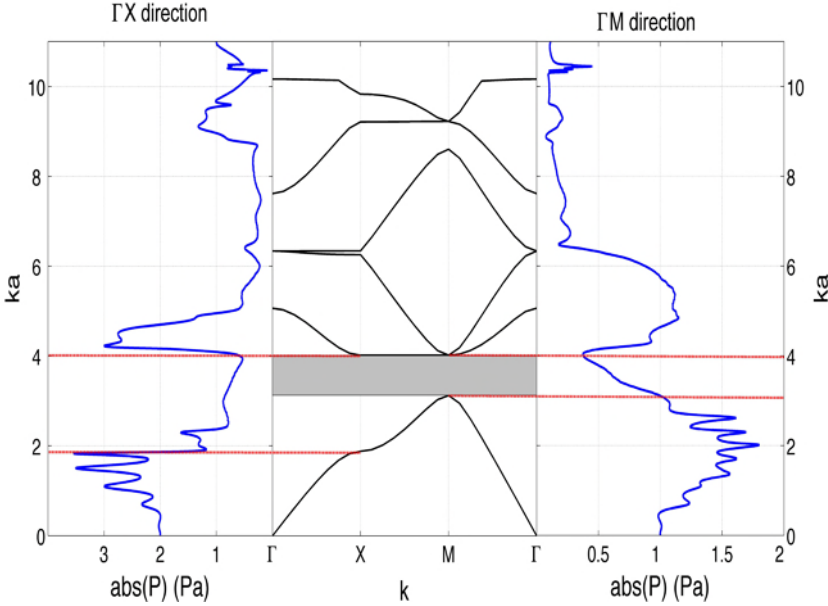


Figure 3.4: Band Structure for a SC made of rigid cylinders in square array with lattice constant a and filling fraction $ff = 50\%$. Central panel: Band structures calculated using PWE. Left panel: Spectrum for the ΓX direction of a finite array of size $5a \times 5a$ with $ff = 50\%$. Right panel: Spectrum for the ΓM direction of a finite array of size $5a \times 5a$ with $ff = 50\%$. Spectra measured at a point situated a distance $0.6a$ from the end of the crystal and in the symmetry axis.

By solving the system given in Equation (3.58) for each Bloch vectors in the

irreducible area of the first Brillouin zone, $N \times N$ eigenvalues, ω^2 , are obtained and they can be used to represent the band structures, $\omega(\vec{k})$.

In the central panel in Figure 3.4 one can observe the band structures of a SC made of rigid cylinders in square array with lattice constant a and filling fraction $ff = 50\%$. The frequencies are represented in terms of ka versus the Bloch vector in the first Brillouin zone related to the incident direction of the wave. Grey area represents the full BG of the structure. Red dash dotted lines represent the pseudogaps in both ΓX and ΓM directions. In the left and right panels we represent the spectra calculated by MST for a finite array of size $5a \times 5a$ with $ff = 50\%$ in the ΓX and ΓM directions respectively. In the calculated spectra the absolute value of the pressure in a point placed at $0.6a$ in the symmetry axis behind the periodic structure can be observed. We note the good agreement between both MST and PWE calculations for the case of the pseudogaps.

3.2.2 $k(\omega)$ method: extended plane wave expansion

Propagating waves inside a periodic media are a set of solutions of the wave equations satisfying the translational symmetry, and they are characterized by the transmission bands in PWE method. However, finite periodic media or periodic media with point defects, where the translational symmetry is broken, can support the well known evanescent modes characterized by a complex wave number, k .

In the $\omega(\vec{k})$ formulation, the existence of BG is indicated by the absence of bands in determined ranges of frequencies. BG could be understood by the evanescent behaviour of the modes inside it. This explanation was predicted by some authors [joannopoulos08] approximating the second band near the BG by expanding $\omega(k)$ in powers of k around the edge $k = \pi/a$. The authors claim that, as the BG is traversed the exponential decay grows as the frequency reaches the center of the BG.

At a given frequency ω inside the BG, the evanescent wave is characterized by a complex valued Bloch vectors $\vec{k}(\omega)$ that represent the decay of the mode

inside the periodic structure. The complex band structures for phononic crystal were recently presented by Laude *et al.* [Laude09] based on the work of Hsue *et al.* [Hsue05]. In a similar way, the problem for the case of Sonic Crystal is extended in this Section, also showing the supercell approximation.

From Equation (3.58) we define the following vector,

$$\Phi_i = \Sigma \Gamma_i P. \quad (3.64)$$

With this definition it is possible to reformulate the eigenvalue problem (3.58) as the equation system

$$\begin{aligned} \Phi_i &= \Sigma \Gamma_i P \\ \omega^2 \Omega P &= \sum_{i=1}^3 \Gamma_i \Phi_i. \end{aligned} \quad (3.65)$$

In order to obtain an eigenvalue problem for $\vec{k}(\omega)$, we write $\vec{k} = k\vec{\alpha}$, where $\vec{\alpha}$ is a unit vector. Then (3.60) can be written as

$$\Gamma_i = \Gamma_i^0 + k\alpha_i I, \quad (3.66)$$

where I is the identity matrix, and

$$\Gamma_i^0 = \begin{pmatrix} G_i & 0 & \dots & 0 \\ 0 & G_i & \dots & 0 \\ \vdots & \vdots & \ddots & \vdots \\ 0 & \dots & \dots & G_i \end{pmatrix}, \quad (3.67)$$

$$\alpha_i = \begin{pmatrix} \alpha_i & 0 & \dots & 0 \\ 0 & \alpha_i & \dots & 0 \\ \vdots & \vdots & \ddots & \vdots \\ 0 & \dots & \dots & \alpha_i \end{pmatrix}. \quad (3.68)$$

Then, equation (3.58) can be written as

$$\begin{pmatrix} \omega^2 \Omega - \sum_{i=1}^3 \Gamma_i^0 \Sigma \Gamma_i^0 & 0 \\ -\sum_{i=1}^3 \Sigma \Gamma_i^0 & I \end{pmatrix} \begin{pmatrix} P \\ \Phi' \end{pmatrix} = k \begin{pmatrix} \sum_{i=1}^3 \Gamma_i^0 \Sigma \alpha_i & I \\ \sum_{i=1}^3 \Sigma \alpha_i & 0 \end{pmatrix} \begin{pmatrix} P \\ \Phi' \end{pmatrix} \quad (3.69)$$

where $\Phi' = \sum_{i=1}^3 \alpha_i \Phi_i$.

Equation (3.69) represents a generalized eigenvalue problem with $2N$ eigenvalues k , possibly complex numbers, for each frequency. Complex band structures on the incidence direction $\vec{\alpha}$ can be obtained by solving the eigenvalue equation for a discrete number of frequencies and then sorting them by continuity of k . In contrast with the $\omega(\vec{k})$ method, in this formulation the periodicity is not relevant and $k(\omega)$ does not follow the first Brillouin zone.

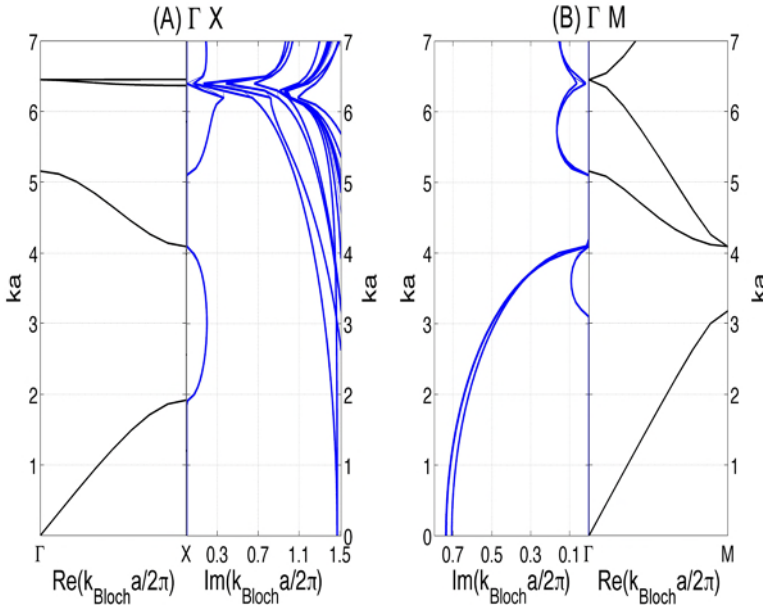


Figure 3.5: Band Structure for a SC made of rigid cylinders in square array with lattice constant a and filling fraction $ff = 50\%$. (A) Left panel: Band structures calculated using PWE. Right panel: Complex band structures for the ΓX direction calculated using EPWE. (B) Left panel: Complex band structures for the ΓM direction calculated using EPWE. Right panel: Band structures calculated using PWE.

Because of the periodicity of the system, Bloch waves can be expanded in series of harmonics where each harmonic corresponds with a value of k . Then if k is a complex number, the evanescent behaviour of a wave with a predetermined frequency would be multiexponential [Engelen09]. The Complex Band Structures show the values of all of these complex values of k which

contribute to the multiexponential decay of the mode in the BG. As it will be seen later, for the case of SC analysed in this work, the evanescent behaviour of the modes inside the BG is characterized considering the first term of the harmonic expansion in terms of k .

Figure 3.5 shows the results obtained using EPWE for the two main directions of symmetry. One can observe the real part of the band structures which coincides with the bands calculated using PWE. Moreover, one can observe the imaginary part of the band structures, observing the complex value of the Bloch vector in the region inside the BG.

One of the properties of the complex band structures is that they connect the real bands at the symmetry points (Γ , X or M) where holding bands is expected due to periodicity. Through this mechanism, the overall number of bands at any frequency is globally preserved which is a direct evidence of conserving the overall number of modes.

It can be noted that even at very low frequencies (subdiffractive regime), there exist complex bands simultaneously with the propagating bands in the real part. They could be understood as higher-order diffracted waves within the crystal that are frustrated. Consider periodic array with square periodicity a in the horizontal plane (xy plane) and a wave impinging on the crystal on the x direction. The wave number on the crystal is $\vec{k} = (k_x, k_y, k_z)$, in such a way the wave can be composed of a superposition of plane waves,

$$u(x, y, z) = \sum_n a_n e^{i(k_x x + k_y y + k_z z)}, \quad (3.70)$$

where harmonic temporal dependence has been considered.

The modulus of the wave vector is (ω/c) . Then, the component z of the \vec{k} is $k_z = \sqrt{(\omega/c)^2 - (k_y)^2 - (k_x)^2}$, where $k_y = 2\pi n/a$ and $k_x = 2\pi m/a$ can be any Bloch vector in the reciprocal space. For low frequencies (subdiffractive regime), there is only one transmission wave ($Im(k_z) = 0$, $Re(k_z) \neq 0$) corresponding to the order $n, m = 0$. However for $n, m > 0$, k_z is complex and the amplitude of the wave decays exponentially (see previous Equation 3.70). Thus, the high order of diffraction, which is a composition of two vibrational patterns, one due to k_x and other one due to k_y , are frustrated because of the

complex value of the k_z , thus this modes present evanescent behaviour for this high-orders, and both waves are exponentially killed. Similar explanation based on the diffraction gratings can be found in the reference [Laude09].

One can observe also that as the frequency increases, these bands become a real band. Following the evolution of such bands with increasing frequency, it can be noticed that after some onset frequency these initially evanescent waves can become propagative.

3.2.3 Supercell approximation

Breaking the periodicity of the structure locally can generate defect modes within the BG. These defect modes are strongly localized around the point defect: once the wave is inside the defect, it is trapped as the borders of the defect act as perfect mirrors for waves with frequencies in the BG. Localization depends on several parameters as for example the size of the point defect but, in finite periodic structures, the strength of sound localization also depends on the size of the structure around the defect [Wu09a, Wu09b] due to the exponential decay of the outgoing wave.

To analyse the propagation of waves inside periodic structures with defects, authors have traditionally used PWE with supercell approximation. The supercell method requires as low an interaction as possible between defects. This results in a periodic arrangement of supercells that contain the point defect. With this method it is possible to obtain the relation $\omega(\vec{k})$ for crystal with local defects and for instance one can explain the physics of wave guides [Khelif04, Vasseur08] or filters [Khelif03].

In this Section, we apply the approximation of supercell to the EPWE. This methodology allows us to obtain the relation $k(\omega)$ for defect modes. It would be interesting to know how the imaginary part of the wave vector inside the BG changes with the creation of the defect.

We consider a SC with primitive lattice vectors \vec{a}_i ($i = 1, 2, 3$). The supercell is a cluster of $n_1 \times n_2 \times n_3$ scatterers periodically placed in the space. Then, the primitive lattice vectors in the supercell approximation are $\vec{a}'_i = n_i \vec{a}_i$, and

the complete set of lattices in the supercell approximation is $\{R' | R' = l_i \vec{a}'_i\}$, where n_i and l_i are integers. The primitive reciprocal vectors are then

$$\vec{b}'_i = 2\pi \frac{\epsilon_{ijk} \vec{a}'_j \times \vec{a}'_k}{\vec{a}'_1 \cdot (\vec{a}'_2 \times \vec{a}'_3)} \quad (3.71)$$

where ϵ_{ijk} is the three-dimensional Levi-Civita completely anti-symmetric symbol. The complete set of reciprocal lattice vectors in the supercell is $\{\vec{G} | \vec{G}_i = N_i \vec{b}'_i\}$ where N_i are integers.

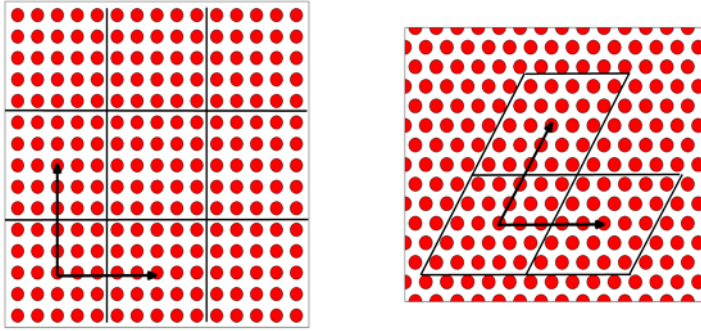


Figure 3.6: Examples of both square and triangular supercells.

3.2.3.1 Complete arrays

With the previous definition of supercell, the expression similar to Equation (3.55) for the case of the supercell approximation is obtained. The filling fraction of a cylinder in a supercell is $ff = \pi r^2/A$, where A is the area occupied by the supercell. If we consider a supercell with N cylinders organized in an array of size $n_1 \times n_2$ then

$$\beta(\vec{G}) = \begin{cases} \beta_A N ff + \beta_B (1 - N ff) & \text{if } \vec{G} = \vec{0} \\ (\beta_A - \beta_B) F(\vec{G}) & \text{if } \vec{G} \neq \vec{0} \end{cases} \quad (3.72)$$

where $F(\vec{G})$ is the structure factor of the supercell.

In this approximation, the structure factor of the supercell has to be computed taking into account its size. If we consider a 2D SC with cylindrical scatterers with radius r and size of the supercell $n_1 \times n_2$, the structure factor is expressed by

$$F(\vec{G}) = \sum_{i=-(n_1-1)/2}^{(n_1-1)/2} \sum_{j=-(n_2-1)/2}^{(n_2-1)/2} e^{i(a|\vec{G}_1|+ja|\vec{G}_2|)} P(\vec{G}) \quad (3.73)$$

where

$$P(\vec{G}) = \frac{2ff}{Gr} J_1(Gr). \quad (3.74)$$

where a is the lattice constant inside the supercell and $G = |\vec{G}|$.

3.2.3.2 Arrays with defects

If the supercell presents N_p point defects at the sites labelled by (l_s, m_s) in the periodic system, with $s = 1, \dots, N_p$, then the Fourier coefficients of the expansion of the physical parameters involved in the problem follow the following equation

$$\beta(\vec{G}) = \begin{cases} \beta_A(N - N_p)ff + \beta_B(1 - (N - N_p)ff) & \text{if } \vec{G} = \vec{0} \\ (\beta_A - \beta_B)F(\vec{G}) & \text{if } \vec{G} \neq \vec{0} \end{cases} \quad (3.75)$$

The structure factor of such a supercell with N_p point defects is

$$F(\vec{G}) = \left(\sum_{i=-(n_1-1)/2}^{(n_1-1)/2} \sum_{j=-(n_2-1)/2}^{(n_2-1)/2} e^{i(a|\vec{G}_1|+ja|\vec{G}_2|)} - \sum_{s=1}^{N_p} e^{i(l_s a|\vec{G}_1|+m_s a|\vec{G}_2|)} \right) P(\vec{G}). \quad (3.76)$$

The interaction among the defect points in the supercell approximation must be as low as possible between the neighboring supercells in order to decrease the overlap in between, thus the size of the supercell should be big enough to place the point defects separated in consecutive supercells.

By introducing the previous expressions in the matrices of PWE (3.58) or in the case of EPWE (3.69) the band structure of a periodic structure with and without a point defect using the supercell approximation are calculated.

3.3 Finite elements method

Sometimes the geometrical shape of the scatterers or the concurrence of several effects are difficult to solve by means of an analytical method. Numerical methods show a good alternative to find, in these cases, solutions to a problem. For the problem we are dealing with, SC, we can use FEM to solve both the scattering and the eigenvalue problems considering periodic boundary conditions.

FEM have been conceptually developed for the numerical discretization of problems with bounded domains and they are specially applicable for solving Helmholtz problems. In the case of periodic systems, the determination of the band structures by means of the solution of the eigenvalue problem represents the bounded problem. The application of FEM to unbounded domains, as for example the case of the scattering problems, involves a domain decomposition by introducing an artificial boundary around the obstacle. At the artificial boundary, the discretization can be coupled in various ways to some discrete representation of the analytical solution. In this work, only the radiation condition and the Perfectly Matched Layers are developed.

The commercial software COMSOL Multiphysics 3.5 is used as it has a simulation environment with a friendly user interface in all the steps of the modelling process: definition of geometry, specification of physics, meshing, solving and post-processing of results. Moreover COMSOL Multiphysics has the ability to define and couple any number of arbitrary, nonlinear partial differential equations which is very indicated for the cases where, for instance, we are interested in the coupling between acoustic and elastic properties of different media.

3.3.1 Bounded problem: eigenvalue problem

The acoustic wave Equation 8.6 considering temporal harmonic dependence of the type $e^{i\omega t}$ becomes the Helmholtz equation:

$$(\nabla^2 + \omega^2)p = 0. \quad (3.77)$$

In problems involving 2D periodic systems, separation of variables are used to solve the problem splitting the equation in two independent equations, one in the plane where the periodicity is and another one in the homogeneous direction where there is free field. Then, considering $p(r, \theta, z) = p_{\parallel}(r, \theta)p_{\perp}(z)$,

$$\frac{1}{r} \frac{\partial}{\partial r} \left(r \frac{\partial p_{\parallel}}{\partial r} \right) + \frac{1}{r^2} \frac{\partial^2 p_{\parallel}}{\partial \theta^2} + \omega^2 p_{\parallel} = \beta^2 p_{\parallel}, \quad (3.78)$$

$$\frac{\partial^2 p_{\perp}}{\partial z^2} = -\beta^2 p_{\perp}. \quad (3.79)$$

The solution of the Equation 3.79 follows the following expression:

$$p_{\perp} = e^{i\beta z} \quad (3.80)$$

where β indicates the direction of the incidence of the wave with the z -axis. This solution is a plane wave propagating in the z -axis. However if one considers that the direction of the waves is perpendicular to the symmetry axis of the cylinder (z -axis), meaning normal incidence, then $\beta = 0$ and there is no propagation in the z direction. Although some authors have considered oblique incidence [Guenneau04], here we consider only normal incidence on 2D periodic system.

The general planar equation is

$$\frac{1}{r} \frac{\partial}{\partial r} \left(r \frac{\partial p_{\parallel}}{\partial r} \right) + \frac{1}{r^2} \frac{\partial^2 p_{\parallel}}{\partial \theta^2} + (\omega^2 - \beta^2)p_{\parallel} = 0. \quad (3.81)$$

And considering normal incidence, the previous equation presents the following form,

$$\frac{1}{r} \frac{\partial}{\partial r} \left(r \frac{\partial p_{\parallel}}{\partial r} \right) + \frac{1}{r^2} \frac{\partial^2 p_{\parallel}}{\partial \theta^2} + (\omega^2)p_{\parallel} = 0. \quad (3.82)$$

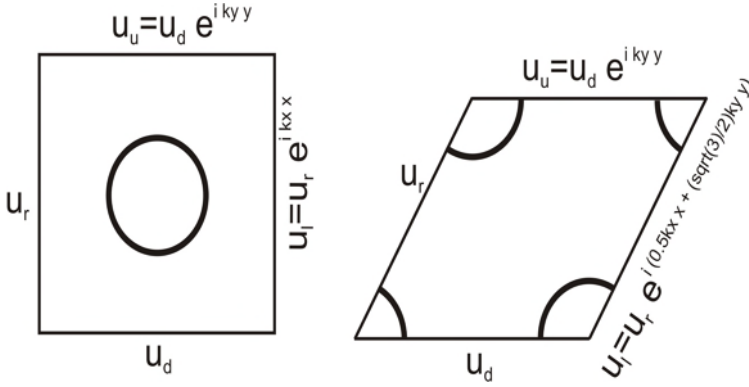


Figure 3.7: Unit cells for both square and triangular lattices. The periodic boundary conditions applied at the borders of each unit cell are shown. The cylinders are considered rigid then Neumann boundary condition are considered in their surface.

For the case of cylindrical symmetry of the problem, considering the Laplace operator in cylindrical coordinates:

$$(\nabla^2 + \omega^2)p_{||} = 0 \tag{3.83}$$

which is the Helmholtz equation.

For solving the problem using FEM, it is necessary to define the symmetry, discretize the domain and consider the boundary conditions. In the boundary of each cylinder both the continuity of the pressure and the velocity are considered as in Equations 3.36 and 3.37 respectively. However, for the case of rigid cylinders one can approximate the problem by considering Neumann boundary condition which expression is shown in Equation 3.20.

As it has been shown in Section 2.1, due to the translational symmetry, Bloch theorem is applied to solve the problem. The properties of the Bloch states constrains the solution to a unit cell with Bloch vectors in the first Brillouin zone. These features transform the unit cell in a bounded domain to solve the problem with the next boundary condition at the borders of the unit cell,

$$p(\vec{r} + \vec{R}) = p(\vec{r})e^{i\vec{k}\vec{R}} \tag{3.84}$$

CHAPTER 3. THEORETICAL MODELS AND NUMERICAL TECHNIQUES

Table 3.1: Directions of incidence, ranges of k , and ranges of phase changes, $k \cdot R_1$ and $k \cdot R_2$, for each of the segments required to traverse the boundary of the irreducible first Brillouin zone for both square and triangular lattices.

Direction	Square lattice		
	\vec{k}	$\vec{k} \cdot \vec{R}_1$	$k \cdot \vec{R}_2$
ΓX	$[(0,0)(0,\pi/a)]$	$[0,\pi/a]$	$[0,0]$
XM	$[(\pi/a,0)(\pi/a,\pi/a)]$	$[\pi/a,\pi/a]$	$[0,\pi/a]$
$M\Gamma$	$[(\pi/a,\pi/a)(0,0)]$	$[\pi/a,0]$	$[\pi/a,0]$
Direction	Triangular lattice		
	\vec{k}	$\vec{k} \cdot \vec{R}_1$	$\vec{k} \cdot \vec{R}_2$
ΓX	$[(0,0),(\pi/a,-\pi/(\sqrt{3}a))]$	$[0,\pi/a]$	$[0,0]$
XJ	$[(\pi/a,-\pi/(\sqrt{3}a)),(4\pi/(3a),0)]$	$[\pi/a,4\pi/(3a)]$	$[0,2\pi/(3a)]$
$J\Gamma$	$[(4\pi/(3a),0),(0,0)]$	$[4\pi/(3a),0]$	$[2\pi/(3a),0]$

where k is the Bloch vector and it scans the first irreducible Brillouin zone. Figure 3.7 shows both the square and triangular unit cells with the corresponding periodic boundary conditions. With the previous boundary conditions it is said that the domain is bounded and we will be able to solve the problem by FEM.

In order to determine eigenfrequencies of the SC with FEM solver, the periodicity must be established. Table 3.1 shows the values of k for calculate the band structures.

Unfortunately, it is not possible to calculate a band structure with the aid of the COMSOL software's user interface; to do so a parametric eigenvalue solver that varies the Bloch vector and obtains all eigenvalues would be required. A workaround is offered by COMSOL Script or MATLAB (we use the MATLAB interface). The results of a band structure calculation for both square and triangular lattices of rigid cylinders with $r = 0.4a$ are shown in Figure 3.8. One can compare FEM results with the ones obtained using PWE. The agreement between both techniques is very good.

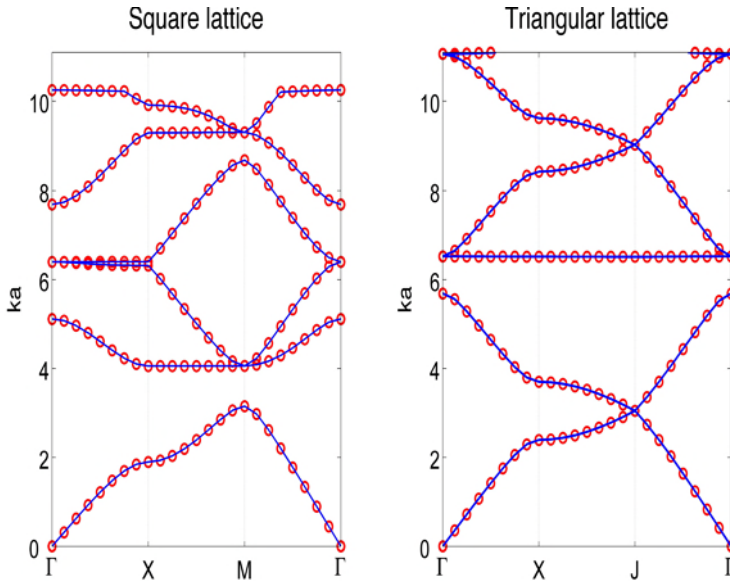


Figure 3.8: Band structure for both square and triangular lattices. The radius of the scatterer is $r = 0.4a$ in both cases. Blue continuous lines represent band structures calculated using FEM and open red circles show the same ones calculated using PWE.

3.3.2 Unbounded problem: scattering problem

Considering the wave propagation in free space (unbounded acoustic domain) the assumption that no waves are reflected from infinity is taken. This is known as the Sommerfeld condition. The mathematical expression for this far-field condition is obtained from Helmholtz integral equation in several references [ihlenburg98]. Let $p(\vec{r})$ be a solution of the Helmholtz equation $\nabla^2 p + k^2 p = 0$ in an unbounded domain. The Sommerfeld condition indicates that waves are absorbed at infinity if

$$p = O(R^{-1}), \tag{3.85}$$

$$ikp - \frac{dp}{dR} = o(R^{-1}), \tag{3.86}$$

$$R \longrightarrow \infty. \tag{3.87}$$

Where the notation $f(x) = o(g(x))$, $x \rightarrow \infty$, means that $f(x)/g(x)$ approaches zero as $x \rightarrow \infty$, while $f(x) = O(g(x))$ means that this ratio is bounded for all x .

The solutions of exterior Helmholtz problems that satisfy the Sommerfeld conditions are called radiating solutions. Using FEM, it is only possible to obtain some approximation of the radiating solutions in unbounded domains by applying some artificial boundaries in the numerical domain. Several techniques can be used for this purpose [ihlenburg98] and among them in the next Sections the radiation boundary condition and the perfectly matched layers will be presented.

3.3.2.1 Radiation boundary conditions

One of the possibilities to obtain an approximation of radiating solutions using FEM is considered in the surrounding boundaries of the modelling domain, a condition that allows an outgoing wave to leave the domain with minimal reflections. This kind of conditions are called radiation boundary conditions. In the case of the 2D domains this condition is

$$-\vec{n} \left(-\frac{1}{\rho} \nabla p \right) \frac{p}{\rho} = \left(i|\vec{k}| + \kappa(r) - i(\vec{k} \cdot \vec{n}) \right) \frac{p_0}{\rho} e^{-i(\vec{k} \cdot \vec{r})}, \quad (3.88)$$

where \vec{k} is the wave number and $\kappa(r)$ is a function whose form depends on the wave type: Plane wave: $\kappa(r) = 0$ and Cylindrical wave: $\kappa(r) = 1/(2r)$, with r being the shortest distance from the point $\vec{r} = (x, y, z)$ in the boundary to the source. The right-hand side of the equation represents an optional incoming plane pressure wave with amplitude p_0 and wave vector $\vec{k} = k\vec{n}_k$, where \vec{n}_k denotes the unit vector in the direction of propagation.

As an example, the scattering by a square array of size $5a \times 5a$ ($ff = 50\%$) was analysed using the COMSOL interface. The cylindrical source is located at point $(x, y) = (0, 5a)$ and Neumann conditions at the boundary of the cylinders as well as radiation boundary conditions in the sides of the domain have been considered. Figure 3.9 shows the corresponding maps and spectra of such a structure. One can compare these results with the ones calculated

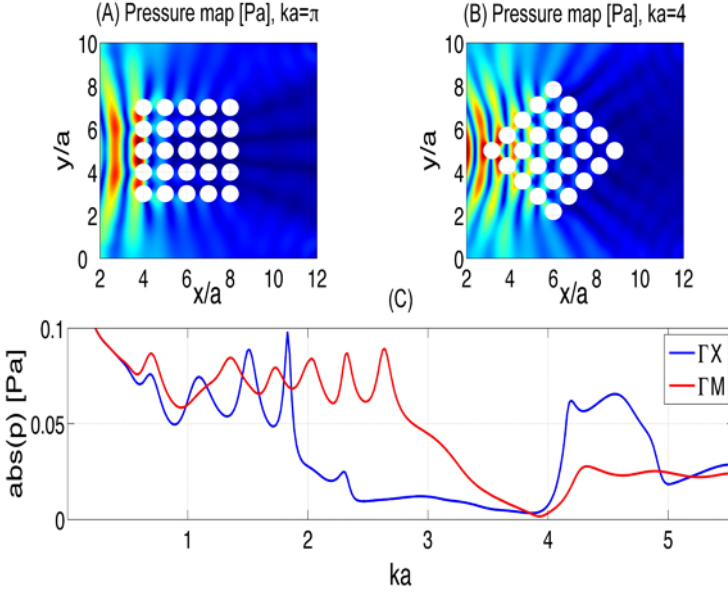


Figure 3.9: FEM calculations considering radiation boundary condition. A cylindrical source is considered at point $(x/a, y/a) = (0, 5)$. (A) Acoustic field produced by the scattering of waves for a SC with square lattice in the ΓX direction for the frequency inside the pseudogap at $ka = \pi$. (B) Acoustic field produced by the scattering and the incidence waves in a SC with square lattice in the ΓM direction for the frequency inside the pseudogap at $ka = 4$. (C) Spectra for the ΓX and ΓM direction, calculated at point $(x/a, y/a) = (11, 5)$.

using MST for $ka = \pi$ (ΓX direction) and for $ka = 4$ (ΓM direction) observing Figure 3.3. Although the maps and spectra seem to be the same, there are some small differences produced by the minimal reflections in the boundaries of the domain. Boundary radiation condition should be used in problems where the boundary is far away from the scattering medium, then the reflected waves can be considered to be negligible.

In order to reduce these spurious reflections coming back into the computational domain from the artificial boundaries, one can use the so called absorbing boundary conditions (ABC) [ihlenburg98], which are employed to prevent artificial boundary reflections. Several kinds of ABC have been pro-

posed in the last decades as, for example, the Dirichlet-to-Neumann Operator (DtN Operator) or the Atkinson-Wilcox expansion. Recently, the perfectly matched layer (PML) [Berenguer94] method received attention from scientists. The PML technique, that uses a perfectly matched layer with a damping mechanism to absorb the artificial boundary reflections, is presented in the next Section as an alternative to the boundary radiation condition.

3.3.2.2 Perfectly matched layers

An alternative approach to deal with truncation of unbounded domains is the so called perfectly matched layer (PML) method which was introduced by Berenger [Berenguer94]. PML are an efficient alternative for emulating the Sommerfeld radiation condition in the numerical solution of wave radiation and scattering problems. The idea, originating from electromagnetic computations, is based on simulating an absorbing layer of damping material surrounding the domain of interest, like a thin sponge which absorbs the scattered field radiated on the exterior of this domain. The method was immediately applied to different problems based on the scalar Helmholtz equation [Harari00] acoustics [Abarbanel99, Qi98], elasticity [Basu03], poroelastic media [Zeng01], shallow water waves [Navon04], other hyperbolic problems [Lions02], etc. Here, the interest is focused on the wave propagation time-harmonic scattering problems in linear acoustics, i.e., on the scalar Helmholtz equation. In this method, the interface between the physical domain and the absorbing layer does not produce spurious reflections inside the domain of interest, this is the reason because it is called PML.

PML consists of a coordinate transformation [Liu99, Collino98]. The transformation is a scaling to complex coordinates so that the new medium becomes selectively dissipative in the direction perpendicular to the interface between the PML and the physical domain. In this work, the PML domain absorbs waves in the coordinate direction d following the following coordinate transformation inside the PML:

$$d' = \text{sign}(d - d_0) |d - d_0|^n \frac{L}{\delta D^n} (1 - \iota) \quad (3.89)$$

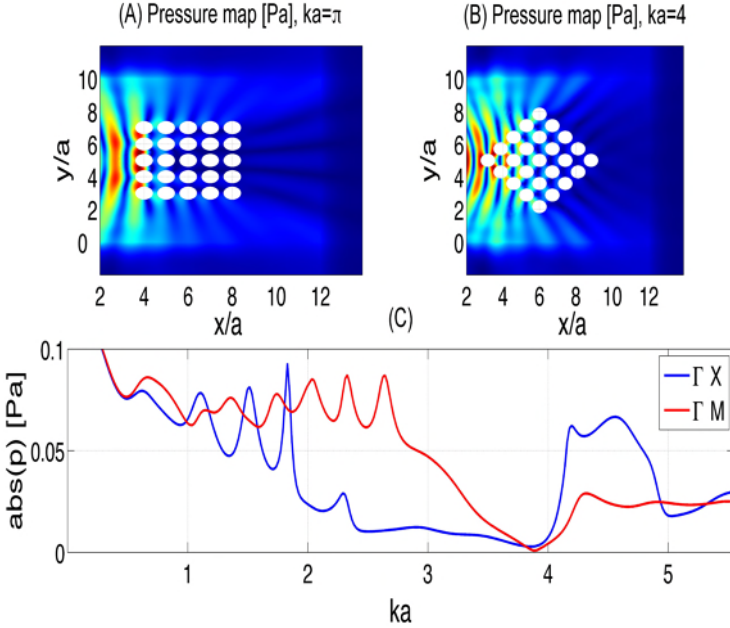


Figure 3.10: FEM calculations considering the PML regions. A cylindrical source is considered at point $(x/a, y/a) = (0, 5)$. (A) Acoustic field produced by the scattering of waves for a SC with square lattice in the ΓX direction for the frequency inside the pseudogap at $ka = \pi$. (B) Acoustic field produced by the scattering and the incidence waves in a SC with square lattice in the ΓM direction for the frequency inside the pseudogap at $ka = 4$. (C) Spectra for the ΓX and ΓM direction, calculated at point $(x/a, y/a) = (11, 5)$.

where L is the scaled PML width, d_0 is the coordinate of the inner PML boundary, the width of the PML is D and n is the scaling exponent.

For acoustic waves, the appropriate value of L is one wavelength that, for acoustic waves propagating along the absorbing coordinate direction d , is enough to absorb it. On the other hand the appropriate value of the scaling exponent for acoustic waves is 1. For scattering problems where different wavelengths are considered, n takes values between 1 and 2. Increasing the value of the exponent allows us to use fewer mesh elements to resolve wavelengths much smaller than the scaled PML width.

CHAPTER 3. THEORETICAL MODELS AND NUMERICAL TECHNIQUES

In practice, since the PML has to be truncated at a finite distance of the domain of interest, its external boundary produces artificial reflections. Theoretically, these reflections have minor importance due to the exponential decay of the acoustic waves inside the PML. In fact, for Helmholtz-type scattering problems, it was proven that the approximate solution obtained using the PML method exponentially converges to the exact solution in the computational domain as the thickness of the layer goes to infinity [Lassas98]. This result was generalized using techniques based on the pole condition [Hohage03]. Similarly, an analogous result for the convected Helmholtz equation was proven [Becache04].

Figure 3.10 shows the results of the calculations done to obtain Figure 3.9 but considering PML. The maps calculated using PML are very close to the ones calculated using MST (see Figures 3.3a and 3.3b) but, with this approach, the reflections in the boundaries of the numerical domain in these Figures disappear (Figures 3.10A and 3.10B).

4

Optimization: genetic algorithms

SC as acoustic finite devices present wave propagation properties depending on several parameters such as the external shape and the arrangement of the lattice, the range of frequencies or the filling fraction [[Sigalas05](#)]. Thus, changing these parameters, one can achieve tunable devices to control the wave propagation through them.

One possibility is the creation of defects in the crystalline structure. Some authors have demonstrated the possibility of increasing the attenuation capability of these materials by creating a periodic distribution of vacancies in the array [[Caballero01](#)]. A periodic distribution of vacancies in a host medium introduces additional sound transmission properties. The resulting SC, called the Suzuki phase, holds the attenuation bands of the host structure and it also presents additional ones associated to the periodicity of the missing cylinders. Following this idea, recent works have used the creation of vacancies in conjunction with optimization algorithms, such as the genetic algorithm, as a method of increasing the attenuation properties or of creating lenses based on SC [[Hakansson04](#), [Hakansson05b](#), [Hakansson06](#), [Romero06](#)]. The basic idea is to find an optimum distribution of vacancies from a starting and complete SC so that the acoustical properties are optimized in some sense.

This Chapter is devoted to present the fundamentals of genetic algorithms (GA) which constitute an optimization algorithm based on the principle of the natural selection, showing how we have adapted it to the optimization of SC.

In this work GA and MST have been used jointly to improve the acoustical properties of the SC by means of the creation of defects in the crystal.

4.1 Optimizing sonic crystals

In the last decade SC have been developed in order to create efficient acoustic filters [[Martinez95](#), [Sanchez98](#), [Kushwaha97](#), [Shen01](#), [Cervera02](#)] to use them as, for example, an alternative to classic acoustic barriers. Using the physical properties of the SC, specifically the BG, some authors [[Sanchez02](#)] have proven the possibility of using 2D SC made of isolated cylindrical scatterers made of rigid materials to construct acoustic barriers (see [Figure 4.1](#)).



Figure 4.1: (A) SC used as acoustic barrier; (B) Classical acoustic barrier.

There are some technical advantages in the use of SC as acoustic attenuation devices. One of them being the easy way to build this systems. This is because their structure allow air to pass through them, hence reducing the air pressure on the SC barrier. On the other hand, the design of efficient acoustic focalization systems can provide promising application in the range of ultrasounds [[Fang06](#), [Guenneau07](#)]. Nevertheless, their technological use should be developed in order to solve some acoustical disadvantages that they present compared to classic barriers.

Several parameters are involved in the design of acoustical devices based on SC. Especially both the number and size of scatterers and the lattice constant

of the arrays should be taken into account. Thus, the attenuation or focalization peaks change with an increase of both the number and the diameter of the cylinders. Moreover, the position in the frequency spectrum of these peaks depends on the distance between cylinders. Obtaining an optimum arrangement of cylinders to ensure the best acoustic attenuation or focalization is not an easy problem in general.

The optimization of the acoustical properties of SC by creating vacancies in order to design both attenuation and focalization devices could be based on the optimization of the values of the acoustic pressure. As it has been seen in Chapter 3, MST is a self-consistent method that can be used to calculate the pressure field produced by a SC. So, a good possibility is the use of MST in conjunction with some optimization techniques. But, from the mathematical point of view, the coefficients of the series expansions in MST (see Section 3.1), A_{ls} , which are determined numerically from the equations obtained by means of the application of the boundary conditions, depend on the parameters defining the crystal as well as on the frequency. As a consequence, the acoustic pressure given in Equation (3.25), simultaneously depends on discrete and continuous variables being in general difficult to optimize.

Generally, the methods of optimization search the best solution in the decision space (also known as search space), this means the space occupied by all the possible solutions of our problem. Any distribution of vacancies in a starting SC made of N scatterers constitutes a possible solution of our problem. Then, in the decision space we have to find the best solution among a very great number of solutions (2^N). This number indicates the dimension of the decision space in optimization methods, and it is an important parameter to take into account. The larger the size of the decision space, the more difficult the resulting optimization problem. In the optimization procedure presented here, the dimension of the decision space is large due to the size of the starting SC.

Finally, the computational time to calculate A_{lq} increases approximately with the third power of the number of cylinders, N^3 , therefore large numbers of cylinders imply a high computational time (see Appendix B). The use of SC as either attenuation or focusing devices means structures with many scatterers and this again indicates the complexity of the problem.

All of these arguments, together with the complexity of the mathematical functions involved in the calculus, indicate that SC are suitable to use optimization algorithms in order to improve their acoustical capability by means of the creation of vacancies.

4.2 Evolutionary algorithms: genetic algorithms

The problem presented in the previous Section is complex and has a high computational cost requiring new optimization algorithms to solve it. One interesting alternative to solve this problem is based on the use of evolutionary algorithms (EA). This is made possible thanks to the nature of EA based on populations of individuals. The good results obtained with EA, together with their capacity to handle a wide variety of problems with different degrees of complexity, explain why they are used more frequently. Indeed, they are currently one of the branches in which the most progress is being made within the field of EA [[fonseca95](#), [zitzler99](#), [coello02](#), [alander02](#), [coello05b](#)].

Here the genetic algorithms (GA), one of the most popular algorithms among the EA, have been used. GA, initiated by Holland [[holland75](#)], is a stochastic search technique based on the mechanics of natural selection and natural genetics. Although GA were not well-known at the beginning, after the publication of Goldberg's book [[goldberg89](#)], GA received a great deal of attention regarding their potential as optimization techniques to solve discrete optimization problems or other difficult optimization problems.

4.2.1 Fundamentals

GA work with sets of potential solutions of the problem to optimize. GA start with an initial *population* of potential solutions randomly generated. We can consider a set of N potential solutions, each one being called *individual*. These individuals evolve through successive iterations called *generations*. During each generation, the individuals are evaluated with some measure of the function to optimize, called *cost function*. Then the individuals

4.2. EVOLUTIONARY ALGORITHMS: GENETIC ALGORITHMS

are mixed by means of the *genetic operators*: *Selection*, *Crossover* and *Mutation*. Then the new population is created through genetic operators. The procedure continues until the termination condition is satisfied. The general framework of GA is described as follows, where $P(t)$ denotes the population at generation t :

```
procedure:Genetic Algorithms  
begin  
     $t := 0$   
    initialize  $P(t)$ ;  
    evaluate  $P(t)$ ;  
    while (not termination condition) do  
        begin  
             $t := t + 1$   
            select  $P(t)$  from  $P(t-1)$   
            alter  $P(t)$ ;  
            evaluate  $P(t)$ ;  
        end  
    end
```

A schematic view of the flowchart of fundamental procedures of GA can be seen in Figure 4.2.

Several programming languages can be used to implement a GA to optimize problems. In this work we have used the functions of GA toolbox of MATLAB [[gaMatlab](#)] that will be briefly described in the next subsections.

4.2.2 Coding

GA use a code in order to interpret the information of each individual in the optimization process. In this Section we show the code use in our optimization algorithm.

The individuals of a population are based on a complete finite SC with N cylinders. Each individual of the first generation consists of a SC with a dis-

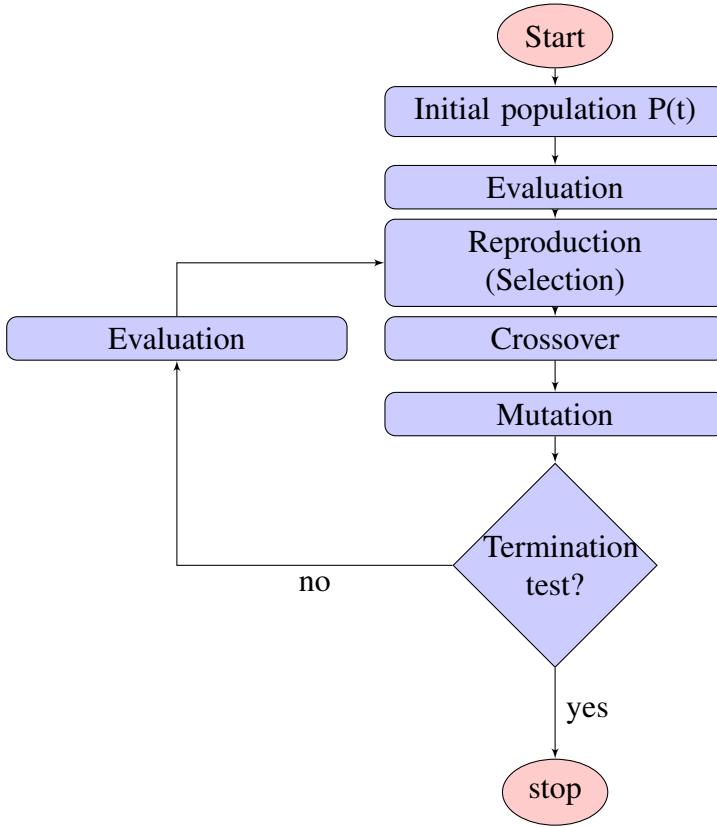


Figure 4.2: Flowchart of fundamental procedures of genetic algorithms

tribution of vacancies in the starting SC. Then, an individual is characterized by a vector of length N , called *chromosome*, whose coordinates, *genes*, represent the existence or not, of a scatterer in a specific position of the starting SC. Each gene is related to the coordinates of a scatterer of the starting SC. Every possible position of the cylinders in the SC is localized with a matrix of positions (X_{cyl}, Y_{cyl}) (the first column represents x position and the second column represents y position). Therefore the i -th gene is related to the i -th row in matrix (X_{cyl}, Y_{cyl}) . Each individual is represented by a value of the decision variable θ in the decision space. The value in each gene of the design variable θ can vary in the $[0, 1]$ range. A gene with a value in $]0.5, 1]$ represents the

4.2. EVOLUTIONARY ALGORITHMS: GENETIC ALGORITHMS

existence of a cylinder in the position associated with it, and a value in $[0, 0.5]$ means the existence of a vacancy at this position.

We can consider the next chromosome for the i -th individual:

$$\theta_i = \theta_{i1}\theta_{i2}\theta_{i3}\dots\theta_{iN}. \quad (4.1)$$

It is said that the values of the chromosome θ_i configure the so-called *genotype* of the i -th individual, so that by applying some uniquely mapping from the chromosome representation into the decision space one can obtain the so-called *phenotype*. In our problem the phenotype of the i -th individual is constituted by the coordinates whose values in the chromosome are 1, and as such, the coordinates where there is a scatterer. It is usually assumed to establish a one-to-one correspondence between genotypes and phenotypes. The mapping from phenotypes to genotypes is called a coding and the mapping from the genotypes to phenotypes is called a decoding. The set of all the possible chromosomes constitutes the decision space where the GA looks for the best solution to the problem.

In Figure 4.3A, one can observe a possible starting SC. The starting SC consists in a finite SC (without any vacancy), therefore the chromosome is a vector of 1s with length equal to the number of cylinders of the starting SC, N . From this starting SC, we generate new structures using the creation of vacancies. In Section 7.1 we will explain in detail this devices. An example of them is shown in Figure 4.3B.

One of the goals of using GA in the optimization of acoustical properties of SC is to find the best strategy to create vacancies. Then, following symmetry restrictions in the creation of vacancies, one can generate these defects in the starting SC in order to obtain new structures with enhanced acoustical properties and with some symmetry properties. For example taking into account the symmetry axis of the starting SC, one could generate vacancies with the next constrains: (i) with symmetry along the X axis (symX); (ii) with symmetry along the Y axis (symY); (iii) with symmetry along both the X and the Y axes (symXY); and (iv) random (nosym). Figure 4.4 shows some examples of several devices generated following the previous conditions.

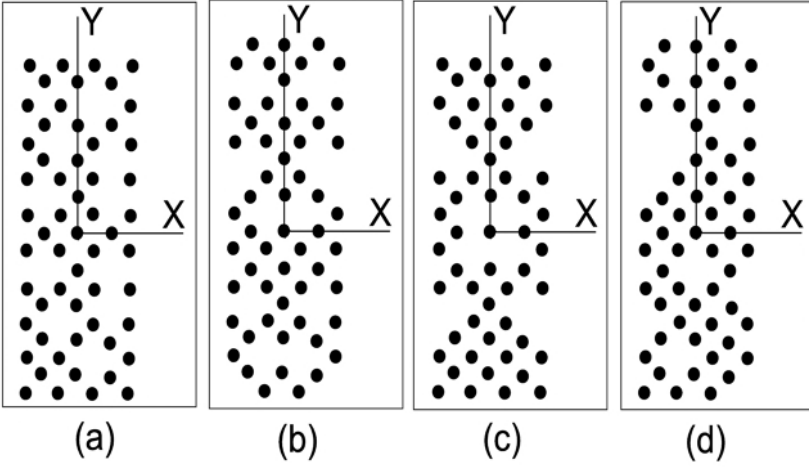


Figure 4.4: Creation of vacancies in a SC; (a) X-symmetric; (b) Y-symmetric; (c) XY-symmetric; (d) non symmetric.

4.2.3.1 Simple genetic algorithm

When decisions about optimal design involve searching for compromises between a unique objective, it is said that a simple optimization process is needed to find the optimal solution to the problem. The decision space and the cost function related to the objective have to be well-defined in order to start the optimization process that can be solved using a simple GA as previously described.

By means of this technique, we introduce the optimization of the attenuation properties of a SC defining a cost function related to the attenuation produced by a SC. Acoustic attenuation at a point (x, y) , due to an incident plane wave of frequency f travelling through a SC formed with an array of scatterers of radius r_l placed at (X_{cyl}, Y_{cyl}) coordinates, is defined as

$$Attenuation(dB) = 20 \log \left\{ \frac{1}{|p(x, y, X_{cyl}, Y_{cyl}, f, r_l)|} \right\} \quad (4.2)$$

where p is the value of the acoustic pressure and is obtained by means of MST. Attenuation is normalized for an incident acoustic pressure equal to unity.

It is necessary to define a cost function based on the Equation (4.2). The goal is to obtain an arrangement of scatterers that produces an attenuation band as flat as possible and as high as possible. To do this we will try to optimize the sum of the mean pressure in the ranges of frequencies of the band and the mean deviation in these ranges:

$$J_{v's}(\vec{x}) = \bar{p} + \sqrt{\frac{\sum_i (|p_i(\vec{x}) - \bar{p}|)^2}{N_f^2}} \quad (4.3)$$

where

$$\bar{p} = \frac{\sum_{i=1}^{N_f} |p_i(\vec{x})|}{N_f} \quad (4.4)$$

4.2.3.2 Multi-objective problems

Attenuation.

This Section defines the objective functions chosen to optimize the acoustic attenuation of a device generated from a starting SC. We would like to maximize the attenuation in a predetermined point of measurement, for a range of frequencies and in the ΓX direction as a multi-objective problem (MOP). Both the acoustic attenuation level and its uniformity in the optimization range of frequencies are the cost functions to maximize. In other words, we want to obtain an IL spectrum with a high attenuation level in a predetermined range of frequencies and with as low as possible fluctuations in the level of attenuation inside this range.

From Equation (4.2), it is easy to conclude that maximizing sound attenuation means minimizing acoustic pressure. Taking this fact into account, we define two objective functions, J_1 and J_2 , representing the mean pressure and the

4.2. EVOLUTIONARY ALGORITHMS: GENETIC ALGORITHMS

mean deviation, respectively, in the range of considered frequencies.

$$J_1(\vec{x}) = \bar{p} = \frac{\sum_{i=1}^{N_f} |p_i(\vec{x})|}{N_f}, \quad (4.5)$$

$$J_2(\vec{x}) = \sqrt{\frac{\sum_i (|p_i(\vec{x}) - \bar{p}|)^2}{N_f^2}}, \quad (4.6)$$

where N_f represents the number of frequencies considered in the range under study and $\vec{x} = (X_{cyl}, Y_{cyl})$ represents the variable under study, meaning the position of the existing cylinders sited in the sample. Minimizing these functions implies obtaining a maximum for the acoustic attenuation with a similar level of attenuation for all the considered frequencies. J_1 is related to the attenuation level in Equation (4.5), and J_2 represents the uniformity of the value of the attenuation level in the range of frequencies considered in Equation (4.6). The attenuation level is considered as the truly important function in this study - stability being a refinement of the obtained results, as shown in Chapter 7.

Focalization.

In this Section, we define the cost function used to optimize the focusing properties of a starting SC in a predetermined point of measurement, for a range of frequencies and in the ΓX direction. Usually, the focalization range of frequencies is just below the first band gap, this means inside the first transmission band. As in the case of the optimization of the attenuation properties, here two objective functions have also been defined, taking into account that the aim is to maximize the acoustic pressure at a predetermined point. The acoustic focusing level is defined as

$$Focalization(dB) = 20 \log \{ |p(x, y, X_{cyl}, Y_{cyl}, f, r_l)| \} \quad (4.7)$$

where p again means acoustic pressure calculated by MST. As in the case of the acoustic attenuation, the objective is to obtain a high pressure level with a small fluctuation of the pressure values in a predetermined range of frequencies. Thus, the objective functions J_3 and J_2 to minimize are defined

as

$$J_3(\vec{x}) = \frac{1}{\bar{p}} = \frac{N_f}{\sum_{i=1}^{N_f} |p_i(\vec{x})|} \quad (4.8)$$

$$J_2(\vec{x}) = \sqrt{\frac{\sum_i (|p_i(\vec{x}) - \bar{p}|)^2}{N_f^2}}, \quad (4.9)$$

where $\vec{x} = (X_{cyl}, Y_{cyl})$ and N_f are defined as in the attenuation case. We note that J_2 is the same objective function used in the optimization case explained above, and this means the uniformity of the values of pressure level is in the range of the considered frequencies. The minimization of J_3 implies a high level pressure (focusing effect). Again, the pressure level has been considered as the main parameter in this study, pushing stability in a second plane of the obtained results.

4.2.4 Operators

After the evaluation of each individual in each generation by means of the fitness function, the genetic operators create individuals of the next generation. The members of the population are altered by the action of three main operators: *Crossover*, *Selection* and *Mutation*.

To explain how these operators work in our algorithm, we present an example with a couple of random individuals. We consider that the starting SC is made of 10 cylinders arranged in triangular array by 5 rows and 2 columns. The lattice constant is a and the radius of the scatterer is $r = 0.4a$.

The first step consists of the selection of the progenitors for the next generation, which is done by the reproduction or selection operator. There are several ways to select the parents individuals of a generation [[michalewicz92](#), [Back94](#)]. Among all of them, two are basically used: the roulette wheel selection, originally proposed by Holland [[holland75](#), [gaMatlab](#)] and the stochastic universal sampling [[gaMatlab](#)]. By means of the reproduction (or selection) operator GA select the highly fitted (the best values of the fitness function) individuals to create the offspring for the next generations.

4.2. EVOLUTIONARY ALGORITHMS: GENETIC ALGORITHMS

After the application of the selection operator, we consider that two of the progenitors of a population are represented, for example, by the next chromosomes

$$Parent_1 = (0000101100), \quad Parent_2 = (1111111101).$$

In Figures 4.5A and 4.5B, one can observe the plot of the phenotypes corresponding to the chromosomes of parents 1 and 2 respectively.

Now, the Crossover operator is applied over the progenitors to create the offspring of the next population, this means that, the genetic information of two individuals of the current generation is exchanged for a probability equal to the crossover rate, p_c [gaMatlab], to create the offspring of the next generation.

The main characteristic of GA with respect to classic optimization methodologies is the use of crossover. Crossover is also known as recombination.

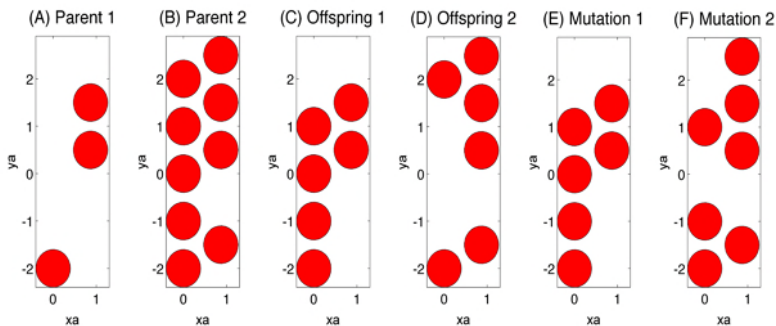


Figure 4.5: Application of the genetic operators from two Parents. (A) Parent 1 and (B) Parent 2. The application of the crossover operator using the multi-point procedure generates Offspring as shown in (C) and (D). The application of the mutation operator over the Offspring produces the final individuals as shown in (E) and (F).

A common implementation of crossover uses the C -point crossover process, in which C crossing sites are randomly chosen along a chromosome and all

genes of a crossing site are exchanged between the two parent chromosomes to create two offspring. We consider that, in the example $C = 2$, the crossing points are 2 and 5. Then the chromosome of the parents is divided into three parts, such that we exchange the genetic information in each chromosome to create the next offspring:

$$Offspring_1 = (0111101100), \quad Offspring_2 = (1000111101).$$

Figures 4.5C and 4.5D show the plot of the phenotypes corresponding to the chromosomes of the offspring 1 and 2 respectively.

Finally, the mutation operator is applied to the offspring. Mutation is a stochastic process used to change some genes of the chromosome of the offsprings by others, in such a way that the final offsprings are generated. The probability of mutation should be low, but different than zero. This operator ensures the exploration of new possible zones in the decision space, and as such, mutation is additionally aimed to maintain the diversity in the population.

Mutation creates a new possible solution in the neighbourhood of a current solution by introducing in some aspect a small change on it. In practice, for example, a single gene in a chromosome is altered with a small probability. For example the mutation of two previous offsprings could be:

$$Mutation_1 = (0111101100), \quad Mutation_2 = (0101111101).$$

Figures 4.5E and 4.5F show the plot of the phenotypes corresponding to the chromosomes of the mutation of offsprings 1 and 2 respectively. We note that, due to the low probability of mutation, the application of the mutation operator can produce the same chromosome for the resulting individual (see Figures 4.5C and 4.5E) or individuals with small differences compared with the initial ones (see Figures 4.5D and 4.5F).

4.2.5 Termination test

The termination test of a GA is not trivial because the algorithm is a stochastic search process and the convergence criterion has to be defined. Common

terminating conditions are: a solution that satisfies minimum criterion; fixed number of generations is reached; an allocated budget is reached; the highest ranking solution fitness is reaching or has reached a plateau in such a way that successive iterations no longer produce better results; manual inspection; combinations of the above . . . In this work, GA stop when a fixed number of generations is reached. Then, the approximation to the solution of the problem is represented by the best fitted individual of the last generation.

4.3 Multi-objective optimization

Decisions on optimal design in many scientific or engineering areas involve searching for compromises between different objectives. It is natural to look for the best solution for each objective. However, if some objectives are in conflict, an improvement in one, or more, objectives means a worsening in one, or more, of the other ones. The difficulty is the absence of a single optimal solution. As it has previously been shown, problems where several conflicting objectives have to be simultaneously optimized are known in the literature as multi-objective optimization problems (MOP).

4.3.1 Pareto front

For the MOP, the optimal solution is a set called the Pareto set Θ_p . The main characteristic of the members of this set is that any of the solutions are better than the other solutions for some of the objectives - meaning that all solutions are optimal in some sense. Basic concepts for these kinds of problems are illustrated in Figure 4.6 for a minimization problem with two objectives (J_1 and J_2) and two decision variables (θ_1 and θ_2). The problem is set as:

$$\min J(\theta) = \min [J_1(\theta), J_2(\theta)] \text{ subject to: } \theta = [\theta_1, \theta_2] \in S \quad (4.10)$$

One of the important definitions in this tool is the concept of dominance: a point $\theta^x = [\theta_1^x, \theta_2^x]$ is dominated by another point $\theta^y = [\theta_1^y, \theta_2^y]$ if at least one

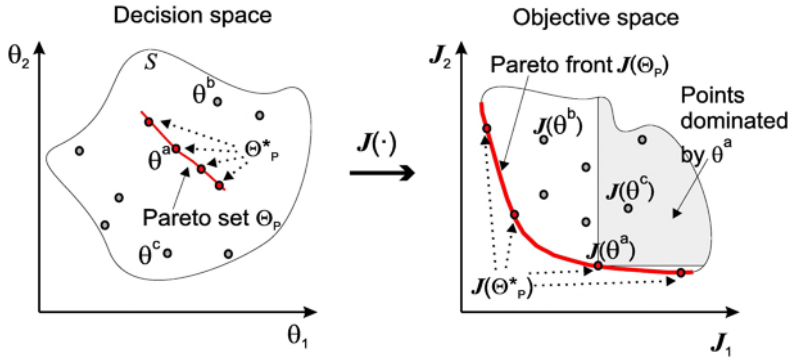


Figure 4.6: Example of a multi-objective optimization problem with two-dimensional decision and objective space.

of the objectives of θ^x ($J_1(\theta^x)$ or $J_2(\theta^x)$) is worse than the corresponding θ^y objective ($J_1(\theta^y)$ or $J_2(\theta^y)$). This is true providing the rest of the objectives are equal.

Figure 4.6 shows, as an example, a situation where θ^a dominates θ^c , but not θ^b . The gray area represents all the points (in the objective space) dominated by θ^a .

We can define the Pareto set (and its corresponding Pareto front) as the set of non-dominated points. The Pareto set in Figure 4.6 is referred to as Θ_p and the Pareto front as $J(\Theta_p)$.

Solving a multi-objective optimization problem by obtaining the Pareto optimal solution (Pareto set and Pareto front) is not in general a trivial problem. For instance, some problems present an infinite number of points, and these problems should be solved by means of classical multi-objective optimization algorithms [miittinen98]. In essence, the aim of these algorithms is to obtain a discrete approximation of the Pareto set Θ_p^* and Pareto front $J(\Theta_p^*)$ in a distribution near $J(\Theta_p)$, while ensuring that solutions are not too near each other (since they would then be more or less the same) and attempting to characterize all of the Pareto front (see Figure 4.6). However, classical algorithms are

sometimes not the best option in problems where the shape of the Pareto front is complicated and shows problems of discontinuity.

An interesting alternative to solve multi-objective optimization problems is based on the use of evolutionary algorithms, which enables the simultaneous generation of several elements of the Pareto optimal set in parallel and in a single run. Evolutionary algorithms (or evolutionary computations) are inspired by biological evolution: crossover, mutation, recombination and selection [back96]. An initial population (a set of possible solutions) evolves by applying genetic operators that combine the characteristics of some of the individuals of the population. At each iteration of the algorithm, the population changes and tries to converge towards the optimal solution $\Theta_p, J(\Theta_p)$.

A number of authors have developed different operators or strategies to convert the original single objective evolutionary algorithms into multi-objective optimization evolutionary algorithms that converge towards the Pareto optimal set able to characterize it [coello02]. The good results obtained with this type of algorithm explain their increasing use in many situations [coello04].

The algorithm used in this work is one of the most recent developments in multi-objective genetic algorithms (MOGA). A brief introduction of the algorithm is presented in the next Section.

4.3.2 Epsilon-variable multi-objective genetic algorithms

The epsilon variable multi-objective genetic algorithm (evMOGA) is an elitist multi-objective evolutionary algorithm based on the concept of epsilon-dominance [laumanns02]. A complete and detailed version of the evMOGA algorithm is described in the references [Herrero07]. The evMOGA algorithm obtains a discrete approximation of the Pareto set, Θ_p^* that converges towards the Pareto optimal set Θ_p in a smart way (in this type of distribution, the more sloped a zone of the Pareto front is, then the more points are used to characterize the zone) and using limited memory resources.

With regard to MOP, a complete and detailed version of the *ev-MOGA* algorithm is developed in [herrero06] where the algorithm is compared with the

epsilon multi-objective evolutionary algorithms (ϵ -MOEA) [Mishra05] by means of a set of five classical benchmarks for MOP (MOP1 to MOP5 extract from [coello02]). ϵ -MOEA algorithm is also based on the concept of ϵ -dominance. In [Mishra05], a comparison between the ϵ -MOEA and other well known algorithms such as (Non-dominated Sorting Genetic Algorithm) NSGA-II, (Pareto Envelope based Selection Algorithm) PESA, (Strength Pareto Evolutionary Algorithm) SPEA2, etc. shows the superiority of the ϵ -MOEA. As stated in [Deb07], ϵ -MOEA is computationally faster and achieves better distributed solutions than NSGA-II or SPEA2.

	PS	GD	HR	SP	BR
MOP1					
<i>ev-MOGA</i>	25	0.00292	0.929	0.00767	0.5145
ϵ -MOEA	25	0.00296	0.929	0.00765	0.5143
MOP2					
<i>ev-MOGA</i>	42	0.00101	0.981	9.625e-7	0.9223
ϵ -MOEA	42	0.00107	0.9798	4.676e-6	0.883
MOP3					
<i>ev-MOGA</i>	39.8	0.0158	0.9605	0.0632	0.8379
ϵ -MOEA	38.8	0.0222	0.9603	0.0658	0.8374
MOP4					
<i>ev-MOGA</i>	53	0.00299	0.9803	0.0118	0.938
ϵ -MOEA	49.7	0.00309	0.975	0.0168	0.9323
MOP5					
<i>ev-MOGA</i>	53.6	0.00364		0.0182	0.6057
ϵ -MOEA	30.6	0.00531		0.02818	0.6412

Table 4.1: Comparative values of the Pareto solutions (PS), generational distance (GD), hyperarea ratio (HR), spacing (SP) and box ratio (BR) metrics for the MOP1 to MOP5 problems between *ev-MOGA* and ϵ -MOEA algorithm. Bold numbers show the best values obtained for each metric and problem.

Generally, the *ev-MOGA* algorithm presents better values for classical MO metrics (Pareto solutions (PS), generational distance (GD), hyperarea ratio (HR), spacing (SP) and box ratio (BR¹) as shown in Table 4.1. The algorithms optimize each problem ten times with a different initial population (randomly created) and the average values for each metric are shown in this table.

¹For more details on these metrics see [coello02].

ev-MOGA obtains an ϵ -Pareto set, $\hat{\Theta}_P^*$, that converges towards the Pareto optimal set Θ_P in a distributed way and utilizes limited memory resources. Another difference with ϵ -MOEA is that *ev-MOGA* is able to dynamically fit the limits of the Pareto front and prevent the loss of solutions belonging to the extremes of the front.

4.3.2.1 ϵ -dominance

The objective function space is split into a fixed number of boxes forming a grid. For each dimension, n_box_i cells of ϵ_i width calculated as

$$\epsilon_i = (J_i^{max} - J_i^{min}) / n_box_i \quad (4.11)$$

This grid preserves the diversity of $J(\hat{\Theta}_P^*)$ since one box can be occupied by only one solution. This fact prevents the convergence of the algorithm towards just one point or area inside the function space (Figure 4.7).

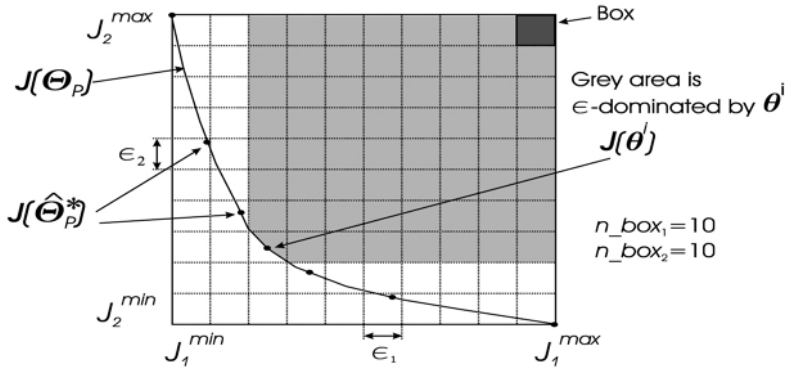


Figure 4.7: The concept of ϵ -dominance. ϵ -Pareto Front $J(\hat{\Theta}_P^*)$ in a two-dimensional problem. J_1^{min} , J_2^{min} , J_1^{max} , J_2^{max} , limits space; ϵ_1 , ϵ_2 box widths; and n_box_1 , n_box_2 , number of boxes for each dimension.

The concept of ϵ -dominance is defined as follows. For a variable in the decision space θ , $box_i(\theta)$ is defined by

$$box_i(\theta) = \left[\frac{J_i(\theta) - J_i^{min}}{J_i^{max} - J_i^{min}} \cdot n_box_i \right] \forall i \in [1 \dots s] \quad (4.12)$$

Let $box(\theta) = \{box_1(\theta), \dots, box_s(\theta)\}$. A solution vector θ^1 with function value $J(\theta^1)$ ε -dominates the vector θ^2 with function value $J(\theta^2)$, denoted by:

$$J(\theta^1) \prec_{\varepsilon} J(\theta^2), \quad (4.13)$$

if and only if:

$$(box(\theta^1) \prec box(\theta^2)) \vee ((box(\theta^1) = box(\theta^2)) \wedge (J(\theta^1) \prec J(\theta^2))) \quad (4.14)$$

Hence, a set $\hat{\Theta}_P^*$ is ε -Pareto if and only if $\forall \theta^1, \theta^2 \in \hat{\Theta}_P^*, \theta^1 \neq \theta^2$

$$\hat{\Theta}_P^* \subseteq \Theta_P \wedge (box(\theta^1) \neq box(\theta^2)) \quad (4.15)$$

4.3.2.2 ε -Pareto front

Next, we describe the procedure to obtain an ε -Pareto front $J(\hat{\Theta}_P^*)$, which is a well-distributed approximation sample of the Pareto front $J(\Theta_P)$. The algorithm, which dynamically fits the width ε_i , is composed of three populations (see Figure 4.8).

1. Main population $P(t)$ explores the searching space D during the algorithm iterations (t). Population size is $Nind_P$.

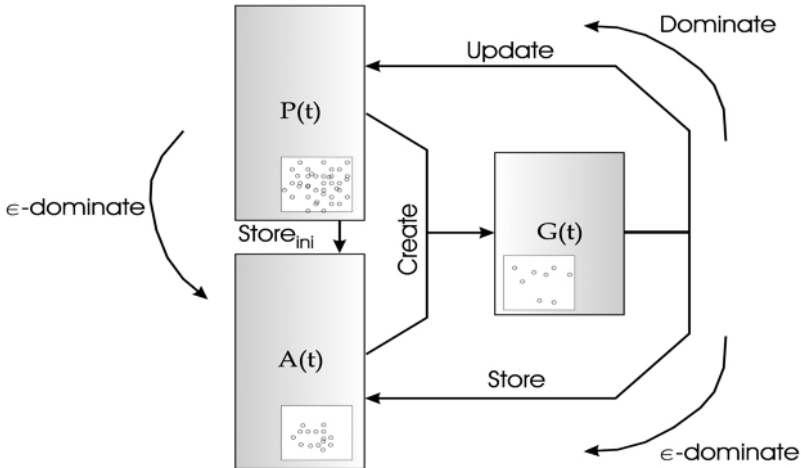


Figure 4.8: *ev-MOGA* algorithm structure. $P(t)$, the main population; $A(t)$, the archive; $G(t)$ the auxiliary population.

2. Archive $A(t)$ stores the solution $\hat{\Theta}_p^*$. Its size $Nind_A$ can be variable and will never be greater than

$$Nind_{max} A = \frac{\prod_{i=1}^s (n_{box_i} + 1)}{n_{box_{max}} + 1} \quad (4.16)$$

where $n_{box_{max}} = \max_i n_{box_i}$.

3. Auxiliary population $G(t)$. Its size is $Nind_G$, which should be an even number.

The pseudocode of the *ev-MOGA* algorithm is given by

1. $t := 0$
2. $A(t) := \emptyset$
3. $P(t) := \text{ini_random}(D)$
4. $\text{eval}(P(t))$
5. $A(t) := \text{store_ini}(P(t), A(t))$
6. while $t < t_{max}$ do

```
7.      G(t) :=create(P(t), A(t))
8.      eval(G(t))
9.      A(t+1) :=store(G(t), A(t))
10.     P(t+1) :=update(G(t), P(t))
11.     t:=t+1
12. end while
```

The main steps of the algorithm are briefly detailed as follows²:

Step three. $P(0)$ is randomly initialized with N_{ind_P} individuals (design vectors θ).

Step four and eight. Function **eval** calculates function values (cost functions values) for each individual in $P(t)$ (step four) and $G(t)$ (step eight).

Step five. Function **store_{ini}** checks individuals of $P(t)$ that might be included in the archive $A(t)$ as follows:

1. Non-dominated $P(t)$ individuals are detected, Θ_{ND} .
2. Function space limits are calculated from $J(\Theta_{ND})$.
3. Individuals in Θ_{ND} that are not ε -dominated will be included in $A(t)$.

Step seven. Function **create** creates $G(t)$ by means of crossover (extended linear recombination technique) and mutation (using random mutation with Gaussian distribution) operators.

Step nine. Function **store** checks which individuals in $G(t)$ should be included in $A(t)$ on the basis of their location in the function space (see Figure 4.9). Thus $\forall \theta^G \in G(t)$

1. If θ^G lies in area Z1 and is not ε -dominated by any individual from $A(t)$, it will be included in $A(t)$. Individuals from $A(t)$ which are ε -dominated by θ^G will be eliminated.

²A more detailed description can be obtained in [Herrero07].

4.3. MULTI-OBJECTIVE OPTIMIZATION

2. If θ^G lies in area Z2 then it is not included in the archive, since it is dominated by all individuals in $A(t)$.
3. If θ^G lies in area Z3, the same procedure is applied as was used with function \mathbf{store}_{ini} but now applied over the population $P'(t) = A(t) \cup \theta^G$. In this procedure, new function limits and ϵ_i widths could be recalculated.
4. If θ^G lies in area Z4, all individuals from $A(t)$ are deleted since they are all ϵ -dominated by θ^G . θ^G is included and function space limits are $\mathbf{J}(\theta^G)$.

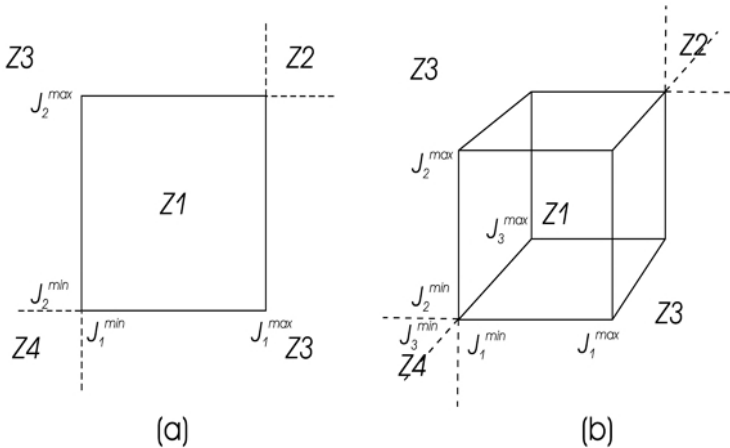


Figure 4.9: Objective function space areas (Z) and limits (J). Showing (a) two-dimensional case (b) three-dimensional case.

Step 10. Function **update** updates $P(t)$ with individuals from $G(t)$. Every individual θ^G from $G(t)$ replaces an individual θ^P meaning that they are randomly selected from among the individuals in $P(t)$ that are dominated by θ^G . θ^P will not be included in $P(t)$ if there is no individual in $P(t)$ dominated by θ^G .

Finally, individuals from $A(t)$ compound the solution $\hat{\Theta}_P^*$ of the multi-objective optimization problem.

4.3.3 Parallelization

One of the limitations of multi-objective optimization evolutionary algorithms is their high computational cost. For each individual of the chosen population, the objective functions have to be computed and in most cases, this represents the costly part of the algorithm.

The high computational cost of the optimization of the SC attenuation capability produces huge execution times, meaning that the average execution time for a population $P(t)$ of 120 individuals, population $G(t)$ of 8, and $t_{max} = 6500$ generations is around 417035 seconds³ (4 days, 19 hours, 50 minutes and 35 seconds). Improvements of execution time were obtained with a parallel implementation of the *ev-MOGA* described. Several alternatives for parallelization are possible [cantupaz95]. In this work, the Master-Slave configuration has been used. For this architecture, there is one processor working as Master, executing tasks of the *ev-MOGA*, and the rest evaluate the fitness function of a subpopulation (see Figure 4.10).

The Master has to send a subpopulation to each Slave, who makes a fitness evaluation and returns results to the Master. The Master works in a synchronous way, waiting for all fitness values from all the Slaves. After receiving all the fitness values, the Master performs the evolution to produce the next iteration and sends the Slaves the new population for fitness evaluation. This type of implementation is the simplest and does not change the operators of the *ev-MOGA* nor their behaviour. The time reduction is significant since the overall time is theoretically divided by the number of Slaves - if the evolution procedure and Master-Slave communication tasks have no computational cost. With the proposed implementation, the computational cost is important and the theoretical reduction is not achieved. Even then, the saving in time is quite large, for the proposed problem, with eight Slaves, the total execution is reduced to 104204 seconds (1 day, 4 hours, 56 minutes and 44 seconds). The distributed platform is built with eight computers as described:

- All computers are Intel[®] Pentium[®] D 3.4GHz.

³Execution is performed with one of the computers on the distributed platform described later.

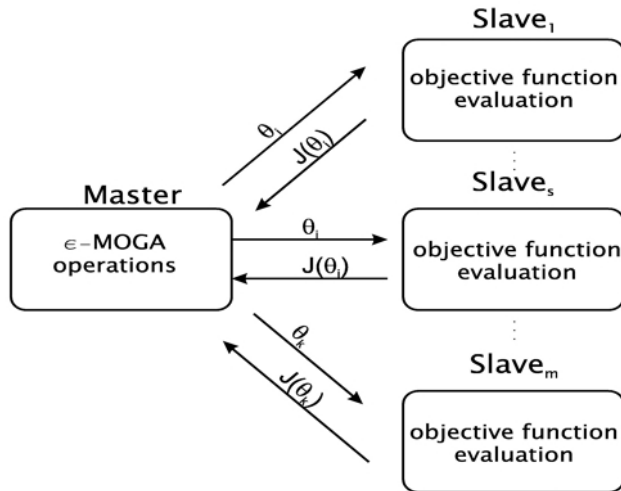


Figure 4.10: Master/Slave architecture for *ev-MOGA*.

- The master computer has 2 GB RAM and the operating system is Windows Server 2003. This computer works as master and has a slave.
- Slave computers have 1GB RAM and Windows XP.
- Local network with Gigabit Ethernet.

All developments (*ev-MOGA* and SC models) have been made in Matlab, parallelization has been performed with Matlab Distributed Computing Toolbox and Matlab Distributed Computing Engine.

5

Experimental setup

The experimental validation of the theoretical predictions is one of the most important steps in the scientific process. In this Chapter, we give a brief description of the experimental setup used for the experimental measurements done in this work.

The first experimental evidence of the sound propagation properties of the sonic crystals was performed in 1995 by Martínez-Sala *et al.* [[Martinez95](#)]. The authors measured in free field conditions the transmission properties of a finite periodic minimalist sculpture by Eusebio Sempere, observing similar behaviour to the electron propagation in solid crystalline structures. Since these experimental results were done, a great number of works have been motivated to explain the correct behaviour of these systems. Thus, better and improved experimental conditions have been needed to check the theoretical results.

All the experimental results shown in this work have been measured under controlled conditions in an anechoic chamber located at the Universidad Politécnica de Valencia. The characterization of the anechoic chamber can be found in reference [[Rubio97](#)] and it will be summarized in Section [5.1](#). In Section [5.1](#), we will also show the system to place the SC in the anechoic chamber and the frames used to introduce the periodicity in the experimental samples.

Two different acquisition systems have been used throughout this work. The

recent development of a robotized acquisition system (3DReAMS) capable of sweeping the microphone through a three dimensional grid of measuring points located at any trajectory inside the echo-free chamber, synchronizing the motion and the acquisition of the signal, has represented a big improvement in the experimental measurements done in this work. At the beginning, the motion and the positioning of the microphone were done manually and B&K PULSE Multi-analyser system, type 3560C, was used for the acquisition. After that, the most recent experiments shown in this work have been measured using the three-dimensional robotized e-acoustic measurement system (3DReAMS). Both experimental setups are briefly explained in Sections 5.2.1 and 5.2.2.

Finally, a list of the scatterers analysed in this work, showing the geometrical shapes and characteristics are shown in Section 5.4. A detailed table of the SC analysed in this work is also shown in this Section.

5.1 Anechoic chamber

From the acoustic counterpart, anechoic chambers are rooms designed to stop reflections of sound waves. They are also insulated from exterior sources of noise. The combination of both aspects means they simulate a quiet open-space of infinite dimension, which is useful when exterior influences would otherwise give false results. The size of the chambers depends on the size of the objects to be tested and on the frequency range of the signals used, although scale models can sometimes be used for testing at shorter wavelengths.

The calibration of the anechoic chamber used and its main properties can be found in reference [Rubio97]. Results on the dependences of the sound pressure level and the phase are tested: for a point source placed elsewhere, the sound pressure level decreases 6 dB when the distance between source and microphone is doubled and the phase also increases linearly with this distance. The dimensions of this anechoic chamber are $8 \times 6 \times 3$. Figure 5.1 shows the distribution of the source, sample, microphone, fast Fourier transform (FFT) analyser and PC in the laboratory.

5.1. ANECHOIC CHAMBER

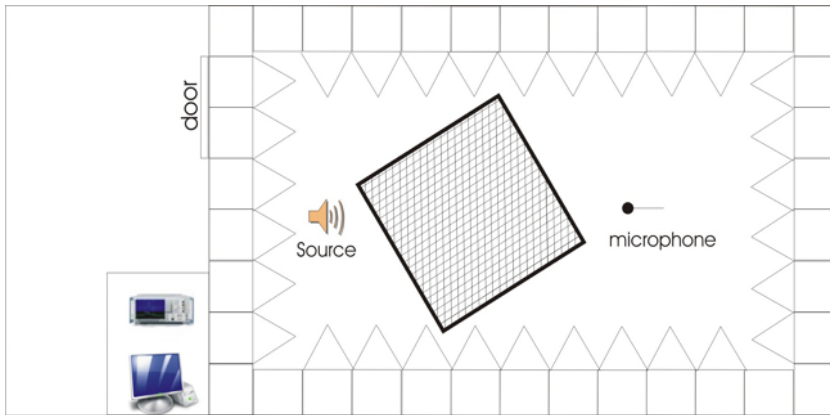


Figure 5.1: Schematic view of the distribution of the source, frame, microphone, FFT analyser and PC in the laboratory.

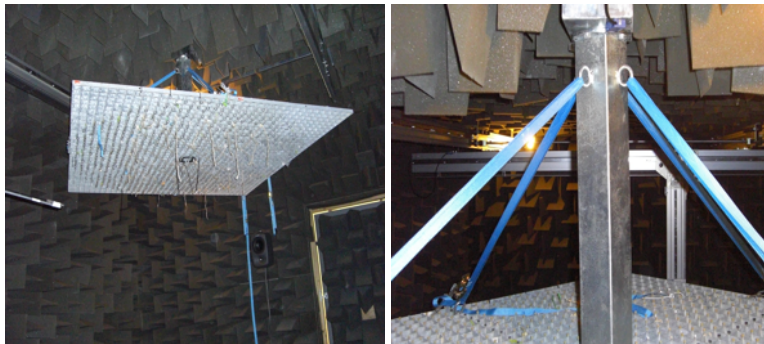


Figure 5.2: Pictures of the distribution of the source, microphone and frame in the anechoic chamber. The hanging system can also be seen.

The main use of this anechoic chamber is the experimental analysis of SC. The samples were designed to be similar to Eusebio Sempere's sculpture. Two different frames with square and triangular periodicities were used to construct different SC with different periodicities and lattice constants. These frames enables the hanging the scatterers in such a way that the SC can present different filling fractions.

These frames have a surface of $2 \times 2 \text{ m}^2$ with a thickness of 5 cm and they are

CHAPTER 5. EXPERIMENTAL SETUP

hung from a ball-and-socket joint making the rotation of the frame possible. The structure can support a weight of approximately 1000 kg. Figure 5.2 shows a picture of the mechanism of the frame and the hanging system. This system enables the rotation of the SC with respect to its center, thus it is possible to analyse the dependence of the sound propagation through the SC on the angle of incidence of the wave.

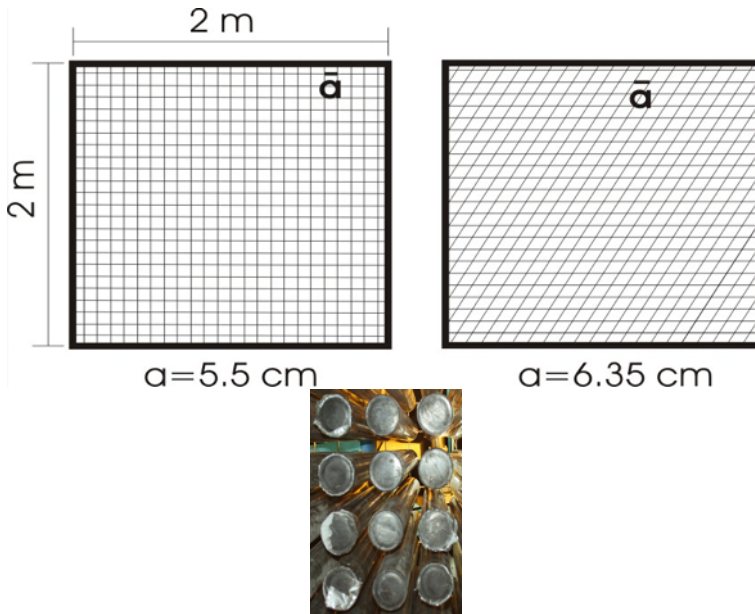


Figure 5.3: Schematic view of both triangular and square frames. Detailed picture of the SC once the scatterers are hung.

The minimum lattice constant achieved with the frame with square array is 5.5 cm, whereas in the case of a triangular periodicity the minimum lattice constant is 6.35 cm. Thus, it is possible to construct SC with lattice constants with a multiple of these values. Figure 5.3 shows the transversal views of both square and triangular frames, as well as a detailed picture of the cylinders placed in the frame.

5.2 Acquisition system

The setup used in this work is as follows: The sample to be analysed is placed between the source and the microphone. Then the microphone is connected to a fast Fourier transform (FFT) analyser where the temporal data are processed using the FFT. The FFT analyser is connected to a computer where the data is represented in the usual form of the sound pressure levels in dB.

In the first stages of this work, a setup was used in which the acquisition and the motion of the microphone and the sample were not synchronized. In this system the microphone, the sample and the source were placed in the desired distribution and then the acquisitions systems were turned on. We recently developed a novel three dimensional positioning system (3DReAMS) for the anechoic chamber in order to control the motion of the microphone, the source, the sample and all of them synchronized with data acquisition.

These two acquisition setups are briefly explained in the next Section.

5.2.1 Non robotized system

At the beginning of this work, the sound pressure measurements were taken by means of a B&K PULSE Multichannel data acquisition unit Type 2827 with a B&K LAN Interface Module Type 7533 and 4/2 ch. Input/Output Module Type 3109.

PULSE, a Multichannel data acquisition unit Type 2827, is a task-oriented analysis system. It provides the platform for a range of PC-based measurement solutions from B&K. A PULSE system with LAN interface consists of a PC, PULSE software, an operative system, the interface, portable data acquisition front-end hardware and analysis motor. System configurations with 4 input channels and 2 generator output channels are possible. Type 2827 can either be powered by two internal Nickel-Metal Hydride batteries, from a 10-32 V DC power supply or from an AC/DC supply.

The maximum sampling rate of the PULSE Type 2827 is 65 kS/s and the

analog inputs present 16-bit resolution ADCs. Then, the range of frequencies that can be analysed with this system is ranged between 0 Hz and 25.2 kHz. With this hardware, the acquired signals were processed by the B&K software for a PULSE system, Noise and Vibration Analysis Type 7700.

5.2.1.1 Sound source

In this setup, a speaker placed in the focus of a parabolic reflector was used as a sound source. The reflector is employed to collimate the beam. Nevertheless, the distance between the source and the sample was not enough to produce a full plane wave front when the sound reached the sample; however this ideal situation could be considered from a theoretical point of view.

5.2.2 3DReAMS

The need for accurate spacial measurements for a better understanding of the experimental behaviour of the SC motivated the development of 3DReAMS. This system was developed in collaboration with the CPOH research group of the UPV and Talleres Ferriols (Valencia). The acoustical part was designed by us, CPOH developed the control of the motion of the robot and Talleres Ferriols designed the structure of the robotized system. The robot was financed by Generalitat Valenciana through the FEDER funds.

In the next Sections, we describe the main characteristics of the control of motion and the acquisition system.

5.2.2.1 Robotized system and control of motion

3DReAMS is a Cartesian robot with three axes (X, Y, Z) installed in the ceiling of the anechoic chamber previously described. The robot was designed to sweep the microphone through a 3D grid of measuring points located at any trajectory inside the echo-free chamber (see Figure 5.4). The robot has a rotatory column (also installed on the ceiling of the anechoic chamber) where

the periodic frames are placed (see Figure 5.2).

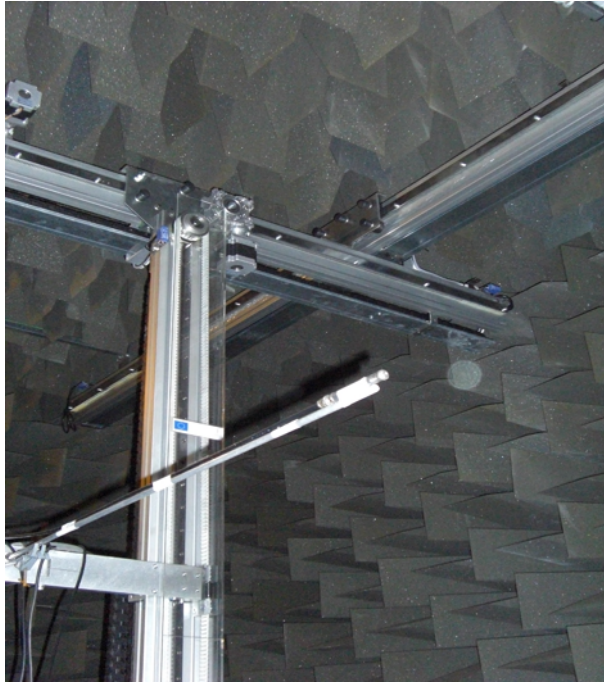


Figure 5.4: Detail of the robotized system

Each one of the three axes has a stepper motor that allows the robot to move with high precision in each axis. The main characteristic of these motors is that one can move 1 step by a tension pulse in the desired direction, thus making it possible to choose both the velocity and the rotatory direction. The motors used in this work need 200 pulses to rotate 360° , meaning that in each pulse, the stepper motor is capable of moving 1.8° . This rotatory movement is transformed in a lineal displacement of each axis. To do this, we use a $xx:yy$ gearbox, in such a way that a tension pulse produces a lineal displacement of xx cm in the X axis, yy cm in the Y axis and zz cm in the Z axis. The rotatory column does not contain gearbox, therefore, each applied pulse produces a rotation of the column of 1.8° .

The control of the robot is shown in Figure 5.5. Each motor contains an associated driver that controls the flux of current inside of the coil of the

CHAPTER 5. EXPERIMENTAL SETUP

motors in order to move it in the proper way. These drivers are controlled by three signals: *enable*, that enables the driver to introduce current into the motor; *direction*, that indicates the direction of the rotation of the motor, and *pulse*, which is a square signal that, when changing from the logical value 0 to 1, makes the driver control the flux of current to rotate the stepper motor (1.8°) in the direction indicated by *direction*.

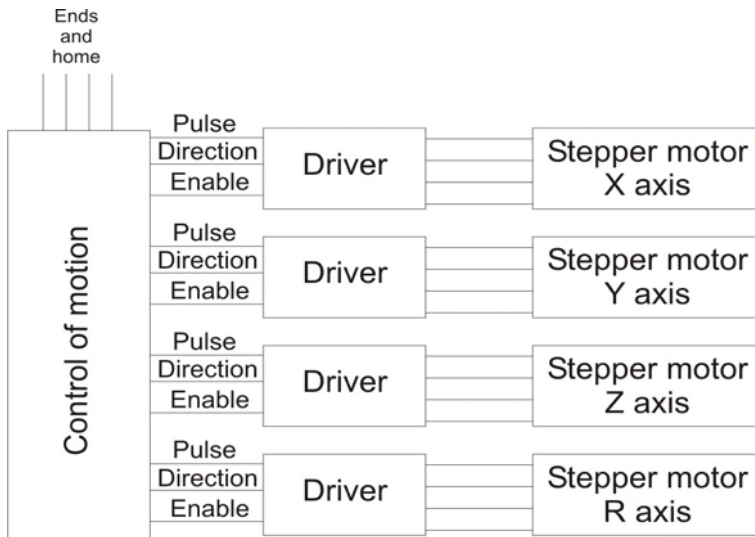


Figure 5.5: Schematic view of the control of the robot.

The drivers are plugged to a board to control the motion. It is a hardware of National Instruments capable of controlling a robot with up to 4 axes (NI-PCI 7334).

After configuring the NI-PCI 7334, it must:

1. Move each one of the axes independently and/or simultaneously.
2. Control the trajectory of the robot, starting from a current position to a desired position which is saved in the driver. By doing so, the acceleration and the velocity are controlled.
3. Detect the ends of the anechoic chamber, stopping the robot when an end is found.

4. Place the robot in a reference position (zero position), with a high precision approximation, based on the home sensors.

Thus, the control process of the robot could be as follows:

1. When the system is turned on, the robot should be at the zero position.
2. Once the robot is at the zero position, the driver records this position as the absolute zero of the anechoic chamber.
3. At this point, only the new position of the robot must be indicated to the driver. Then the driver chooses the direction of movement, the amount of pulses and the frequency in order to do the movement in complete agreement with the acceleration and the velocities previously programmed.
4. Of course, the robot can be turned off at any time.

5.2.2.2 Acquisition hardware

The National Instruments (NI) cards PCI-4474 were used for data acquisition. This hardware presents four dynamic signal acquisition channels to perform high-accuracy audiofrequency measurements. The analogical inputs present 24-bit resolution ADCs that are simultaneously sampled in a software programmable rate. The high resolution provides the necessary accuracy to make the NI PCI-4474 card adequately suited for the applications in audio and vibration signal analysis and it achieves low noise and low distortion.

The analogical inputs have both analogical and real-time digital filters implemented in the hardware to prevent aliasing. Input signals are first passed through fixed analogical filters to remove any signals with frequency components beyond the range of the ADCs; then digital antialiasing filters automatically fit their cutoff frequency in order to remove any frequency components above half the programmed sampling rate. The maximum sampling rate of the NI PCI-4474 is 102.4 kS/s, in our experimental setup 52 kS/s was used, which is sufficient for the range of audible frequencies.

CHAPTER 5. EXPERIMENTAL SETUP

These applications were used together with the Sound and Vibration Toolkit and the Order Analysis Toolkit for LabVIEW. Using these toolkits in conjunction with NI PCI-4474 cards, an acquisition system synchronized with the motion of the robot controlled by the NI PCI-7334 was developed. This software controls the motion of the robot and places the microphone at the desired point and then the motors that move the axes of the robot are turned off in order to prevent distortions and coupling in the acoustic measurement. Once the robotized system is turned off and the acoustic source and the microphone are turned on, the microphone acquires the temporal signal. From this temporal signal, one can obtain the power spectra, the frequency response or the sound-level measurement.

5.2.2.3 Sound source

The GENELEC 8040A is a way active monitoring loudspeakers designed to produce high sound pressure level output, low colouration and broad bandwidth in a small enclosure size.

The free-field frequency response of the system (error of 2.0 dB) is from 48 Hz to 20 kHz. Figure 5.6 shows the horizontal directivity characteristics of the 8040A measured at 1 m. The lower curve shows the system's power response.

The source has a weight of 8.6 kg and its dimensions are 350 mm of height, 237 mm of width and 223 mm of depth.

5.3 Microphones and accelerometers

5.3.1 Microphone

All the acoustic measurements were obtained by a prepolarized free-field microphone 1/2" Type 4189 B&K.

The Type 4189 presents a sensitivity of 49,5 mV/Pa, and due to this great

5.3. MICROPHONES AND ACCELEROMETERS

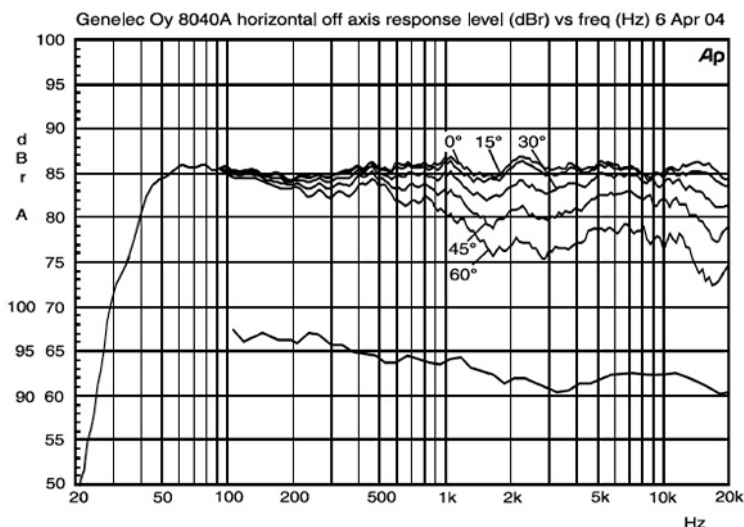


Figure 5.6: The upper line group shows the horizontal directivity characteristics of the source provided by the manufacturer measured at 1 m. The lower curve shows the system's power response.

sensitivity, wide range of frequencies can be analysed and it is adequately suited to general sound measurements requiring frequency analysis. This microphone offers significant advantages when used with portable, low-power instruments not designed to produce a polarization voltage. Another advantage is the greater reliability of the associated preamplifier under humid and polluted conditions. These factors make these prepolarized condenser microphones particularly suitable for field measurements, both outdoors and in industrial environments.

Some important characteristic to take into account when measuring pressure field inside the SC is the dimensions of the microphone. The diameter of the microphone is 1.32cm and its length is 1.76 cm.

The microphone is connected to a Deltatron microphone preamplifier Type 2671, that converts several protocols of intensity, such as DeltaTron or ICP constant current line drive (CCLD) (which must be between 2 and 20 mA (nominal 4mA)), into a constant 12 V DC level. This point is fundamental to

couple the B&K microphones with the NI PCI-7334. The output signal from the microphone swings around this DC level. Since no polarization voltage is available, only prepolarized condenser microphones such as the Type 4189 can be used. The frequency response is calibrated between 20Hz and 50 kHz.

5.3.2 Accelerometer

The analysis of wall vibrations was done measuring with the miniature accelerometer B&K Type 4393. The sensitivity of the accelerometer is 0.317 pC/ms^2 . This accelerometer is made of Titanium with a weight of 2.2 g. Type 4393 of B&K are suitable for measurements on lightweight structures and it was used to analyse the wall vibration of the U-profile scatterers (see Section 5.4) which accomplishes the conditions to be measured with the miniature accelerometer Type 4393. The typical frequency response of the Type 4393 is a flat response from 200 Hz to 18 kHz.

5.4 Scatterers

In this work, we have carried out measurements on SC made of both rigid and resonant scatterers. In Figure 5.7 we can see all of the scatterers analysed in this work. SC made of rigid scatterers have been built with two different filling fractions, changing both the diameter of the cylinder and the lattice constant. Figure 5.7B shows the aluminium cylinder of 4 cm diameter and Figure 5.7C shows the PVC cylinders of 20 cm diameter. Both cylinders has been used to build SC with rigid scatterers.

Balloons, split ring resonators and U-profiles have been used as resonant scatterers. Figure 5.7A shows the picture of the balloons. They are made of low density polyethylene (LDPE), whose density is 921 kg/m^3 , and the thickness of the wall is 500 gauge. The split ring resonators have been performed making slits in a PVC rigid hollow cylinder. An example of the sample can be observed in Figure 5.7D. The aperture of the resonator is 2 cm of length. Finally, the U-profile scatterer, made of low density Polyethylene foam can be

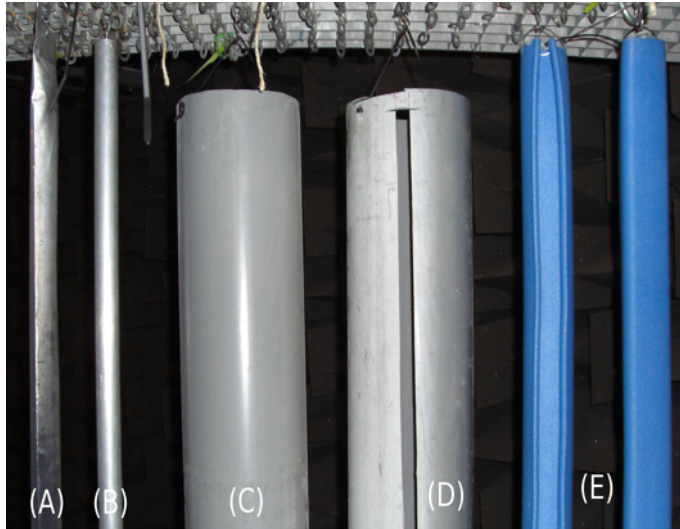


Figure 5.7: Pictures of scatterers analysed in this work. A) Ballon. B) Rigid Scatterer (Aluminium). C) Rigid Scatterer (PVC). D) Split Ring Resonator (SRR) (PVC). E) U-profiles, front and back of the scatterer.

seen in Figure 5.7E. We show a detail of the back and the front of the scatterer.

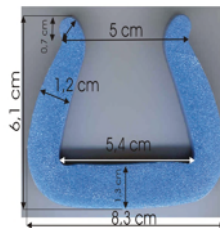


Figure 5.8: Transversal view of the U-profile scatterer. Dimensions of different parts of the profile are indicated in the picture.

Figure 5.8 shows the transversal view of the different parts U-profile scatterer where the dimensions are indicated. Table 5.1 shows the elastic properties of low density Polyethylene foam [mills07].

Several SC can be built with the different scatterers shown in Figure 5.7. A summary of the SCs experimentally analysed in this work is presented in the

CHAPTER 5. EXPERIMENTAL SETUP

Table 5.1: Elastic properties of Low Density Polyethylene Foam.

	LDPE Foam
Density (kg/m^3)	100
Young's modulus (10^9 Pa)	0.35
Poisson's ratio	0.4

Table 5.2. We have included the scatterers used to build each SC as well as the type of lattice and the lattice constant considered in the corresponding experiments. Table 5.2 is horizontally divided in two parts. The upper part shows the scatterers used to construct SC made of rigid elements and the lower part shows the scatterers used to construct SC made of resonant elements.

Table 5.2: Experimental SC analysed in the work.

Scatterer	Lattice Constant a (cm)	Lattice
Aluminium	6.35	Triangular
PVC	22	Square
	33	Square
Balloons	12.7	Triangular
U-profiles	12.7	Triangular
SRR	33	Square

6

Low number of vacancies: point defects in sonic crystals

Sonic crystals containing defects in their structure show additional sound transmission properties [Sigalas97, Caballero01, Hakansson04]. In the case of the low number of defects with respect to the total number of scatterers in the structure, the periodicity is locally broken and an increasing interest in this situation has arisen in the last years: high precision wave filters [Sigalas98] or waveguides [Khelif03, Khelif04] can be designed by the creation of point defects in periodic systems [Pennec04, Tanaka07, Vasseur08].

The effect of single point defects in SC showing the localization of sound waves in the vacancy as well as the evanescent behaviour of the localized mode outside the vacancy have been analysed in this Chapter. We note that the behaviour of the wave inside the vacancy can be assimilated with the behaviour of the same wave impinging over a complete SC because, in both cases, the wave observes the same periodic structure. Therefore a comparison between the two cases has been done in order to obtain the evanescent behaviour of both modes located inside the BG. Moreover novel data demonstrating the localized modes are reported here.

In this Chapter we also show novel results on the imaginary part of the Bloch vector for the localized modes inside the SC with multi-point defects. The localization of waves inside these defects is mainly characterized by three

CHAPTER 6. LOW NUMBER OF VACANCIES: POINT DEFECTS IN SONIC CRYSTALS

properties. Firstly, the modes are separated in the frequency domain, meaning that, there is a splitting of the localization frequency if the point defects are close enough. Secondly, the modes present symmetries in the vibrational pattern depending on the number of vacancies in the crystal. Thirdly, the localized modes are evanescent and they decay outside the defect but inside the SC. We show results of a double point defect in very good agreement with the measurements of the symmetric and antisymmetric vibrational pattern of the localized modes. Evidently, the oscillation modes of N_p -point defects with $N_p > 2$ will present more complicated vibrational patterns than the ones appearing in the double point defect, then they cannot be classified into such simple modes as symmetric and antisymmetric ones. The PWE and the EPWE (see Chapter 3) have been used to characterize the evanescent and propagating properties of localized modes in point defects. Experimental results are in very good agreement with the analytical ones.

6.1 Point defects in sonic crystal

One particularly interesting aspect of SC is the possibility of creating point defects to confine acoustic waves in localized modes [Sigalas98, Zhao09]. Due to the locally breaking of the periodicity of the structure and the presence of the BG, defect modes can be created within this inhibition range of frequencies. Consider a wave with frequency inside the BG impinging over a periodic system with a vacancy. Once the wave is inside the cavity created by the defect, it is trapped because the borders of the defect act as perfect mirrors for waves with frequencies in the BG [joannopoulos08]. Thus, the wave is strongly localized in the point defect creating the localized mode or defect mode. Localization depends on several parameters as for example the size of the point defect [Sigalas98, Zhang04].

In Chapter 2, the evanescent behaviour of the modes inside the BG was mentioned. Localized modes have their frequencies inside the BG, therefore they should present an evanescent behaviour. Recent experimental results [Wu09a] show the measurements of the sound pressure level recorded inside of a point defect and behind the SC. The authors observed that this level is larger inside

the cavity than behind the crystal. This fact clearly shows both the localization of sound in the cavity and the evanescent behaviour of the localized mode. In the electromagnetic regime some authors measured the evanescent modes in photonic crystals [Engelen09] showing a multi-exponential decay.

Making use of the EPWE, presented in Chapter 3, a deeper explanation of the localized mode has been introduced in this Section. Using the $k(\omega)$ method for defect modes, we observe that k can have real and imaginary parts, giving rise to complex band structures; the real part of the complex band structures gives information about the frequency of the localized mode in the vacancy, whereas the imaginary part is related to the decay of the localized mode outside the vacancy. Particularly, although it has been shown that the localized modes present multiexponential decay [Engelen09], we observe that only the first harmonic of the imaginary part of the band structures substantially contributes to the decay rate of the mode in a SC made of rigid cylinders.

This Section presents results of a 2D SC consisting of PVC cylinders of radius $r = 0.1$ m embedded in air arranged in square lattice with lattice constant $a = 0.22$ m. The material parameters employed in the calculations are $\rho_{air} = 1.23\text{kg/m}^3$, $\rho_{PVC} = 1400\text{ kg/m}^3$, $c_{air} = 340$ m/s and $c_{PVC} = 2380$ m/s. We consider a filling fraction $ff = \pi r^2/a^2 \simeq 0.65$.

6.1.1 Localized modes

One of the characteristics of SC with point defects is the localization of waves in the vacancy. The EPWE with the supercell approximation has been used to calculate the complex band structures of the considered SC with a point defect. Figure 6.1 shows the complex and real band structures for such periodic system. 1225 plane waves have been used for the calculations using the EPWE.

The black area in Figure 6.1B shows the BG of the complete structure and one can observe that the BG appears between 627 Hz and 1111 Hz.

The generation of one vacancy is analysed using the supercell of size $5a \times 5a$ shown in the inset of Figure 6.1A (left panel). The imaginary and real band

CHAPTER 6. LOW NUMBER OF VACANCIES: POINT DEFECTS IN SONIC CRYSTALS

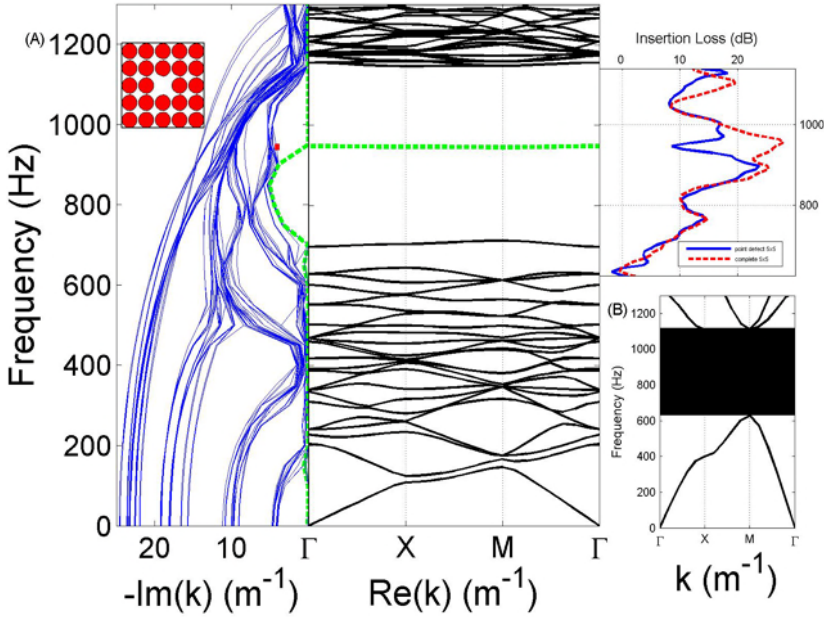


Figure 6.1: Band Structures versus experimental results for a complete SC and for a SC with a defect point. (A) Left panel: Complex Band Structure calculated using the EPWE with the supercell approximation. Central panel: Real Band Structure. Dashed line represents the localized mode. Right panel: Experimental Insertion Loss in the Band Gap of both the complete SC (dashed line) and the SC with a point defect (continuous line). The inset shows the supercell used in the calculations. Red Square marks the value of the imaginary part of the wave vector $\text{Im}(k) = -5.6 \text{ m}^{-1}$. (B) Band structures for a complete SC.

structures of a SC with a point defect are shown in the left and central panels in Figure 6.1A respectively. In the real part of the band structures one clearly observes the passing mode generated inside the BG due to the point defect (green dashed line). Related to this mode, it is possible to obtain the frequency of the localized mode, 920 Hz.

These results are compared with measurements of the Insertion Loss (IL) behind the SC with and without the point defect. The finite 2D SC used in this experiment forms a square array with lattice constant $a = 22 \text{ cm}$. The size

6.1. POINT DEFECTS IN SONIC CRYSTAL

of the SC is $5a \times 5a$ and the radius of the cylinders is $r = 10$ cm (the same as the supercell). We use the prepolarized free-field 1/2" microphone Type 4189 B&K (see Chapter 5) that has a diameter 1.32 cm, which represents approximately $0.06a$. We expect a low perturbation of the acoustic field due to the microphone.

In Figure 6.1A (right panel), we can observe that the experimental IL for the localized mode at frequency 920 Hz (blue continuous line) is lower than in the case of the complete SC (red dashed line), meaning that, the localized mode can travel through the crystal. Then, it can be concluded that there is a passing mode. This occurs as the localized mode is not completely extinguished by the SC around the point defect (see also [Wu09a]). In fact, this result shows that the localized mode has an evanescent behaviour and that, as we will see later, in this case there are not enough rows around the point defect to extinguish it.

Both the PWE and the EPWE predict a localized mode with a determined frequency but, due to the finite size of the SC, the localized mode is centered in a narrow range of frequencies [Wu09a]. It seems interesting to analyse how the localization is created in a finite SC. Figure 6.2 represents the measured 3D spectra for a SC with a point defect. The spectrum at point x_0 is plotted in the YZ-plane, so that the frequency is in the y-axis and the absolute value of the pressure is in the z-axis. The 3D spectra is constructed by plotting the spectra for all the points inside the SC between two rows. Because the range of frequencies of interest is inside the BG, only the frequencies in the range [750, 1000] Hz were plotted. Figure 6.2 shows the experimental evidence showing that the localization is not produced for a unique frequency, but for a narrow range of frequencies.

In the literature related to this field there is a great number of works analysing the localization of sound in point defects [Sigalas98, Wu01, Khelif03] however a few works present experimental results of the localization modes. Figure 6.3A presents the numerical results of the acoustic field inside a point defect in a SC. The absolute value of the sound pressure inside the point defect of the SC has also been experimentally analysed by moving the microphone using the 3DReAMS (see Chapter 5). Figure 6.3B represents the experimen-

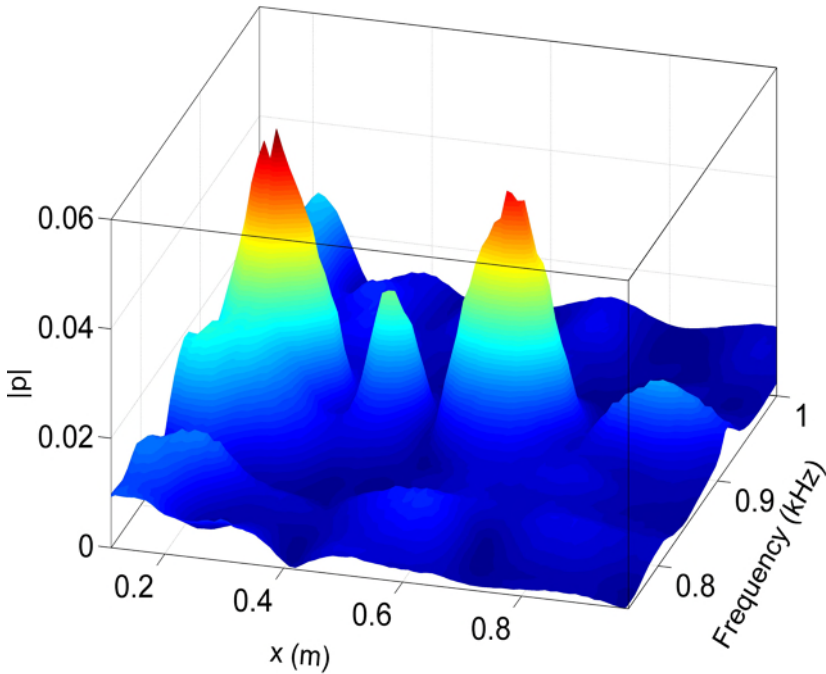


Figure 6.2: 3D spectra for the SC with a point defect. Measured 3D spectra for all the points inside the inner path in the SC with a point defect.

tal results obtained for the first time inside a point defect. One can see the agreement between numerical and experimental results although it is possible to observe a perturbation of the acoustic field produced by the microphone in the zones where the microphone is near the walls of the cylinders surrounding the point defect.

6.1.2 Evanescent behaviour

As we have just seen in the previous Section, the generation of point defects produces a passing mode which is localized in the point defects. Due to the periodicity surrounding the point defect, the wave sees a complete SC in every directions from inside the point defect. Thus, the localized mode should

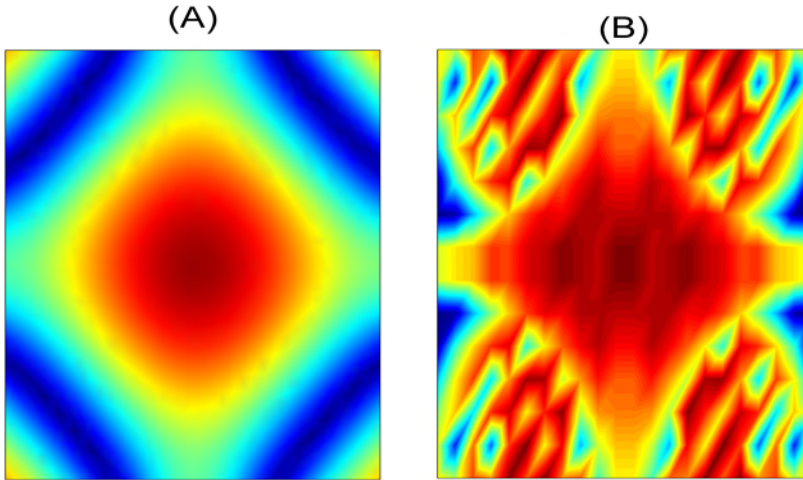


Figure 6.3: Acoustic field inside the point defect calculated using FEM (A) and experimentally measured (B).

appear inside the BG of the periodicity, therefore the mode presents evanescent behaviour outside the cavity. The decay rate of the mode is analogous to a wave with the same frequency impinging over a complete SC from outside. Both cases should be represented by the same $Im(k)$, and as such, by the same evanescent behaviour.

To understand this phenomenon, it seems necessary to analyse firstly the evanescent behaviour of a mode with the same frequency as the localized mode, 920 Hz, but propagating through a complete SC. This mode is effectively inside the BG, and it should present an evanescent behaviour. The value of the imaginary part of the first harmonic of the wave vector is marked in the complex band structure with a red square in Figure 6.4. One can see that $Im(k) = -5.6 \text{ m}^{-1}$ for frequency 920 Hz in a complete SC.

In order to observe the exponential decay of the acoustic field, the absolute value of the pressure in the points between two rows of the SC has been numerically calculated, using FEM with radiation boundary conditions in the walls of the cylinders and considering an incident plane wave of 920 Hz. The

CHAPTER 6. LOW NUMBER OF VACANCIES: POINT DEFECTS IN SONIC CRYSTALS

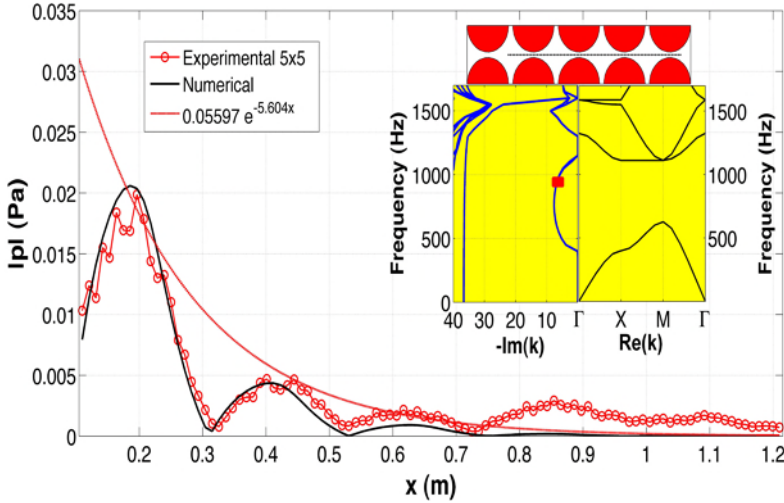


Figure 6.4: Acoustic pressure inside a 5×5 SC with square array with lattice constant $a = 22$ cm, for a frequency in the BG of 920 Hz. Black continuous line (connected red open circles) represents the absolute values of the numerical (experimental) pressure inside the SC. Red dashed line represents the fitting of the exponential decay of the measured acoustic field inside the SC. The inset represents the measurement points inside the SC and both the complex and real band structures.

results are plotted in black continuous line in Figure 6.4. It is possible to observe the decay of the mode with the distance all along the SC. Experimentally, the absolute value of the sound pressure is measured between the two rows of the SC moving the microphone by means of 3DReAMS in steps of 1 cm as in the trajectory shown in the inset of Figure 6.4. The connected open red circles represent the experimental results in good agreement with the numerical data (black continuous line). With these experimental results, the decay of the evanescent mode inside the BG can be fitted. In order to fit an exponential decay ae^{bx} the points with maximum values have been chosen. The values of the parameters in the fit are $a = 0.05597 \pm 0.0103$ Pa, and $b = \text{Im}(k) = -5.60 \pm 1.45 \text{ m}^{-1}$, and the result is plotted in Figure 6.4 (red dashed line). Numerical, analytical and experimental results show the evanescent behaviour of waves with frequencies in the BG.

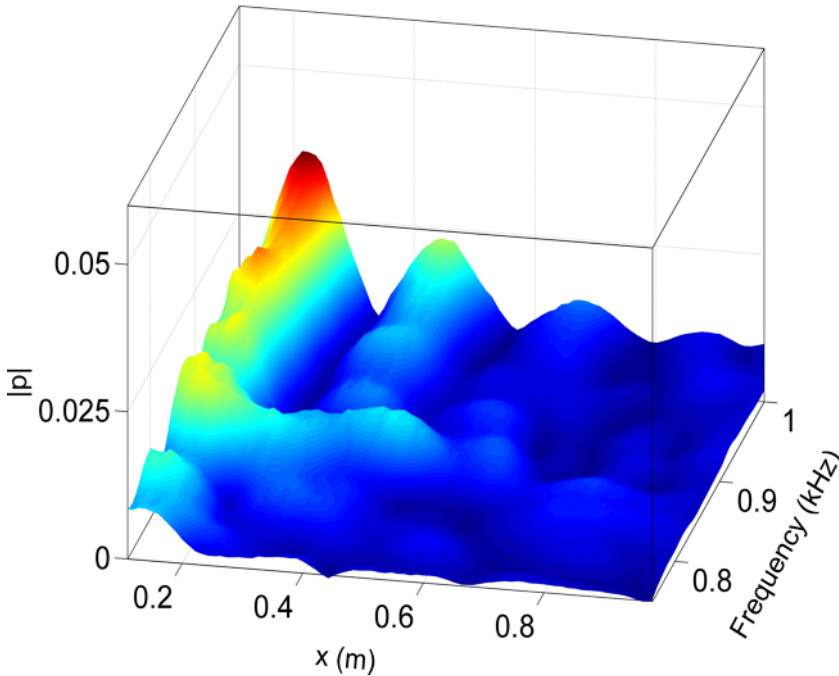


Figure 6.5: 3D spectra for a complete SC. 3D experimental spectra for all the points inside the inner path in the SC.

Figure 6.5 shows the evanescent behaviour for all the modes in the range of frequencies [750, 1100] Hz inside the BG. The represented experimental 3D spectra shows the evidence of the evanescent behaviour for all the modes inside the BG for a complete SC. The situation is similar to the one shown in the previous section in Figure 6.2 in the case of the SC with a point defect, where there is a change in the propagation properties due to the presence of the point defect. The evanescent behaviour for all modes outside the frequencies of the localization range can also be observed in Figure 6.2.

The previous results can be compared with those obtained by analysing the imaginary part of the band structures of a SC with a point defect (shown in Figure 6.1). There are several values of the imaginary part of the wave vector at the localized frequency in the Complex Band structures. This fact shows the multiexponential behaviour of the localized mode [Engelen09]. We note

CHAPTER 6. LOW NUMBER OF VACANCIES: POINT DEFECTS IN SONIC CRYSTALS

that in the complex band structures (left panel) the value of the k number for the modes inside the BG can be obtained using the EPWE and it becomes a purely real value for the localized mode. That value coincides exactly with the value obtained using the plane wave expansion (PWE) with supercell approximation.

In order to study the behaviour of this mode the acoustic field inside the SC is numerically analysed. In Figures 6.6A and 6.6B we can observe the maps obtained using FEM for the complete SC and for the SC with a point defect respectively. Figure 6.6C represents both numerical and experimental absolute values of the pressure for the complete SC and for the SC with a point defect corresponding to the cross sections marked with a red line in Figures 6.6A and 6.6B. Experimental results are also plotted in Figure 6.6C.

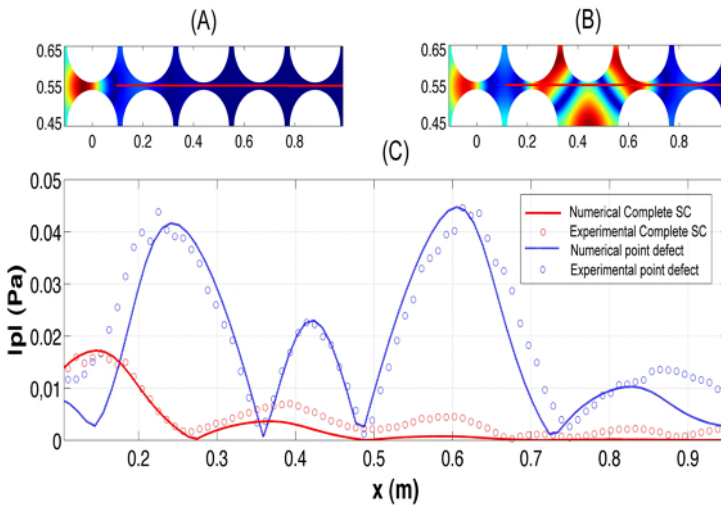


Figure 6.6: Absolute values of the acoustic field inside the SC with and without point defect. Numerical maps calculated by FEM inside the complete SC (A) and inside the SC with a point defect (B). (C) Numerical and experimental results for the interior path marked in (A) and (B) with a continuous line. The dashed line (open circles) represents the numerical (experimental) results for the complete SC. The continuous line (open squares) represents the numerical (experimental) results for the SC with a point defect.

6.2. N-POINT DEFECTS IN SONIC CRYSTALS

In blue line in Figure 6.6C one can observe the effect of the point defect in the acoustic field inside the SC. In the region of the point defect there is an increasing value of the acoustic pressure due to the localized mode. It can also be observed that the absolute value of the pressure for the localized mode is higher than at the end of the complete SC, proving the passing mode shown in Figure 6.1. To enhance the localization of the sound inside the SC a higher number of rows around the point defect is necessary as shown elsewhere [Wu09a].

The border of the cavity is located at approximately $x = 0.6$ m as it can be observed in Figure 6.6B. From this point to the end of the SC, the acoustic field is drastically reduced, but with this evidence, it is not possible to confirm the evanescent behaviour of the localized mode outside the cavity. To do this, the sound inside a bigger SC with a point defect (see inset of Figure 6.7A) has been analysed. Figure 6.7A presents both numerical (blue line) and experimental (blue open circles) values of the acoustic field from the end of the cavity to the end of a SC, showing the evanescent behaviour of the localized mode outside the cavity. Analogously to the case of the complete SC, maximum values (see black open circles in Figure 6.7A) have been chosen in order to fit an exponential decay ae^{bx} . The values of the parameters in the fit are $a = 3.84 \pm 9.92$ Pa and $b = \text{Im}(k) = -5.81 \pm 4.06$ m⁻¹, and the curve is also plotted in Figure 6.7 (red dashed line). From an experimental point of view, the size of the SC constitutes a constraint, and as a consequence a few points for the exponential fit can be used. This results in a big error in the parameters of the fit. Even so, the value obtained for the $\text{Im}(k)$ is very close to the one obtained both analytically (EPWE) and experimentally for the complete SC. The difference is less than 4% in both cases.

6.2 N-point defects in sonic crystals

Since Sigalas *et al.* [Sigalas97] studied the defect mode produced by a point defect in periodic structures, several kinds of defects have been analysed in recent years, showing in all cases the localization of sound for frequencies inside the BG [Li05, Wu03, Zhong05]. Experimental and numerical analysis of

CHAPTER 6. LOW NUMBER OF VACANCIES: POINT DEFECTS IN SONIC CRYSTALS

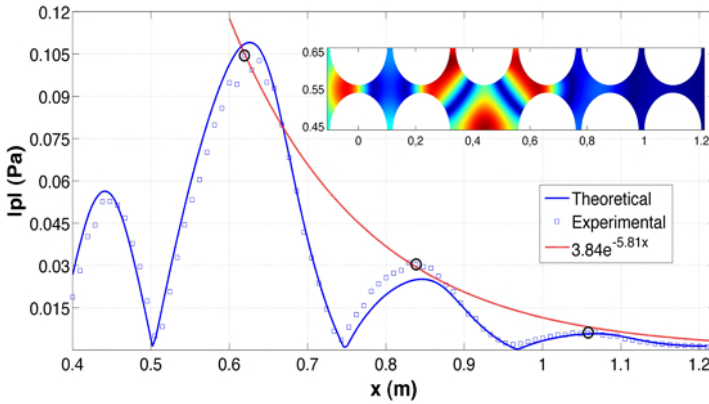


Figure 6.7: Absolute values of pressure inside a 6×5 SC with a point defect: Numerical results (continuous line), experimental results (open squares). The dashed line represents the fitted exponential-like decay of the localized mode using the open circles.

the localization in a point defect considered as a cavity inside the SC were reported in the previous Section. The dependence of the localization on the size of the crystal and on the filling fraction (the bigger the size and filling fraction the bigger the localization in the cavity) was recently studied by Wu *et al.* [Wu09a, Wu09b] and by Zhao *et al.* [Zhao09, Zhao09b]. Moreover, when multi-point defects are considered, the interaction between localized modes in each defect-point shows interesting properties [Khelif03]. In the case of multi-point defects, the interaction depends on the distance between the cavities: the bigger the distance between cavities, the lower coupling between defect points.

The interaction of the defect modes inside a periodic system is explained by their evanescent behaviour. Properties analogous to the case of a system with masses and springs, or to the Zeeman effect appear in periodic systems presenting multi-point defects [Li05]. In a system of masses and springs, an odd number, n , of coupled springs present $n/2$ characteristic modes with frequency bigger than ω_0 (frequency of a single spring) and $n/2$ characteristics modes with frequency lower than ω_0 . If n is an even number one mode has the frequency ω_0 and the rest $n - 1$ modes are distributed symmetrically above

6.2. N-POINT DEFECTS IN SONIC CRYSTALS

and below this mode. The familiarized reader with the Zeeman effect in the atomic spectra will be able to appreciate the analogy with these results. In each case a symmetric splitting of the modes is produced by an interaction (in the case of the Zeeman effect by the application of a magnetic field, in the case of the springs by the coupling of masses by spring, and in the case of point defects by the interaction between the localized modes by its evanescent behaviour) [Li05, marion00]. Figure 6.8 shows the mentioned dependence of the splitting in several modes due to the breaking periodicity by several point defects forming a bigger cavity known as multipoint defect. In Figure 6.8 the splitting in both a double and a triple point defect is shown in comparison with the localized mode in a single defect.

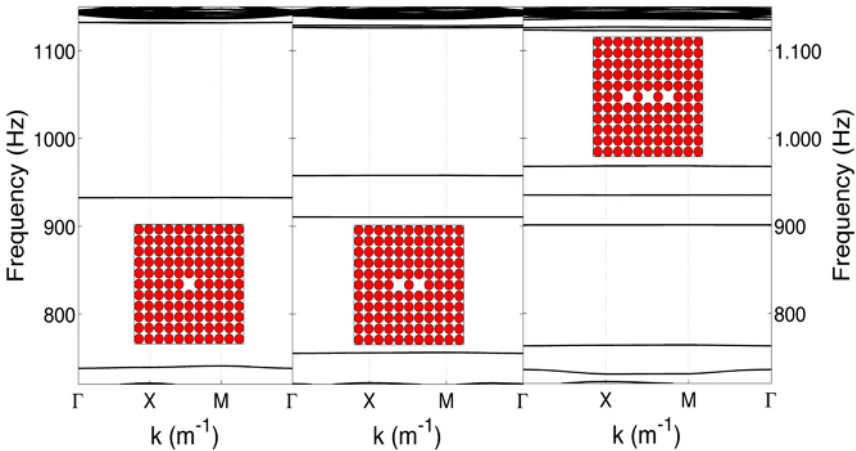


Figure 6.8: Dependence of the localized modes in multipoint defects on the number of single defects. Left panel: single defect, central panel: double point defect and right panel: triple point defect.

The three main characteristics of the modes produced by N-defects in SC are: splitting, localized mode with special symmetry vibrational patterns and evanescent decay of the modes. All of these effects only appear if the N-defects are close enough to interact by means of their evanescent behaviour [Li05]. If the N-defects do not interact, each one acts as a point defect independently of the others.

CHAPTER 6. LOW NUMBER OF VACANCIES: POINT DEFECTS IN SONIC CRYSTALS

The splitting of the frequencies of the modes may be qualitatively understood by considering that the cavities produced by the N -defects are coupled forming a large cavity with two resonant frequencies. In this Chapter the physical phenomena appearing in SC with a double point defect are widely analysed. This simple case allows us to have an insight into the effects of the case of N -point defects and it also enables the novel experimental results proving the theoretical conclusions obtained using the EPWE and MST (Chapter 3).

First the splitting produced by the generation of a double point defect is analysed, showing the effects in both the real and imaginary band structures. From the imaginary complex band structure we can see that the localized modes present different values for the imaginary part of k ; this means that each mode has a different decay rate inside the crystal. This property has been experimentally observed by fitting the exponential decay for each localized mode inside the crystal. The symmetry of the vibrational patterns in double point defect have also been analysed in this Section by means of MST predictions and experiments. Novel experimental evidence shows the symmetric and antisymmetric vibrational patterns in SC with double point defects. Finally, using the different decay rate of both vibrational modes, a new methodology to determine different vibrational modes in periodic media is presented.

6.2.1 Double point defect

In addition to the study of the complex and real band structures, MST has been used to observe the vibrational patterns of the localized modes in a double point defect in finite SC. In the double point defect, when the distance between both defects is short enough, a symmetric and antisymmetric vibrational modes appear [Li05]. The splitting has been attributed to the coupling between the single-cavity modes confined to each single cavity. In this case, the original lower single cavity level is splitted in two with the completely breaking of degeneracy.

In the case of double point defect, the splitting of the localized modes is analogous to the degenerate atomic levels in diatomic molecules. This splitting is analogous to that of the electron states in diatomic molecules such as H_2 ,

6.2. N-POINT DEFECTS IN SONIC CRYSTALS

where the interaction of two atoms causes a splitting of the degenerate atomic levels into bonding and antibonding orbitals. In electronic molecules, the bonding strength is given by the Coulomb forces between the nuclei and the electrons, and the exchange interaction between electrons. In contrast, the interaction of the acoustic modes in cavity molecules is determined by the geometry of the molecules and thus can be varied by the structure design through, for example, varying the length or the width of the interconnecting channel. Generally speaking, splitting decreases with the increasing in distance along molecule axis and the decreasing in the width normal to molecule axis.

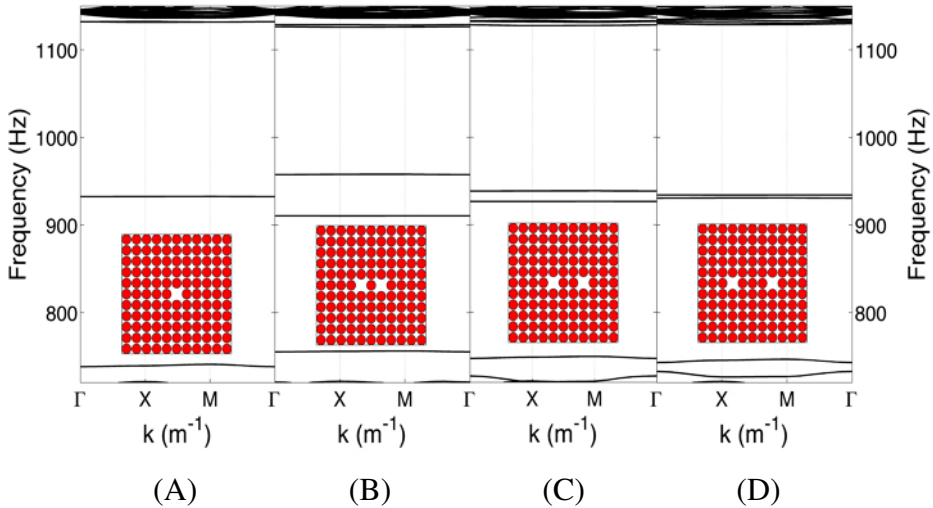


Figure 6.9: Dependence of the localized modes on the distance between the single point defects in a double point defect. (A) single defect, (B) double point defect with $d = 2a$, (C) double point defect with $d = 3a$ and (D) double point defect with $d = 4a$.

The width between the frequencies of the two defect modes decreases as the distance between the single points that configures the double defect increases [Khelif03]. Figure 6.9 shows the calculation for a single point defect (A), for a double point defect with $d = 2a$ (B), for a double point defect with $d = 3a$ (C) and for a double point defect with $d = 4a$ (D). One can observe the dependence on the distance. The coupling is related to the overlapping

CHAPTER 6. LOW NUMBER OF VACANCIES: POINT DEFECTS IN SONIC CRYSTALS

of the evanescent wave from the localized phonons and it is proportional to $\kappa = (\omega_2 - \omega_1)/\omega_0$, where ω_2 and ω_1 are the high and low defect mode frequencies of the system. The result shows that the coupling coefficient κ decreases as d increases. Thus the increase in the splitting of the defect mode frequency with the decrease in d is evidently due to the increase in the coupling of the evanescent wave from the localized phonons as d decreases.

Novel experimental results that are in good agreement with the theory are presented in this Section, showing the symmetry of the vibrational patterns of the localized modes in such a double point defect. Moreover, the decay of the localized modes outside the double point defect is observed in good agreement with the results obtained using EPWE with supercell approximation.

In this Section, the case of a double point defect in a square array at sites $(1, 0)$ and $(-1, 0)$ in a supercell of $11a \times 11a$ is analysed (see Equations 3.75 and 3.76 in Section 3.2.3.2). In this situation the distance between defects is equal to $2a$, and the distance between two double point defects in different supercells is equal to $20a$. The interaction of the point defects in the supercell approximation must be as low as possible between the neighboring supercells in order to decrease the overlap between defects, thus the size of the supercell should be big enough to place the point defects separately in consecutive supercells.

6.2.1.1 Localization

In order to analyse the splitting of the localized modes, we have calculated the Real and the Complex Band Structures of a SC with a double point defect by using the EPWE with the supercell approximation. We have analysed a 2D SC consisting of PVC cylinders of radius r in air background arranged in square lattice with lattice constant a , with the same properties as the SC analysed in the previous Section. In this case, $N = (2 \cdot 15 + 1)^2 = 961$ plane waves have been considered for the calculations. Several calculations have been carried out in order to obtain a good convergence of the solution. This number of plane waves is higher than the one used in previous works [Laude09] and it provides a good convergence of the solution of the eigenvalue problem.

6.2. N-POINT DEFECTS IN SONIC CRYSTALS

In contrast with the modes in the BG, localized modes can travel up to the point defect where the wave is localized. The right panel of Figure 6.10A represents the real band structures calculated using PWE with supercell approximation for a SC with a double point defect (right panel). In the previous Section we observed that the localized mode generated by a point defect in the SC appears at frequency $\nu_0 = 932$ Hz whereas the frequencies of the localized modes of a double point defect were split (right panel of the Figure 6.10). The frequencies of the two localized modes is due to the double point defect split around the localized mode of a single defect: One with a lower frequency, $\nu_1 = 910$ Hz, than the corresponding frequency of the localized mode in a single defect, and another one, $\nu_2 = 958$ Hz, with a higher frequency than the single defect. This phenomenon is analogous to the splitting of the degenerate atomic levels in diatomic molecules.

The splitting in two peaks may be qualitatively understood if we consider that the double cavity in the double point defect are coupled forming a large cavity with two resonant frequencies. Because of the surrounding periodicity, the walls of the cavity act as a perfect mirrors producing the localization of the wave inside the cavity. This results in a coupling inside the double point defect producing two localized modes depending on the distance between the point defects [Li05, Khelif03, Zhao09].

As the splitting depends on the distance and on the shape of the multi-point defect, one can study the vibrational patterns that appear inside the multi-point defect, analysing the differences in frequency of the localized modes. Factor $(\nu_1 - \nu_2)/\nu_0$ indicates how the splitting will be produced. For big values of this factor, one can expect separated modes in frequencies (as many as the number of single point defects constitute the multi-point defect), whereas a small factor represents a weak overlapping between the point defects in the multi-point defect, which produces narrow splitting.

The complex band structures give additional information about the properties of the localized modes. Figure 6.10B represents the complex (left panel) and the real (right panel) band structures for a SC with a double point defect. For each localized mode, a determined imaginary k becomes a pure real value, in good agreement with the results of the PWE with supercell approxima-

CHAPTER 6. LOW NUMBER OF VACANCIES: POINT DEFECTS IN SONIC CRYSTALS

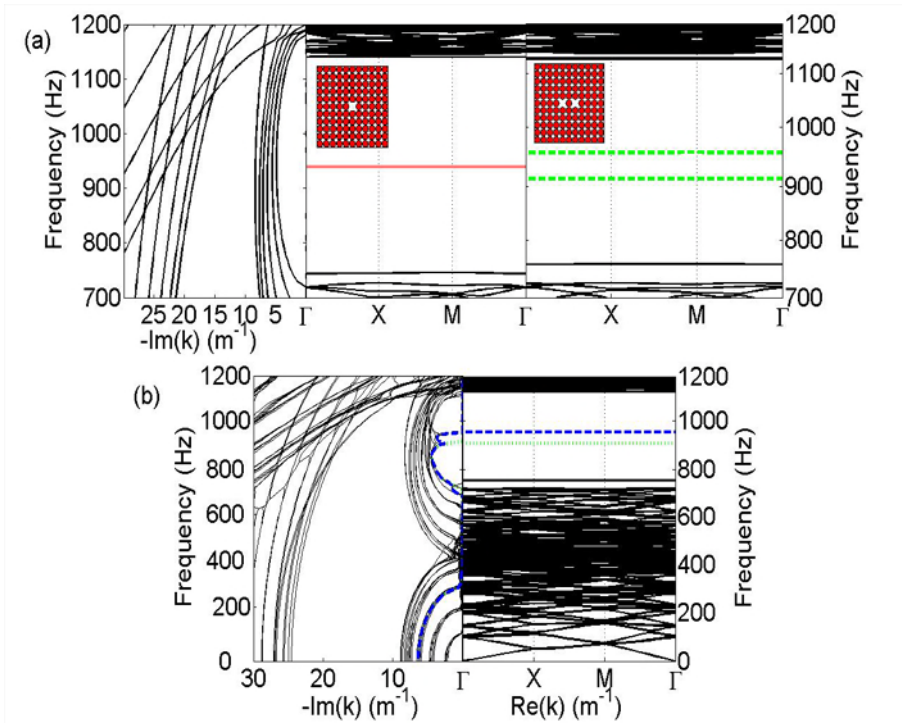


Figure 6.10: Real and Complex band structures for a SC with and without point defects. (a): Complex band structure of a complete SC calculated using EPWE with supercell approximation (left). Band structures calculated using PWE with supercell approximation of a SC with a point defect, the continuous red line represents the defect mode (center). Band Structures for a SC with a double point defect, the dashed green line represents the defect modes of a double point defect (right). The insets show the supercell used in the calculations. (b): Complex and real band structure of a double point defect.

tion. This real part is related to the wave vector for the localization frequency whereas the imaginary part of the localized mode is related to the rate of decay outside the defect but inside the SC. As we have seen, the localized modes in the double point defect are distributed around the localized mode of a single point defect. However, the localized mode of the single point defect appears a little above the midgap frequency (926 Hz). Thus, it is expected that the imaginary part of the localized modes of double point defects presents differ-

ent values for each mode and, as a consequence, each mode presents different evanescent behaviour outside the defect. This prediction of the EPWE will be used to experimentally distinguish the symmetric with respect to the antisymmetric modes.

6.2.1.2 Symmetry of vibrational patterns

The previous discussion about the splitting of the modes in multi-point defects does not provide information about the localization of the modes or the acoustic field pattern inside the double cavity. This will be discussed now.

The results obtained using the PWE or EPWE for the localized modes could be used to plot the modal shapes for the defect modes using the eigenvectors. However, these modal shapes do not take into account the effect of the finite size of the crystal. Thus, to compare it with the experimental results corresponding to a SC of finite size, in this Section, we have calculated the modal shapes inside the double point defect using MST. MST predictions provide complementary information with respect to that one provided by the EPWE in the case of the infinite structures.

MST [linton01, Chen01] has been used to analyse the pressure field inside a SC with point defects. A SC of $7a \times 5a$ size with $a = 0.22$ m of rigid cylinders with radius $r = 0.1$ m is considered in this Section. A double point defect with individual defect points separated by a distance of $d = 2a$ has been considered due to the experimental constraints, and to look for a compromise between the experiment and the theory in order to be able to compare both predictions and data.

For the crystal considered in this Section the frequencies of the localization modes differ somewhat with respect to the ones calculated using the PWE and the EPWE with supercell approximation. This difference can be explained taking into account that a finite SC is considered for the study, and as it has been shown in the literature related to this field, the localization frequencies depend on the size of the crystal as well as the filling fraction, and the amount of rows around the defect. In this case, the localization frequency for the

CHAPTER 6. LOW NUMBER OF VACANCIES: POINT DEFECTS IN SONIC CRYSTALS

antisymmetric mode is $\nu_1 = 940$ Hz and for the symmetric mode it is $\nu_2 = 895$ Hz. At these frequencies they present the maxima values of the acoustic spectra inside the point defects. We note the small difference with respect to the ones obtained using the PWE and the EPWE ($\nu_1 = 910$ Hz and $\nu_2 = 958$ Hz).

The pressure fields calculated using MST inside the SC with a double point defects for the localization frequencies are shown in Figure 6.11. One can see in the Figure that the pressure field for the mode with high frequency has an antisymmetric pattern (Figure 6.11A), whereas the pressure field for the mode with low frequency has a symmetric pattern (Figure 6.11B).

In Figure 6.11, one can also observe the values of $|p|$ for the space between two rows of the SC containing the double point defect. The vibrational patterns of the defect modes in double point defect are characterized with respect to a symmetry plane (see the dashed line in Figure 6.11) situated just in the midpoint between the two defects in the double point cavity. There is a symmetric mode and an antisymmetric mode with respect to this plane. The symmetric vibrational mode is characterized by a vibration in phase of the pressure field in each point defect, whereas the antisymmetric mode is characterized by a vibration of the pressure field in opposition of phase. Due to these properties, the point just in the symmetry plane (see the arrows in the Figure 6.11) presents different values of $|p|$ for each localized mode. For the antisymmetric mode, one can observe a minimum value of $|p|$ at this point (Figure 6.11A), whereas one can find a maximum value for the symmetric mode (Figure 6.11B).

Figure 6.12 shows the values of $|p|$ obtained using MST versus the data experimentally measured using 3DReAMS. The experimental results are in very good agreement with those obtained using MST. We note the different values of $|p|$ in the midpoint. As MST predicts, a maximum is observed for the symmetric mode at $\nu = 895$ Hz (Figure 6.12B), and a minimum is observed for the antisymmetric mode at $\nu = 940$ Hz (Figure 6.12A). The good agreement between theoretical (MST) and experimental results is remarkable. These measurements constitute the first experimental evidence of the symmetric and antisymmetric vibrational modes inside the SC with a double point defect.

6.2. N-POINT DEFECTS IN SONIC CRYSTALS

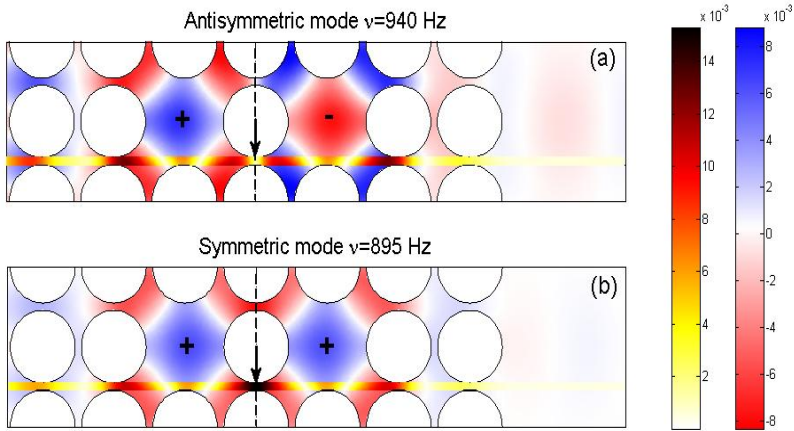


Figure 6.11: Pressure maps of a double point defect separated by a distance of $d = 2a$. The $|p|$ values between two rows of the SC containing the point defects is also plotted. The pressure maps of the antisymmetric (A) and symmetric (B) coupling of the localized modes inside the double point defect. The arrows represent the values of $|p|$ in the midpoint between the two rows of cylinders containing the double point defect.

6.2.1.3 Evanescent decay

As the mode of a single point defect is a little above the midgap, one can observe in Figure 6.10B that the localized modes in a double point defect present different imaginary part of k : The values of the imaginary part of k for the antisymmetric mode are lower than the corresponding values for the symmetric mode, meaning that, the rate of decay outside the cavity of the symmetric mode must be higher than that of the antisymmetric case. In Figure 6.12 one can observe the decay of the localized modes outside the double point cavity. The border of the double point defect are marked with dotted lines.

In order to analyse the decay of the modes outside the cavity, the behaviour of the maximum analytical values of $|p|$ outside the cavity (see the open squares in Figure 6.12) has been analysed and calculated using MST in a SC of rigid

CHAPTER 6. LOW NUMBER OF VACANCIES: POINT DEFECTS IN SONIC CRYSTALS

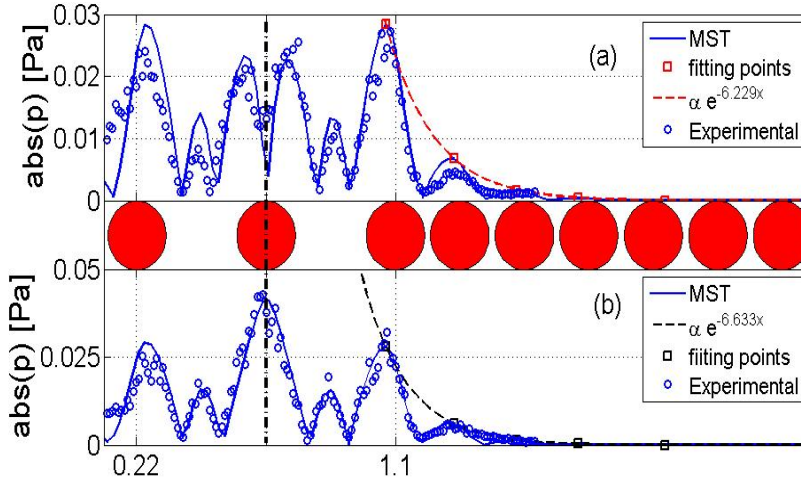


Figure 6.12: Numerical (continuous line) and experimental (open circles) profile of the $|p|$ values between the two rows containing the double point defect (see Figure 6.11). (A) Antisymmetric mode ($\nu = 940$ Hz) and (B) symmetric mode ($\nu = 895$ Hz). The dashed line represents the exponential-like decay of the localized modes outside the double point defect fitted from the maximum values of the analytical data represented by open square points.

cylinders with size $11a \times 5a$. Although the decay of the modes outside the cavity is multiexponential [Engelen09], it is possible to fit these values to an exponential-like ae^{bx} for analysing the differences in the rate of decay due to the differences in the imaginary part of the k for each localized modes.

Both fitted exponential-like decays are represented in Figure 6.12 (dashed lines). The decay rate for the antisymmetric mode is $b = -6.229 \pm 0.237 \text{ m}^{-1}$, while the decay rate for the symmetric mode is $b = -6.633 \pm 0.178 \text{ m}^{-1}$. Thus, as it was discussed in the results obtained in the previous Section, due to the symmetric distribution of the frequencies of the localized modes in double point defect with respect to the localized mode in a single cavity, the decay rate of the antisymmetric mode in a double point defect should be lower than that of the symmetric mode close to the center of the BG. On the other hand, one can observe that the values of the decay rate of the symmetric and of the antisymmetric modes are similar and the difference between them

6.2. N-POINT DEFECTS IN SONIC CRYSTALS

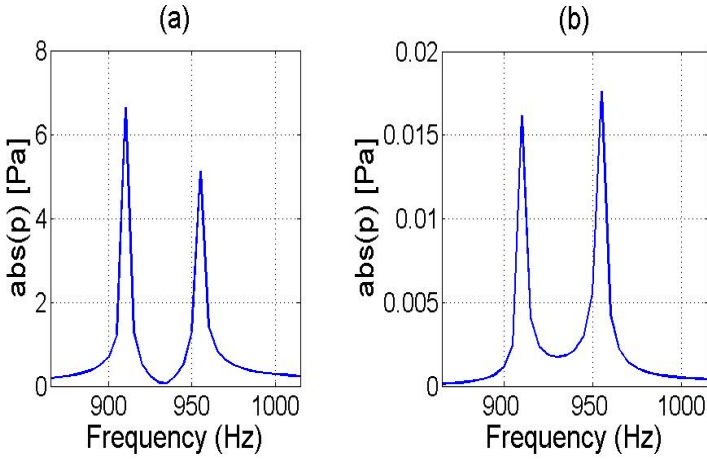


Figure 6.13: Spectra for a SC made of PVC cylinders arranged in $9a \times 5a$ with lattice constant $a = 0.22$ m in square array with a double point defect. (a) Spectrum measured inside one of the point-defect in the double point defect. (b) Spectrum measured outside the crystal at a distance of $10a$ from the start of the SC.

is small. The splitting of the frequencies of the localized modes in a double point defect around the frequency of the single cavity implies that the rate of decay in double point defect has to be different, but also one of them should be smaller than the other as its distance to the center of the gap is greater, in agreement with the theoretical results.

In finite crystals, where the localized modes can travel outside the periodic structure, the previous results indicate that the symmetric mode will be extinguished more easily than the antisymmetric mode. Thus, the design of filters based on the SC with point defect should take into account this kind of result. In Figure 6.13A, the spectrum inside a point defect in a SC with a double point defect is shown. In this case, the value of pressure of the peak of the symmetric mode (lower frequency) is higher than the peak of the antisymmetric mode. In Figure 6.13B one can see the spectrum for the same SC with a double point defect but measured outside the SC at a distance of $10a$ from the beginning of the SC. Here, the values of pressure for the symmetric mode are lower than the values of the antisymmetric mode, thus the symmetric mode was damped more by the crystal outside the double point defect than in the an-

CHAPTER 6. LOW NUMBER OF VACANCIES: POINT DEFECTS IN SONIC CRYSTALS

tisymmetric mode. Similar results can be observed in Figure 6.11, where the acoustic field behind the crystal for the antisymmetric mode is greater than the corresponding one for the symmetric mode. These results are in complete agreement with the differences in the imaginary part of k . Moreover, the difference in the value of imaginary part of complex wave vector is a direct evidence of the existence of different vibrational modes in multi-point defects and reveals the existence of a coupling between them.

6.3 Discussion

In this Chapter, we have shown the extraordinary transmission properties of periodic systems presenting vacancies in their structure, being the number of vacancies lower than the number of the scatterers in the structure.

The propagation of waves inside periodic structures consists of propagating and evanescent modes. In this Chapter, we have shown how the EPWE can be used to analyse the evanescent behaviour of waves inside periodic systems with a low number of defects, predicting the evanescent nature of the modes inside the BG of a SC with and without defects. This particular behaviour has been experimentally observed in good agreement with the numerical and analytical predictions. The exponential-like decay of the acoustic field inside a SC has been observed from both the analytical and experimental points of view. The EPWE predicts a value for the imaginary part of the first harmonic of the wave number that has been exponentially fitted. As a conclusion, only the first harmonic contributes to the exponential-like decay of the evanescent mode for modes inside the BG of the SC. We have also shown that the imaginary part of the wave vector connects propagation bands and conserves the overall number of modes.

By analysing the localized mode in the vacancy, it has been observed both analytically and experimentally that the localized modes present evanescent behaviour outside the cavity with the same exponential-like decay as a wave with the same frequency in the BG impinging over a complete SC. Due to the local breaking of the periodicity, the physical situation is very different for

both the complete SC and the SC with point defects. Even so it is possible to conclude that the space observed by the localized wave from the inner part of the cavity is topologically equivalent to the one observed by the same wave from the outside of a complete SC.

The EPWE with the supercell approximation can be used to study the evanescent behaviour of the modes inside the SC with multi-point defects. The localized modes in the SC with several point defects are mainly characterized by three properties: splitting of frequencies, symmetry of the vibrational patterns and evanescent behaviour inside the crystal. The whole properties of the localized modes in a SC with a double point defect has been used in this Chapter to analyse both theoretically and experimentally the behaviour of the SC with multi-point defects. Firstly, the splitting produced by the generation of a double point defect was analysed, showing the effects in both the real and imaginary band structures. From the imaginary complex band structure we can deduce that the localized modes present different values for the imaginary part of k , this means that each mode has a different decay rate inside the crystal. This property was experimentally observed by fitting an exponential decay for each localized mode inside the crystal. The symmetry of the vibrational patterns in double point defect have also been analysed in this Section by means of MST calculations and experimental results. Novel experimental evidence has been presented showing the symmetric and antisymmetric vibrational patterns in the SC with double point defects. Finally, using the different decay rate of both vibrational modes, the obtained conclusions have been confirmed giving a new methodology to determine different vibrational modes in periodic media.

Analytical, numerical and experimental results reproduce a very good agreement with the complex values of the wave vector inside the BG, meaning that these methodologies obtain good values for the exponential-like decay of the evanescent modes in a SC. These results are the basis for the correct understanding of the design of narrow filters and wave guides based on phononic or sonic crystals with point defects.

7

High number of vacancies. Optimization

As Caballero *et al.* [Caballero01] have shown, N-point periodic defects in a complete SC introduces an attenuation band in the transmission properties of these periodic systems below the BG and its position in the range of frequencies corresponds to the periodicity of the distribution of vacancies. On the other hand, the creation of vacancies using optimization techniques, such as GA, has been used to create efficient focalization or attenuation devices [Hakansson04, Romero06, Romero08, Herrero09]. In this Chapter we show an optimization procedure to obtain a specific distributions of vacancies in a complete array of scatterers in order to produce certain transmission properties through the resulting device. We call the resulting structure of the complete array and the distribution of vacancies Quasi-ordered structures (QOS).

The combination of GA and MST (see Chapter 4) offers a good way to find a distribution of vacancies in the SC optimized to improve both the attenuation and the focusing properties in predetermined ranges of frequencies [Hakansson04]. In this Chapter, we show the resulting structures obtained using the ev-MOGA (see Chapter 4) with MST. The resulting QOS are designed to optimize both the attenuation and the focalization of sound waves in a predetermined range of frequencies, and present a number of vacancies N_p in the same order as the total number of scatterers in the structure N_{cyl} . Several procedures to create point-defect in complete SC are analysed in this

Chapter.

Basically, given a starting SC, the GA generates QOS offspring that are classified in terms of a fitness function based on the pressure values at a specific point. The simulation of the sound scattered by every structure analysed by the GA is performed by the two-dimensional MST. After a predetermined number of generations, the algorithm stops selecting the best-fitted QOS. In our case, we try to optimize some features of the acoustic spectrum in a predetermined range of frequencies, in the ΓX direction (0°) at a point placed 1 m behind the crystal in the symmetry axis. Obviously these conditions constraints the resulting device to structures that do not present any improvement with respect to the angle dependence or in a finite region behind the crystal. If these dependences had taken into account, more complicated techniques would have considered to chose the best distribution of vacancies. Moreover, more parameters would be involved in the optimization problem and the interpretation of the results would be more complicated and difficult to do. In this case we would note that a high number of objective functions should be considered and, as a consequence, the difficulty of the problem would increase with the dimensionality of the Pareto fronts. The goal of the Chapter is to show how GA+MST can be used in the design of acoustic filters in a simple case. More intensive research have to be done to obtain the full optimization of such a systems.

The use of these optimization algorithm introduce some possibilities, for example, to design sophisticated filters. However, it would be interesting to know some general rules to improve the attenuation capabilities of a complete SC by means of vacancies. This Chapter will answer the immediate questions: How and how many vacancies one should produce in a starting SC to improve its attenuation? To do this, the parameters related to the asymmetry and to the fraction of vacancies will be analysed both theoretically and experimentally.

7.1 Quasi ordered structures (QOS)

The notion of quasi periodic order has been considered by authors working in different fields. From a theoretical point of view, the necessity to achieve a good understanding of the transport properties of disordered systems has led to a number of researchers addressing the issue of quasi periodicity as somewhat intermediate between periodic order and purely random disorder. From this perspective, the notion of quasi periodic order assumes a subsidiary role as a merely way to describe the conceptual transition from periodic order to randomness.

From a practical point of view, physicist have progressively realized that devices with this particular kind of structure offer interesting possibilities for technological applications. For example, quasicrystals are structural forms that are both ordered and nonperiodic. They form patterns that fill the whole space but lack translational symmetry. The classical theory on crystals allows only 2, 3, 4, and 6-fold rotational symmetries, but quasicrystals display symmetry of other orders (folds). Just like crystals, quasicrystals produce modified Bragg diffraction, but where crystals have a simple repeating structure, quasicrystals are more complex.

The structures obtained generating N_p point defects in a complete SC are called by us quasi-ordered structures: SC with a nonperiodic and random distribution of vacancies which produce a nonperiodic and random distribution of cylinders. However, due to the periodicity of the SC in which the vacancies are created, there are some parts of the system that present this periodicity. As we will see later, these systems present some interesting propagation properties, for waves related to the distances between the scatterers. For this reason, we have called these systems quasi-ordered structures (QOS).

Since this QOS are partly periodic they do not have a lattice constant, and thus, the effect of the N_p point defects on the acoustic response of the system is the creation of an acoustic band with some properties due to the multiple scattering in the optimized range of frequencies. In the case of the optimization of the attenuation properties this band will be called attenuation band, whereas for the case of the focalization properties it will be called focaliza-

tion band. We would like to note that the attenuation band presents different nature than the Bandgaps in periodic media which comes from the periodicity of the structure. Attenuation or focalization band is a more general denomination and in this work they make reference to the attenuation or focalization bands produced by an acoustic filter.

7.2 Simple genetic algorithm optimization

This Section aims at answering the following question: Can we obtain new attenuation bands different than the BG of the SC only by removing cylinders? The first approximation to the answer can be obtained by applying a simple GA in order to optimize a unique cost function that tries to find a QOS whose spectrum presents a flat and high attenuation band in a predetermined range of frequencies. In the following, the results obtained by optimizing the cost function $J_{V's}$ (see Equation 4.3 in Section 7.2) by means of a simple GA are shown.

We consider a SC made of rigid cylinders placed in triangular array with lattice constant $a = 6.35$ cm as starting sample (Figure 7.1). This starting SC has been designed following the following constraints: A large number of scatterers involves long computational times, and the SC topology should be simple to allow its implementation in the anechoic chamber for experimental testing purposes. We note that the first BG of this SC appears around 3090 Hz (Bragg's frequency).

In this simple GA, the starting structure is improved to obtain attenuation bands 600 Hz wide and centred at 1100, 1400, 1700 and 2000 Hz respectively. In the general procedure of GA, the best-fitted QOS not only are compared with the starting SC, but also with all the individuals of every generation. Here, we compare the resulting QOS with the starting SC to observe the improvement with respect to starting situation. We note that, in all cases, the considered frequency band lies under the first Bragg's frequency (3090 Hz). The insets in Figures 7.2A and 7.2B show examples of the optimized QOS for the ranges centred at 1700 and 2000 Hz. One can also observe in the insets of

7.2. SIMPLE GENETIC ALGORITHM OPTIMIZATION

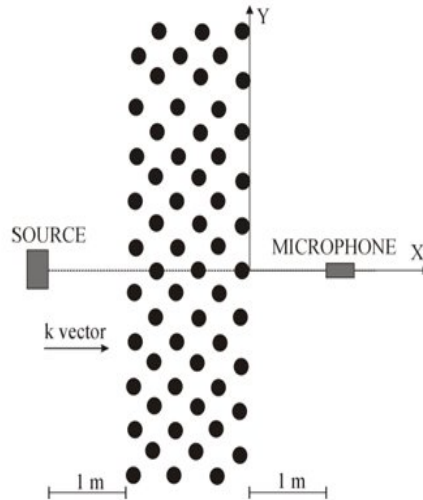


Figure 7.1: Starting SC consisting of hollow cylindrical aluminium rods, 1 m long mounted in a triangular pattern with lattice constant $a = 6.35$ cm. The diameter of the cylinders is $d = 4$ cm. The sample under study consists of an array of 6 rows with 10 cylinders per row, and rectangular external shape.

Figure 7.2 that the total number of cylinders in the optimized crystals varies between 40% and 46% with respect to the number of cylinders in the starting SC.

In Figure 7.2, one can see the theoretical spectrum of the QOS calculated using MST (red line), the experimental spectrum of the QOS (blue open circles) and finally the experimental spectrum of the starting SC (green dashed line). One can observe that in the QOS an attenuation peak appears at the predetermined selected frequency range, this means that it is absent in the spectrum of the starting SC and, moreover, the corresponding Bragg's peak vanishes at 3090 Hz. We notice that for the starting SC a sound reinforcement exists in this frequency range selected for the optimization process.

In order to quantitatively compare the obtained attenuation for the different

CHAPTER 7. HIGH NUMBER OF VACANCIES. OPTIMIZATION

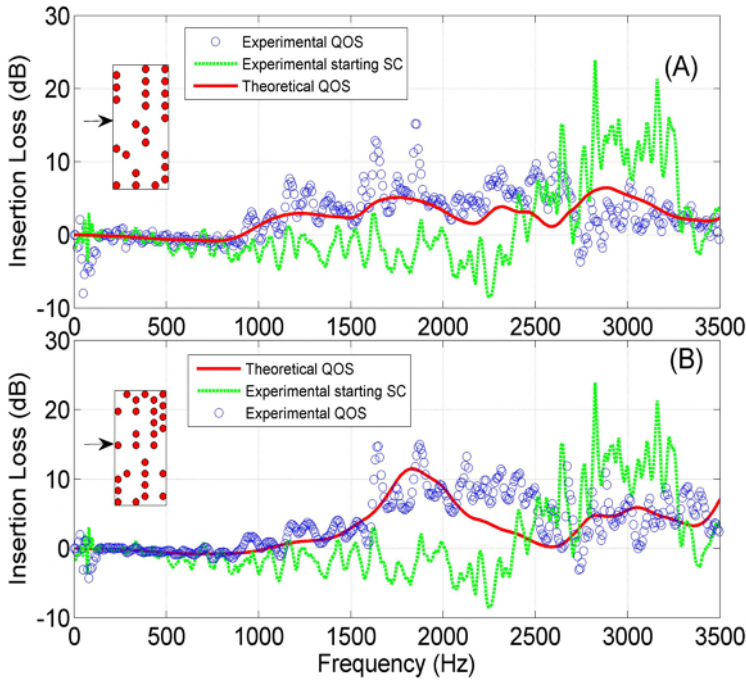


Figure 7.2: Spectra produced by the QOS resulting in the optimization of the Cost function $J_{v,s}$ in the ranges (A) 1400-2000 Hz and (B) 1700-2300 Hz. The insets in the Figure represent the QOS obtained in the optimization process for each range of frequencies. The red line represents the theoretical spectrum calculated using MST, the blue open circles represents the experimental spectrum of the QOS and the green dashed line is the experimental spectrum of the complete SC (Starting SC).

QOS, the Attenuation Area (AA) parameter (area enclosed between the positive spectrum and the 0 dB threshold in the selected frequency range, (see Section 2.2)) is calculated for the several QOS optimized in different ranges of frequencies. Table 7.1 shows the AA and the average attenuation values for the four QOS designed in the four different ranges of frequencies mentioned above. We notice that the AA for the starting SC is approximately equal to zero.

The analysis of the AA for the several ranges of frequencies optimized indicates that the improvement in the attenuation by means of the QOS is easier

7.3. MULTI-OBJECTIVE OPTIMIZATION

Table 7.1: AA (Attenuation Area) and average attenuation for the QOSs obtained by means of a simple GA.

Optimization range (Hz)	Central Frequency (Hz)	Attenuation Area (AA) (dB Hz)	Averaged Attenuation (dB)
(800-1400)	1100	731	1.21
(1100-1700)	1400	3411	5.61
(1400-2000)	1700	3420	5.7
(1700-2300)	2000	5088	8.48

when the range of frequencies is near the BG.

7.3 Multi-objective optimization

The preliminary results shown above indicate the possibility of achieving attenuation bands below the first BG of the complete SC by creating vacancies in the SC. In this Section, the results of a deeper analysis of the creation of N-point defects following a multi-objective optimization are presented. The optimization of both the focusing and the attenuation properties in SC by means of the creation of vacancies and following several strategies in the generation of defects are studied. Finally, the dependence of the solution of the multi-objective optimization on the path followed in the search space looking for the best structure is also analysed.

The ev-MOGA (see Chapter 4) working together with the MST (see Chapter 3) is the methodology used in this Section. The ev-MOGA tries to simultaneously solve a problem with two cost functions. The cost functions used were defined in Section 4.2.3.2: J_1 relates to the mean attenuation obtained in the range of frequencies to be optimized, J_2 is the mean deviation in such a range and J_3 represents the focusing capability of the device. For the optimization of the attenuation the ev-MOGA tries to simultaneously minimize J_1 and J_2 . For the focalization case the multi-objective problem is defined by J_2 and J_3 .

7.3.1 Starting conditions. Strategies in the creation of holes

The improvement of the acoustical properties of two dimensional SC formed with isolated and rigid cylinders in air is searched for in this Section. The starting SC containing 73 (4 cm diameter) cylinders, is positioned in seven rows in a triangular pattern with a lattice constant $a = 6.35$ cm. The acoustic pressure of the optimized samples is calculated by means of MST for a pre-determined range of frequencies, at a point located 1 m from the middle of the SC and in the ΓX direction (Figure 7.3).

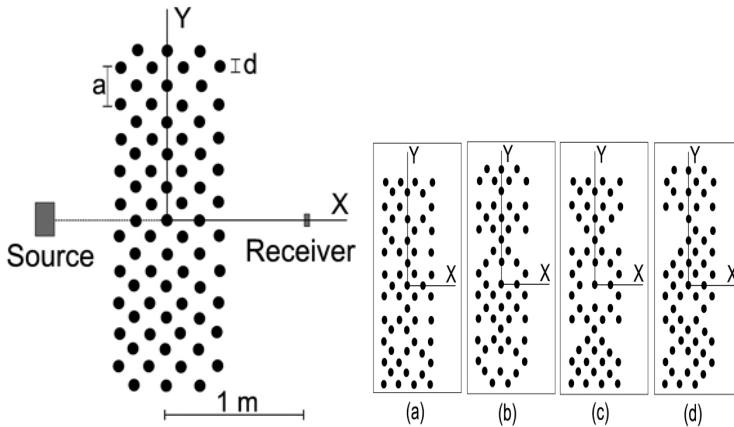


Figure 7.3: Starting conditions of the analysis. Starting SC (Left panel) and examples of each of the different strategies used in the creation of vacancies in the starting SC (right panel): (a) symmetry X, (b) symmetry Y, (c) symmetry XY and (d) no symmetry.

The optimized structures are obtained by means of the creation of vacancies, which means removing the cylinders in the starting SC. To design these structures, four strategies in the creation of vacancies are used by taking into account the symmetry axis of the starting SC (Figure 7.3): (i) symmetry around the X axis (symX); (ii) symmetry around the Y axis (symY); (iii) symmetry around both the X and Y axes (symXY); and (iv) random (nosym).

7.3.2 Characterization of the QOS

Due to the nature of multi-objective problems, the optimized solution is represented by a set of structures (Pareto set, see Chapter 4). It seems necessary to define suitable tools to characterize these optimized structures. Moreover, these tools will enable a comparison among the different optimized samples. Next, both optimizing and structural tools are defined. The former help us to classify the resulting samples as a function of their acoustic properties. These tools are: Pareto front (PF), optimizing factor (O_f) and area of the spectrum (AS). Structural tools help us to establish the best arrangement of vacancies to enhance the acoustic properties of the resulting devices. These parameters are: fraction of vacancies (F_v), and asymmetry (A). Some of these optimizing or structural parameters were defined in the Section 2.2 devoted to parameters defining SC. One can read there the definitions of the Fraction of vacancies (F_v), the Asymmetry (A) and the Area of Spectrum (AS).

The rest of the parameters are defined as follows:

Pareto front (PF): As it was mentioned in Chapter 4, when approaching the multi-objective optimization problems, the notion of optimized structures changes as the solution is a good compromise among the objectives involved in an optimization process. Thus, a single solution is not normally obtained but a set of solutions constitute the so-called the Pareto optimal set, which is mapped using the cost functions in the Pareto front (see Figure 4.6). All points representing the PF correspond to optimum solutions. However, in the case of two cost functions, one can see in Figure 4.6 that an optimal solution with respect to one of the cost functions implies a low optimization with respect to the other one. Therefore, it is necessary to define some decision criteria to choose the most suitable solution. This solution is characterized by the definition of the \vec{Q} -vector. If k cost functions are considered, the \vec{Q} -vector whose extreme is a point of the PF , is defined in such a way that its distance to the origin is minimal in the objective space,

$$\vec{Q}/min \left\{ \sqrt{\sum_{i=1}^k J_i(\vec{Q})^2} \right\}. \quad (7.1)$$

CHAPTER 7. HIGH NUMBER OF VACANCIES. OPTIMIZATION

This point is a compromise among all the cost functions optimized, and offers the best stability with respect to the optimization procedure.

Optimizing factor (O_f): This parameter help us to determine how much better each optimization is with respect to previous optimizations, quantifying the improvement of the optimization process. Given several Pareto fronts for the same optimization problem, the optimization factor (O_f) can be defined as the Euclidean distance between the \vec{Q} points of any two different PF. Thus, if \vec{Q}_1 and \vec{Q}_2 are considered as two PF \vec{Q} -vectors, then

$$O_f = \sqrt{\sum_{i=1}^N (Q_{1i} - Q_{2i})^2}. \quad (7.2)$$

An important parameter used to measure the improvement obtained using the Pareto fronts is the so-called ideal point (IP) (see references [Ehrgott03, miettinen98]). The ideal point is defined as the vector formed with the lowest components among all points in the PF . This means that, the first components of the ideal point are the minimum value of all first components of the points in the PF ; the second component is obtained in the same way. Distances to the ideal point, measured in the objective space, are one of the classical solution quality indexes in multi-objective optimization. However, the ideal point is not easy to find in practice. The \vec{Q} -vector that corresponds to a real structure is easy to find in practice, and it is near to the value of the ideal point in the optimization problem studied in this work. In addition, the \vec{Q} -vector provides information about the goodness of the optimization results.

7.3.3 Improving the attenuation capabilities with QOS

In this section, the ev-MOGA is used to generate QOS with attenuation properties higher than the starting SC in a predetermined range of frequencies, for the ΓX direction and in a point located at 1 m from the end of the system. Making use of the objective functions J_1 and J_2 defined in Section 4.2.3.2 the QOS present maximum values of both the acoustic attenuation level and the stability in the optimization range of frequencies (see Section 4.2.3.2). In

other words, the QOS produce high attenuation level in a predetermined range of frequencies, with the least possible fluctuation in the attenuation spectrum.

7.3.3.1 Initial test: Improvement of the preliminary QOS

In Section 7.2 we showed the preliminary results of QOS. They allow us to affirm that by creating vacancies in a starting SC one can generate attenuation bands in a predetermined range of frequencies. We have improved the simple GA by using the evMOGA. In this Section we check this new algorithm applying it to the improvement some of the preliminary results shown in Section 7.2. In this Section, the ev-MOGA is used to generate a QOS for its use as an attenuation device in the range of frequencies between 1400 and 2000 Hz. The objective functions J_1 and J_2 defined in Section 4.2.3.2 are analysed in intervals of $v=20$ Hz. We have selected the random generation of vacancies in the starting SC, as it was done in the preliminary results.

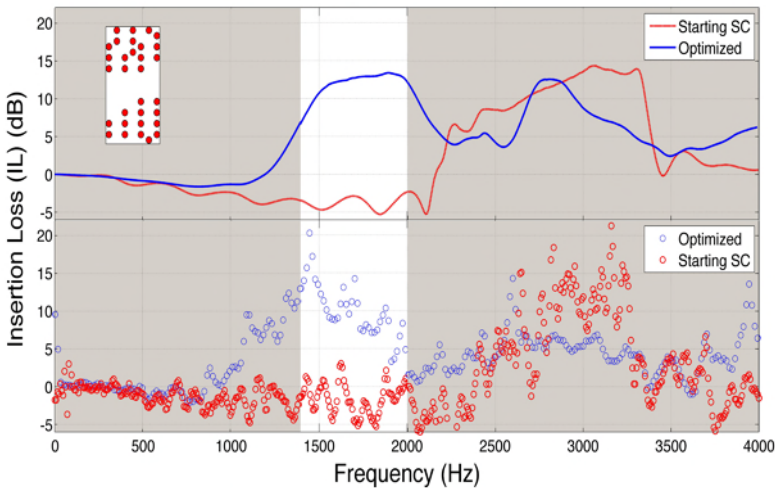


Figure 7.4: Insertion Loss spectra of the optimized QOS and of the starting SC. The optimized range of frequency is marked in the the white area. The optimization is obtained in a point situated 1 m behind the crystal. The inset shows the distribution of cylinders of the QOS. Upper panel: Results predicted by the MST. Lower panel: Experimental measurements

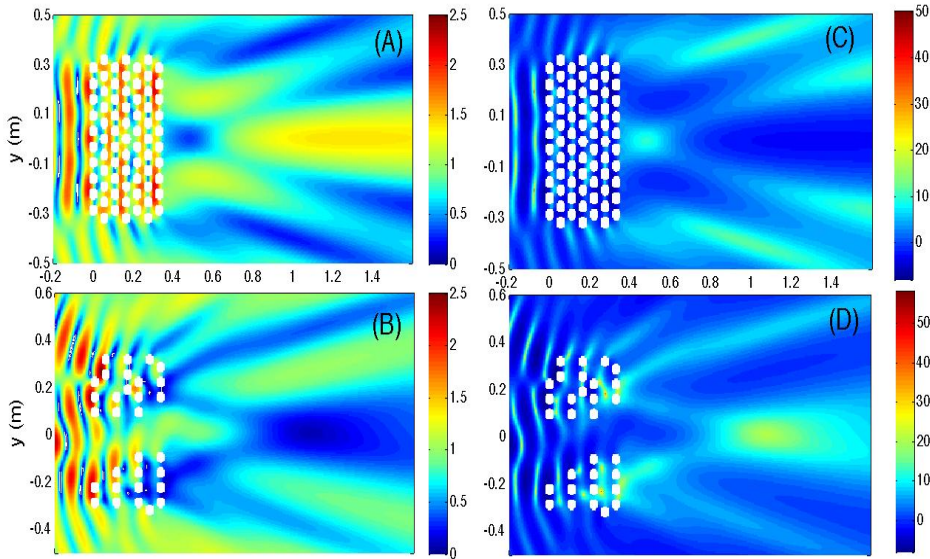


Figure 7.5: Acoustic field of the starting SC and the QOS for 1700 Hz, calculated using MST. (A) and (B) show the pressure maps of the starting SC and for the QOS respectively. (C) and (D) show the insertion loss maps for starting SC and for the QOS respectively.

Inset of Figure 7.4 shows the QOS obtained using evMOGA. The insertion loss spectra calculated using MST for both the QOS (blue line) and the starting SC (red line) are also shown in the upper panel of Figure 7.4. One can observe that the spectrum corresponding to the QOS presents an attenuation band at the optimized range of frequencies, and it is absent in the spectra of the starting SC. Moreover, we can observe that the insertion loss inside the optimized range of frequencies presents the desired results: flat and high attenuation level. The experimental validation of the calculus of MST is shown also in the lower panel of Figure 7.4.

The optimization has been done for a point behind the structure situated 1 m away from the end of the starting SC. Thus, it would be interesting to analyse what is the attenuation zone behind the structure. Figure 7.5 shows both the pressure ((A) and (B)) and the insertion loss ((C) and (D)) maps for the starting and the QOS calculated for the central frequency of the optimized

7.3. MULTI-OBJECTIVE OPTIMIZATION

range, 1700 Hz. One can observe that, around the optimization point ($x \sim 1.33$ m) there is a focusing zone, i.e., reinforcement in its insertion loss spectra. However, the QOS produces an attenuation zone centred at this point due to the optimized multiple scattering in the QOS that produces an negative interference around the optimized point and for the whole optimized range of frequencies.

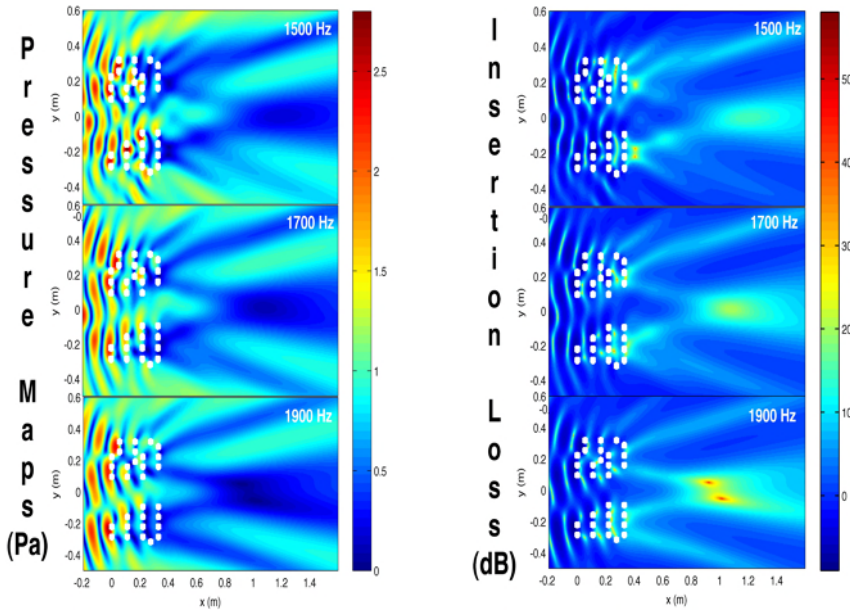


Figure 7.6: Acoustic field produced by the QOS for several frequencies inside the optimized range of frequencies calculated using MST. Left panel: Pressure maps for the frequencies 1500, 1700 and 1900 Hz. Right panel: Insertion loss maps for the frequencies 1500, 1700 and 1900 Hz.

In Figure 7.5, one can observe the desired behaviour for the central frequency of the optimized range, but, it would be interesting to analyse what is the attenuation zone for several frequencies inside the optimized range of frequencies. Figure 7.6 shows acoustic field produced by the QOS for several frequencies inside the optimized range of frequencies calculated using MST. One can observe that the QOS present similar attenuation region behind the structure for all the frequencies inside the optimised range.

7.3.3.2 Symmetries in the generation of vacancies

In this Section, the ev-MOGA is used to generate QOS for its use as attenuation devices in the range of frequencies between 2300 and 3700 Hz. The objective functions J_1 and J_2 defined in Section 4.2.3.2 are analysed in intervals of $\nu=50$ Hz.

Figure 7.7A shows the Pareto fronts for the results obtained using the ev-MOGA with the four strategies of generation of vacancies. Their position in the plot implies the improvement in their attenuation capability. The closer the Pareto fronts are to the origin of the coordinates, the better the optimization. This is because a low J_1 implies a high attenuation level following Equation (4.5); and a low J_2 represents lower mean deviation. We can sort the strategies used as a function of the results shown: nosym>symY>symX>symXY. We can see that the nosym strategy presents the highest optimization levels for the cost functions used and symXY seems to be the worst.

Moreover, one can compare the acoustic attenuation level for both the optimized samples and the starting SC. To do this, the optimizing factor parameter has been used. Taking into account that the \vec{Q} -vector for the PF corresponding to the nosym strategy is $(J_1, J_2) = (0.0575, 0.0052)$ and the values for the starting SC are $J_1 = 0.4633$ and $J_2 = 0.056$, the value of the optimizing factor, $O_f = 0.4090$, can be obtained. It seems that the attenuation level (J_1) is the truly important function in our study. This is because, in both cases, the difference between their values is similar to the O_f value. So, it seems that J_2 plays a secondary role in the attenuation study, representing the stability of the attenuation level. Finally, the value of O_f indicates that, physically, the creation of vacancies in a starting SC seems a suitable strategy to improve the attenuation characteristics of SCs. Thus, the value of O_f means that there is a difference in the attenuation capability between the starting SC and the best sample of the nosym strategy value of 18.5 dB.

After looking at Figure 7.7A, it seems possible to quantify the differences among the acoustic attenuation obtained for the four considered strategies. Regarding the \vec{Q} -vectors of the best (nosym) and of the worst (symXY) strategy, the value of the O_f parameter is 0.0907. This value represents a differ-

7.3. MULTI-OBJECTIVE OPTIMIZATION

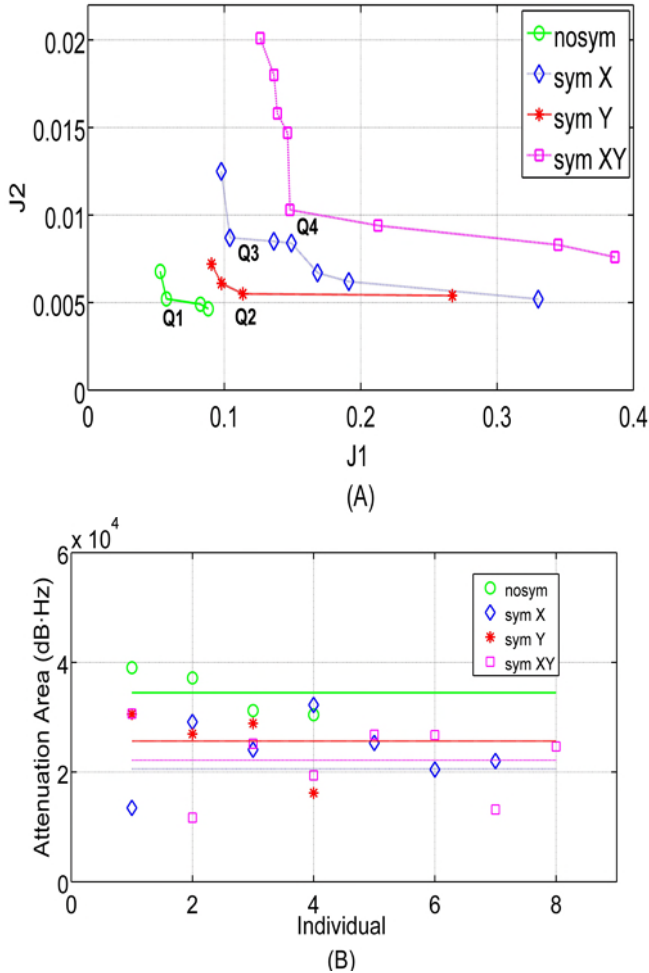


Figure 7.7: (A) Pareto fronts for the different symmetries of generation of vacancies used for the attenuation effect; (B) Attenuation area for each analysed symmetry.

ence in attenuation of 8.2 dB between both optimized samples.

To quantify how much better each strategy of vacancy generation is when compared to the others, the attenuation area (AA) parameter is analysed. This parameter has been calculated for the spectra of all the optimized samples shown in Figure 7.7A. The points in Figure 7.7B represent the value of the AA

CHAPTER 7. HIGH NUMBER OF VACANCIES. OPTIMIZATION

parameter for each resulting optimized structure in each one of the symmetries of generation of vacancies used and the lines represent the average value of the parameter in each case. The biggest AA corresponds to the nosym strategy and this fact means that the resulting optimized samples obtained with this strategy show the best improvement in their attenuation capabilities.

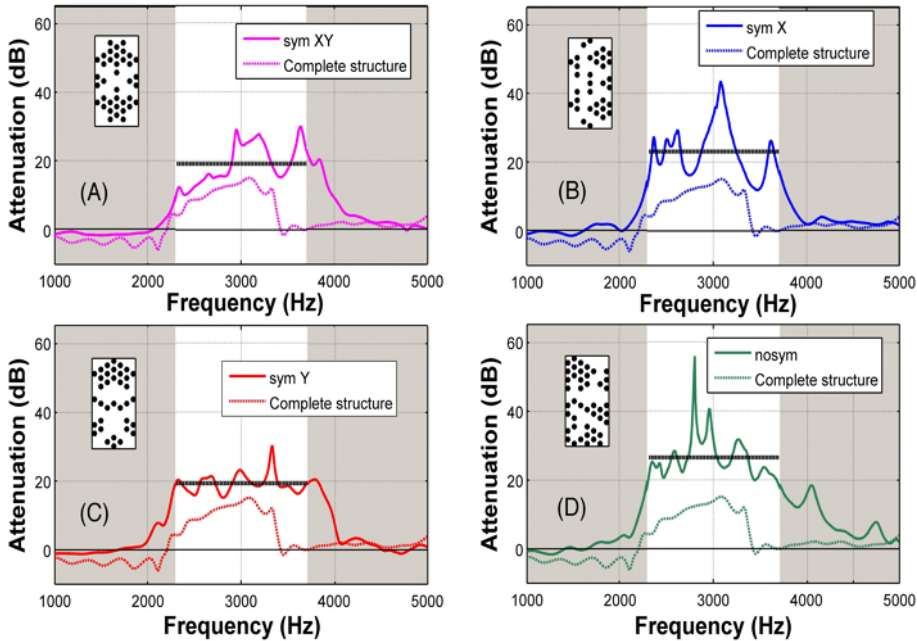


Figure 7.8: Spectra of the resulting optimized samples: (A) Q_1 ; (B) Q_2 ; (C) Q_3 ; and (D) Q_4 shown in Figure 4(A) (continuous line); and of the starting SC (dotted line). The range of frequencies optimized is delimited by two vertical dashed lines. The attenuation average level in the optimized range of frequencies for each of the symmetries used is represented (horizontal dotted line). Configurations of the optimized samples corresponding to each Q -vector are included as an inset.

Figure 7.8 can help to understand Figures 7.7A and 7.7B. Here, one can see the attenuation spectra of the resulting samples marked in Figure 7.7A as Q_1 , Q_2 , Q_3 , and Q_4 , corresponding to the \vec{Q} -vectors of each strategy of generation of vacancies, analysed together with the corresponding \vec{Q} -vectors of to the starting SC. The best average, as it has been mentioned above, corresponds to

7.3. MULTI-OBJECTIVE OPTIMIZATION

the nosym strategy.

We note that the values of the cost functions for the resulting samples shown in Figure 7.7A are in very good agreement with MST spectra simulations shown in Figure 7.8. Thus, it is possible to compare the improvement of both J_1 (mean pressure) in Figure 7.7A and the average attenuation in Figure 7.8. In Figure 7.7A, we can see that $J_1^{Q_4} > J_1^{Q_2} > J_1^{Q_3} > J_1^{Q_1}$ and this is in good agreement with the results obtained in Figure 7.8: nosym > symY > symX > symXY. We can also observe that the improvement of J_2 in the process is not as significant as the improvement of J_1 . In Figure 7.8, one can see the predominance of the attenuation level criterion in the attenuation spectra of the resulting samples.

In Table 7.2, one can observe the results of the optimization process for the four independently considered strategies and the corresponding values for the initial SC (complete structure). (J_{1min}, J_{2min}) represent the coordinates of the IP of the Pareto set for each strategy, AA_{av} means the average of the AA for each Pareto set of the considered problem which, as it has been explained above, does not have an unique solution. By examining the AA values, it is possible to classify the strategies as follows: nosym > symY > symX > symXY. This means that the strategy with the minimum IP (nearest to the origin of the coordinates) presents the maximum AA, meaning that J_1 and J_2 are well defined in order to achieve the objective pursued. Moreover, it is possible to quantitatively obtain the increase in the attenuation capability for each analysed strategy with respect to the starting structure. This increase is around 200% in the case of the nosym strategy (see Table 7.2).

Table 7.2: Optimization values obtained by independently analysing each of the considered symmetries.

	J_{1min}	J_{2min}	AA_{av}
symXY	0.1263	0.0076	22406
symX	0.0977	0.0052	23808
symY	0.0906	0.0054	25643
nosym	0.0530	0.0046	34464
Complete structure	0.5633	0.056	11965

In short, taking into account the results obtained for the optimizing tools defined in Section 7.3.2 (*PF* and O_f) together with *AA* and the Asymmetry, the nosym strategy to create vacancies in a starting SC seems the most suitable method to improve the acoustic attenuation capability of SC.

7.3.4 Improving focusing capabilities with QOS

This Section examines the optimization of the focusing properties of SC by means of the creation of vacancies in a starting SC. Especially, the aim is to increase the focusing properties of these materials, in a predetermined point of measurement, for a range of frequencies from 1400 to 2000 Hz, analysed at intervals of $\nu=50$ Hz and in the ΓX direction. We note that the chosen range of frequencies is just below the first band gap, and as such, inside the first transmission band. As in the case of the attenuation optimization, we have defined two objective functions, taking into account that the aim is to maximize the acoustic pressure J_3 and minimize its deviation, J_2 , at the predetermined point (see Section (4.2.3.2)).

Figure 7.9A shows the PF with the optimization results using the four strategies to create vacancies obtained using the evMOGA for focusing structures. Here, as in the case of the attenuation analysis, the same order can be seen in the strategies used as a function of the obtained optimization: nosym > symY > symX > symXY. Figure 7.9A shows that the nosym strategy offers higher optimization levels for the cost functions and symXY offers the worst strategy. However, due to the small separation between the Pareto fronts, it can be concluded that the vacancy creation strategy chosen to optimize focusing properties of the SCs is unimportant.

Moreover, the creation of vacancies seems less efficient in the optimization of the focusing than in the case of the attenuation. Again, we can evaluate the optimization process by comparing the values of the O_f parameter between the nosym strategy and the starting SC. The \vec{Q} -vector for the nosym strategy is $(J_3, J_2) = (0.6196, 0.0027)$ and the corresponding cost function for the starting SC is $J_3 = 0.6428$; $J_2 = 0.0437$. The calculated value of the optimizing factor is $O_f = 0.0471$. This means an improvement in the focusing properties

7.3. MULTI-OBJECTIVE OPTIMIZATION

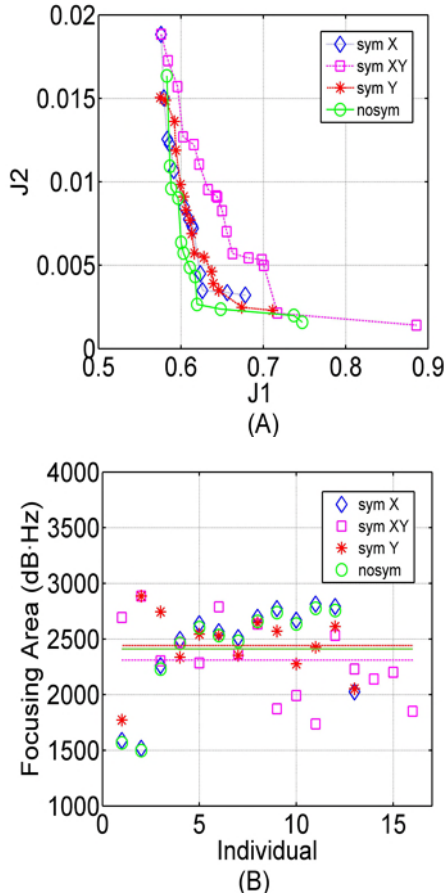


Figure 7.9: (A) Pareto fronts for the different vacancy generation symmetries used for focusing effect; (B) focusing area for each analysed symmetry. The points represent the value of the parameter for each of the optimized structures obtained and the line represents their average value.

equal to 0.4280 dB. In this case, O_f means a low optimization level compared with that obtained in the attenuation case ($O_f = 0.4090$ meaning 18.5 dBs) in the focusing properties of the SC.

To support these results, the focusing area (FA) parameter has been measured. This optimization parameter has been calculated in the same way as in the

CHAPTER 7. HIGH NUMBER OF VACANCIES. OPTIMIZATION

attenuation case. Figure 7.9B shows the *FA* for the analysed strategies and the similarity between the average values for all the strategies used can also be seen.

Figure 7.10 shows the increases in the acoustic level in the range of frequencies under study, and for the predetermined point of measurement with coordinates (1,0). We can clearly see that the differences in acoustic level between the analysed symmetries is smaller when compared with the attenuation case (see Figure 7.8).

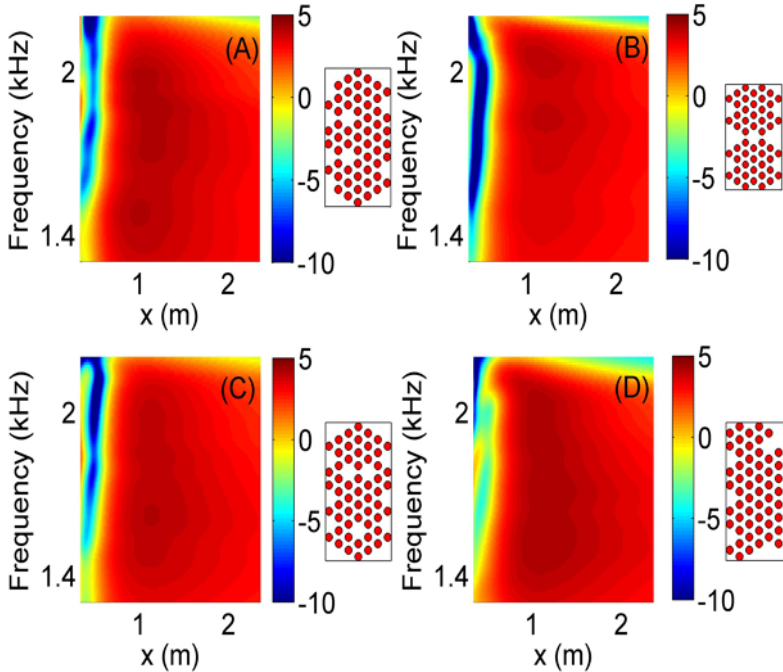


Figure 7.10: Acoustic level in the focusing area. On the OX axis, the distance along the direction of the incident wave is shown and the frequencies for the four strategies analysed on the OY axis are also shown. The colour bar represents the acoustic level in dBs. The corresponding samples are also included.

7.4 Dependence on the searching path

The results presented in the previous Section show that each symmetry can accomplish a limit of optimization, such that the best optimization is obtained using the random generation of vacancies in the starting SC. Specifically, we observed that the sort of the capability to improve the attenuation is nosym, symY, simX and symXY in decreasing way. On the other hand we have shown that the focusing capabilities are similarly improved with all the symmetries.

Then, the question is: could we improve the attenuation capabilities of a QOS mixing symmetries in the optimization process, and as such, changing the searching path of the optimization process? To answer this question, two procedures are analysed in the next Sections.

7.4.1 Procedure 1

The first strategy for the creation of vacancies that we have proven consists of mixing the four strategies defined earlier. In this search path, 12 runs of the optimization process in four different steps have been executed, taking again as an initial population in each run the best individuals obtained in the previous run and following the order of the strategies obtained in Table 7.2: (i) the three starting run constraints for the solutions with symXY, (ii) the next three run constraints with only symX, (iii) the next three with symY and (iv) the final three executions imposing nosym restrictions. In Figure 7.11B, one can see the PF corresponding to the solutions in each step of this mixed optimization process, together with the PF corresponding to just the nosym strategy analysed in the previous Section. One can see the superposition of both PF (nosym and mixed nosym) and we can conclude that a similar solution is obtained in both cases. This result indicates that the search for the minimum of our problem is independent of the search path and therefore the stability of the optimization process is ensured.

Another argument to select the objective functions is shown in Figure 7.12B. The optimized structures obtained for the points of the PF that define the IP

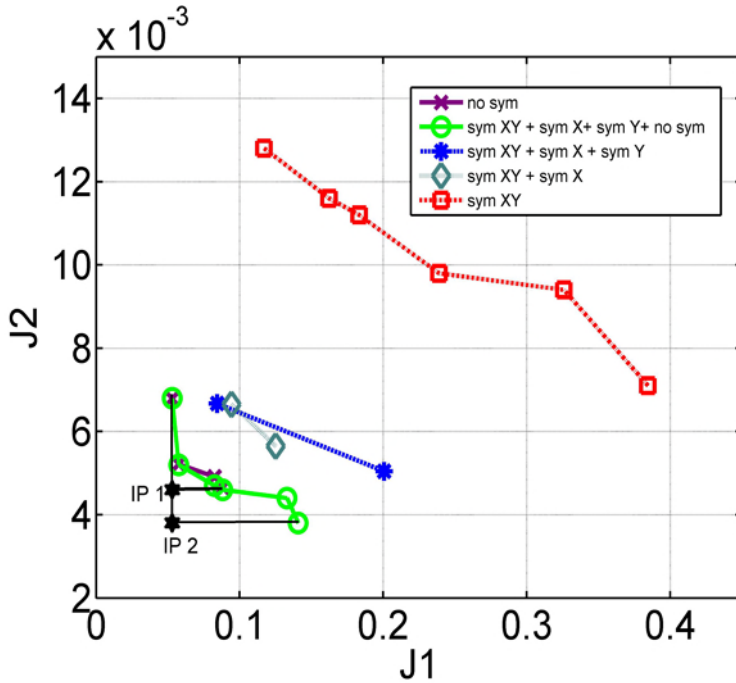


Figure 7.11: PF for the mixed method showing each of the steps in the optimization process. The PF for the independent nosym strategy is also represented.

for the nosym case of the mixed strategy (IP₂ in Figure 7.11B) are presented. The left structure (optimized (1)) represents the point corresponding to the PF with the minimum average acoustic pressure J_1 (maximum attenuation level) and maximum standard deviation (J_2). The example on the right-hand side (optimized (2)) represents the structure with maximum J_1 and minimum J_2 . The corresponding attenuation spectra can also be seen. Both structures show the variation in the attenuation spectra due to the different extreme values of both objective functions (J_1, J_2) in the considered PF.

In Figure 7.12B the best structure obtained with the optimization process and the corresponding attenuation spectra can be seen. This structure corresponds to the point of the nosym PF with the minimum distance to the origin of the coordinates. This point means that an agreement between both objective functions is the nearest to the IP. To confirm the validity of the theoretical results

7.4. DEPENDENCE ON THE SEARCHING PATH

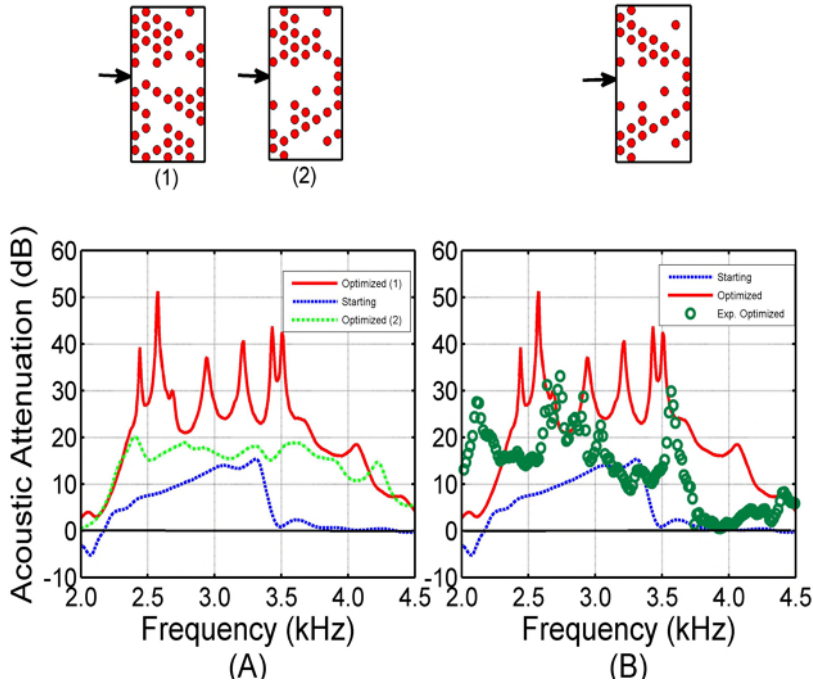


Figure 7.12: (A) Attenuation spectra for the nosym samples corresponding to the points that define the IP of the PF. The corresponding structures are also represented at the top. (B) Best nosym structure obtained in the optimization process; theoretical and experimental attenuation spectra are represented. The spectrum of the initial sample is also included.

obtained, the experimental spectra of this optimum structure is drawn with a resolution of 8 Hz. The good agreement between the theoretical and the experimental spectra can be seen by calculating the corresponding AA parameter ($AA_{theor} = 31202$ Hz dB and $AA_{expt} = 30215$ Hz dB). In any case, the differences in the shape between both optimized attenuation spectra (theoretical and experimental) can be explained in terms of the real experimental conditions compared with the ideal conditions considered in MST model: aluminum cylinders infinitely large, little changes in the length of the experimental lattice constant, acoustic conditions of the anechoic chamber, etc.

7.4.2 Procedure 2

Multiple execution of the algorithm has been performed to increase the reliability of the results. The executions started with the different constraints and the initial populations. An increasing SC structure complexity policy is selected (figure 4.4): the three first run constraints of the solutions with SC symmetry in both axes, X symmetry plus Y symmetry; the next six run constraints only in one axis, three with X symmetry and three with Y symmetry. The final three executions impose no symmetry restriction. The computational complexity is lower when symmetry constraints are imposed. Thus, no symmetry restriction means more complex calculation.

To improve the results in each execution, the following procedure is followed:

- **symxy**: X plus Y symmetries and random initial population.
- **symxy2**: X plus Y symmetries and the solutions of symxy is included in the initial population. The rest of the population is randomly generated.
- **symxy3**: X plus Y symmetries and the solutions of symxy and symxy2 are included in the initial population. The rest of the population is randomly generated.
- **symy**: Y symmetry and random initial population.
- **symy2**: Y symmetry and the solutions of symy and symxy3 are included in the initial population. The rest of the population is randomly generated.
- **symy3**: Y symmetry and the solutions of symy2 is included in the initial population. The rest of the population is randomly generated.
- **symx**: X symmetry and random initial population.
- **symx2**: X symmetry and the solutions of symx and symxy3 are included in the initial population. The rest of the population is randomly generated.
- **symx3**: X symmetry and the solutions of symx2 is included in the initial

7.4. DEPENDENCE ON THE SEARCHING PATH

population. The rest of the population is randomly generated.

- **nosym**: Without symmetry constraint and random initial population.
- **nosym2**: Without symmetry constraint and the solutions of nosym, symy3, symx3 and symxy3 are included in the initial population. The rest of the population is randomly generated.
- **nosym3**: Without symmetry constraint and the solution of nosym2 solution is included in the initial population. The rest of the population is randomly generated.

The fact that each problem is executed several times with the best solutions from the previous runs is a common technique to prevent early exhaustion when the population diversity drops below a threshold. In the literature related to this field, it is known as ‘restart and phase’. For instance, see CHC algorithm [[eshelman91](#)]. The three runs of the algorithm can be understood as a unique run with a mechanism of ‘restart and phase’. When the algorithm is exhausted, it is restarted with a new population that includes the best individuals.

Figure 7.13 shows the best results for all symmetries and the relative position compared with the ideal point. The ideal point is formed with the best attenuation and mean deviation obtained with the best values of points P1 (whose minimise means pressure in a single objective sense) and P9 (whose minimise means deviation in a single objective sense) of nosym3 Pareto Front. This point is not achievable, but it gives an order of magnitude of the best performances attainable. As we can see, the execution without symmetry constraints presents the best results because the structure has more flexibility. Y symmetry and X symmetry offer similar results. The worst results are for XY symmetry - due to the limited degree of freedom in the creation of vacancies.

Figures 7.14, 7.15, 7.16 and 7.17 show the acoustic attenuation spectra supplied by some of the points of the Pareto front obtained in the optimization phase. The points are labelled as P1, P2, etc. (see figure 7.13) in decreasing order of mean attenuation. For the fronts of more than two points, such as

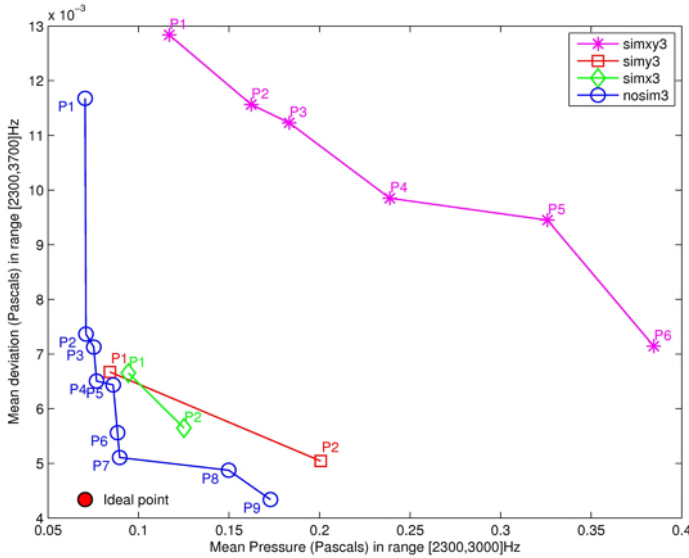


Figure 7.13: Comparison of the best result for each symmetry constraint.

nosym3 and symxy3, for simplicity sake and without loss of generality, only the extremes of the front and the nearest point to the ideal are considered for the next analysis.

Figure 7.14 represents the results of points P1, P4 and P6 of the Pareto front of symxy3. P1 has the best mean attenuation in the range of optimization ([2300, 3700] Hz) and P6 the best mean deviation in the same range; P4 is an intermediate solution between P1 and P6, and is the nearest to the ideal point. An interesting characteristic is that P1 has the worst mean deviation, but when observing the frequency diagram of attenuation, this is seen not to be a drawback because the larger variations in attenuation are in a positive sense and this behaviour is favourable to the main objective. In essence, the objective is to obtain a high attenuation bands and all variations in this sense should be considered positive. Even with a higher variation in attenuation with respect to P4 and P6, the attenuation for nearly every frequency in the range of interest is normally above the values of P4 and P6. Then a good

7.4. DEPENDENCE ON THE SEARCHING PATH

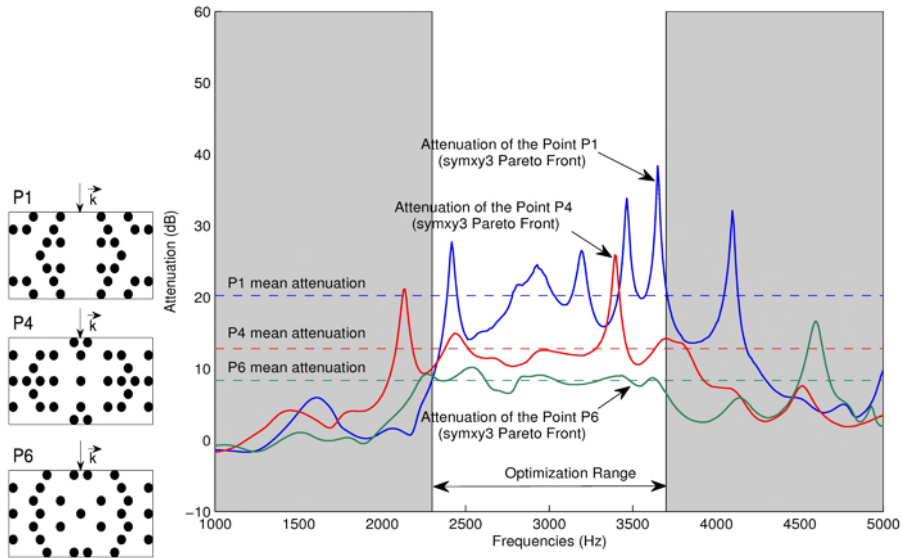


Figure 7.14: Attenuations spectra for points P1, P4, and P6 of the Pareto front in the symxy3 case. Mean attenuations have been calculated in the selected ranges of frequencies (from 2300 to 3700 Hz).

solution for a final choice with XY symmetry is point P1.

Figure 7.15 represents the results of points P1 and P2 in the symx3 case, in the complete Pareto front obtained in the optimization process. P1 has the best mean attenuation in the range of optimization ([2300, 3700] Hz) and P2 the best mean deviation in the same range. In both cases, the mean attenuation is quite similar. The deviation analysis in the optimization range reproduces similar characteristics as in the symxy3 case. The higher deviation of P1 is not a drawback because the main deviation is in a positive sense. Again, a good choice for a final solution can be point P1.

For the results presented in Figure 7.16, the analysis is quite similar to the previous one and the best choice for a final solution with Y symmetry is P1.

Figure 7.17 represents the results of points P1, P7, and P9 of the Pareto front in the nosym3 case. P1 has the best mean attenuation in the range of optimiza-

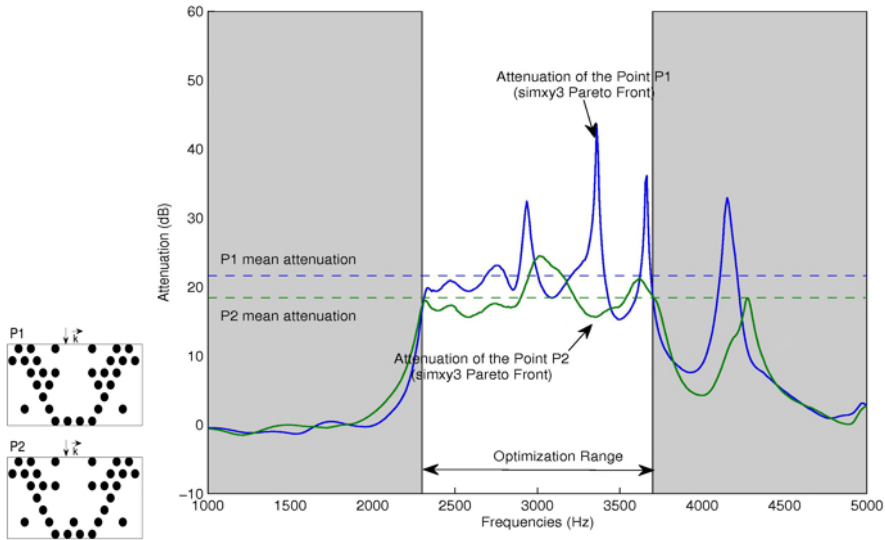


Figure 7.15: Attenuations for points P1 and P2 of the Pareto front in the symx3 case. Mean attenuations have been calculated in ranges [2300, 3700] Hz.

tion ([2300, 3700] Hz), P9 the best mean deviation in the same range and P7 (the nearest to the ideal point) is an intermediate solution between P1 and P9. The analysis of XY, X, and Y symmetries shows an important characteristic: those responses with high deviations are not necessarily the worst as they are mostly in a positive sense which is good for the higher attenuation. A good choice for a final solution could be P1 point. Moreover, this solution can be the best choice for all symmetries as it obtains the best mean attenuation.

7.5 General rules for creating vacancies in sonic crystals

Results obtained in the previous Section reveal that the optimization of SC by means of the creation of vacancies asymmetrically distributed in the structure, produces a good results for the creation of attenuation bands, better than

7.5. GENERAL RULES FOR CREATING VACANCIES IN SONIC CRYSTALS

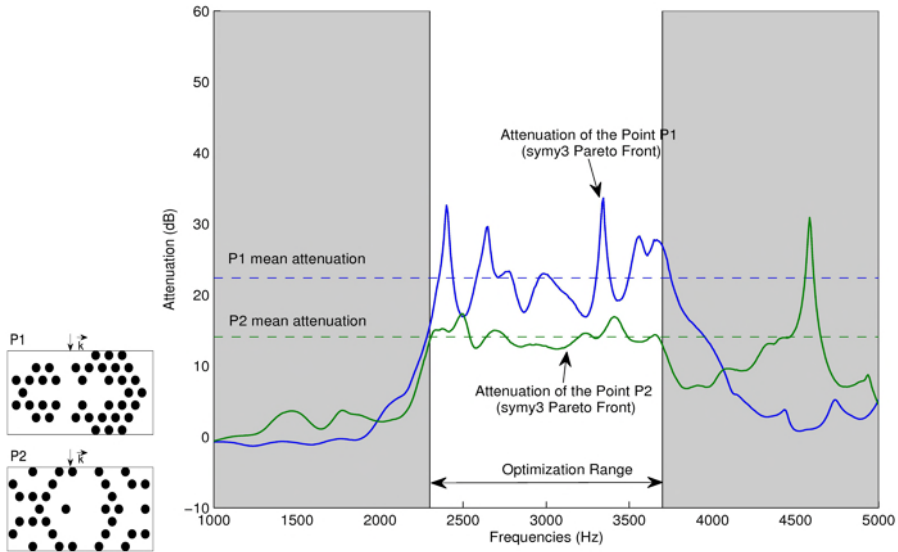


Figure 7.16: Attenuations for points P1 and P2 of the Pareto front in the symy3 case. Mean attenuations have been calculated in ranges [2300, 3700] Hz.

the ones obtained using the symmetric distribution of vacancies. We showed that the best results of the optimization process appear when, in some steps of the evolutionary algorithm, we introduce an asymmetric distribution of vacancies. In contrast, the results obtained for the optimization of the focusing properties of the SC indicate that although the creation of vacancies provides an improvement in the focusing properties of SCs, this increase is smaller than that obtained in the attenuation case. In addition, there are not any geometry of distribution of vacancies that produces better results than other.

From the results obtained in the optimization process considering symmetries for the generation of vacancies, it would be possible to obtain some general rules to build QOS that present better attenuation and focalization capabilities than the starting SC in a predetermined point behind the structure and in a previously fixed predetermined range of frequencies. This Section answers the immediate question: How and how many vacancies one should produce in a starting SC to improve the its attenuation? To do this, the parameters related to the asymmetry and to the fraction of vacancies will be analysed

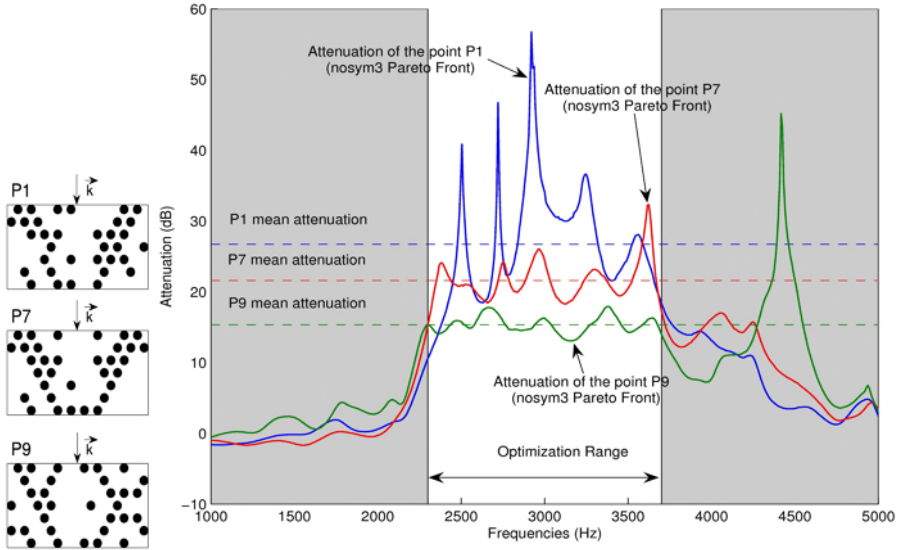


Figure 7.17: Attenuations for points P1, P7 and P9 of the Pareto front in the nosym3 case. Mean attenuations have been calculated in ranges [2300, 3700] Hz.

both theoretically and experimentally.

In this Section, we are interested in obtaining general rules on the number of vacancies and their distribution on the starting SC, as required to obtain structures with optimized attenuation and focalization properties in the way we have explained above. The parameters that we have defined to give us information about the distribution and the number of vacancies were defined in Section 7.3.2: The fraction of vacancies (F_v) and the asymmetry (A).

In the different optimization process considered, one for each of the symmetries of creation of vacancies, the behaviour of the Asymmetry parameter has firstly been analysed. In Figure 7.18A, one can see the values of the asymmetry parameter for each of the analysed symmetries in the creation of vacancies. One can observe that, in the case of the nosym strategy, the optimized value of this structural parameter appears around 60%, whereas the other symmetries present a values around 20%. These results indicate that the level of asymmetry of each generation of vacancies is an adequate param-

7.5. GENERAL RULES FOR CREATING VACANCIES IN SONIC CRYSTALS

eter to obtain devices with high attenuation level. We note that, in the case of the nosym symmetry, the optimized QOS can be obtained using a distribution of vacancies that presents the previous value of asymmetry. From the definition of the assymetry parameter, it is easy to see that he corresponding value of this parameter for the symXY generation of vacancies is $A_{symXY} = 0$. This is the reason why it is not analysed in this Section. Moreover, taking into account the Pareto fronts shown in Figure 7.7A, symXY becomes the worst strategy to increase the attenuation properties of the SC and therefore, the value of the A parameter is in good agreement with the results obtained using the PF . Accordingly, only the three remaining symmetries will be analysed.

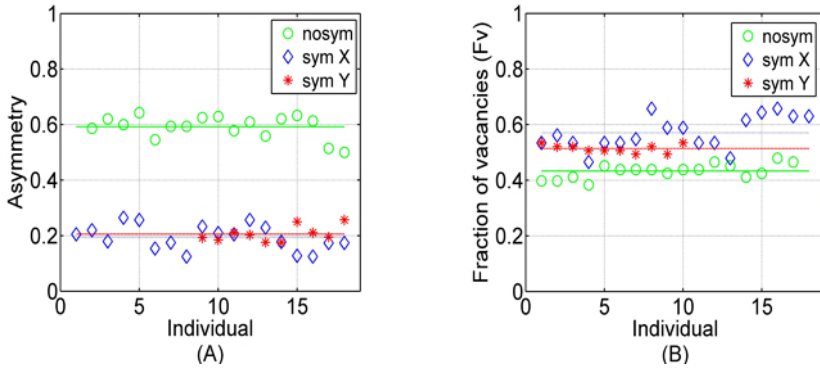


Figure 7.18: (A) asymmetry parameter and (B) fraction of vacancies for the analysed symmetries in the Attenuation case. The points represent the value of the parameter for each of the optimized structures obtained and the line represents their average value.

It would be interesting to know which is the number of vacancies which is necessary to create in a starting SC in order to obtain a predetermined attenuation level. To do this the Fraction of vacancies parameter has been analysed. Figure 7.18B shows the results of the study of the fraction of vacancies. This parameter gives the optimum number of vacancies for each of the considered strategies. We can see that, for the best strategy (nosym), the value of this parameter is the lowest and it is around 43% of the total number of cylinders in the starting SC.

We have shown in this Section, by means of the use of both optimization and

CHAPTER 7. HIGH NUMBER OF VACANCIES. OPTIMIZATION

structural parameters that: (i) the creation of vacancies is a suitable method to increase the acoustic attenuation properties of the SC and (ii) the nosym strategy seems the best method to create vacancies. Moreover, general rules to create random (nosym) vacancies in a SC based on the defined structural parameters are obtained. The optimal values of A and F_v to build an optimal structure should be around 60% of the asymmetry and 40% of the vacancies. These values correspond to the best devices in terms of improved acoustic attenuation.

In the current Chapter we have also analysed the optimization of the SC in order to produce the focusing of sound. Thus, it would be interesting to analyse again the Asymmetry and the Fraction of vacancies in order to obtain general rules for the focalizing sound. Figure 7.19A shows the variation of the asymmetry parameter for each of the analysed strategies. As in the attenuation case, the value for the nosym strategy is around 0.6 and for other symmetries between 0.38 and 0.45. Figure 7.19B shows the results regarding the fraction of vacancies necessary to optimize the focusing properties of SCs. In all cases, this parameter is around 20% of the total number of cylinders in the starting SC.

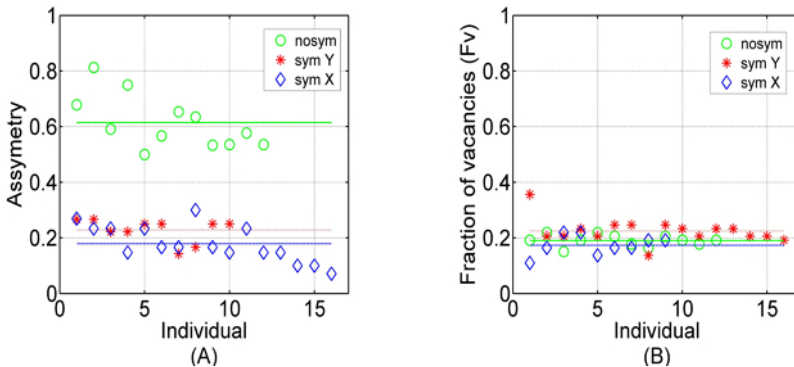


Figure 7.19: (A) Asymmetry parameter and (B) fraction of vacancies for the analysed symmetries in the case of the focusing devices. The points represent the value of the parameter for each of the optimized structures obtained and the line represents their average value.

7.5. GENERAL RULES FOR CREATING VACANCIES IN SONIC CRYSTALS

Taking into account the results obtained using both optimization and structural parameters, it can be concluded that the strategy of vacancy creation does not seem a decisive factor in the optimization process for the focusing capabilities with the cost functions used in the optimization algorithm. In the next Section, experimental results proving the general rules obtained for the improvement of the attenuation capabilities of the SC will be shown.

7.5.0.1 Experimental evidence

In this Section, we will try to confirm the applicability and the robustness of the optimization rules obtained in the previous Sections in the case of the attenuation devices. To achieve this, we have designed the following experi-

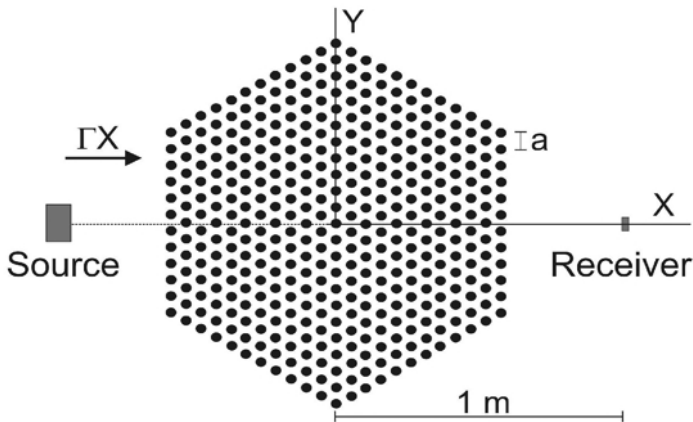
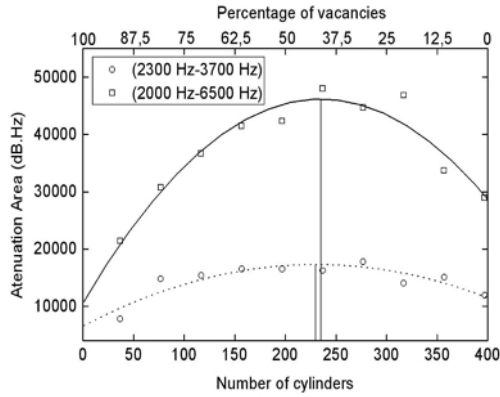


Figure 7.20: Experimental measurement set up. The starting SC consists of hollow aluminium rods 1 m long and 4 cm in diameter arranged in a triangular pattern with constant lattice $a = 6.35$ cm. There are 397 cylinders.

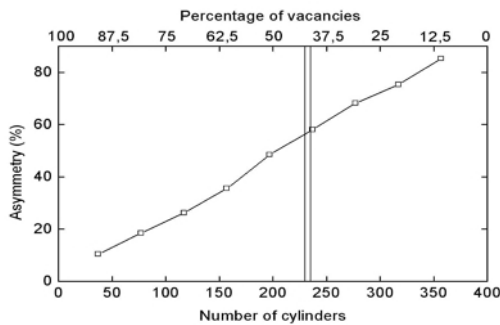
ment. In order to observe the generality of the obtained rules, a starting SC with an external shape and a number of cylinders that differ from the SC used in the theoretical development has been built. In this SC, a specific number

CHAPTER 7. HIGH NUMBER OF VACANCIES. OPTIMIZATION

of vacancies has been randomly created removing each time a predetermined number of cylinders. Then the sound attenuation spectrum (IL) in the ΓX direction (0°) was measured. We have also calculated the AA , F_v , and A parameters for each of the samples obtained. The experiments were performed in an anechoic chamber. We have especially used a SC with a honeycomb external shape, made of 397 cylinders of 4 cm diameter 1 m long of hollow aluminium and placed in a triangular array with parameter $a = 6.35$ cm (Figure 7.20). Ten samples were created by removing randomly 40 cylinders each time.



(A)



(B)

Figure 7.21: (A) Attenuation area versus number of cylinders for both analysed cases. (B) Variation of the asymmetry of the nine structures obtained as a function of the vacancies created. The vertical lines represent the optimum number of vacancies.

In Figure 7.21A, one can see the value of the AA parameter as a function of the number of cylinders and of the two ranges of frequencies analysed (2300 – 3700 Hz and 2000 – 6500 Hz). In both cases, we can see that there is a maximum of AA for a percentage of the existing vacancies of around 40% of the total cylinders of the starting SC. This value agrees with the value obtained in the optimization process.

The variation of the asymmetry A of the samples as a function of the number of vacancies is plotted in Figure 7.21B. We can see that the asymmetry is near 60% for the optimum number of vacancies corresponding to the best samples (around 40%) obtained in both analysed cases. Again, this value is in good agreement with the theoretical result obtained in the optimization study.

Experimental attenuation spectra for both the best optimized sample (larger AA) and the complete starting SC are plotted in Figure 7.22 corresponding to the range of frequencies from 2300 Hz to 3700 Hz in Figure 7.22A and from 2000 Hz to 6500 Hz in Figure 7.22B. The best sample is also shown in each inset. In both cases, the increase of the AA when compared to the starting SC can be seen in those samples with vacancies.

In short, the validity of the general rules theoretically obtained has been experimentally checked. Moreover, the devices built by means of the creation of vacancies in the starting SC, when taking into account the theoretical general rules obtained, offer the best attenuation capability - in the predetermined range of frequencies analysed; and also in a wider range.

7.6 Discussion

Motivated by the ideas of Caballero *et al.* [Caballero01] and Hakansson *et al.* [Hakansson04], SC with several distribution of vacancies in their structure have been analysed in order to study the possibility of creating acoustic devices with specific enhanced properties. Based on the numerical results obtained by means of the evMOGA in conjunction with MST, the mechanism for the creation of vacancies in a starting SC has been analysed in order to

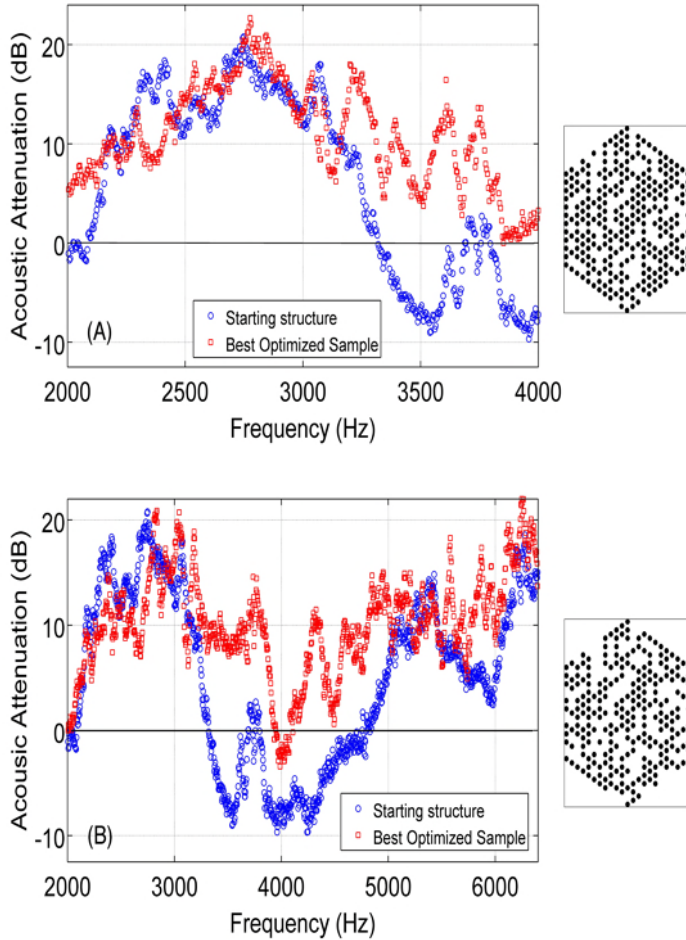


Figure 7.22: Comparison of attenuation spectra corresponding to the starting SC, and the best sample obtained by means of the creation of vacancies: (A) (2300 – 3700 Hz); (B) (2000 – 6500 Hz). The best corresponding structure obtained is shown in the inset.

develop a tool to increase the acoustic properties. The optimization of the attenuation and focusing properties of these materials has specifically been studied. Acoustic attenuation and focusing phenomena are not the same, from the optimization point of view, for the considered objective functions. Due to

the range of applicability of the wave crystal theory, the results obtained could be used as a guide to construct devices with different wave fields.

Finally, different strategies in the creation of defects (vacancies) in an initial SC have been analysed in order to determine which is optimal to achieve the objective of increasing both the acoustic attenuation and the focusing properties in a predetermined range of frequencies. The creation of vacancies has been shown as a good alternative to increase both the attenuation and the focusing properties. However, although in the case of the optimization of the focusing properties, we showed that there is no preferable symmetry of generation of vacancies, in the case of the optimization of the attenuation properties, the QOS with a distribution of vacancies without any symmetry (nosym) has doubled the attenuation capability of the initial SC. Thus, the nosym strategy has revealed a good alternative among the analysed strategies to increase the attenuation properties.

In this Chapter, general rules to build attenuation devices based on the SC in an optimal approach have been presented and the main conclusions are:

- the strategy used in the creation of vacancies seems an important factor and we have proven that the random strategy is best among the other ones considered in this work for the considered objective functions.
- the optimal number of created vacancies is around 40% of the total number of cylinders in the starting SC and the optimal asymmetry, meaning that the approach to distribute the vacancies is near 60%. Moreover, the validity of these theoretical rules has been experimentally checked and we have shown that the results obtained are independent of both the SC characteristics (external shape, number of cylinders) and the acoustic parameters to optimize (range of frequencies).

8

Improving the acoustic properties of the scatterers

Sound attenuation has become a standard topic of science and technology over the years. The traditional technique to reduce noise consists of increasing the thickness or the mass per unit area of the sonic shield materials used. However, one of the main disadvantages of this technique is the normally large size of the devices necessary to obtain suitable results. Then, the use of SC can be an alternative to the classical devices due to their capability to include some others attenuation mechanism like the Multiple Scattering or resonances. But, the use of SC as effective filters or even as acoustic barriers requires an optimization.

In this Chapter, the attention is focused on the acoustical properties of the scatterers as building blocks of the periodic systems. The properties of the scatterers themselves could be used to optimize the acoustical behaviour of the periodic systems. Scatterers can enhance the acoustical properties of a SC in addition to the BG effect due to the periodicity. In this Chapter, the improvement of the attenuation properties of the array is analysed from the properties of each scatterer.

In Chapter 7, we showed the possibility of creating attenuation bands with SC made of rigid scatterers, with a particular distribution of vacancies in air and in a predetermined range of frequencies. The GA+MST method was previ-

CHAPTER 8. IMPROVING THE ACOUSTIC PROPERTIES OF THE SCATTERERS

ously used in the design of acoustical devices based on SC [Hakansson04]. In this case, the mechanism used was the creation of vacancies in a starting complete SC built with aluminum cylinders in air. Consequently the so-called quasicrystalline structures (QOS) were obtained [Romero06, Romero09].

The angular dependence of the position and the width of the attenuation bands of a SC can still be a serious problem to design acoustic devices based on SC with air as host material. Moreover, the continuous dispersion relation allows propagating modes for frequency lower than the BG frequency range. One possibility to avoid these modes is to use scatterers with acoustical properties in such a way that SC present stop bands in addition to the BG of the structure.

Specific research was recently done to obtain attenuation bands in the low frequency range using resonators. The so-called locally resonant sonic materials [Liu00a] break the constant lattice dependence. It was shown that the attenuation bands can be obtained in several ranges of frequencies which do not depend on the periodicity of the crystal but on the resonance frequency of the resonators. Thus, it is possible to create an acoustic attenuation bands for specific and relatively low frequencies, breaking the mass law. On the other hand, some authors have investigated the effect of absorbing material covering rigid scatterers in SC, observing that in this array the IL is more uniform in frequency. Moreover, arrays with coated scatterers provide higher average attenuation than similar arrays of rigid cylinders [Umnova06].

In this Chapter, different types of scatterers developed in the last years are shown. They present several properties such as elastic or cavity resonances and sound absorption that can be used to improve the behaviour of the SC. In the following Sections, SC made of balloons are developed showing the resonance effect of the individual scatterers. The design of scatterers based on resonators that combine several effects as cavity resonances and/or elastic resonances is presented. The scatterers shown here do not destroy the BG of the array, adding their acoustic properties to those of the crystal structure. MST and FEM have been used to model both the scatterers and the SC.

8.1 Balloons as resonant scatterers in sonic crystals

Research on SC made of soft scatterers embedded in air was focused on the use of balloons containing different gases as scatterers. Kushwaha and Halevi [Kushwaha97b] theoretically studied the behaviour of three-dimensional (3D) sonic crystals made with spherical balloons containing hydrogen gas and embedded in air. In these systems, the authors analysed the band gap creation for three different 3D configurations as a function of some parameters like the filling fraction, the latex wall thickness and the pressure inside the balloons, explaining their appearance in terms of the multiple scattering theory.

In this Section, some evidence on the resonant behaviour of an array of resonators (balloons containing a blend of air and helium) embedded in air are presented. The experimental transmission results obtained suggest that there is no possibility of explaining the attenuation peaks observed as a function of Bragg's law or using the multiple scattering theory. Moreover, the resonant properties of balloons were used to design mixed structures formed with both rigid cylinders and balloons in air. The results obtained show the creation of full attenuation bands in predetermined ranges of frequencies.

The experiments was performed in an echo-free chamber (see Chapter 5). In all cases, the sound attenuation spectrum, meaning that, the IL was measured. Rigid (aluminum) cylinders or resonators were used (balloons) as scatterers arranged in two triangular configurations with lattice constants $a = 6.35$ and 12.7 cm, respectively. The aluminium cylinders used had a diameter of $d=4$ cm and a length of 1 m. The common balloons used in the experiments had a cylindrical shape, with a 1 m length and diameters of between 3.5 and 4.5 cm. The variation of the diameter is due to their commercial origin which consequently involves differences in shape and small deformations. The balloons were inflated with a standard blend of air and helium with a density of $\rho_{He}=0.9$ kg/m³ and an average of inner pressure of $p_{He} = 140.000$ Pa. Moreover, the latex wall thickness was considered negligible compared to the diameter of the balloon. In order to keep the balloons in the vertical position, we tied down a little weight at their free extreme. In particular, the measure-

CHAPTER 8. IMPROVING THE ACOUSTIC PROPERTIES OF THE SCATTERERS

ments along the two high-symmetry directions on the Brillouin zone ($\Gamma X-0^\circ$ and $\Gamma J-30^\circ$) of the sample were performed. The geometry that we used and the analyzed direction of the measurements are represented in Figure 8.2A.

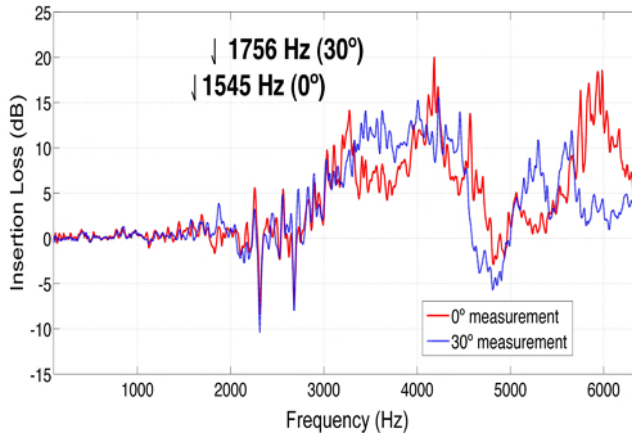
8.1.1 Results

Firstly, some measurements were taken in order to verify the acoustic behaviour of an array made only with balloons. Their acoustic response was checked by varying the filling fraction, the direction of the incident wave and the lattice constant. For this purpose, an array of balloons formed in five rows of ten elements per row and with two lattice constants $a = 12.7$ cm and $a = 6.35$ cm were measured. Throughout this process, the IL along both the ΓX and ΓJ directions was measured. In Figure 8.1A, one can see the IL for the array formed with lattice constant $a = 12.7$ cm. An attenuation peak around the same range of frequencies (from 2700 to 4700 Hz) could be seen for both incident wave directions. These peaks do not correspond to the second attenuation peaks due to the Bragg's law in the ΓX and ΓJ directions centred at $\nu_{0^\circ} = 3090$ Hz and $\nu_{30^\circ} = 3570$ Hz, respectively. Moreover, the first attenuation peaks related to the periodicity of the SC (first Bragg peaks at the ΓX and ΓJ directions centred at $\nu_{0^\circ} = 1545$ Hz and $\nu_{30^\circ} = 1756$ Hz), do not appear in the spectrum.

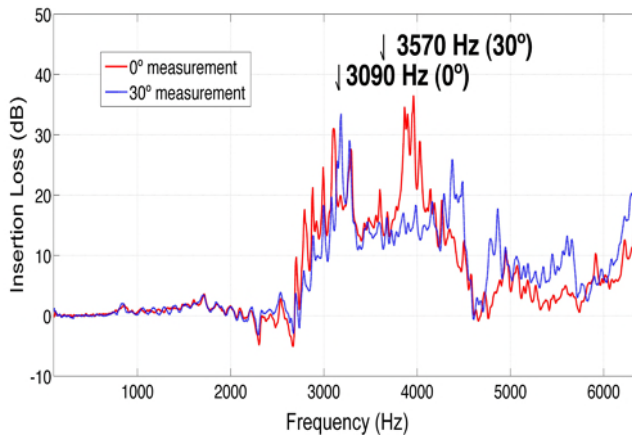
Figure 8.1B shows the results obtained for the lattice constant $a = 6.35$ cm. Again, there is no difference between the spectra in the ΓX and ΓJ directions. Finally, the difference among the level of attenuation between both spectra (figures 8.1A and 8.1B) can be explained in terms of the variation of the filling fraction of the balloons in both samples. Also, we note that the range of the attenuated frequencies is the same for both lattice constants.

Although the existence of the attenuation peaks shown cannot be explained in terms of Bragg's law, the results obtained are compatible with a resonant phenomenon due to the non-dependence of the attenuation peaks on the angle of the incident wave over the array and on the lattice constant. The resonant frequency due to the length of the balloons (1 m) would be less than 2700 Hz, and then, the most important contribution in the attenuation peak observed

8.1. BALLOONS AS RESONANT SCATTERERS IN SONIC CRYSTALS



(A)

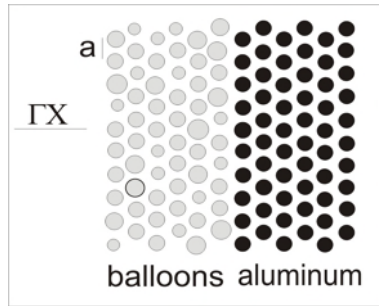


(B)

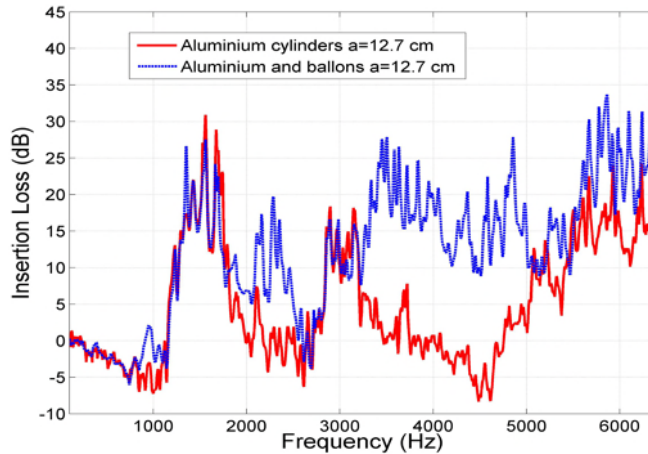
Figure 8.1: Attenuation spectra of an array formed with five rows of ten balloons in triangular lattice and for two incident directions (0° (blue line) and 30° (red line)). (A) Lattice constant $a = 12.7$ cm and (B) lattice constant $a = 6.35$ cm.

would correspond to the oscillation of the balloons in a transversal plane. Thus, experimental evidence show that arrays formed with balloons filled with gas with physical properties similar to that of the air act as arrays of resonators against the theoretical results showed in reference [Kushwaha97b].

CHAPTER 8. IMPROVING THE ACOUSTIC PROPERTIES OF THE SCATTERERS



(A)



(B)

Figure 8.2: Experimental acoustic attenuation spectra of both an array of six rows of ten aluminium cylinders and a mixed structure of 12 rows formed with the previous one plus six rows of ten cylindrical balloons. In both cases, the lattice constants are $a = 12.7$ cm, the incident direction is from left to right and the measurements were taken along the ΓX direction. (A) Schematic of the analysed mixed structure. (B) Acoustic attenuation obtained for the two structures (SC and mixed structure).

In Figure 8.2A a mixed structure formed with an array of cylinders made with six rows of ten aluminum scatterers plus six rows of balloons is shown. The lattice constant of the mixed structure is $a = 12.7$ cm. In Figure 8.2B, one can see both the attenuation spectra measured at 0° of the SC formed with rigid

8.2. SPLIT RING RESONATORS IN SONIC CRYSTALS

cylinders and the one corresponding to the mixed structure. We can see that the spectrum of the mixed structure shows the acoustic attenuation due to the SC with rigid cylinders plus the attenuation produced by the balloons due to the resonance phenomena. This fact means that the mixed structure allows an enhancement of the attenuation bands by a superposition of the resonance and multiple scattering.

In this Section we have proven that it is possible to increase the attenuation band of a SCs by including of some rows formed with resonant scatterers behind it. The sum of both effects (resonance and multiple scattering) allows the design of structures with enhanced acoustic attenuation. Moreover, one can perform high technology with these systems combining the effects of the resonators with the QOSs. This combining effects are shown in the next Chapter, in Section 9.1.

8.2 Split ring resonators in sonic crystals

The original concept of split ring resonators (SRR) was introduced by Pendry *et al.* in 1999 [Pendry99] in the context of the electromagnetism. In the last years the application of such scatterers in the design of left handed materials has been intensively analysed by several research groups.

Analogously, SRR have been used to build up periodic structures in order to manipulate and control the flow of classical waves. Authors have specifically constructed a thin convergent lens with very good focusing effect using the SRR [Hu05]. Moreover, SRR introduce ranges of frequencies related to the resonant frequency where waves cannot propagate through the system [Movchan04]. Authors have usually considered the SRR as 2D Helmholtz resonators, however this approximation needs some special geometrical approximations [mechel08]: The thickness of the walls or both the length and the aperture of the neck of the resonator must follow some approximation to consider the resonator as a Helmholtz resonator. Otherwise, one should solve the scattering problem of the resonator in order to know the resonant frequency of the SRR. Thus, once the resonant frequency of the SRR is known,

CHAPTER 8. IMPROVING THE ACOUSTIC PROPERTIES OF THE SCATTERERS

several applications can be done. For example, SRR could be used to create attenuation bands in the range of frequencies below the BG.

In this Section, a design of SRR is proposed solving the scattering problem and comparing the theoretical results obtained with the experimental results. The resonant frequency is designed to appear in the range of frequencies below the BG produced by the periodic distribution of scatterers. After that, the eigenvalue (band structures) and the scattering (attenuation spectrum) problems of a SC made of SRR will be analysed. The eigenvalue problem gives information about the ranges of attenuated frequencies and their dependence on the angle of incidence. The scattering problem shows that the effect of the resonances is proportional to the number of resonators. Both the eigenvalue and the scattering problem have been solved using COMSOL 3.5a (FEM).

The theoretical data were tested using experimental measurements in both the isolated SRR and the SC made of SRR cases. The results were obtained in the anechoic chamber described in Chapter 5. SRR have been constructed from split ring tubes of PVC (rigid) cylinders.

The objective is to design SRR and to construct SC that present an attenuation band in the range of selected frequencies, eliminating some reinforcements of the SC. This design will be used in Chapter 9 in order to design an acoustic barrier based on the SC with SRR and absorbent materials.

8.2.1 Design of single resonators

The expressions to determine the resonant frequency of SRR shown in the literature are based on the Equation of the resonances produced in a Helmholtz resonator [Movchan04, Hu05]. This approximation is only valid for certain geometries of the SRR where the resonator should present an aperture low enough to consider the cavity as a Helmholtz resonator [Movchan04]. Then, determining the exact values of such parameters could be complicated and highly dependent on the geometry of the cavity.

The procedure followed in this Section to obtain the geometry of the SRR is the next: first, the scattering problem of several SRR with different wall

8.2. SPLIT RING RESONATORS IN SONIC CRYSTALS

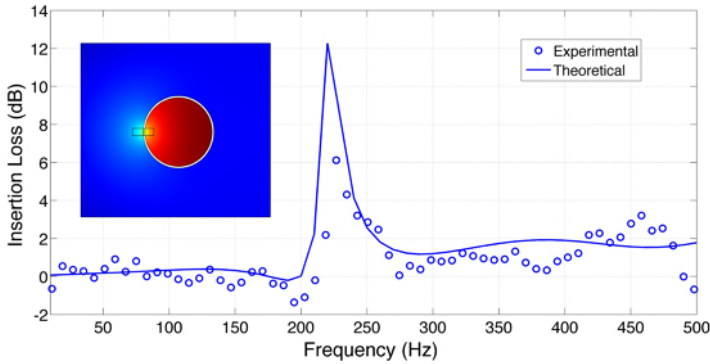


Figure 8.3: Resonance of a single SRR obtained using FEM. The blue line (Blue open circles) represents the numerical (experimental) IL of the single SRR shown on the inset. The inset represents the localized pressure field in the cavity for the resonant frequency.

thickness and apertures is studied and second the most suitable SRR for our purpose is selected. In this Section, a SRR with the resonant frequency in the range of frequencies below the BG of a SC with periodicity $a = 0.33$ m, meaning $v_{Bragg} < 515$ Hz, is presented. For this purpose, a SRR of PVC with the next values has been designed: external radius $r = 0.1$ m, inner radius $r = 0.095$ m and aperture width $L = 0.02$ m.

A wave impinging the SRR from the left is considered and the SRR presents its aperture in this side. In the inset of Figure 8.3, one can observe this orientation of the SRR. Then the IL produced by the SRR can be numerically obtained using FEM. Figure 8.3 shows the IL produced with the designed SRR, presenting a clear resonance peak around 220 Hz. The open blue circles represent the experimental measurements of the IL in the anechoic chamber. One can observe a good agreement between both theoretical and experimental results. The localization of the pressure inside the cavity for this resonance frequency, can be observed in the inset of Figure 8.3.

We note that, if the usual formula of the 2D Helmholtz resonator¹ is used for

¹ $v_{Helmholtz} = \frac{c}{2\pi} \sqrt{\frac{A}{LS}}$, where A is the aperture, L is the wall thickness and S is the surface

CHAPTER 8. IMPROVING THE ACOUSTIC PROPERTIES OF THE SCATTERERS

the SRR presented in this Section, the first resonant mode could be obtained at a frequency of 610 Hz, which is far away from the obtained by the analysis of the scattering problem. This shows that the considered SRR does not behave as a 2D Helmholtz resonator. The resonant mode of the SRR designed, presents the first resonant peak at 210 Hz and its position is independent of the BG position corresponding to the periodic structure. In the analysis we use a periodic structure made of rigid scatterers placed in a square lattice of $a = 0.33$ m. We note that the resonance is below the BG of the structure (515 Hz). In the next Section, the effect of such resonators in the Band Structure and in the Scattering problem of a periodic array of SRR is presented.

8.2.2 Eigenvalue problem: band structures of SC made of SRR

Following the procedure based on FEM explained in Chapter 3, the band structures of a square array of the SRR have been calculated using COMSOL 3.5.a. As we mentioned in the previous Section the objective of using the SRR is to improve the attenuation behaviour of a complete SC made of rigid cylinders in the range of frequencies below the BG. To compare the SC made of rigid cylinders with the one made of SRR, the corresponding band structures for the rigid scatterers have also been presented in this Section. The rigid cylinders present the same radius as the SRR (external radius).

The red continuous lines in Figure 8.4 represent the band structures for the SRR, whereas the black lines represent the band structures of the rigid scatterers. One can observe in this Figure, in the case of rigid cylinders, that there is not a full BG, but a pseudogap appears in the ΓX direction. This design was chosen as it will be used in the Chapter 9 for the design of an acoustic barrier based on SC. For the purpose of this Section, it is not necessary for the structure to present a full BG. The interest here is to observe the effect of the SRR in the propagation properties.

If we focus the attention on the band structures of the SRR (red continuous
of the cavity

8.2. SPLIT RING RESONATORS IN SONIC CRYSTALS

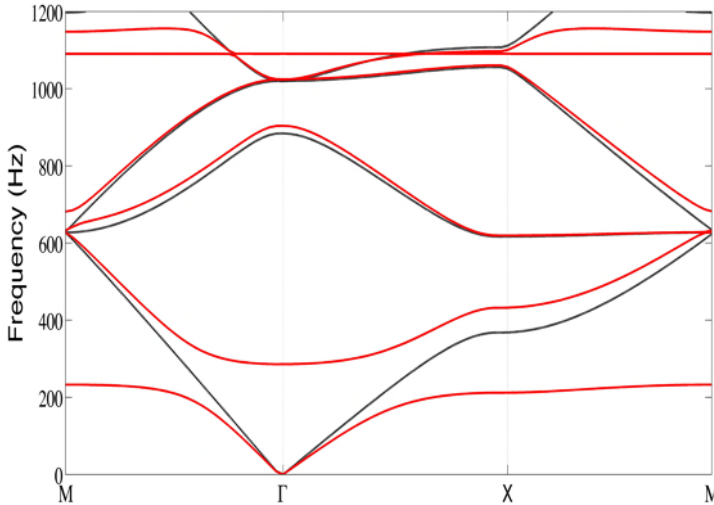


Figure 8.4: Band structures of a square lattice of both SRR and Rigid Scatterers. The red lines represent the band structures for the SC made of SRR, whereas the black lines represent the band structures for the same lattice made of rigid scatterers.

line), we can observe a full attenuation band in the region of the resonance of the SRR, meaning an attenuation band independent of the incident direction of the wave. This attenuation band does not exist in the case of the band structures of the SC made of rigid cylinders (black line), in this case there is a transmission band. Thus, an additional stop band appears due to the resonance of the single elements configuring the SC. The SRR as scatterers in a periodic array, introduce an easy control of the position in the frequencies of the new attenuation peak: changing the geometry of the SRR one can move it in the range of the frequencies below the BG.

8.2.3 Scattering problem of finite SC made of SRR

The analysis of the band structures allows us to know both the propagating and the attenuating ranges of frequencies of the periodic structure, but they do

CHAPTER 8. IMPROVING THE ACOUSTIC PROPERTIES OF THE SCATTERERS

not provide any information about the height of the attenuation peaks nor the dependence of the attenuation level with the number of scatterers. To do this, one needs to analyse the scattering problem of finite structures. The scattering problem was numerically solved using FEM, considering a cylindrical source placed at the origin of the coordinates. The size of the finite structure is $4a \times 4a$ and with $a = 0.33$ m. The SC is placed 1.5 m away from the source and the IL was calculated at a point located 3 m from the origin of coordinates in the x -direction.

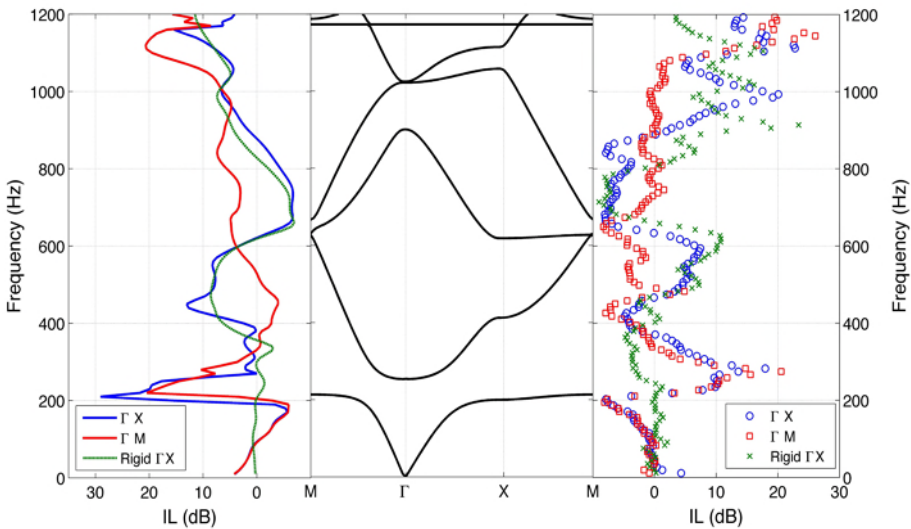


Figure 8.5: IL of a finite SC made of SRR of size $4a \times 4a$ with $a = 0.33$ m. Left panel: Blue line (Red line) represents the numerical predicted IL in the ΓX (ΓM) direction. Green dashed line represents the IL for the array of rigid cylinders in the ΓX direction. Central panel: Band structures of the SC made of SRR. Right panel: Red open circles (Blue open squares) represents the experimental measurements of the IL in the ΓX (ΓM) direction. Green crosses represent the experimental measurements of the IL for the rigid cylinders in the ΓX direction

Figure 8.5 shows the results of the sound scattering in terms of the IL of a finite square periodic structure made of both rigid and SRR scatterers. The Figure is divided in three parts. The left panel shows the IL obtained using

8.2. SPLIT RING RESONATORS IN SONIC CRYSTALS

FEM of both structures: The blue line (Red line) represents the numerically predicted IL in the ΓX (ΓM) direction and the green dashed line represents the IL for the array of rigid cylinders in the ΓX direction. The central panel shows the band structures of the SC made of SRR. Finally, the right panel shows in red open circles (Blue open squares) the experimental measurements of the IL for a SC made of SRR in the ΓX (ΓM) direction. The green crosses represent the experimental measurements of the IL for the rigid cylinders in the ΓX direction.

First of all, one can observe the good agreement between the band structures and the calculated IL. The scattering problem reproduces both the first pseudogap at ΓX direction and the resonance of the SRR. We notice in the band structures that at ΓM there is no pseudogap. One can observe that the resonance is independent of the incidence direction: both red (45°) and blue (0°) lines show the same peak at low frequencies in accordance with the band structures. However, the dependence of the Bragg scattering on the incidence direction is also shown in the scattering problem: the pseudogap only appears in the ΓX direction. The right panel in Figure 8.5 shows the experimental measurements. One can observe the good agreement with both the scattering and the eigenvalue problem numerically solved. In the experimental results, one can observe that both blue open circles (0°) and red open squares (45°) show the attenuation peak due to the resonance at the same frequency range, thus the non dependence on the incidence direction is also experimentally shown in good agreement with the numerical simulations. On the other hand the experimental results also show the properties of the Bragg scattering.

One can also compare both the numerical and the experimental results of the SC made of SRR with the ones of the SC made of rigid cylinders. In Figure 8.5, one can see that the structure made of SRR preserves the attenuation peak related to the periodicity of the array (515 Hz). In ΓX direction both structures present the pseudogap (see the blue and green lines, or open blue circles and green crosses). Moreover, the SC made of SRR improve the attenuation properties of the same structure made of rigid cylinders due to the additional attenuation peak in the low frequency range.

As we have previously seen, the attenuation band related to the resonances of

CHAPTER 8. IMPROVING THE ACOUSTIC PROPERTIES OF THE SCATTERERS

the SRR is independent of the incident direction, but in addition the depth of this sound attenuation bands (in dB) should proportionally increase with the number of consecutive scatterers passing through the incoming acoustic wave. In this Section, a numerical analysis of the dependence on the resonance depth with the number of resonators is also given.

8.2.3.1 Dependence on the number of rows and on the incidence direction

A numerical study using COMSOL of the propagation properties in a finite SC made of SRR is shown in this Section. It would be interesting to analyse the dependence of both the resonant and Bragg scattering effect on the number of scatterers in the finite structure. Obviously, both effects depend on the number of scatterers, the Bragg scattering following the evanescent behaviour of modes inside the structure and the resonant effect increasing the number of building blocks of the crystal.

In order to observe these properties, the attenuation spectra for several structures with different number of rows and different angles of incidence have been calculated. The spectra for four finite structures with 1, 2, 3 and 4 rows, and for the two main directions of symmetry, 0° and 45° have been specifically studied. As in the previous Section, the sound source is placed at the origin of coordinates and the IL for all the analysed cases was measured at a point situated 3 m away from the source behind the SC.

The results are shown in Figure 8.6. The Figure is divided into three parts. The upper panel shows the IL for the four structures purposed in the ΓX (0°) direction and the lower panel shows the IL in the ΓM (45°) direction. Blue, green, cyan and red lines represent the IL for finite SC made of SRR in one, two, three and four rows respectively. In the central panel the band structures are again shown to make the comparative easy between the eigenvalue and the scattering problems.

First, one can observe in all cases that the IL in the range of frequencies produced by the resonances of the SRR, increases the attenuation level with

8.2. SPLIT RING RESONATORS IN SONIC CRYSTALS

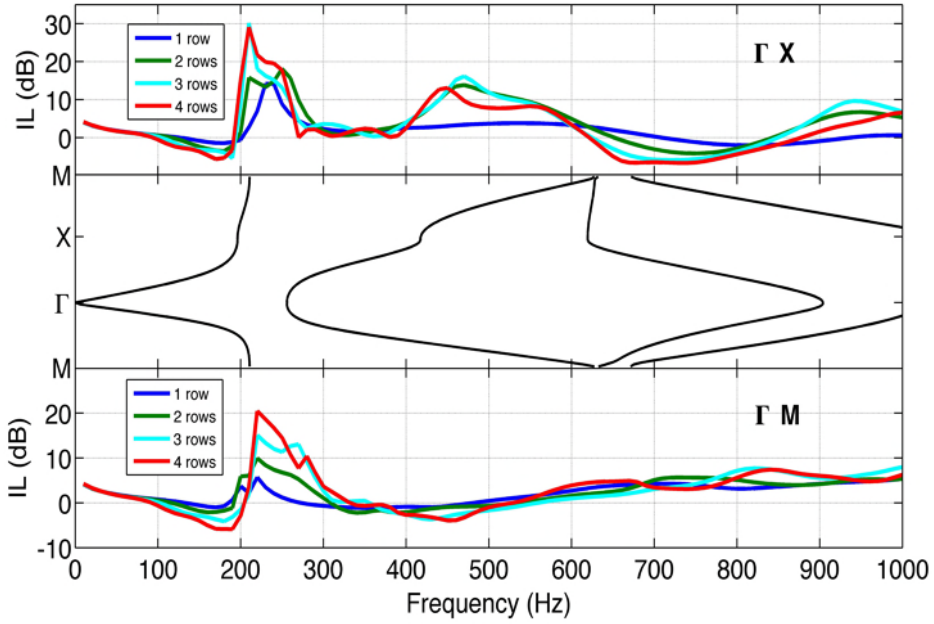


Figure 8.6: Dependence of the resonance on the number of resonators and on the angle of incidence. Upper panel: IL of structures made from 1 to 4 rows of SRR. The angle of incidence is 0° (ΓX) direction. Central panel: Band structures of a periodic square array of SRR with $a = 0.33$ m. Lower panel: IL of structures made from 1 to 4 rows of SRR. The angle of incidence is 45° (ΓM) direction.

the number of resonators. Moreover, comparing the results of both the upper and the lower panels, one can observe that the attenuation peak produced by the resonance appears at the same frequency range independently of the angle of incidence of the wave. One can also observe the dependence of the Bragg scattering on the number of scatterers in the structure.

The SC consisting of SRR yield strong attenuation bands at selected frequencies, with a far superior performance with respect to the usual SC (based on Bragg's scattering only). With regard to application and exploitation, they can be used to predict the structural parameters needed to fabricate custom-tailored SC.

8.3 Elastic U-profile scatterers

In this Section, we investigate the propagation of acoustic waves in SC formed of elastic scatterers whose geometrical shape presents a cavity. Due to the shape of the scatterers, they can be referred as U-profiles. These scatterers add new attenuation bands in a regime of frequencies below the BG ($ka < \pi$) due to both the elastic properties of the material and the cavity resonances. The material the scatterers are made of is a low density polyethylene closed-cell foam (LDPE)² whose conventional applications can be found in the packaging industry and shock absorbing and vibration damping techniques. In this Section, a phenomenological analysis of a SC made of these kind of scatterers is presented and the numerical results based on FEM show good agreement between the measured IL obtained for both the single scatterer and the periodic array of scatterers made of LDPE foam. Experimental results of the sound propagation in a periodic array of triangular unit cell with lattice constant $a = 12.7$ cm shows the potential improvement introduced in the SC by these kind of scatterers.

As we have seen, SC can be analysed by several numerical methods, including the plane wave expansion, MST, variational methods and the FDTD. However, since the acoustic wavelength of the attenuation band in the subwavelength regime is much longer than the lattice constant of periodic system, one can define a Locally Resonant Acoustic Metamaterial (LRAM) whose effective properties can provide an accurate and simple description of the wave interaction with the associated LRAM. This methodology is applied to analyse the acoustic behaviour of SC made of LDPE foam scatterers.

8.3.1 Motivating results

In this Section, the interest is focused on the behaviour of the SC made of U-profiles, in the subwavelength regime, meaning that $ka \ll \pi$, where a is

²Low Density Polyethylene foam properties are reported in reference [mills07]: density, $\rho = 100 \text{ kg/m}^3$, Young's modulus, $E = 0.35 \text{ GPa}$ and Poisson's ratio, $\nu = 0.4$.

8.3. ELASTIC U-PROFILE SCATTERERS

the periodicity of the array and k is the wavenumber. Hereinafter, this range of frequencies will be called low frequency range.

Figure 8.7A shows the acoustic response of a commercial scatterer made of the recycled material: LDPE closed-cell foam (see inset). The red dashed line in the upper graph illustrates the IL of a U-profile. One can see the existence of two attenuation peaks appearing in the low frequency range, around 700 Hz and 1000 Hz. These peaks will be called first and second attenuation peaks, respectively. The nature of both can be understood by analysing the eigenvalue and scattering problems for the basic geometrical shapes such as rectangular elastic beam and rectangular cavity, as it will be seen later.

On the other hand, this resonant behaviour could be used to improve the acoustic behaviour of the SC introducing attenuation peaks in the range of low frequencies, independent of the incidence direction of the wave as in the case seen in the previous Section. The attenuation bands shown in Figure 8.7 are obtained with SC made of U-profiles placed in triangular array with lattice constant $a = 12.7\text{cm}$. For this lattice constant it is possible to consider that the upper bound of the low frequency range corresponds to the first Bragg's frequency of that SC with value 1545 Hz.

8.3.2 Phenomenological analysis

The nature of both attenuation peaks can be understood by analysing the acoustical properties of basic geometrical shapes like rectangular elastic beams and rectangular resonance cavities. In the next two subsections the resonances of both the elastic beam (elastic resonances) and the rectangular cavity (cavity resonance) are analysed.

8.3.2.1 Elastic resonances

Consider a 2D elastic beam (EB) made of LDPE foam with L length and t width (see the schematic view in Figure 8.8A); the density of material ρ . Considering that the EB has a free end and the other end is fixed, the vibra-

CHAPTER 8. IMPROVING THE ACOUSTIC PROPERTIES OF THE SCATTERERS

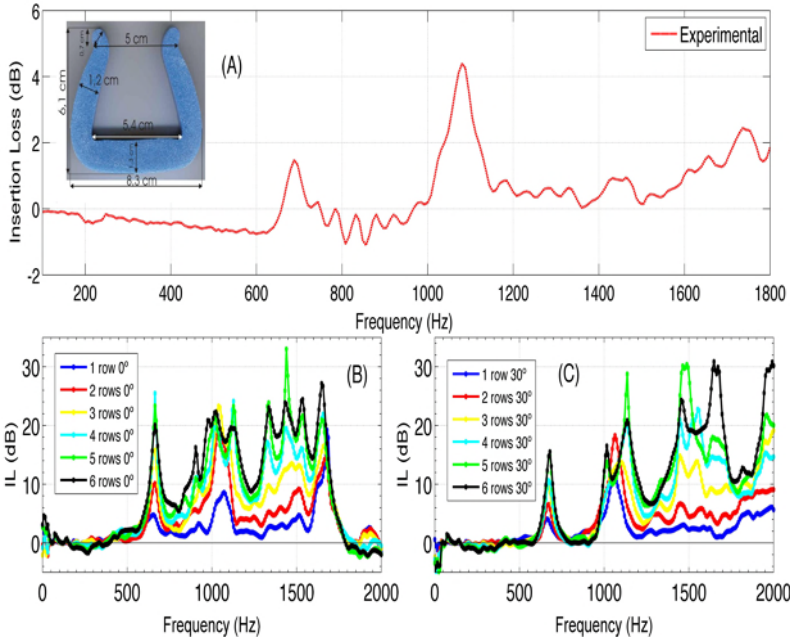


Figure 8.7: Experimental data. (A) IL of one U-profile. (B) and (C) show the IL of a SC made of different numbers of U-profiles in a triangular array, $a = 12.7$ cm, measured at 0° and 30° respectively. The inset shows the transversal view of a U-profile.

tion modes can be analysed by means of the following Equation [voltera65, gere97],

$$EI \frac{\partial^4 v(x, t)}{\partial x^4} = -\lambda_m \frac{\partial^2 v(x, t)}{\partial t^2} \quad (8.1)$$

where $\lambda_m = \rho L t$ is the linear mass density of the EB, E is Young's modulus and I is the second moment of inertia. The EI product is known as flexural rigidity. Appendix D shows a brief explanation of the Equations used in this section.

The eigenfrequencies of the EB can be obtained from the following Equation,

$$\cos(k_n L) \cosh(k_n L) + 1 = 0; \quad (8.2)$$

8.3. ELASTIC U-PROFILE SCATTERERS

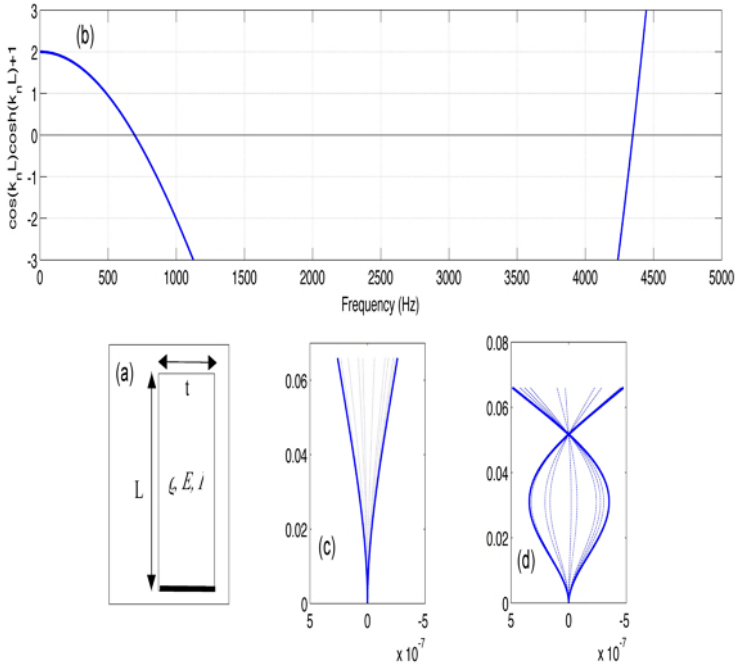


Figure 8.8: Eigenfrequencies of an elastic bar of LDPF, density $\rho = 100 \text{ kg/m}^3$, Young's modulus $E = 0.35 \text{ GPa}$ and Poisson's ratio $\nu = 0.4$. (A) Schematic view of the EB. (B) Graphical solution for Equation 8.2. The first four resonances of an elastic bar can be obtained from the plot. (C) Displacement of first vibrational mode and (D) Displacements of second mode. In (C) and (D) The continuous line represents the maximum displacement and the dotted line represents intermediate displacements.

where $k_n = \sqrt[4]{\omega_n^2 \rho L t / E I}$, ω_n is the angular frequency of the mode n , related to the frequency as $\omega_n = 2\pi\nu_n$.

The graphical solution of Equation 8.2 is shown in Figure 8.8B. We can observe that the first and second modes appear at $k_1 = 28.41 \text{ m}^{-1}$ and $k_2 = 71.12 \text{ m}^{-1}$. Using Taylor's series, it is possible to approximate the first mode as

$$k_1 \simeq \frac{\sqrt[4]{12}}{L}. \quad (8.3)$$

This first low-frequency solution is particularly interesting for this work.

CHAPTER 8. IMPROVING THE ACOUSTIC PROPERTIES OF THE SCATTERERS

From the values of k_n and considering that the material of the EB is LDPE, the resonance frequencies of the first and second mode are $\nu_1 = 693.8$ Hz and $\nu_2 = 4348$ Hz respectively. Displacements of the elastic beams for each resonance frequency can be calculated using the Equations briefly presented in Appendix D. These displacements for the first and second resonances are shown in Figures 8.8C and 8.8D for different times in order to reproduce the complete movement of the EB. The maximum displacements in each direction are plotted with a continuous line whereas the dashed lines represent the displacements in several intermediate instants.

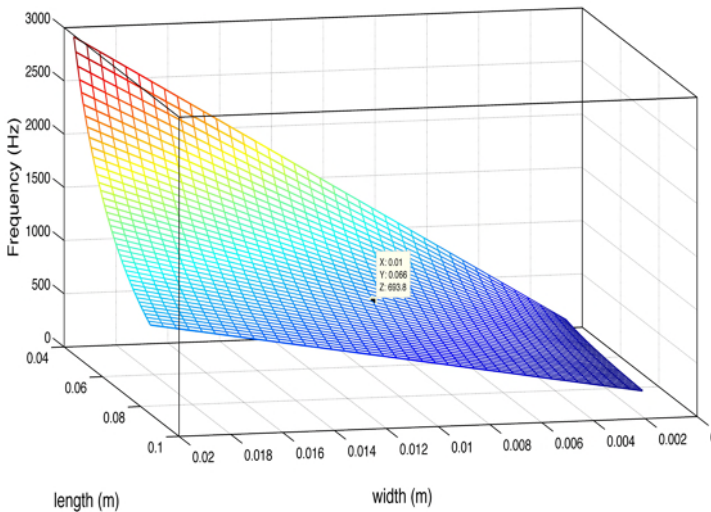


Figure 8.9: Dependence of the first eigenfrequency on both the length and the width of the EB made of LDPE.

The resonances of a EB made of a fixed material can be tuned by varying its geometrical parameters. Figure 8.9 shows the dependence of eigenfrequency of the first mode on both the length and the width of the EB made of LDPE foam. The black point marks the position of the first resonant frequency for the geometrical properties of the EB analysed in this Section ($t = 0.01$ m and $L = 0.066$ m). One can observe that the bigger the length, the lower the frequency of the first mode, and that the bigger the width, the higher the frequency of the first mode. The intersection point of the black lines corresponds

to the eigenfrequency for the EB with the geometrical parameters considered in this work.

8.3.2.2 Cavity resonances

Another interesting property of the U-profiles is that they present, in addition to the elastic properties of the material, a cavity where sound could be localized due to resonances. Several works in the literature have analysed the effect of cavity resonators in periodic structures. In addition to the BG of the periodicity, the systems made of resonators show low frequency attenuation bands produced by the resonances of Helmholtz or split-ring resonators. Due to both the control of the resonances of the EB and the resonance of the cavity, periodic structures made of U-profiles elastic scatterers can be easily tunable in the range of low frequencies.

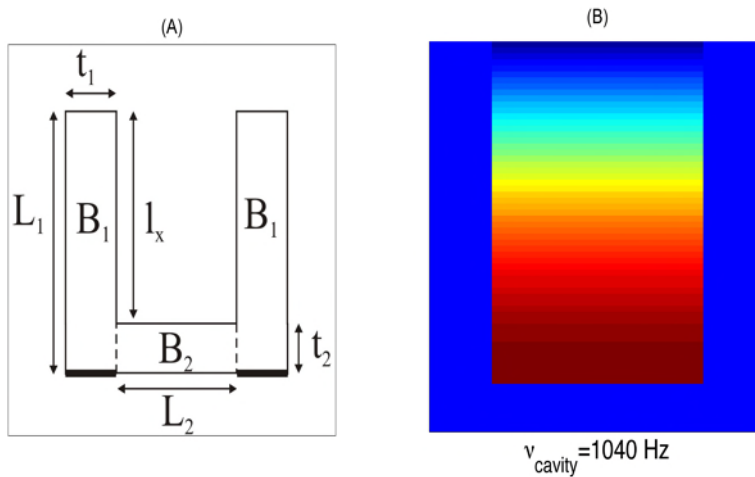


Figure 8.10: U-profile elastic scatterers. calculated using FEM. (A) Geometrical shape and parameters characterizing the size of the U-profile. (B) Acoustic field inside the cavity for the resonant frequency.

The eigenfrequencies of a rectangular cavity with several boundary conditions

CHAPTER 8. IMPROVING THE ACOUSTIC PROPERTIES OF THE SCATTERERS

has been widely analysed in the literature. As one can see in Figure 8.10A, the cavity of the U-profile has a length and a width equal to $l_x = 0.066$ m and $L_2 = 0.04$ m respectively. To solve the problem, one can consider that the walls of the U-profile are perfectly rigid. Thus, Neumann boundary conditions should be considered at the boundaries, and Dirichlet conditions in the boundary in the open side of the U-profile. The solution of the analytical problem results in an eigenfrequency problem whose fundamental mode has a eigenfrequency equal to $\nu_r = c_{air}/(4l_x)$. However, we have shown that the air immediately outside the end of the cavity takes part in the acoustic oscillation. This air makes the cavity appear to be acoustically somewhat longer than its physical length. This effective length gives rise to a displacement of the resonance frequencies, for this reason it is called in the literature, the end correction of the cavity. In order to compute the correct resonance frequency, this effective length and the corresponding frequency correction have to be considered. A more rigorous analysis of the cavity would be required to find the exact resonance frequencies, but it has been assumed that the end correction of the cavity of the U-profile is similar to the corresponding one of a closed cylinder adapted to the 2D case.

$$\nu_r = \frac{c_{air}}{4(l_x + 0.4L_2)}. \quad (8.4)$$

Then, in the case of the cavity considered in this work, the frequency of the first mode is $\nu_r = 1040$ Hz. In Figure 8.10B, one can observe the acoustic field inside the cavity for this resonance frequency.

8.3.3 Acoustic-structure interaction

8.3.3.1 FEM model

We start this Section by analysing the propagation of acoustic waves inside periodic structures made of solid scatterers, B , embedded in a fluid host, A using FEM. Due to the physical properties of the host material, the eigenmodes of the whole system are pure longitudinal waves, while transverse modes can-

8.3. ELASTIC U-PROFILE SCATTERERS

not propagate. Then, the governing Equation in A is

$$-\frac{\omega^2}{c_A^2}p = \nabla \cdot \left(\frac{1}{\rho_A} \nabla p \right) \quad (8.5)$$

where p is the pressure, ρ_A is the density and c_A is the sound velocity in the host material.

The propagation of elastic waves inside the scatterers, locally isotropic medium, is governed by

$$-\rho_B \omega^2 u_i = \left\{ \frac{\partial \sigma_{ij}}{\partial x_j} \right\}, \quad (8.6)$$

where ρ_B is the density of the elastic material and u_i is the i th component of the displacement vector. The stress tensor is defined by

$$\begin{aligned} \sigma_{ij} &= \lambda_B u_{ll} \delta_{ij} + \mu_B u_{ij} \\ u_{ij} &= \frac{1}{2} \left\{ \frac{\partial u_i}{\partial x_j} + \frac{\partial u_j}{\partial x_i} \right\}, \end{aligned} \quad (8.7)$$

where λ_B and μ_B are the Lamé coefficients.

In this problem the acoustic wave is incident on the scatterer and then the pressure acts as a load on the elastic medium. On the other hand, the elastic waves in the scatterer act as an additional acceleration on the acoustic field. In order to simultaneously solve 8.6 and 8.7 we introduce the following boundary conditions,

$$\begin{aligned} \frac{\partial p}{\partial n} \Big|_{\partial B} &= \rho_A \omega^2 \vec{u} \vec{n} \\ \sigma_{ij} n_j \Big|_{\partial B} &= -p n_i. \end{aligned} \quad (8.8)$$

where ∂B is the boundary of the medium B and \vec{n} is the outward-pointing unit normal vector seen from inside the scatterer medium.

To solve the stated problem COMSOL MULTIPHYSICS has been used, as well as a finite-element analysis and solving software package. FEM is a good

CHAPTER 8. IMPROVING THE ACOUSTIC PROPERTIES OF THE SCATTERERS

technique when the geometries are complicated and several physical problems are coupled. In the numerical problem, the domain in which the solution is obtained was surrounded by a PML region in order to emulate the Sommerfeld radiation condition in the numerical solution (see Chapter 3). As an example, Figure 8.11 shows the specific pressure field distribution obtained for 1660 Hz. One can observe the absorption of the waves, produced by the transformation to the complex plane in the PML region, eliminating all the possible reflections in the boundaries and emulating a Sommerfeld condition.

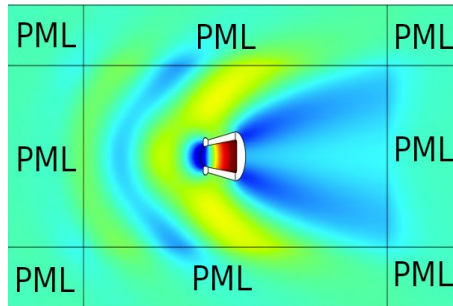


Figure 8.11: Pressure field distribution produced by the scattering of a plane wave of 1660 Hz by an U-profile. The PML regions are marked with the PML.

8.3.4 Numerical results

8.3.4.1 Scattering problem

Single scatterer

First of all, the frequency response of the U-profile is analysed. The geometry of the U-profiles was implemented using the CAD tools of COMSOL. In the inset of Figure 8.12, one can see the considered model of the scatterer, this geometry slightly differs from the real one. In the numerical model, a plane wave impinging the scatterer from the left side has been considered and the IL at a point behind the scatterer is calculated.

Figure 8.12 shows the numerical results obtained using COMSOL. One can

8.3. ELASTIC U-PROFILE SCATTERERS

observe similar frequency response to the one experimentally observed in Figure 8.7. Two attenuation peaks numerically calculated appear near 700 Hz and 1200 Hz. A sensibility analysis varying the geometry of the U-profile was done, and one can observed that the first peak is very sensitive to changes in geometry. However the second one does not substantially change with the variations of the geometry of the U-profile. These changes are in good agreement with the predictions of the resonances of a rectangular elastic beam profile with a resonant cavity.

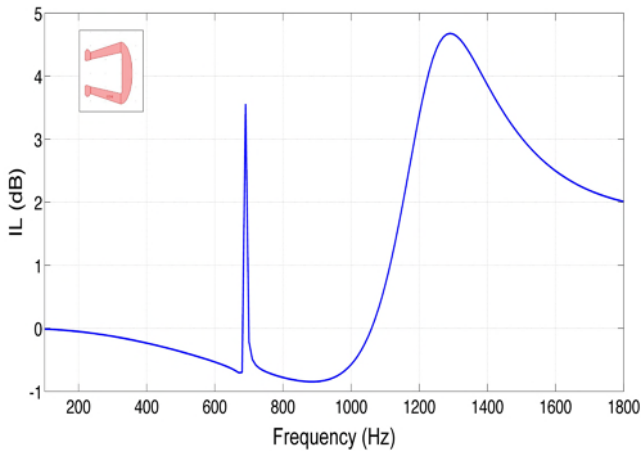


Figure 8.12: Numerical results of single scatterer. IL produced by a U-profile. The inset shows a image of the numerically modelled U-profile.

As we have previously explained, the first peak corresponds to the resonances of the EB of the U-profile, therefore small changes in the geometry can produce high changes in the resonant frequencies (see Figure 8.9). This provides a powerful design tool in the first of the low frequency attenuation peaks.

On the other hand, if we compare Figures 8.7 and 8.12 we can observe again a difference between the numerical and experimental frequencies of the second peak. As we previously mentioned in the analysis of the cavity resonances, the air immediately outside the end of the cavity takes part in the acoustic oscillation and the effective length of the cavity increases, therefore an end correction is needed to obtain the resonances of the cavity. However one cannot consider this end correction from the numerical problem, because changes

CHAPTER 8. IMPROVING THE ACOUSTIC PROPERTIES OF THE SCATTERERS

in the length of the EB would produce a change in the resonance. Therefore the numerical model is only used here to obtain the tendencies of the system.

Periodic array

Once the numerical results of the acoustical behaviour of an isolated U-profile have been analysed, the next step is to analyse a periodic distribution of this elastic scatterers following a triangular lattice with lattice constant $a = 0.127$ m. Here, a plane wave impinging from the left side is considered and the numerical domain is again surrounded by a PML region. Thus the numerical solution accomplishes an approximated Sommerfeld condition. Figure 8.13, shows an schematic view of the numerical problem.

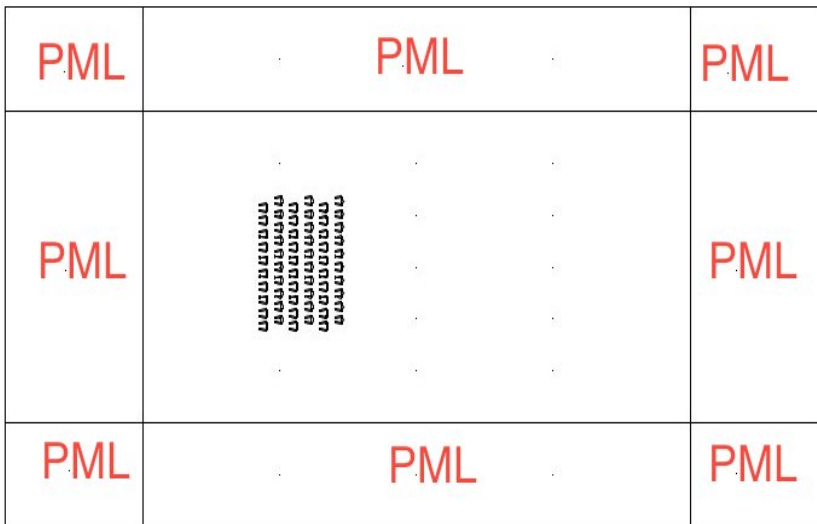


Figure 8.13: Schematic view of the numerical model to analyse the scattering problem of an array of U-profiles scatterers.

The blue continuous line in Figure 8.14A shows the numerically predicted IL of a finite structure made of 6 rows of 10 U-profiles for an incident wave in the direction of 0° . By comparing the results of the scattering of an isolated U-profiles (see Figure 8.7), one can observe that the resonances of the elastic beams, as well as the cavity resonance, have been increased due to the increase

8.3. ELASTIC U-PROFILE SCATTERERS

in the number of resonators. Moreover, an attenuation peak around 1600 Hz appears and it can be related to the periodicity of the array, as we will show in the next Section.

In the Figure 8.14B, the measured IL for the same array as the numerically calculated is also plotted. One can observe a clear correspondence between the attenuation peaks numerically predicted with those experimentally obtained. However, the experimental attenuation peak related to the elastic resonances presents a higher attenuation level than the one numerically predicted. A possible explanation for this effect could be the existence of some absorption effect of the material that it is not considered in the model.

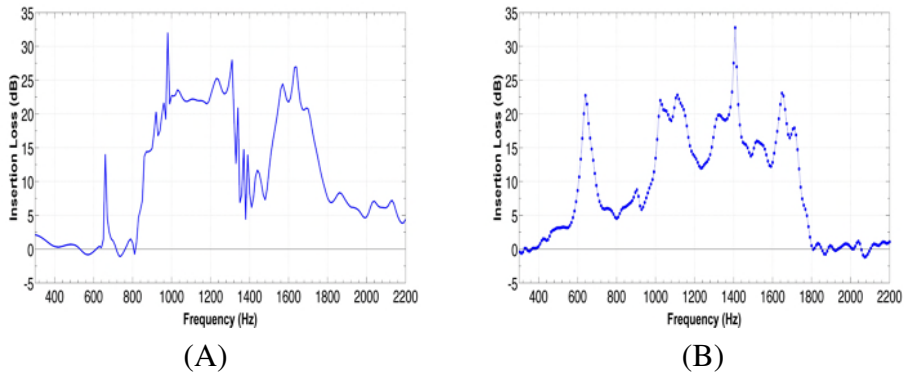


Figure 8.14: (A) Numerically predicted IL of an array of U-profile scatterers. (B) Measured IL of an array of U-profile scatterers. A plane wave impinges the structure from the left side to the right side.

Then, the resonance effect of the scatterers is not destroyed by the multiple scattering inside the structure, therefore one can combine resonances with multiple scattering in order to obtain several attenuation peaks. As we explained in the beginning of this Section, an interesting feature of these scatterers is that they show two resonances in the range of frequencies below the first BG of the periodic structure.

CHAPTER 8. IMPROVING THE ACOUSTIC PROPERTIES OF THE SCATTERERS

8.3.4.2 Eigenvalue problem

We analyse the propagating properties of a periodic arrangement of U-profiles by means of the application of the Bloch periodic boundary conditions in a unit cell. This methodology was described in Chapter 3. Figure 8.15 shows the Band structures of a periodic arrangement of U-profiles arranged in triangular lattice of $a = 12.7$ cm. The black line represents the band structures considering the perfectly rigid U-profiles, this means that we can consider Neumann boundary conditions in the wall of the scatterer. One can observe that this arrangement presents the pseudogaps related to the periodicity as well as the stop band due to the resonance of the cavity.

If the elastic properties of the U-profiles are considered, then the band structures are represented by the blue continuous line. One can observe the BG due to the periodicity (1600 Hz), the stop band of the resonance of the cavity (1100 Hz) and the resonance of the elastic beams of the U-profile (700 Hz). In the representation the non propagating ranges of frequencies is presented by the black surfaces.

In order to compare the numerical results with those experimentally obtained a new plot was added in the right panel, where the IL of a triangular periodic distribution of U-profiles was measured in the main symmetry directions: 0° (blue line) and 30° (red line). One can observe the low dependence on the direction of incidence of the resonance due to the vibration of the elastic beams and the resonance of the cavity, but the directionality appears in the frequencies of the BG due to the periodicity.

8.3.5 Experimental results

The acoustic attenuation capabilities of the single LDPE foam scatterers as well as of the periodic structures of these scatterers have been measured in terms of IL. The sample is excited by white noise.

8.3. ELASTIC U-PROFILE SCATTERERS

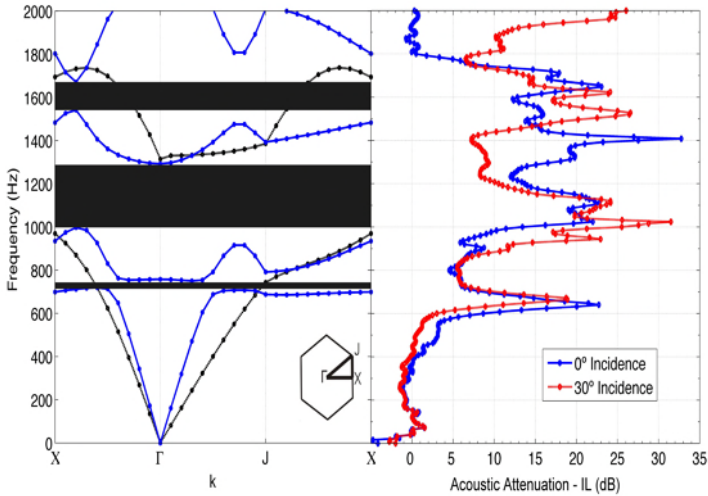


Figure 8.15: Band Structures for a periodic arrangement of U-profiles in triangular lattice of $a = 12.7$ cm. Left panel: Black dashed line represents the band structures for a rigid U-profiles, whereas the blue line represents the bands for the elastic U-profile. The black surfaces indicate the non propagating ranges of frequencies. Right panel: Measured IL of a triangular lattice of elastic U-profiles measured in the two main symmetry directions, 0° (blue line) and 30° (red dashed line)

8.3.5.1 Single scatterer

The experimental analysis of the single LDPF scatterers has been divided into two parts, acoustic and vibrational analysis.

The IL of the single scatterer is shown in Figure 8.16A in red dashed line. The real shape of the scatterer was modelled using FEM. Using the acoustic-elastic coupling previously presented, the IL was numerically obtained (see the blue line in Figure 8.16A). One can observe that the numerical method previously used is in good agreement with the experimental results. The observed discrepancy between the numerical and experimental results in the second peak can be explained by the lack of precision in the representation of the scatterer profile in the numerical method.

CHAPTER 8. IMPROVING THE ACOUSTIC PROPERTIES OF THE SCATTERERS

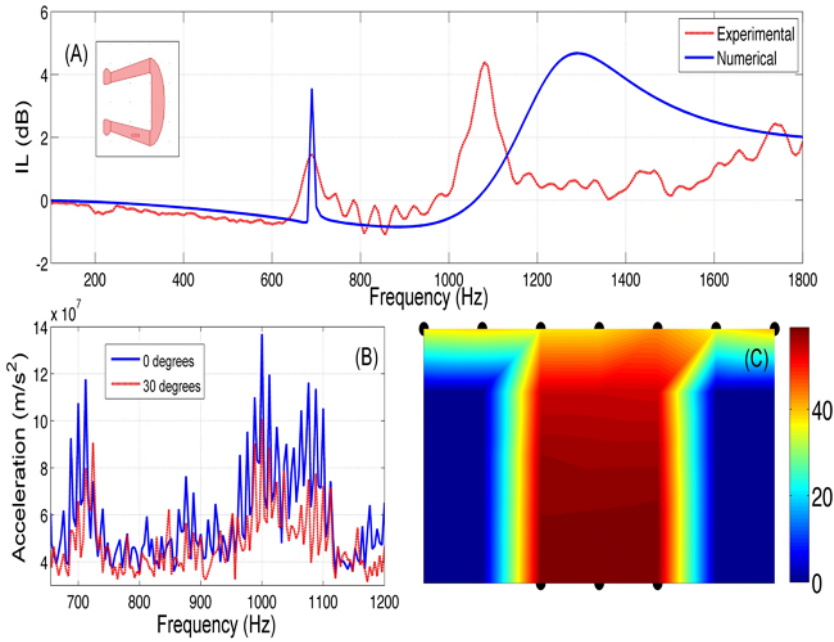


Figure 8.16: Experimental results of a single scatterer. (A) IL (dB) measured behind the scatterer. Red dashed line represents the experimental results and Blue line represents the numerical simulation using FEM, (B) Experimental measurements of the vibration of the EB of the LDPE foam scatterer. Blue line represents 0° of incidence and red dashed line represents 30° of incidence. (C) Sound level map measured inside the cavity for the resonant frequency for $\nu = 1104$ Hz. Step $\Delta x = \Delta y = 1$ cm.

In Figure 8.16A one can see the presence of the cavity and the EB resonances. To experimentally explain these resonances, on the one hand the vibration of the EB with an accelerometer, and on the other hand, the acoustic field inside the cavity of the LDPE foam for the resonant frequency of the cavity were measured. In Figure 8.16B, one can observe the vibration of the EB for two different incidence direction of the acoustic wave. Blue continuous line represents the vibrations of the wall of the U-profile for the incident wave in the ΓX direction. Red dashed line, represents the vibrations of the walls for a wave impinging in the ΓJ direction. The vibration of the wall of the elastic beam increases at the resonant frequencies. Figure 8.16B shows the

increasing in the vibration of the wall in the resonance of the material and in the cavity resonance independently of the incident direction of the acoustic wave.

Figure 8.16C shows the acoustic field inside the cavity of the LDPE foam obtained by moving the microphone with the 3DReAMS in 1 cm steps inside the cavity. The field inside the cavity is similar to the one analytically obtained in Figure 8.10D. The resonance of the cavity induces the vibration of the walls observed in Figure 8.16B at frequencies around 1000 Hz.

8.3.5.2 Periodic array

Dependence on the number of resonators

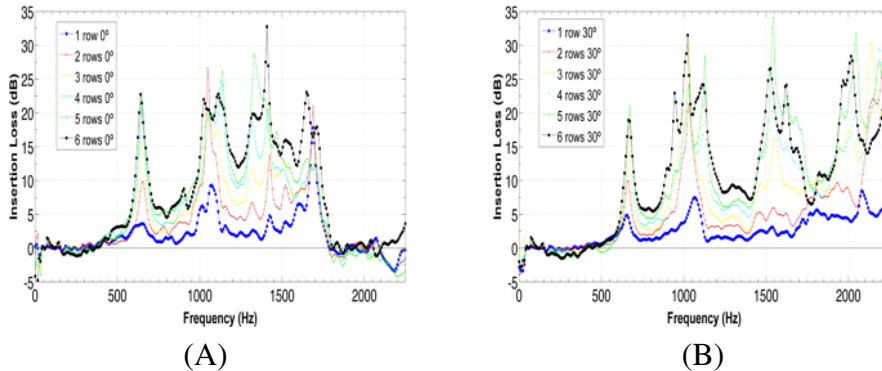


Figure 8.17: Experimental measurement of the IL for determining the dependence of the attenuation peaks on the number of scatterers. Open colored circles represent the IL for six structures made of different number of rows (from 1 to 6 rows of 10 cylinders per row). IL measured 1 m away from the end of the complete structure. (A) Measurement in the Γ_X direction. (B) Measurements in the Γ_J direction.

One can expect that both the resonant effect and the multiple scattering depend on the number of scatterers in the array. To prove it, we built and measured six configurations with an increasing number of scatterers. The final

CHAPTER 8. IMPROVING THE ACOUSTIC PROPERTIES OF THE SCATTERERS

structure presents 6 rows of 10 scatterers per row. We measured the IL at the same point for the six structures that have from 1 to 6 rows respectively. Figure 8.17 shows these experimental results. The coloured open circles represent the IL measured 1 m away from the end of the complete crystal. Blue open circles show the IL of a structure made of 1 row of U-profiles for 0° incidence whereas the black open circles represent the IL of structure made of 6 rows of U-profiles for 30° of incidence.

We can observe that both resonances due to the elastic material and the cavity, depend on the number of cylinders in the structure. Also, in the case of only 1 row, where there is no periodicity in 2D, the resonance peaks are present in the attenuation spectrum whereas Bragg's peaks do not appear. The attenuation spectra of structures made of rigid scatterers always present ranges of frequencies where there is sound reinforcement, meaning negative IL. However, it is interesting to note that these structures do not present ranges of frequencies with sound reinforcement.

Dependence on the incidence direction

One of the main characteristic of the stop bands produced by periodic arrays is their dependence on the incident direction. As we have observed in the previous Chapters, in periodic systems the BG results from the intersection of the frequencies of the pseudogaps in the main symmetry directions, the upper and lower bands of each main direction being dependent on the incident direction. However, it is known that the resonance effect must be independent from the incidence direction.

Here, we measure this dependence of both the resonance and the multiple scattering in a periodic array of U-profiles in the direction of incidence. We have especially measured the IL of a complete structure for several incident directions, between the two main symmetry directions (0° and 30°). Figure 8.18 shows these experimental results measured in the anechoic chamber.

One can observe in Figure 8.18 the low dependence on incidence direction of

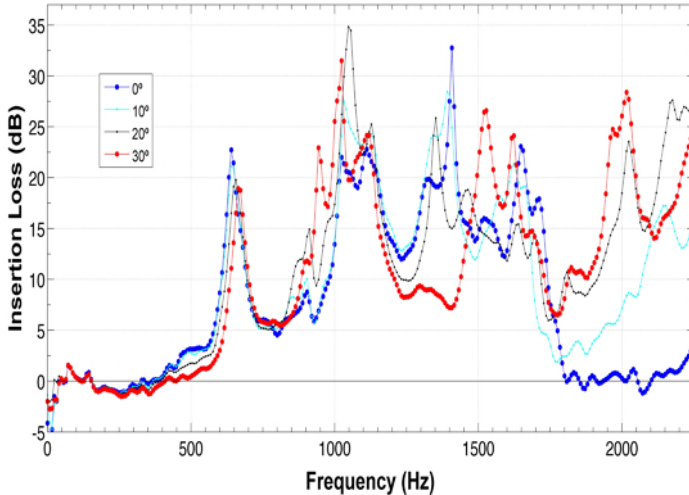


Figure 8.18: Experimental measurement of the IL to determine the dependence of the attenuation peaks on the direction of incidence of the wave. Open coloured circles represent the IL for four different directions, 0° , 10° , 20° and 30° . IL measured 1m away from the end of the complete structure (6 rows of 10 cylinders per row).

the attenuation peaks produced by the resonances of the elastic walls and by the cavity of the U-profile. However, one can see that the behaviour of the attenuation peak produced by the multiple scattering in the periodic system is highly dependent on the incidence direction.

8.3.6 Discussion: locally resonant acoustic metamaterial

Artificially designed subwavelength electromagnetic materials, denoted metamaterials [Veselago67, Pendry96, GarciaVidal97, Pendry99], have motivated a great effort to develop, both theoretically and experimentally, the acoustic analogue metamaterial [Liu00, Movchan04, Hu05, Fang06, Guenneau07]. Recent works have shown that SC can be employed as these acoustic metamaterials [Torrent06, Torrent07]. In the diffraction regime theoretical predictions and experimental results have shown the existence of BG. However, in

CHAPTER 8. IMPROVING THE ACOUSTIC PROPERTIES OF THE SCATTERERS

the regime of large wavelengths, in comparison with the separation between the scatterers, SC behave like effective homogeneous acoustic metamaterial and this can be characterized by effective physical parameters.

The pioneering work of Liu *et al.* [Liu00] proposed a novel three-dimensional (3D) arrays of coated spheres that exhibited attenuation bands, whose respective wavelength was about two orders of magnitude larger than the periodicity of the structure. The origin of this phenomenon was explained in terms of the localized resonances associated with each scattering unit [Sheng07]. Then, sound attenuation within the stop bands increases with the number and density of the local resonators, whereas the resonance frequency can be tuned by varying their size and geometry. These results open the way towards the acoustic analogous of the electromagnetic metamaterial. Due to the properties of the system, these structures are known as locally resonant acoustic metamaterial (LRAM).

In LRAM, the sound speed is proportional to $\sqrt{\kappa_{eff}/\rho_{eff}}$, where κ_{eff} and ρ_{eff} are the effective modulus and the mass density, respectively. For natural materials κ and ρ must be positive numbers to maintain the stability. Depending on the values of these parameters the metamaterial presents several responses in frequency. It has previously been shown that SC made of rigid scatterers with no resonant properties can be analysed as an acoustic metamaterials showing real and positive effective properties [Torrent07]. However, some interesting differences can appear due to the effective medium with low-frequency resonances.

In order to have a propagating plane wave inside the medium, we should have either both positive κ_{eff} and ρ_{eff} or both negative κ_{eff} and ρ_{eff} . Moreover, with these values the Poynting vector for a propagating plane wave is defined by

$$\vec{S} = \frac{i}{2\omega\rho} p \nabla p^* = \frac{|\vec{p}|^2 \vec{k}}{2\omega\rho}. \quad (8.9)$$

If κ_{eff} and ρ_{eff} are positive, the Poynting vector, \vec{S} , presents the same direction as \vec{k} and the Snell law is normally accomplished. However if κ_{eff} and ρ_{eff} are negative, \vec{S} and \vec{k} present opposite directions, and the metamate-

8.3. ELASTIC U-PROFILE SCATTERERS

rial behaves as a left handed material, where the negative refraction appears. Physically, the negativity of κ_{eff} and ρ_{eff} means that the medium displays an anomalous response at some frequencies such that it expands upon compression (negative bulk modulus) and moves to the left when being pushed to the right (negative density) at the same time. This materials present unique properties due to the double-negative medium, such as negative refractive index and subwavelength focusing [Guenneau07].

However, if only one of both parameters κ_{eff} and ρ_{eff} are negative, the sound velocity is complex, and the vector presents a complex value. Thus, when the real component of the expression of the Poynting vector is negative and sufficiently large, we can observe a narrow frequency range, corresponding to the region of negative modulus, where $Re(\vec{k}\vec{S}) < 0$. A direct consequence of such behaviour is the exponential wave attenuation in such frequencies. It has previously been shown that low-frequency attenuation bands can be induced by an effective bulk modulus that becomes negative near the resonance frequencies, giving rise to exponential attenuation of [Fang06].

In the system studied here, the stop bands at low frequencies are independent of the angle of incidence and of the lattice constant³. Moreover, there is not transmission wave in the resonance frequencies, consequently we do not observe any negative refraction or subwavelength imaging near the resonance. These properties would imply propagation is some frequency region. Thus, we can conclude that, as in the case of reference [Fang06], the periodic structure made of U-profile presents only negative bulk modulus as attenuation peaks show this behaviour. If the effective mass density were negative, some propagating mode with negative refraction would appear and, consequently, would produce some subwavelength imaging.

A rigorous parameter retrieval procedure on the line of those developed for electromagnetic and acoustic cases will be required to be implemented on this system to obtain the κ_{eff} and ρ_{eff} . But since the LRAM structure, in our case, is not a far subwavelength in size of the operating frequency ($\lambda \sim a$), such a homogenization of all properties via effective medium parameters is difficult. However, one can follow the formalism of the electromagnetic

³We have also experimentally observed non dependence on the height of the U-profiles.

CHAPTER 8. IMPROVING THE ACOUSTIC PROPERTIES OF THE SCATTERERS

material to phenomenologically analyse the behaviour of the system in the subwavelength regime analogously as in reference [Fang06].

The acoustic properties of a 2D SC can be mapped into an electromagnetic counterpart, where p , \vec{v} , ρ , k correspond to H_z , \vec{E} , ϵ , μ , respectively. Following the formalism of the electromagnetic metamaterials, one can consider that the systems behave as a metamaterial with an effective bulk modulus $k_{eff}(\omega)$ in the form,

$$k_{eff}^{-1}(\omega) = \sum_{j=1}^{N_{res}} \left(\frac{E}{3(1-2\nu)} \right)^{-1} \left(1 - \frac{F\omega_{0j}^2}{\omega^2 - \omega_{0j}^2 + i\Gamma\omega} \right), \quad (8.10)$$

where F is the filling fraction, ω_{0j} represents the resonant frequencies of the LDPF scatterer, Γ is the dissipation loss in the resonating elements and N_{res} is the number of resonances of the scatterers. The loss term Γ cannot be determined a priori therefore it should be experimentally determined. In our system $N_{res} = 2$ and the resonances are represented by:

$$\omega_{01} = \frac{\sqrt{12}}{L^2} \left(\frac{\rho L t}{EI} \right)^{-1/2}, \quad (8.11)$$

$$\omega_{02} = \frac{2\pi c_{air}}{4(l_x + 0.4L_2)}. \quad (8.12)$$

In Figure 8.19A, one can observe the effective bulk modulus of the material. The imaginary part of the effective bulk modulus presents this particular frequency-dependent response which is essential to the range of frequencies where a stop band is expected.

To obtain the transmission coefficient of a slab of the metamaterial with the bulk modulus shown in Equation 8.10, it is necessary to determine the size of the effective material. The filling fraction of the structure is,

$$f = \frac{\sum_{i=1}^N A_{cyl}}{A_{eff}} \quad (8.13)$$

where N is the number of scatterers, A_{cyl} is the area of each scatterer and A_{eff} is the area occupied by the homogeneous scatterer. For a homogeneous

8.3. ELASTIC U-PROFILE SCATTERERS

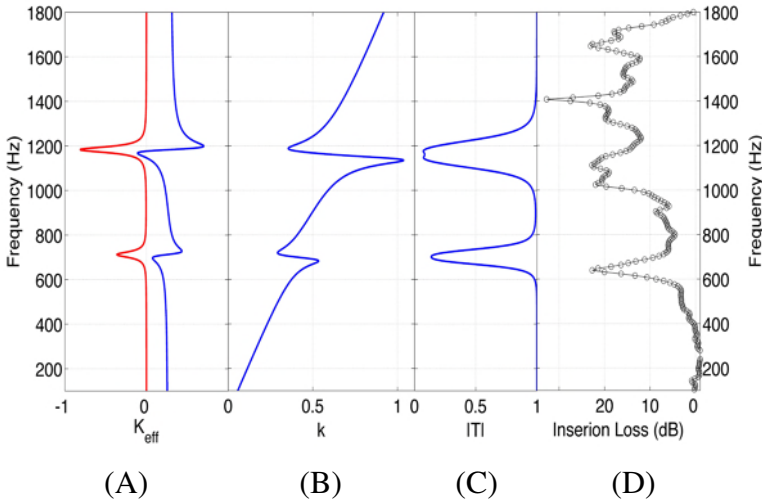


Figure 8.19: Effective parameters. (A) Effective bulk modulus. Imaginary part is plotted in red line whereas real part is plotted in blue continuous line. (B) Dispersion relation. (C) Transmission coefficient for a slab of metamaterial with $L_{eff} = 0.66$ m. (D) Measured IL of an array of U-profiles.

scatterer of N scatterers of area A_{cyl} in a lattice whose unit cell has an area A_{uc} , the filling fraction gives the following Equation

$$\frac{A_{cyl}}{A_{uc}} = \frac{NA_{cyl}}{A_{eff}}. \quad (8.14)$$

For the homogenized system with square shape, the effective area will be related to that of a square of side L_{eff} , then

$$L_{eff} = \sqrt{Na} \quad (8.15)$$

where a is the lattice constant of the square array of the inner structure of the homogeneous material. For the parameters considered in this work, $L_{eff} = 0.66$ m.

Finally, the density of the effective medium is considered here as a lineal combination of the densities of the scatterers and the host material, where the coefficients of the lineal relation are related to the filling fraction of the

CHAPTER 8. IMPROVING THE ACOUSTIC PROPERTIES OF THE SCATTERERS

structure. In such a way,

$$\rho_{eff} = f\rho_s + (1 - f)\rho_h, \quad (8.16)$$

where, ρ_s is the density of the scatterer and ρ_h is the density of the host material.

It would be interesting to know what dispersion relationship corresponds to these media with negative elastic modulus. In the regime of low frequencies, the real ($x = Re(k)$) and imaginary ($y = -Im(k)$) parts of the bulk modulus can be related to the propagation constant of the media as [Fang06],

$$Re(k) = -\frac{\omega}{2} \sqrt{\frac{\rho}{x^2 + y^2}} \left(\sqrt{x^2 + y^2} - x \right)^{1/2} \quad (8.17)$$

$$Im(k) = \frac{\omega}{2} \sqrt{\frac{\rho}{x^2 + y^2}} \left(\sqrt{x^2 + y^2} + x \right)^{1/2} \quad (8.18)$$

In Figure 8.19B, one can observe the dispersion relation obtained from the effective elastic modulus in Equation 8.10. Two spectral bands of no propagating modes are expected in the vicinity of the resonances of the local resonators.

From the Fresnel Equation of stratified media, it is possible to calculate the transmission coefficient of a slab of 0.66 m of the acoustic metamaterial analysed here. In Figure 8.19C, we can observe the absolute value of the transmission coefficient. One can observe a reduction of the transmission around the resonant frequencies.

In Figure 8.19D, we show data from measurements of the IL of a periodic array of U-profiles distributed in a triangular lattice. We observe that the attenuation peaks predicted by using the effective medium approximation are also experimentally seen. On the other hand, we would like to note that the diffraction limit is near to the second peak, and in the experimental measurements, one can observe Bragg's peak due to the periodicity.

In summary, the resonances of a scatterer with complex geometry have been studied from the analysis of the resonances of simpler geometries. The easy way to design the resonances of the scatterers presented in this Section open

8.4. TOWARDS SUPERSCATTERERS FOR ATTENUATION DEVICES BASED ON SC

several possibilities to create an arrangement of resonant scatterers that attenuate a wide range of frequencies below the BG of the structure. The first possibility is to analyse the acoustical behaviour of a periodic array made of several scatterers with different length and cavities. Following the rules for the design of the resonance frequency of both elastic beam and cavity resonances, it is possible to design tunable stop bands in the propagating range of a SC if it were made of rigid scatterers.

8.4 Towards superscatterers for attenuation devices based on SC

The periodicity of the system and the acoustical properties of the scatterers should work together in the same devices based on SC in order to produce the best effect for a predetermined situation. The previous Sections have shown how the attenuation properties of a periodic array of scatterers can be improved by changing the properties of the scatterers, therefore how the properties of the scatterers complement the acoustical properties of a periodic system.

A very recent work [Yang08] developed the electromagnetic “superscatterer”. In contrast to invisibility cloak, Yang *et al.* designed an EM transformation media device to enlarge the scattering cross-section of a small object. In this way, the object can be effectively magnified to a size larger than the object plus the device so that it is much easier to detect the EM wave. The scatterers shown in this work, could be considered as being the preliminary acoustic superscatterer. In fact, the properties of the periodic systems in the ranges of frequencies where the waves cannot see the inner structure of the periodic structure, due to the fact that the wavelength is much smaller than the size of scatterers ($\lambda \ll r$), can be modified for instance by stopping the passing of the wave through the crystal due to the properties of the individual scatterers. In such a way, the preliminary superscatterer for the acoustical counterpart are presented here.

However additional optimization is needed to find the best acoustical super-

CHAPTER 8. IMPROVING THE ACOUSTIC PROPERTIES OF THE SCATTERERS

scatterer. Even more so the design of the optimized scatterer with specific acoustical properties requires a deep study on the properties of materials, shapes, absorbing properties, etc. In this work, some possibilities of scatterers to improve the acoustical properties of the SC in the range of the low frequencies below the BG have been shown. The scatterers contribute absorbent, scattering and resonant behaviors and these are combined with lattice effects in several frequency ranges.

The ideal scatterer for its use in attenuation devices based on the SC, should improve the attenuation in the ranges of frequencies where the lattice effects do not work properly.

9

Engineering and design of Sonic Crystals

Up to now different tools to improve the acoustical behaviour of SC have been presented: on the one hand the creation of defects in SC (Chapter 6) and, on the other hand the possibility of improving the acoustical properties of the scatterers that conform to the periodic acoustic medium (Chapter 8).

The creation of N-point defects statistically distributed in SC allow the design of attenuation bands in a predetermined range of frequencies. We have observed that the best results for the attenuation devices in the optimization process have been obtained by the structures with a random distribution of vacancies. On the other hand, one can increase the attenuation properties of SC, by introducing scatterers with added acoustical properties inside a QOS. In this case it would be interesting to preserve the multiple scattering process inside the QOS. It is well known that the attenuation band appearing in the spectra of the QOS is mainly due to the multiple scattering phenomenon, thus it would be interesting to combine rigid and other kind of scatterers to obtain additional attenuation peaks without destroying the optimization previously achieved in the spectra of the QOS. Here, we study the combination of a QOS with balloons (resonant scatterers studied in Chapter 8) observing the sum of both effects in the same SC.

One of the most important technological uses of the SC in the range of the

audible frequencies is design and the construction of acoustic barriers based on SC. As Sánchez-Pérez *et al.* mentioned in their work in 2002 [Sanchez02], SC made of rigid scatterers are suitable structures to be used as acoustic barriers, but they present several disadvantages. One of them is the wide thickness of the SC necessary to obtain an attenuation similar to the predicted one by Maekawa for rigid walls. One possible solution consists of combining several effects, such as multiple scattering, resonances or absorption in the same SC.

Finally, we present a possibility of sonic crystal acoustic barrier (SCAB) design introducing scatterers that combine scattering, absorption and resonance phenomena in order to produce a high and wide range of attenuated frequencies. Both the absorption and resonance effects are proportional to number of scatterers, but their optimization requires an optimization of the material properties and the shapes of the scatterers that are outside the scope of this work. A simple geometry of scatterers based on the works of Movchan and Guenneau [Movchan04] and Umnova *et al.* [Umnova06] is shown. SRR covered with a layer of absorbent material are used for the design. Because of the geometrical shape of the scatterers, FEM seems a suitable method to model the scattering problem of this SCAB.

9.1 Targeted attenuation band creation using mixed sonic crystals including resonant and rigid scatterers

In the previous Sections and Chapters, we have given some general rules to create QOS so that they can present an attenuation band bigger than the original BG of the structure. Other possibility is to run the evolutionary algorithm to obtain a QOS optimized in a predetermined range of frequencies. In this case, the GA (or ev-MOGA) selects the best structure fitted to the objective functions to be minimized in such a way that the multiple scattering inside the QOS produces attenuation bands in predetermined ranges of frequencies in which the QOS is optimized. In all cases, the final structure is based on the initial SC but presenting a distribution of vacancies with a 40% vacancies and

9.1. TARGETED ATTENUATION BAND CREATION USING MIXED SONIC CRYSTALS INCLUDING RESONANT AND RIGID SCATTERERS

60% asymmetry.

Then, could we introduce new scatterers in these vacancies without destroying the multiple scattering in order to add new attenuation bands to the final spectrum of the complete structure?

Independently of the generation of QOS, we also was explained in Chapter 8 that one can improve the attenuation capabilities of SC by using of scatterers with added properties: absorption or resonances. Then, in this Section the following idea has been developed: to complete the QOS with scatterers with acoustical added properties in such a way that the final structure combines several effects to attenuate a wide range of frequencies.

In this sense, one can introduce in a QOS one of the resonant scatterers analysed in Chapter 8: balloons. A mixed structure is formed by one of the QOS proposed in Section 7.2 optimized for a range of frequencies centred at 2000 Hz, plus a set of balloons placed in the vacancies of the QOS, which present an attenuation band centred at 4000 Hz due to their resonances. The chosen QOS is formed by rigid (aluminum) cylinders and was optimized to attenuate a range of frequencies from 1700 to 2300 Hz. The starting SC has 6 rows of 10 aluminium cylinders per row and a lattice constant $a = 6.35$ cm, which corresponds to a Bragg frequency of 3090 Hz. We have proven the existence of a complete attenuation band at a frequency range from 1700 to 2300 Hz in this QOS (see Chapter 6). Due to the locations of the balloons, the width of the mixed structure and the total number of elements are the same as the starting SC. Figure 9.1A shows the resulting mixed structure. In Figures 9.1B and 9.1C, we compare the acoustic attenuation spectra obtained in the two main symmetry directions of the starting SC, 0° and 30° , with those obtained only with the QOS. In both cases, the attenuation level increases when the balloons are located in the place of the vacancies. In Figure 9.1D, one can see a large full band gap obtained in the predetermined range of chosen frequencies.

In this Section we show that it is possible to increase the attenuation band of the SC made with rigid scatterers embedded in air, using mixed structures of rigid scatterers and resonators filled with gas with physical properties similar to those of the air. The advantage of these mixed structures, compared to those formed only by resonators, is that we can choose both the range of

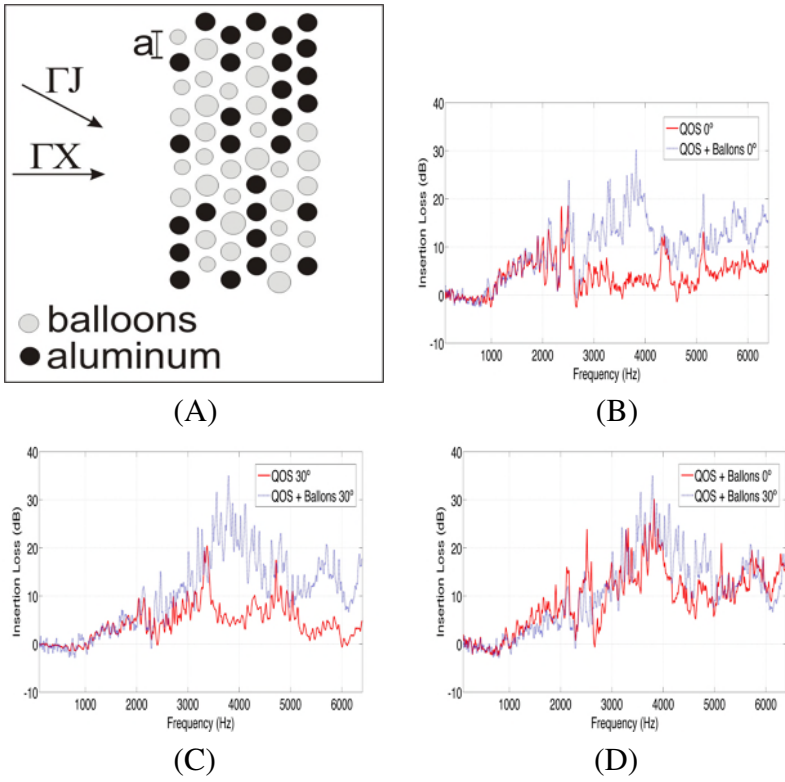


Figure 9.1: Mixed structure proposed. (A) Resulting mixed structure proposed, QOS + balloons. (B) Attenuation spectra obtained for both structures, QOS with and without balloons, at 0° , (C) for the previous structures measured at 30° , and (D) for the mixed structure measured at 0° and 30° .

resonant frequencies (here by means of the diameter of the balloons) and the range of multiple scattering frequencies creating vacancies using GA in a SC made with rigid cylinders with a reasonable lattice constant. The sum of both effects (resonance and multiple scattering) allows us to design structures with enhanced acoustic attenuation, creating a full attenuation bands in a predetermined range of frequencies. Intensive research needs to be done to develop the necessary technology to use these structures like for example, acoustic barriers.

9.2 Design of a sonic crystal acoustic barrier

The properties of SC were used by Sánchez-Pérez *et al.* [Sanchez02] to introduce for the first time the concept of Sonic Crystal Acoustic Barrier (SCAB), showing that structures made of two-dimensional arrays of hollow rigid cylinders in air with a low number of elements produce fairly good sound attenuation values, able to compete with conventional acoustic barriers. These structures have some important advantages with respect to the classical ones. On the one hand they are lighter and easier to build and, on the other hand, they can be tuned by varying the properties of the crystal and the scatterers. However, they also present some disadvantages. The dependence of the BG on the incidence direction of the wave is problematic for attenuation of noise from moving sources. In addition, the lower the frequency of sound to be attenuated is, the higher the size of the SCAB needed, which results in new problems related to the restrictions of the available space in which to put the screen.

As we saw in Chapter 8 and in the previous Section, the attenuation peaks produced by the resonant scatterers are independent of the incidence direction, so one possibility to reduce this angle dependence could be the use of resonators. However, the use of SCs as outdoor SCAB, requires scatterers made of robust and long-lasting materials like PVC, wood, or aluminium. This requirement cannot be easily met using soft materials, like for instance balloons. This is the reason why it seems interesting to analyse the possibility of optimizing the attenuation capability of SCs made with scatterers that combine rigid resonant scatterers with some resistible covering of absorbent material, in such a way that different attenuation mechanism will be used in the design.

The methodology is the following. First of all, one can design a SC presenting the BG in a range of frequencies of interest. Once the filling fraction and the lattice constant of the SC are adequate for the design conditions, then one can introduce the resonators to attenuate different ranges of frequencies. The resonant scatterers should also be designed to present the resonant peak at the desired frequency. Finally, the absorbent material should be introduced in the periodic system to make the IL of the array more uniform in frequency and to

increase the average attenuation.

In this Section, a hypothetical design of a SCAB made of SRR covered with a thin layer of absorbent material is proposed. Following the design of the SRR shown in Chapter 8, the attenuation properties of these resonant scatterers are improved by adding a layer of woollen felt covering the SRR. The SCAB made of this scatterers present good attenuation properties in the range of the audible frequencies, being suitable to acoustically compete with the classical acoustic barriers. The possibility of combining several mechanism involved in the attenuation process, such as multiple scattering, resonances and absorption allows us to control the transmission properties of the SCAB. The possibility of designing predetermined SCAB for specific ranges of frequencies is an advantage of the SCAB with respect to the classical barriers.

9.2.1 Combining absorption, resonances and multiple scattering

In this Section, we study the use of periodic distributions of absorbent and resonant scatterers embedded in air to attenuate a wide range of frequencies. The scatterers consist of a rigid SRR core with a radius of $r = 0.1$ m and an aperture of $L = 0.02$ m resonant cavity, covered with a layer of absorbent material of a thickness $t = 0.04$ m. The absorbent SRR scatterers distributed in square array with lattice constant $a = 0.33$ cm are considered, arranged in 4 rows of 4 cylinders per row. This size was chosen due to the constraints of our experimental setup. Figure 9.2 shows a transversal view of the resonant absorbent scatterer used in this Section.

Rigid cores covered with absorbent material were analysed by Umnova *et al.* [Umnova06], presenting a MST procedure to study the scattering problem of scalar waves by periodic arrays of absorbent scatterers. The scatterer consist of a rigid core covered with a layer of absorbent modelled using the Delany-Bazley model. Motivated by the idea of Umnova *et al.* an analysis on the behaviour of the SRR covered with a layer of absorbent material is presented. An IL more uniform in frequency and with greater average attenuation results are expected to be obtained. One of the goal of this Section is to determine

9.2. DESIGN OF A SONIC CRYSTAL ACOUSTIC BARRIER

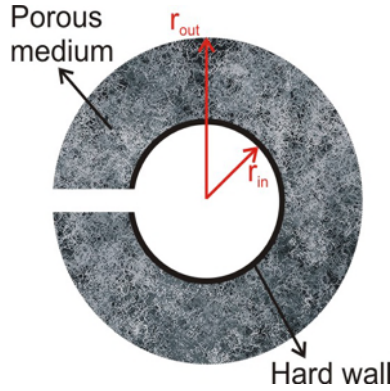


Figure 9.2: Transversal view of the absorbent SRR. A rigid SRR core is covered by a layer of porous material.

how the absorbent covering affects the multiple scattering and the resonant phenomena in SC.

In this Section, a FEM model is used which introduces the Delany-Bazley model as a type of damping in the model to characterize the absorbent layer. Then, the absorbent covering was modelled using the Delany-Bazley model with the following Equations,

$$Z(\nu) = 1 + 0.0571 \left(\frac{\rho_0 \nu}{R} \right)^{0.754} - i 0.087 \left(\frac{\rho_0 \nu}{R} \right)^{-0.732}, \quad (9.1)$$

$$k(\nu) = k_0 \left(1 + 0.0928 \left(\frac{\rho_0 \nu}{R} \right)^{-0.7} - i 0.189 \left(\frac{\rho_0 \nu}{R} \right)^{-0.597} \right), \quad (9.2)$$

where ρ_0 , c_0 represent the density and the sound velocity of the air respectively; k_0 is the wave number of the wave propagating in air; R is the flow resistivity; and ν is the frequency of sound. Here $R = 23000 \text{ kPa s m}^{-2}$ corresponds to the woollen felt covering. This model presents some ranges of applicability dependent on both the resistivity of flow and the frequency. For the range of values of these parameters, the Delany-Bazley model works properly in the range of frequencies $186 < \nu < 18700 \text{ Hz}$, which is basically the range of frequencies in the audible range (20-22000 Hz).

In the model a point source is placed at the origin of the coordinates and the

structure is placed 1.5 m away from the source. The IL is calculated at the point (3,0), meaning that, 3 m behind the structure in the X axis. The numerical domain is surrounded by a PML region in order to reduce the spurious reflection in these boundaries in order to simulate free-field conditions.

The numerical model was developed using COMSOL 3.5a. The behaviour of rigid SRR were numerically and experimentally analysed in Section 8.2. The agreement between the numerical (both the eigenvalue and the scattering problems) and the experimental results was very good. However, now a test of the model using only rigid cores covered with absorbent material is needed.

Appendix C show an analytical model of the scattering of scalar waves by rigid cores covered with a layer of absorbent material. The model is analogous to one the presented by Umnova *et al.* in 2006 [Umnova06], but using different matrix of coefficients. With this model it is possible to reproduce some results from the Umnova work in order to test the analytical model. Then, the analytical results are compared with the ones obtained using our numerical model programmed in COMSOL 3.5a. In Appendix C, one can see the good agreement between both the analytical and the numerical models. The use of FEM as a design tool here can be considered a good choice.

9.2.1.1 Scattering of a SCAB made of absorbent SRR

The scattering of sound waves by a SCAB made of absorbent SRR is shown in Figure 9.3 in terms of the IL. The upper panel of Figure 9.3 shows the results of the scattering by a finite array of absorbent SRR. Red and blue line represent the IL produced by an array of 4×4 absorbent SRR in the ΓX and ΓM directions respectively. In the graph the IL of an array of rigid scatterers (green line) is also plotted in order to make the results easy to understanding. Finally, due to the comparison between the acoustical behaviour of a SCAB and a classical barrier, Maekawa's prediction of a wall with the same dimensions as the SCAB is also plotted in the upper panel of Figure 9.3 in a black dotted line.

The lower panel of Figure 9.3 shows the band structures of a SCAB made

9.2. DESIGN OF A SONIC CRYSTAL ACOUSTIC BARRIER

of rigid SRR. Although the scattering problem was solved for the absorbent materials, and the eigenvalue problem in the case of the rigid SRR, one can compare both results (upper and lower panels of the Figure 9.3) to observe whether or not the absorbent covering used in this Section destroys the scattering and the resonance effect. In the lower panel of the Figure 9.3, the blue dotted lines represent the band structures of the rigid SRR used in our SCAB and the red lines represent the band structures of the rigid SRR with the same dimensions as the total dimensions of the SRR plus the absorbent layer ($r = 0.14$ m, being the inner radius $r = 0.095$ m).

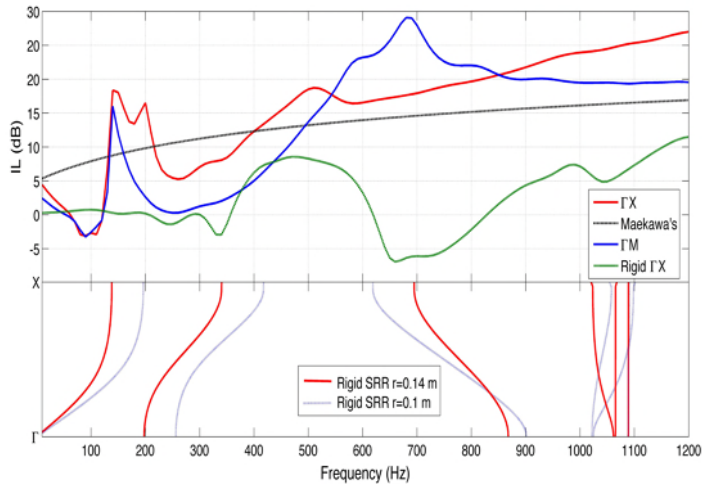


Figure 9.3: Scattering and eigenvalue problem of a SCAB made of absorbent SRR of $4a \times 4a$ size. Upper panel: Red (Blue) line represents the IL in the ΓX (ΓM) direction of the SCAB made of absorbent SRR. Black line represents the Maekawa's predictions for a rigid wall with the same dimensions. Green dashed line represents the IL in the ΓX direction of a SC made of rigid cylinders. Lower panel: Band structures of the rigid SRR. Blue dashed line represents the Band Structures for the rigid SRR with external radius $r = 0.1$ m, inner radius $r = 0.095$ m and $L = 0.02$ m. Red line represents the band structures for the rigid SRR with external radius $r = 0.14$, inner radius $r = 0.095$ m and $L = 0.02$ m.

First of all, comparing the results in the upper panel of Figure 9.3 of the SC made of absorbent SRR (red line) with the results of the SC made of rigid

cylinders (green dashed line), one can observe that the average IL produced by the SCAB is increased by the absorbing covering of the SRR practically in the whole range of frequencies. Moreover, one can observe that the IL of the SCAB and the IL of a classical barrier (Maekawa's prediction) reveals ranges of frequencies in which the SCAB produces better attenuation and ranges in which the SCAB works worse than the classical barriers. Thus, SCAB made of absorbent SRR is suitable to be used as acoustic barriers in certain ranges of frequencies.

The band structures shown in the lower panel of Figure 9.3 (lower panel) predict a BG centred in 515 Hz, meaning that there is no propagation in the Γ X direction through the periodic array for this range of frequencies (blue dotted line). In the IL of the SCAB made of the absorbent SRR, shown in the upper panel of Figure 9.3 (red line), one can observe the corresponding peak of the multiple scattering. From the values of the IL of the SCAB, it seems that the absorbing material introduces a base line of attenuation and that the peak of multiple scattering appears over this base line of attenuation.

The resonant effect in a SC made of rigid SRR introduces an attenuation band in the low frequency range ($\nu = 220$ Hz), below the BG, as the band structures predict it in the low panel of Figure 9.3 (see blue dotted lines). However the corresponding peak appearing in the IL spectra for the SCAB made of the absorbent SRR, is shifted in frequency to the lower frequencies. This interesting effect is produced because the absorbent covering becomes part of the resonator increasing the wall thickness and producing a shifting of the resonance frequency. To prove this, the band structures of a SC made of rigid SRR with the same dimensions as the corresponding absorbent SRR has been calculated. The red lines in the lower panel of Figure 9.3 shows the results of this calculation. One can observe that the attenuation band due to the resonance effect predicted by the band structures is reproduced in the IL spectrum. This interesting result can be used as a design tool that could be exploited to attenuate other near ranges of frequencies. One could use several thickness of absorbent covering in order to improve the attenuation properties of the SCAB.

Then, the IL of a SCAB is characterized mainly by three properties: *i*) the

9.2. DESIGN OF A SONIC CRYSTAL ACOUSTIC BARRIER

attenuation shows a high attenuation base line comparable with the one predicted by Maekawa for a classical barriers; *ii*) The structures preserve the properties of the periodicity, meaning that, it preserves the BG although the absorbing covering is surrounding the scatterers; *iii*) The resonances of each scatterer are also preserved in the structure. Then, multiple scattering, resonances and absorption co-exist in the same structure without negative interference between them.

9.2.1.2 Dependence of the IL on the number of rows and on the incidence direction

Up to now, the main characteristics of attenuation properties in a SCAB made of absorbent SRR have been observed. However, both the dependence on the mass law and the dependence on the incident direction are important aspects of the attenuation devices. In this Section the IL for several structures with different number of scatterers and different incident directions is analysed.

The structures analysed in this Section present the same size as in the previous Section, $4a \times 4a$. Four structures from 1 to 4 rows in square lattice for two different angles of incidence (the two symmetry directions of the periodicity of the structure, 0° and 45°) have been chosen for the analysis.

Figure 9.4 shows the results of the dependence of the IL on both the number of cylinders and on the angle of incidence. Blue, green, cyan and red lines represent the IL of the structures made of 1, 2, 3 and 4 rows respectively. In the upper panel, Figure 9.4 shows the IL for the ΓX direction (0°), whereas the lower panel analyses the IL for the ΓM direction (45°). To compare the results, the band structure for the rigid SRR with the same dimensions as the absorbent SRR is shown in the middle panel of Figure 9.4.

The attenuation level shown in both, ΓX and ΓM directions depends on the number of scatterers. The greater the number of rows, the higher IL. Obviously, this result is in agreement with the mass law. However, it does not seem obvious that the multiple scattering and the resonance phenomena continue to present the same properties as the rigid SRR when the absorbent material is

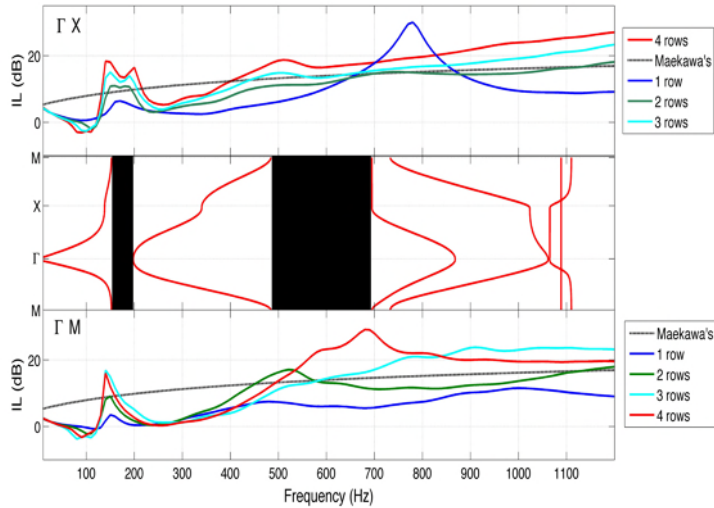


Figure 9.4: Dependence of the IL of a SCAB made of absorbent SRR on the number of rows and on the incidence direction. Blue line, green, cyan and red lines present the IL of the structures made of 1, 2, 3 and 4 rows respectively. Upper panel: IL for the ΓX direction (0°). Lower panel: IL for the ΓM direction (45°). Middel panel: Band structure for the rigid SRR with the same dimensions than the absorbent SRR. Red lines are the band structures for the rigid SRR with $r = 0.14$ m.

introduced. One can observe that the multiple scattering and the resonant phenomenon are also increased with the number of absorbent SRR. In both ΓX and in ΓM we can observe how the resonance peak increases with the number of the absorbent SRR. Moreover, the same behaviour can be observed with the multiple scattering peak, of course, this peak only appears in the structures with three and four rows.

10

Concluding remarks

The main conclusions of the work are summarized in this Chapter and a concise explanation of the future work is also presented.

10.1 Conclusions

The work reported in this Ph.D. Thesis can be divided into two main parts: (i) The study of vacancies and the optimization of the SC by means of the generation of vacancies and (ii) the design of scatterers with added acoustical properties. Finally, both parts were applied together in order to develop the application of SC as attenuation devices, especially as acoustic barriers. The following conclusions have been obtained:

10.1.1 Defects in sonic crystals

- From the theoretical point of view, an extension of the plane wave expansion (EPWE) in the case of both complete SC and SC with vacancies have been presented. This methodology allows us to analyse the inverse problem $k(\omega)$ and, as such, the complex band structures in SC.
- The analysis of the complete SC by means of the EPWE introduces

a new perspective in the understanding of the BG: frequency regimes where no real k exists, meaning the ranges of frequencies in which only the modes characterized by a complex wave vector are excited inside the crystal. Thus, for the frequencies inside the BG, the modes present evanescent behaviour. We have proven that these modes present, inside the crystal, an exponential-like decay characterized by a complex value of the first Bloch vector. The agreement between measurements and theoretical predictions is very good. For the specific SC analysed, the EPWE predicts a value for the imaginary part of the first harmonic of the wave number, $Im(k) = -5.6 \text{ m}^{-1}$; and by fitting an exponential decay, ae^{bx} , the experimental value obtained is $b = Im(k) = -5.60 \pm 1.45 \text{ m}^{-1}$. This procedure could be used to determine the effective thickness of filtering devices based on SC to achieve a determined attenuation level.

- Apart from the evanescent nature of the modes inside the BG with negative complex Bloch vectors, the evanescent behaviour of a localized mode inside the SC was also observed. From both the analytical predictions and the experimental results one can conclude that localized modes present evanescent behaviour outside the cavity with the same exponential-like decay as waves with the same frequency inside the BG impinging over a complete SC. Due to the local breaking of periodicity, the physical situation is very different between the complete SC and the SC with point defects, but it can be concluded that the medium observed by the localized wave trapped inside the cavity formed by the vacancy is topologically equivalent to the one observed by the wave itself when it tries to pass through a complete SC from the outside.
- EPWE with supercell approximation allows us to study the evanescent behaviour of modes inside SC with multipoint defects. Localized modes in multipoint defects in SC are mainly characterized by three properties: the splitting of frequencies, the symmetry of the vibrational patterns and the evanescent behaviour inside the crystal. Here, without any loss of generality, all the properties of the localized modes in a SC with a double point defect have been analysed.

The splitting produced by the generation of a double point defect shows the effects in both the real and the imaginary band structures. From the imaginary complex band structure we observe that the localized modes present different values for the imaginary part of k , meaning that each mode has a different decay rate inside the crystal (different evanescent behaviour). This property was experimentally observed by fitting the exponential decay for each localized mode inside the crystal. The symmetry of the vibrational patterns in double point defect was also analysed in the Ph.D. Thesis by means of MST calculation and experimental data. The novel experimental evidence presented in this work show the symmetric and antisymmetric vibrational patterns in SC with double point defects. These data are in very good agreement with the analytical calculations.

These interesting results could be used to determine the thickness of the periodic medium around the point defect in order to find a localization or to produce a passing mode. In this sense, the results are the basis for the correct understanding of the design of narrow filters and waveguides based on periodic structures with single or multi-point defects.

- The physical properties of SC with the N-point defects are well characterized by the EPWE, however in the case of N random point defects one cannot use EPWE for the analysis of the resulting structure due to the high level of breaking of the periodicity. Here, a novel multi-objective optimization technique based on genetic algorithms (epsilon variable multi-objective genetic algorithm (ev-MOGA)) working together with multiple scattering theory (MST) were used. The methodology can be highly parallelizable and the computational time was drastically reduced using a master-slave architecture. This procedure was used to generate N random point defects in a starting SC in order to obtain Quasi-ordered structures (QOS): structures obtained by generating N-point defects in a complete SC that presents optimum values of two objective functions based on both the mean pressure level and the mean deviation of the pressure in a predetermined range of frequencies. QOS consist of nonperiodic and random distribution of vacancies in a complete starting SC thus, some parts of the system show the initial period-

CHAPTER 10. CONCLUDING REMARKS

icity of the SC, in such a way that, after removing an important number of scatterers (around 40%), the resultant structure is non-periodical but locally preserves the periodicity of the original lattice of the complete starting SC.

- Simple GA showed the evidence of the possibility to obtain attenuation bands in a predetermined range of frequencies. *evMOGA* improve the results showing that the QOS produce an attenuation zone around the optimization point due to the optimized multiple scattering in the QOS that produces a negative interference around the optimized point and for the whole optimized range of frequencies.
- The Pareto front, using the optimization factor (O_f), was revealed as an easy and intuitive technique to decide the optimal structure in the case of the two objective functions.
- The analysis of QOS to obtain ranges of both attenuated and focalized frequencies in a point behind the structure was carried out here. Different strategies in the creation of defects were used for the exhaustive search of QOS: symmetry X, symmetry Y, symmetry XY and no symmetry.

For the objective functions considered in this work, the enhancement of the focalization properties of the QOS is similar for all the considered symmetries of generation of vacancies. However, in the case of attenuation devices, we showed that the generation of random vacancies without any symmetry in a SC produces QOS with the best attenuation properties among the other symmetries considered in the work. The optimization process reveals that the best results have always been obtained considering a random step in the optimization process, being the optimized solution independent of the search path, if this random step is considered.

- Several parameters were introduced for the characterization of the QOS. Among them, the Asymmetry (A) is very important because it gives information about the level of asymmetry of a QOS, meaning how the vacancies are distributed inside the crystal. It has been found that 40%

of vacancies randomly generated with a value of the Asymmetry of 60% produces the QOS with the best attenuation properties. The generation of vacancies following this procedure generate structures that produce double attenuation level than compared to the starting SC.

10.1.2 Intrinsic properties of the scatterers

- Apart from the generation of vacancies in SC, one can consider scatterers with intrinsic acoustical properties in order to improve the overall properties of the periodic systems, adding new acoustic effects different from those generated by the periodicity phenomenon. In this work we investigate four types of scatterers: balloons, split ring resonators (SRR), elastic-acoustic scatterers (U-profiles) and absorbent SRR.
- Experimental results show that balloons containing a blend of air and helium present a resonant behaviour and they are soft enough not to produce distortion in the overall effect due to the periodicity of the SC. Interesting results were obtained from the analysis of the IL produced by two different SC consecutively placed, one made of balloons and the other one made of rigid cylinders. The acoustical phenomena generated by both systems, balloons producing resonances and rigid scatterers producing Bragg's scattering, appear together. This fact means that mixed structures can be used to get an enhancement of the attenuation bands.
- Split ring resonators (SRR) have been extensively analysed in the literature in the recent years, however in all cases the geometrical shape accomplishes some conditions, in such a way that the SRR can be analysed as a Helmholtz resonator. Thus, when the wall thickness, the length of the neck or the aperture of the resonator are big enough, then the resonator cannot be treated as a Helmholtz resonator and the design of the scatterers should be done using different techniques. In this work the design of a SC with SRR was done by solving the scattering and the eigenvalue problems. The resonance frequency of the SRR calculated using the Helmholtz formula is far from both the one numer-

ically predicted using FEM and the one experimentally measured. The scattering and the eigenvalue problems of a SC made of SRR are in very good agreement with measurements. The predicted frequency is in very good agreement with the experimental results including in the cases of a change in the number of resonators and different incident directions of the wave. The strong attenuation bands at the resonant frequencies represent a higher performance with respect to the SC made of rigid scatterers. Moreover, because of the simplicity of the design of SRR, they can be used to design custom-tailored SC.

- Scatterers made of soft material (Low Density Polyethylene foam, LDPE foam) combining elastic and cavity resonances were also studied here. The elastic resonance produces a vibration of the walls of the scatterers introducing an attenuation band in the range of low frequencies below both the attenuation peak produced by the cavity resonance and the Bragg peak. This resonance was explained by analysing the vibrations of an elastic beam, both analytically and numerically. Moreover the resonant frequency is easy to design because it depends on the geometrical parameters of the scatterers. The complex geometry of the scatterers was performed numerically in order to analyse both the scattering and the eigenvalue problems of a SC made of these scatterers. The agreement between the experimental results and the numerical calculations are very good. These scatterers open the possibility to create periodic arrangements of resonant scatterers designed with different geometrical shapes in order to attenuate a wide range of frequencies. Following the rules of the design of these scatterers, one can generate tunable resonances to produce stop bands at the desired range of frequencies.
- The properties of a SC made of the presented elastic-acoustic resonant scatterers were derived in a brief discussion on the homogenization of the structure. The analysis of the behaviour of these systems in the subwavelength regime was done following the formalism of the electromagnetic materials. With this formalism, one can observe the negative response of the effective parameters of the system near the resonance frequency. The dispersion relation obtained using these effective parameters is in good agreement with the measurements and with the

numerical predictions.

10.1.3 Combining physical phenomena

- The combination of the scattering and the acoustic properties of the scatterers was analysed in the last part of this Ph.D. Thesis. On the one hand mixed structures of rigid and resonant structures were analysed. Interesting results show that it is possible to increase the attenuation bands of the SC made with scatterers embedded in air by using mixed structures made of rigid scatterers and soft resonators. As an example, the distribution of vacancies in a QOS was filled by balloons forming a mixed structure that sums both physical effects to create a full attenuation band in a predetermined range of frequencies. The advantage of these systems is that one can choose both the range of resonant frequencies by electing the resonator and the range of attenuated frequencies using multiple scattering, because the QOS are the resultant structure of an optimization process.
- Finally a SC made of scatterers presenting a hard core, an absorbent covering and a resonant cavity is proposed as an alternative to the classical acoustic barriers. The insertion loss produced by this type of structures present the sum of the three different physical phenomena: scattering, absorption and resonances. The periodicity of the structure was designed to produce a BG around 500 Hz and the cavity of the scatterer was designed to produce a resonance peak around 210 Hz. Both attenuation peaks are shown in the structure over a high attenuation baseline produced by the covering of absorbing material. An interesting result is that the covering material becomes part of the resonant cavity shifting the resonance to lower frequencies. The produced IL was compared with the Maekawa predictions for the rigid panel (classical acoustic barrier). The results indicate that the proposed SC present an average attenuation similar to the one produced by classical noise barriers. The acoustic attenuation of this SC presents both ranges of frequencies with better attenuation and ranges of frequencies with worse acoustic atten-

uation than the barrier. However the easy control of the sound propagation properties of the SC is an advantage with respect to the classical structures.

10.2 Future work

The analysis of the QOS produced very interesting results, but several improvements have to be developed in the future. Until now, the optimization of the attenuation and focalization properties in a range of frequencies in a point behind for the normal incidence on the structure has been studied. However, it would be interesting to improve the same properties in a zone behind the structure for several angles of incidence. This procedure requires intensive developments in the multi-objective optimization algorithm used. One possibility consists of considering two objective functions for each point of the surface to be optimized and several objective functions to take into account the behaviour of the acoustical properties from an overall point of view in the surface. Thus, the number of objective functions could be high, therefore the Pareto Fronts could be multidimensional and the decision techniques would have to be improved.

From a fundamental point of view, very recent works have presented the design of 2D, isotropic, disordered photonic crystals with complete BGs blocking all directions and polarizations [Torcuato03, Florescu09, Zachary09]. In these works, the notion of hyperuniformity has a particular importance. The hyperuniformity characterizes the local fluctuations in the volume fraction. Interesting results show that hyperuniformity, combined with uniform local topology and short-range geometric order, can explain how complete photonic BGs are possible without long-range translational order. The immediate question is: can QOS be characterized by the hyperuniformity? or is the Asymmetry parameter defined in this PhD Thesis a special case of hyperuniformity? These characterizations could be useful to produce distinct classes of materials with novel phononic properties.

On the other hand, the extended plane wave expansion allows us to analyse

the behaviour of the imaginary values of the wave vector inside the crystal for frequencies inside the BG. Intensive work should be done to obtain more conclusions about the influence of the evanescence on the propagation of waves inside the crystal. Can the evanescent behaviour of the waves inside the BG produce some kind of diffraction?

The optimization of the scatterers with additional properties has recently been receiving an increasing interest, and new materials as well as new geometrical shapes can be developed and analysed. Motivated by the recent work of Yang *et al.* [Yang08] a superscatterer could be developed to be used in the periodic system in such a way that the conjunction of the scatterers and the periodicity of the array would presents wide and high attenuation peaks.

When using cylinders as scatterers in a 2D system, one can consider that the system is infinitely long in the third dimension. However, this approximation is very different in certain experimental situations. For example, it would be interesting to know the diffraction produced at the end of the finite cylinders and how it influences the scattering. Also, the scatterers are sometimes placed over a ground that could introduce some effects in the overall behaviour of SC. In this sense, it would be very interesting to know the effect of the different kinds of grounds.

The exploitation of both the periodicity and the properties of the scatterers show potential application of these systems for the control of noise propagation. Although this work has solved several interesting problems, intensive research needs to be done to develop the necessary technology in order to use these systems as efficient attenuation devices, like for example, acoustic barriers.

A

Appendix: Addition theorems

One of the most important tools in the multiple scattering theories is the addition theorems. They are used to transform one expansion over some point in space into a similar expansion over a different point. In this appendix we show some important two dimensional addition theorems for cylindrical coordinates.

We consider two origins, i and j . Let \vec{r}_k be the position vector of a general point P with respect to k , for $k = i, j$. Let \vec{r}_{ij} be the position vector of i with respect to j , so that $\vec{r}_j = \vec{r}_i + \vec{r}_{ij}$. Let $\vec{r}_k = (r_k \cos \theta_k, r_k \sin \theta_k)$ with $k = i, j$ and $\vec{r}_{ij} = (r_{ij} \cos \theta_{ij}, r_{ij} \sin \theta_{ij})$. See Figure A to observe a schematic view of all of these vectors and angles. In the Appendix J_n and H_n are the n -th order Bessel and Hankel functions of first kind respectively.

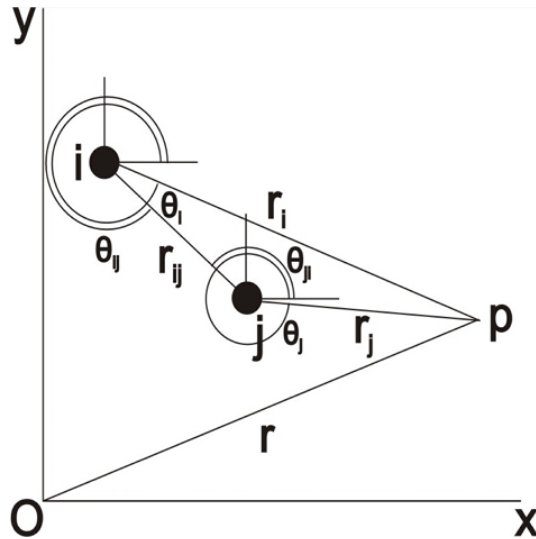


Figure A.1: Notation used for the addition theorems.

Neumann's additional theorem

$$J_m(kr_j) = \sum_{n=-\infty}^{n=+\infty} (-1)^n J_n(kr_{ij}) J_n(kr_i) e^{in(\theta_i - \theta_{ij})} \quad (\text{A.1})$$

$$= \sum_{n=0}^{n=\infty} \varepsilon_n (-1)^n J_n(kr_{ij}) J_n(kr_i) \cos(n(\theta_i - \theta_{ij})), \quad (\text{A.2})$$

where $\varepsilon_0 = 1$ and $\varepsilon_n = 2$ for $n > 0$.

Graf's additional theorem for $J_m(kr)e^{im\theta}$

For $m = 0, \pm 1, \pm 2, \dots$, we have

$$J_m(kr_j)e^{im\theta_j} = \sum_{n=-\infty}^{n=+\infty} J_n(kr_{ij})e^{in\theta_{ij}}J_{m-n}(kr_i)e^{i(m-n)\theta_i} \quad (\text{A.3})$$

$$= \sum_{n=-\infty}^{n=+\infty} J_{m-n}(kr_{ij})e^{i(m-n)\theta_{ij}}J_n(kr_i)e^{in\theta_i}. \quad (\text{A.4})$$

Graf's additional theorem for $H_m^{(1)}(kr)e^{im\theta}$

For $m = 0, \pm 1, \pm 2, \dots$, we have

$$H_m(kr_j)e^{im\theta_j} = \sum_{n=-\infty}^{n=+\infty} H_{m-n}(kr_{ij})e^{i(m-n)\theta_{ij}}J_n(kr_i)e^{in\theta_i} \quad (\text{A.5})$$

for $r_i < r_{ij}$, and

$$H_m(kr_j)e^{im\theta_j} = \sum_{n=-\infty}^{n=+\infty} J_{m-n}(kr_{ij})e^{i(m-n)\theta_{ij}}H_n(kr_i)e^{in\theta_i} \quad (\text{A.6})$$

for $r_1 > r_{ij}$.

B

Appendix: Computational time multiple scattering theory

The computational time of the calculation of the acoustic pressure by means of the multiple scattering theory (MST) obviously depends on several parameters. First of all, it depends on the computer in which the calculation is run and on the program used to make the simulation.

We programmed MST using the matrix formulation of the problem in MATLAB 2007a. We performed the simulations in this Appendix in a standard Centrino Due Core personal computer platform, we specifically used a HP Compaq nx9420 laptop with 1Gb of RAM.

We calculated the computational time for a fixed frequency at a point in space. We changed the number of cylinders from 2 to 300. In Figure B.1, we represent the computational time measured by the computer as well as its quadratic and cubic fits. We can observe that the time presents a cubic behaviour.

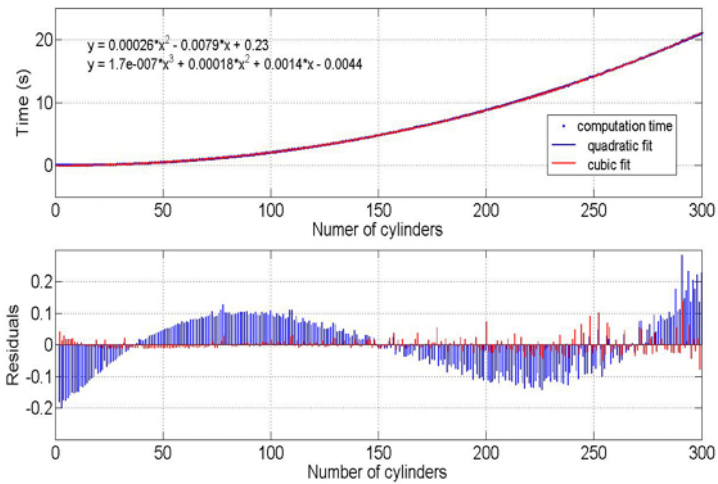


Figure B.1: Computational time of the pressure calculation by means of MST. Blue points represent the computational time measure by the computer. Blue line (Red Lie) represents a quadratic (cubic) fit. The residuals of both fits are also plotted in the Figure.



Appendix: multiple scattering of arrays of cylinders covered with absorbing material

In this Appendix we briefly present the multiple scattering of a 2D array of scatterers made of a rigid core covered with a layer of absorbing material. The interior rigid core is a cylinder with a radius r_{in} , and the covering of the absorbing material has a thickness of t , so that the external radius is $r_{ext} = r_{in} + t$. Figure C.1 represents a transversal view of the scatterer.

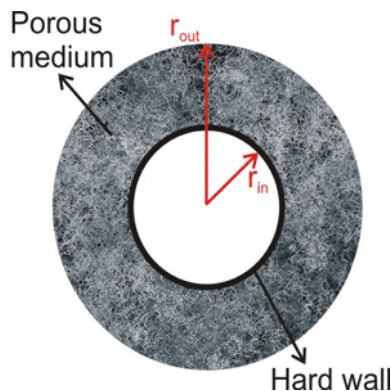


Figure C.1: Transversal view of the absorbent scatterer. A rigid core is covered with a layer of porous material.

Absorbing materials usually present a complex impedance, $Z_c(\omega)$ and propagation constant, $k_c(\omega)$, both being frequency dependent. The formalism has been obtained independently from the expression used to model the absorbing material.

In this case, an acoustic source transmitting monochromatic waves is placed at point \vec{r}_s , some distance from the system of scatterers. For the sake of simplicity, without compromising generality, we approximate the acoustic source as a line source located at origin, i. e. $\vec{r}_s = \vec{0}$. The acoustic wave emitted by such a source follows the Equation in cylindrical coordinates:

$$P(\vec{r}) = i\pi H_0(kr), \quad (\text{C.1})$$

where H_0 is the zero- th order Hankel function of the first kind. The solution represents a line source located at origin.

The incident wave over i -th cylinder is:

$$P_{in}^i(\vec{r}) = \sum_{n=-\infty}^{\infty} B_n^i J_n(k|\vec{r} - \vec{r}_i|) e^{in\phi_{\vec{r}-\vec{r}_i}}. \quad (\text{C.2})$$

On the other hand, the scattered wave produced by i -th cylinder is:

$$P_{sc}^i(\vec{r}, \vec{r}_i) = \sum_{n=-\infty}^{\infty} i\pi A_n^i H_n^{(1)}(k|\vec{r} - \vec{r}_i|) e^{in\phi_{\vec{r}-\vec{r}_i}}, \quad (\text{C.3})$$

where H_n is the n - th order Hankel function of the first kind, and J_n is the n - th order Bessel function of the first kind.

The wave on the interior of the absorbing material of i -th cylinder is:

$$P_{int}^i(\vec{r}, \vec{r}_i) = \sum_{n=-\infty}^{\infty} A_n^i (X_n^i H_n^{(1)}(k_c(\omega)|\vec{r} - \vec{r}_i|) + Y_n^i J_n(k_c(\omega)|\vec{r} - \vec{r}_i|)) e^{in\phi_{\vec{r}-\vec{r}_i}}. \quad (\text{C.4})$$

Then, the exterior wave outside the i -th cylinder is:

$$P_{ext}(\vec{r}, \vec{r}_i) = \sum_{n=-\infty}^{\infty} B_n^i J_n(k|\vec{r} - \vec{r}_i|) e^{m\phi_{\vec{r}-\vec{r}_i}} + \sum_{n=-\infty}^{\infty} i\pi A_n^i H_n^{(1)}(k|\vec{r} - \vec{r}_i|) e^{m\phi_{\vec{r}-\vec{r}_i}}. \quad (\text{C.5})$$

Due to the scatterers considered in this Appendix, the problem presents two different kinds of boundary conditions. In the wall of the core, one can consider a rigid wall, i.e, Neumann Boundary conditions. However, in the absorbing material-host medium interface, one should consider the continuity of the pressure and the velocity. Thus, the boundary conditions in the rigid wall, Γ , inside i -th scatterer is:

$$\frac{\partial P_{int}^i}{\partial n} \Big|_{\Gamma_i} = 0 \quad (\text{C.6})$$

and the boundary conditions in the exterior interface of the scatterer are,

$$P_{ext}^i \Big|_{\partial\Omega_j} = P_{int}^i \Big|_{\partial\Omega_j} \quad (\text{C.7})$$

$$\frac{Z_c(\omega)k_c(\omega)}{k_0} \frac{\partial p_{ext}}{\partial n} \Big|_{\partial\Omega_i} = \frac{\partial p_{int}}{\partial n} \Big|_{\partial\Omega_j} \quad (\text{C.8})$$

where $\partial\Omega_j$ is the boundary of the i -th scatterer, k_0 is the wave number in the host medium, $k_c(\omega)$ and $Z_c(\omega)$ are the propagation constant and the impedance of the absorbing material of the scatterer i .

By applying the boundary condition C.6, we can obtain a simple relation between coefficients X_n^i and Y_n^i :

$$Y_n^i = X_n^i T_n^i \quad (\text{C.9})$$

$$T_n^i = -\frac{H_n'(k_c(\omega)r_{in}^i)}{J_n'(k_c(\omega)r_{in}^i)}. \quad (\text{C.10})$$

where the prime as superscript represents the derivative with respect to the normal of the surface as in Chapter 3.

Finally, applying the boundary conditions at the $\partial\Omega$ interfaces, we get:

$$B_n^i = i\pi Z_n^i A_n^i, \quad (\text{C.11})$$

where,

$$Z_n^i = -\frac{f(\omega)H_n'(kr_{out}^i) - H_n(kr_{out}^i)}{f(\omega)J_n'(kr_{out}^i) - J_n(kr_{out}^i)}, \quad (\text{C.12})$$

$$f(\omega) = \frac{Z(\omega)k(\omega)H_n k_c(\omega r_{out}^i) + T_n J_n(k_c(\omega)r_{out}^i)}{k H_n' k_c(\omega r_{out}^i) + T_n' J_n'(k_c(\omega)r_{out}^i)}. \quad (\text{C.13})$$

C.1 Numerical test

When SC are made of scatterers of complex geometrical shapes, an analytical solution following similar methodologies as the ones shown in this Appendix could not be possible. In this situation, the finite element method (FEM) or finite difference time domain (FDTD), can be good alternatives to solve the problem. In this Section we test the solution obtained using the commercial package of FEM, COMSOL 3.5, in the case of rigid cores covered by absorbing material.

The model introduces the Delany-Bazley model as the type of damping in the domain of the absorbent material. Moreover the numerical domain is surrounded by a PML region in order to avoid reflections of the boundaries.

We compare our numerical and analytical results with the ones previously obtained by Umnova *et al.* in their work of 2006 [Umnova06]. An array of 7 by 3 scatterers in a square array with lattice constant $a = 1.5$ cm is analysed in this Section. The scatterers present a rigid core with an inner radius of $r_{in} = 0.635$ cm and the thickness of the wollen felt is $t = 0.175$ cm, thus the exterior radius of the scatterer is $r_{out} = 0.98$ cm. The source is placed 1.5 m away from the crystal and the receiver is at 3 cm away from the crystal. The disposition is the same as in Figure 9 of reference [Umnova06].

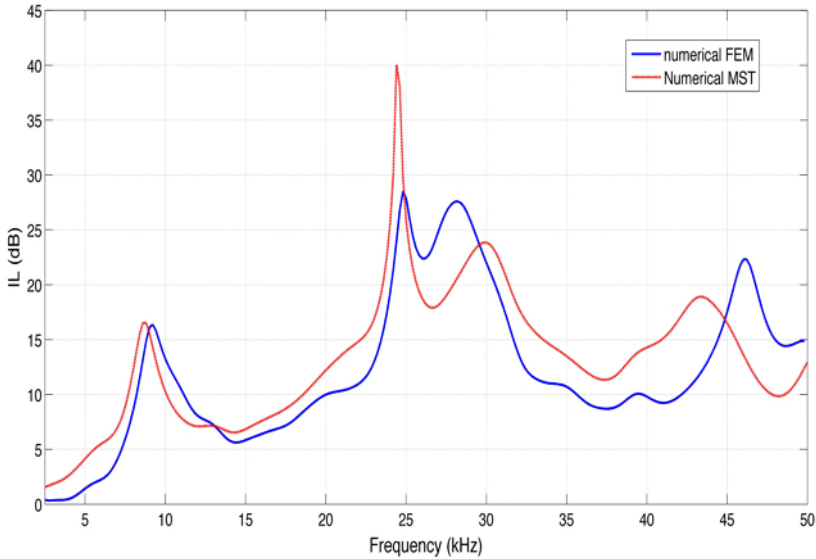


Figure C.2: IL of a finite SC made of absorbent scatterers of size $7a \times 3a$ with $a = 0.015\text{m}$ in the direction of incidence ΓX . Blue line represents the results obtained using FEM model and red dashed line represents the IL obtained using MST with absorbent boundary conditions.

Figure C.2 shows the IL obtained using both models FEM model (blue line) and MST with absorbing boundary conditions (red dashed line). One can observe that both models represent the same behaviour of the IL. All the attenuation peaks appear at the same positions in both models except those at a very high frequency. This discrepancy could be produced by the size of the mesh in FEM model. The agreement with the results shown in the work of Umnova *et al.* is very good.

Thus, we are confident with our two approaches and we will use them in our study of periodic systems made of absorbent scatterers.

D

Appendix: Vibration of an elastic beam

Equation 8.1 can be solved by means of the separation of variable technique. Then, we can separate the temporal part of the Equation, by obtaining the next spatial Equation,

$$\frac{\partial^4 X(x)}{\partial x^4} - k_n^4 X(x) = 0 \quad (\text{D.1})$$

To solve this Equation we present the boundary conditions of the problem. We consider that the elastic bar has a free end and the other end is fixed. The fixed end must have zero displacement and zero slope due to the clamp. The free end cannot have a bending moment or a shearing force. Then,

$$x = 0 \implies \begin{cases} X(0) = 0 \\ \frac{\partial X(0)}{\partial x} = 0 \end{cases}$$

$$x = L \implies \begin{cases} \frac{\partial^2 X(L)}{\partial x^2} = 0 \\ \frac{\partial^3 X(L)}{\partial x^3} = 0. \end{cases}$$

The general solution for D.1 is a combination of sines, cosines and hyperbolic sines and cosines. The application of the boundary condition and considering

that the dynamic solution for the displacement must be equal to the static solution at time $t=0$, we can find,

$$X_n(x) = \frac{1}{2} (\cos(k_n x) - \cosh(k_n x)) + \frac{1}{2} \left(\left(\frac{-\cos(k_n L) - \cosh(k_n L)}{\sin(k_n L) + \sinh(k_n L)} \right) (\sin(k_n x) - \sinh(k_n x)) \right).$$

Considering that the elastic bar starts its vibration when is displaced of its resting point, the displacement can be expressed [voltera65]

$$v(x, t) = X_n(x) A_n \cos(\omega_n t), \quad (\text{D.2})$$

where

$$A_n = \frac{-4PL}{EI \lambda_n k_n^4 (\sin(k_n L) e^{k_n L} + e^{2k_n L} - 1)} \\ ((3 \sin(k_n L) (e^{2k_n L} + 1) - (2(k_n L)^3) e^{k_n L}) + \cos(k_n L) (3 - (k_n L)^3 (e^{2k_n L} + 1)) - 3e^{2k_n L}).$$

P is the applied force in the free end perpendicularly to the long side of the elastic bar.

E

Publications

E.1 International Journals

1. Romero-García, V.; Sánchez-Pérez, J.V.; Garcia-Raffi, L.M.
Propagating and evanescent properties of double-point defects in Sonic Crystals.
New Journal of Physics, **12**, 083024, (14 pp.), 2010
2. Romero-García, V.; Sánchez-Pérez, J.V.; Garcia-Raffi, L.M.
Evanescent modes in sonic crystals: complex dispersion relation and supercell approximation.
Journal of Applied Physics, **108**, 044907, (6 pp.), 2010
3. Romero-García, V.; Sánchez-Pérez, J.V.; Castiñeira-Ibáñez, S.; Garcia-Raffi, L.M.
Evidences of evanescent Bloch waves in phononic crystals.
Applied Physics Letters, **96**, 12402-1 124102-3, 2010
4. Romero-García, V.; Sánchez-Pérez, J.V.; Garcia-Raffi, L.M.; Herrero, J.M.; García-Nieto, S.; Blasco, X.

- Holes distribution in phononic crystals: Design and optimization.
Journal of the Acoustic Society of America, **125**, 3774-3783, 2009
5. Herrero, J.M.; García-Nieto, S.; Blasco, X.; Romero-García, V.; Sánchez-Pérez, J.V.; Garcia-Raffi, L.M.
Optimization of sonic crystals attenuation properties by ev-MOGA multiobjective evolutionary algorithm
Structural and Multidisciplinary Optimization, **39**, (2), 203, 2009
 6. Romero-García, V.; Sánchez-Pérez, J.V.; Garcia-Raffi, L.M.; Herrero, J.M.; García-Nieto, S.; Blasco, X.
Attenuation properties of acoustic metamaterials by means of the creation of defects.
Applied Physics Letters, **93**, 223502, 2008
 7. Romero-García, V.; Fuster-Garcia, E.; Sánchez-Pérez, J.V.; Garcia-Raffi, L.M.;
Interferometric method to determine the refraction index of two dimensional sonic crystals.
Physical Review B, **75**, 224305, 2007
 8. Fuster-Garcia, E.; Romero-García, V.; Sánchez-Pérez, J.V.; Garcia-Raffi, L.M.;
Targeted band gap creation using mixed sonic crystals arrays including resonators and rigid scatterers.
Applied Physics Letters, **90**, 244104, 2007
 9. Romero-García, V.; Fuster-Garcia, E.; Garcia-Raffi, L.M.; Sánchez-Pérez, E.A.; Sopena, M.; Linares, J.; Sánchez-Pérez, J.V.
Band gap creation using quasi-ordered structures based on sonic crystals

tals.

Applied Physics Letters, **88**, 174104, 2006

10. Fuster-Garcia, E.; Romero-García, V.; Garcia-Raffi, L.M.; Sánchez-Pérez, E.A.; Sopena, M.; Sánchez-Pérez, J.V.

A phenomenological model for sonic crystals based on artificial neural networks.

Journal of Acoustical Society of America, **120**, (2), 1, 2006

E.2 International meetings

1. Romero-García, V.; Sánchez-Pérez, J.V.; Garcia-Raffi, L.M.
Sonic Crystal Acoustic Barriers based on scatterers with added acoustical properties.
39th International Congress on Noise Control Engineering
Lisboa, Portugal, 2010
2. Romero-García, V.; Sánchez-Pérez, J.V.; Krynkin, A.; Garcia-Raffi, L.M.
The behaviour of sonic crystal barrier made of resonant scatterers
Euronoise.
Edimburg, 2009
3. Romero-García, V.; Krynkin, A.; Sánchez-Pérez, J.V.; Castiñeira-Ibáñez, S.; Garcia-Raffi, L.M.
On the Numerical Modeling of Elastic Resonant Acoustic Scatterers.
European COMSOL Conference
Milán, 2009

4. Romero-García, V.; Fuster-Garcia, E.; Sánchez-Pérez, J.V.; Garcia-Raffi, L.M.
Acoustic Barriers based on Sonic Crystals.
ASME International Design Engineering Technical Conferences and
Computers Information in Engineering Conferences
Las Vegas, Nevada (U.S.A.), 2007

5. Fuster-Garcia, E.; Romero-García, V.; Garcia-Raffi, L.M.; Sánchez-Pérez, E.A.; Sánchez-Pérez, J.V.;
Mathematical techniques for the design of band gap materials.
ASME International Design Engineering Technical Conferences and
Computers Information in Engineering Conferences
Las Vegas, Nevada (U.S.A.), 2007

6. Romero-García, V.; Fuster-Garcia, E.; Garcia-Raffi, L.M.; Sánchez-Pérez, J. V.; Blasco, X.; Herrero, J.M. Genetic Algorithm in the optimization of the Acoustic Attenuation Systems.
9th International Work-Conferences on Artificial neural networks, IWANN
San Sebastián, 2007

7. Romero-García, V.; Fuster-Garcia, E.; Garcia-Raffi, L.M.; Sánchez-Pérez, E.A.; Sánchez-Pérez, J.V.;
Band Gap creation using quasi ordered structures based on sonic crystals.
151st Meeting of the Acoustical Society of America
Providence, Rhode Island (U.S.A), 2006

E.3 Invited Conferences

1. Optimization of the acoustic attenuation capabilities of sonic crystals: Genetic Algorithms.
University of Salford, Manchester, 2008

2. Absorción acústica en materials porosos.
Universidad de Ciudad Real
Ciudad Real, 2008

E.4 Awards

1. **Acoustical Society of America**
Second Place Best Student Paper Award in Engineering Acoustics.
151st meeting of the A.S.A. Rhode Island. 2006.

2. **European Acoustics Association**
EAA Best paper presentation Award for young researchers for Euronoise.
Edinburgh. 2009.

E.5 Patents

1. Inventors: Castiñeira-Ibáñez, S.; Garcia-Raffi, L.M.; Romero-García, V.; Sánchez-Pérez, J.V.

Title: Pantalla acústica modular, portátil y con aspecto escultórico basada en cristales de sonido.

Country: Spain

Main Entity: Universidad Politécnica de Valencia.

Abbreviations

A	Asymmetry
AA	Attenuation area
ABC	Absorbing boundary conditions
AS	Attenuation spectrum
BG	Band gaps
EA	Evolutionary algorithms
EB	Elastic beams
EM	Electromagnetic/Electromagnetism
EPWE	Extended plane wave expansion
evMOGA	Epsilon variable multi-objective genetic algorithms
ff	Filling fraction
FA	Focusing area
FEM	Finite Element Methods
FDTD	Finite Differences Time Domain
GA	Genetic Algorithms
IP	Ideal Point
IL	Insertion Loss
LDPE	Low density polyethylene
LRAM	Locally resonant acoustic metamaterial
MOGA	Multi-objective genetic algorithms
MOP	Multi-objective problems
MST	Multiple Scattering Theory
PC	Phononic crystals
PF	Pareto fronts

PML	Perfectly matched layers
PWE	Plane wave expansion
QOS	Quasi-ordered structures
SC	Sonic crystals
SCAB	Sonic crystal acoustic barrier
SRR	Split ring resonators
1D	One dimensional
2D	Two dimensional
3D	Three dimensional
3DReAMS	Three dimensional e-Acoustic Measurement System

Symbols

N	Number of scatterers in complete SC
N_{cyl}	Number of scatterers in a structure
N_p	Number of point defects
\vec{R}	Lattice
\vec{a}_i	vectors of the primitive cell
\vec{b}_i	reciprocal vectors of the primitive cell
ϵ_{ijk}	completely antisymmetric Levi-Civita symbol
a	Lattice constant
\vec{k}	Bloch's vector
$\phi_{\vec{k}}$	Bloch state
\vec{G}	vector of the reciprocal lattice
p	pressure
ω	angular frequency
c	sound velocity
ρ	density
v	frequency
λ	wavelength
γ_A	distribution of symmetry
$\delta_{ss'}$	Kronecher's delta
B	bulk modulus

A_{uc}	Area of the unit cell
A_{cyl}	Area of the scatterer
J	Cost function
N_f	Number of discrete frequencies in a predetermined range
F_v	Fraction of vacancies
O_f	Optimization factor
i	imaginary unit

List of Figures

1.1	Kinematic sculpture by Eusebio Sempere placed at the Juan March Foundation in Madrid.	2
2.1	Examples of periodic systems: (A) 1D, (B) 2D and (C) 3D. The Figures correspond to Photonic crystals.	19
2.2	2D periodic systems. (A) 2D lattices. (B) Square lattice. (C) Triangular lattice (also called hexagonal lattice).	20
2.3	Band Structure of a square lattice of rigid cylinders with radius $r = 0.07$ m and lattice constant $a = 0.15$ m. $ff \simeq 68.4\%$.	24
2.4	Band Structure of rigid cylinders. (A) Square lattice with infinitesimal radius and lattice constant $a = 0.15$ m in air. (B) Square lattice with $r = 0.03$ m and lattice constant $a = 0.15$ m. (C) Square lattice with $r = 0.07$ m and lattice constant $a = 0.15$ m.	27
2.5	Isofrequency surfaces of the first transmission band for the square lattice with lattice constant $a = 0.15$ m and (A) infinitesimal radius, (B) $r = 0.03$ m and (C) $r = 0.07$ m	28
2.6	Complex band structures for a SC with square lattice with lattice constant $a = 0.15$ m and cylindrical scatterers with radius $r = 0.06$ m	30

LIST OF FIGURES

2.7	Absolute value of the pressure inside SC in the positions between two rows. Blue squares represent these values for a frequency outside of the BG, 442 Hz. Red circles represent these values for a frequency in the BG, 920 Hz. The green line represents a decay exponential fit to the evanescent mode inside the BG. The black continuous line represents the absolute values of the pressure obtained using the Finite Element Methods.	31
2.8	Point defects in 2D periodic systems. (A) Scatterer in an interstitial position. (B) Vacancy by removing a scatterer. (C) Scatterer of different material placed in an interstitial position. (D) Scatterer of different material placed in a position of the periodic system.	33
2.9	Localization for a localization frequency of 1340 Hz. Left panel: Pressure field inside the vacancy in a square lattice with $a = 0.15\text{m}$ and $r = 0.075\text{m}$. Right panel: Sound pressure spectrum calculated in the center of the cavity. Results obtained using the Finite Element Method.	34
2.10	Waveguides. Guided wave with frequency $\nu = 1260$ Hz, inside a lattice square with lattice constant $a = 0.15$ m and $r = 0.05$ m.	36
2.11	Attenuation Area (AA). The attenuation area is plotted in blue between the frequencies 2100 and 4800 Hz.	39
3.1	Notation used for the addition theorems.	46
3.2	Maps and spectra of absolute values of pressure calculated using MST for a plane wave impinging on the crystal. (A) Acoustic field produced by the scattering of waves in a SC with square lattice in the ΓX direction for the frequency inside the pseudogap at $ka = \pi$. (B) Acoustic field produced by the scattering and the incidence waves in a SC with square lattice in the ΓM direction for the frequency inside the pseudogap at $ka = 4$. (C) Spectra for the ΓX (blue line) and ΓM (red line) direction, calculated at the point $(x/a, y/a) = (11, 5)$	49

3.3 Maps and spectra calculated using MST for a cylindrical wave impinging a $5a \times 5a$ square array of rigid cylinders with a filling fraction $ff = 50\%$. (A) map for a frequency $ka = \pi$ inside the pseudogap at ΓX direction. (B) map for a frequency $ka = 4$ inside the pseudogap at ΓM direction. (C) Blue line (Red line) represents the spectrum for the ΓX (ΓM) direction measured at the point $(x/a, y/a) = (11, 0)$ from the source location. 55

3.4 Band Structure for a SC made of rigid cylinders in square array with lattice constant a and filling fraction $ff = 50\%$. Central panel: Band structures calculated using PWE. Left panel: Spectrum for the ΓX direction of a finite array of size $5a \times 5a$ with $ff = 50\%$. Right panel: Spectrum for the ΓM direction of a finite array of size $5a \times 5a$ with $ff = 50\%$. Spectra measured at a point situated a distance $0.6a$ from the end of the crystal and in the symmetry axis. 59

3.5 Band Structure for a SC made of rigid cylinders in square array with lattice constant a and filling fraction $ff = 50\%$. (A) Left panel: Band structures calculated using PWE. Right panel: Complex band structures for the ΓX direction calculated using EPWE. (B) Left panel: Complex band structures for the ΓM direction calculated using EPWE. Right panel: Band structures calculated using PWE. 62

3.6 Examples of both square and triangular supercells. 65

3.7 Unit cells for both square and triangular lattices. The periodic boundary conditions applied at the borders of each unit cell are shown. The cylinders are considered rigids then Neumann boundary condition are considered in their surface. 69

3.8 Band structure for both square and triangular lattices. The radius of the scatterer is $r = 0.4a$ in both cases. Blue continuous lines represent band structures calculated using FEM and open red circles show the same ones calculated using PWE. . . 71

LIST OF FIGURES

3.9 FEM calculations considering radiation boundary condition. A cylindrical source is considered at point $(x/a, y/a) = (0, 5)$. (A) Acoustic field produced by the scattering of waves for a SC with square lattice in the ΓX direction for the frequency inside the pseudogap at $ka = \pi$. (B) Acoustic field produced by the scattering and the incidence waves in a SC with square lattice in the ΓM direction for the frequency inside the pseudogap at $ka = 4$. (C) Spectra for the ΓX and ΓM direction, calculated at point $(x/a, y/a) = (11, 5)$ 73

3.10 FEM calculations considering the PML regions. A cylindrical source is considered at point $(x/a, y/a) = (0, 5)$. (A) Acoustic field produced by the scattering of waves for a SC with square lattice in the ΓX direction for the frequency inside the pseudogap at $ka = \pi$. (B) Acoustic field produced by the scattering and the incidence waves in a SC with square lattice in the ΓM direction for the frequency inside the pseudogap at $ka = 4$. (C) Spectra for the ΓX and ΓM direction, calculated at point $(x/a, y/a) = (11, 5)$ 75

4.1 (A) SC used as acoustic barrier; (B) Classical acoustic barrier. 78

4.2 Flowchart of fundamental procedures of genetic algorithms . . 82

4.3 Examples of a starting SC (A) and a QOS (B). The chromosomes are also shown at the bottom of the Figure. From the phenotype, we plot the distribution of the cylinders (see text). . 84

4.4 Creation of vacancies in a SC; (a) X-symmetric; (b) Y-symmetric; (c) XY-symmetric; (d) non symmetric. 85

4.5 Application of the genetic operators from two Parents. (A) Parent 1 and (B) Parent 2. The application of the crossover operator using the multi-point procedure generates Offspring as shown in (C) and (D). The application of the mutation operator over the Offspring produces the final individuals as shown in (E) and (F). 89

4.6 Example of a multi-objective optimization problem with two-dimensional decision and objective space. 92

4.7 The concept of ϵ -dominance. ϵ -Pareto Front $J(\hat{\Theta}_P^*)$ in a two-dimensional problem. J_1^{min} , J_2^{min} , J_1^{max} , J_2^{max} , limits space; ϵ_1 , ϵ_2 box widths; and n_box_1 , n_box_2 , number of boxes for each dimension. 95

4.8 *ev-MOGA* algorithm structure. $P(t)$, the main population; $A(t)$, the archive; $G(t)$ the auxiliary population. 97

4.9 Objective function space areas (Z) and limits (J). Showing (a) two-dimensional case (b) three-dimensional case. 99

4.10 Master/Slave architecture for *ev-MOGA*. 101

5.1 Schematic view of the distribution of the source, frame, microphone, FFT analyser and PC in the laboratory. 105

5.2 Pictures of the distribution of the source, microphone and frame in the anechoic chamber. The hanging system can also be seen. 105

5.3 Schematic view of both triangular and square frames. Detailed picture of the SC once the scatterers are hung. 106

5.4 Detail of the robotized system 109

5.5 Schematic view of the control of the robot. 110

5.6 The upper line group shows the horizontal directivity characteristics of the source provided by the manufacturer measured at 1 m. The lower curve shows the system's power response. . 113

5.7 Pictures of scatterers analysed in this work. A) Ballon. B) Rigid Scatterer (Aluminium). C) Rigid Scatterer (PVC). D) Split Ring Resonator (SRR) (PVC). E) U-profiles, front and back of the scatterer. 115

5.8 Transversal view of the U-profile scatterer. Dimensions of different parts of the profile are indicated in the picture. . . . 115

LIST OF FIGURES

- 6.1 Band Structures versus experimental results for a complete SC and for a SC with a defect point. (A) Left panel: Complex Band Structure calculated using the EPWE with the supercell approximation. Central panel: Real Band Structure. Dashed line represents the localized mode. Right panel: Experimental Insertion Loss in the Band Gap of both the complete SC (dashed line) and the SC with a point defect (continuous line). The inset shows the supercell used in the calculations. Red Square marks the value of the imaginary part of the wave vector $Im(k) = -5.6 \text{ m}^{-1}$. (B) Band structures for a complete SC. 120
- 6.2 3D spectra for the SC with a point defect. Measured 3D spectra for all the points inside the inner path in the SC with a point defect. 122
- 6.3 Acoustic field inside the point defect calculated using FEM (A) and experimentally measured (B). 123
- 6.4 Acoustic pressure inside a 5×5 SC with square array with lattice constant $a = 22 \text{ cm}$, for a frequency in the BG of 920 Hz. Black continuous line (connected red open circles) represents the absolute values of the numerical (experimental) pressure inside the SC. Red dashed line represents the fitting of the exponential decay of the measured acoustic field inside the SC. The inset represents the measurement points inside the SC and both the complex and real band structures. 124
- 6.5 3D spectra for a complete SC. 3D experimental spectra for all the points inside the inner path in the SC. 125
- 6.6 Absolute values of the acoustic field inside the SC with and without point defect. Numerical maps calculated by FEM inside the complete SC (A) and inside the SC with a point defect (B). (C) Numerical and experimental results for the interior path marked in (A) and (B) with a continuous line. The dashed line (open circles) represents the numerical (experimental) results for the complete SC. The continuous line (open squares) represents the numerical (experimental) results for the SC with a point defect. 126

- 6.7 Absolute values of pressure inside a 6×5 SC with a point defect: Numerical results (continuous line), experimental results (open squares). The dashed line represents the fitted exponential-like decay of the localized mode using the open circles. 128

- 6.8 Dependence of the localized modes in multipoint defects on the number of single defects. Left panel: single defect, central panel: double point defect and right panel: triple point defect. . 129

- 6.9 Dependence of the localized modes on the distance between the single point defects in a double point defect. (A) single defect, (B) double point defect with $d = 2a$, (C) double point defect with $d = 3a$ and (D) double point defect with $d = 4a$. . 131

- 6.10 Real and Complex band structures for a SC with and without point defects. (a): Complex band structure of a complete SC calculated using EPWE with supercell approximation (left). Band structures calculated using PWE with supercell approximation of a SC with a point defect, the continuous red line represents the defect mode (center). Band Structures for a SC with a double point defect, the dashed green line represents the defect modes of a double point defect (right). The insets show the supercell used in the calculations. (b): Complex and real band structure of a double point defect. 134

- 6.11 Pressure maps of a double point defect separated by a distance of $d = 2a$. The $|p|$ values between two rows of the SC containing the point defects is also plotted. The pressure maps of the antisymmetric (A) and symmetric (B) coupling of the localized modes inside the double point defect. The arrows represent the values of $|p|$ in the midpoint between the two rows of cylinders containing the double point defect. 137

LIST OF FIGURES

- 6.12 Numerical (continuous line) and experimental (open circles) profile of the $|p|$ values between the two rows containing the double point defect (see Figure 6.11). (A) Antisymmetric mode ($\nu = 940$ Hz) and (B) symmetric mode ($\nu = 895$ Hz). The dashed line represents the exponential-like decay of the localized modes outside the double point defect fitted from the maximum values of the analytical data represented by open square points. 138
- 6.13 Spectra for a SC made of PVC cylinders arranged in $9a \times 5a$ with lattice constant $a = 0.22$ m in square array with a double point defect. (a) Spectrum measured inside one of the point-defect in the double point defect. (b) Spectrum measured outside the crystal at a distance of $10a$ from the start of the SC. 139
- 7.1 Starting SC consisting of hollow cylindrical aluminium rods, 1 m long mounted in a triangular pattern with lattice constant $a = 6.35$ cm. The diameter of the cylinders is $d = 4$ cm. The sample under study consists of an array of 6 rows with 10 cylinders per row, and rectangular external shape. 147
- 7.2 Spectra produced by the QOS resulting in the optimization of the Cost function $J_{\nu's}$ in the ranges (A) 1400-2000 Hz and (B) 1700-2300 Hz. The insets in the Figure represent the QOS obtained in the optimization process for each range of frequencies. The red line represents the theoretical spectrum calculated using MST, the blue open circles represents the experimental spectrum of the QOS and the green dashed line is the experimental spectrum of the complete SC (Starting SC). . 148
- 7.3 Starting conditions of the analysis. Starting SC (Left panel) and examples of each of the different strategies used in the creation of vacancies in the starting SC (right panel): (a) symmetry X, (b) symmetry Y, (c) symmetry XY and (d) no symmetry. 150

7.4 Insertion Loss spectra of the optimized QOS and of the starting SC. The optimized range of frequency is marked in the the white area. The optimization is obtained in a point situated 1 m behind the crystal. The inset shows the distribution of cylinders of the QOS. Upper panel: Results predicted by the MST. Lower panel: Experimental measurements 153

7.5 Acoustic field of the starting SC and the QOS for 1700 Hz, calculated using MST. (A) and (B) show the pressure maps of the starting SC and for the QOS respectively. (C) and (D) show the insertion loss maps for starting SC and for the QOS respectively. 154

7.6 Acoustic field produced by the QOS for several frequencies inside the optimized range of frequencies calculated using MST. Left panel: Pressure maps for the frequencies 1500, 1700 and 1900 Hz. Rigth panel: Insertion loss maps for the frequencies 1500, 1700 and 1900 Hz. 155

7.7 (A) Pareto fronts for the different symmetries of generation of vacancies used for the attenuation effect; (B) Attenuation area for each analysed symmetry. 157

7.8 Spectra of the resulting optimized samples: (A) Q1; (B) Q2; (C) Q3; and (D) Q4 shown in Figure 4(A) (continuous line); and of the starting SC (dotted line). The range of frequencies optimized is delimited by two vertical dashed lines. The attenuation average level in the optimized range of frequencies for each of the symmetries used is represented (horizontal dotted line). Configurations of the optimized samples corresponding to each Q-vector are included as an inset. 158

7.9 (A) Pareto fronts for the different vacancy generation symmetries used for focusing effect; (B) focusing area for each analysed symmetry. The points represent the value of the parameter for each of the optimized structures obtained and the line represents their average value. 161

LIST OF FIGURES

- 7.10 Acoustic level in the focusing area. On the OX axis, the distance along the direction of the incident wave is shown and the frequencies for the four strategies analysed on the OY axis are also shown. The colour bar represents the acoustic level in dBs. The corresponding samples are also included. 162
- 7.11 PF for the mixed method showing each of the steps in the optimization process. The PF for the independent nosym strategy is also represented. 164
- 7.12 (A) Attenuation spectra for the nosym samples corresponding to the points that define the IP of the PF. The corresponding structures are also represented at the top. (B) Best nosym structure obtained in the optimization process; theoretical and experimental attenuation spectra are represented. The spectrum of the initial sample is also included. 165
- 7.13 Comparison of the best result for each symmetry constraint. . 168
- 7.14 Attenuations spectra for points P1, P4, and P6 of the Pareto front in the symxy3 case. Mean attenuations have been calculated in the selected ranges of frequencies (from 2300 to 3700 Hz. 169
- 7.15 Attenuations for points P1 and P2 of the Pareto front in the symx3 case. Mean attenuations have been calculated in ranges [2300, 3700] Hz. 170
- 7.16 Attenuations for points P1 and P2 of the Pareto front in the symy3 case. Mean attenuations have been calculated in ranges [2300, 3700] Hz. 171
- 7.17 Attenuations for points P1, P7 and P9 of the Pareto front in the nosym3 case. Mean attenuations have been calculated in ranges [2300, 3700] Hz. 172
- 7.18 (A) asymmetry parameter and (B) fraction of vacancies for the analysed symmetries in the Attenuation case. The points represent the value of the parameter for each of the optimized structures obtained and the line represents their average value. 173

- 7.19 (A) Asymmetry parameter and (B) fraction of vacancies for the analysed symmetries in the case of the focusing devices. The points represent the value of the parameter for each of the optimized structures obtained and the line represents their average value. 174
- 7.20 Experimental measurement set up. The starting SC consists of hollow aluminium rods 1 m long and 4 cm in diameter arranged in a triangular pattern with constant lattice $a = 6.35$ cm. There are 397 cylinders. 175
- 7.21 (A) Attenuation area versus number of cylinders for both analysed cases. (B) Variation of the asymmetry of the nine structures obtained as a function of the vacancies created. The vertical lines represent the optimum number of vacancies. . . . 176
- 7.22 Comparison of attenuation spectra corresponding to the starting SC, and the best sample obtained by means of the creation of vacancies: (A) (2300 – 3700 Hz); (B) (2000 – 6500 Hz). The best corresponding structure obtained is shown in the inset. 178
- 8.1 Attenuation spectra of an array formed with five rows of ten balloons in triangular lattice and for two incident directions (0° (blue line) and 30° (red line)). (A) Lattice constant $a = 12.7$ cm and (B) lattice constant $a = 6.35$ cm. 185
- 8.2 Experimental acoustic attenuation spectra of both an array of six rows of ten aluminium cylinders and a mixed structure of 12 rows formed with the previous one plus six rows of ten cylindrical balloons. In both cases, the lattice constants are $a = 12.7$ cm, the incident direction is from left to right and the measurements were taken along the ΓX direction. (A) Schematic of the analysed mixed structure. (B) Acoustic attenuation obtained for the two structures (SC and mixed structure). 186

LIST OF FIGURES

- 8.3 Resonance of a single SRR obtained using FEM. The blue line (Blue open circles) represents the numerical (experimental) IL of the single SRR shown on the inset. The inset represents the localized pressure field in the cavity for the resonant frequency. 189
- 8.4 Band structures of a square lattice of both SRR and Rigid Scatterers. The red lines represent the band structures for the SC made of SRR, whereas the black lines represent the band structures for the same lattice made of rigid scatterers. 191
- 8.5 IL of a finite SC made of SRR of size $4a \times 4a$ with $a = 0.33$ m. Left panel: Blue line (Red line) represents the numerical predicted IL in the ΓX (ΓM) direction. Green dashed line represents the IL for the array of rigid cylinders in the ΓX direction. Central panel: Band structures of the SC made of SRR. Right panel: Red open circles (Blue open squares) represents the experimental measurements of the IL in the ΓX (ΓM) direction. Green crosses represent the experimental measurements of the IL for the rigid cylinders in the ΓX direction 192
- 8.6 Dependence of the resonance on the number of resonators and on the angle of incidence. Upper panel: IL of structures made from 1 to 4 rows of SRR. The angle of incidence is 0° (ΓX) direction. Central panel: Band structures of a periodic square array of SRR with $a = 0.33$ m. Lower panel: IL of structures made from 1 to 4 rows of SRR. The angle of incidence is 45° (ΓM) direction. 195
- 8.7 Experimental data. (A) IL of one U-profile. (B) and (C) show the IL of a SC made of different numbers of U-profiles in a triangular array, $a = 12.7$ cm, measured at 0° and 30° respectively. The inset shows the transversal view of a U-profile. . . 198

8.8 Eigenfrequencies of an elastic bar of LDPF, density $\rho = 100\text{kg}/\text{m}^3$, Young's modulus $E = 0.35\text{GPa}$ and Poisson's ratio $\nu = 0.4$. (A) Schematic view of the EB. (B) Graphical solution for Equation 8.2. The first four resonances of an elastic bar can be obtained from the plot. (C) Displacement of first vibrational mode and (D) Displacements of second mode. In (C) and (D) The continuous line represents the maximum displacement and the dotted line represents intermediate displacements. 199

8.9 Dependence of the first eigenfrequency on both the length and the width of the EB made of LDPF. 200

8.10 U-profile elastic scatterers. calculated using FEM. (A) Geometrical shape and parameters characterizing the size of the U-profile. (B) Acoustic field inside the cavity for the resonant frequency. 201

8.11 Pressure field distribution produced by the scattering of a plane wave of 1660 Hz by an U-profile. The PML regions are marked with the PML. 204

8.12 Numerical results of single scatterer. IL produced by a U-profile. The inset shows a image of the numerically modelled U-profile. 205

8.13 Schematic view of the numerical model to analyse the scattering problem of an array of U-profiles scatterers. 206

8.14 (A) Numerically predicted IL of an array of U-profile scatterers. (B) Measured IL of an array of U-profile scatterers. A plane wave impinges the structure from the left side to the right side. 207

8.15 Band Structures for a periodic arrangement of U-profiles in triangular lattice of $a = 12.7$ cm. Left panel: Black dashed line represents the band structures for a rigid U-profiles, whereas the blue line represents the bands for the elastic U-profile. The black surfaces indicate the non propagating ranges of frequencies. Right panel: Measured IL of a triangular lattice of elastic U-profiles measured in the two main symmetry directions, 0° (blue line) and 30° (red dashed line) 209

LIST OF FIGURES

8.16 Experimental results of a single scatterer. (A) IL (dB) measured behind the scatterer. Red dashed line represents the experimental results and Blue line represents the numerical simulation using FEM, (B) Experimental measurements of the vibration of the EB of the LDPE foam scatterer. Blue line represents 0° of incidence and red dashed line represents 30° of incidence. (C) Sound level map measured inside the cavity for the resonant frequency for $\nu = 1104$ Hz. Step $\Delta x = \Delta y = 1$ cm. 210

8.17 Experimental measurement of the IL for determining the dependence of the attenuation peaks on the number of scatterers. Open colored circles represent the IL for six structures made of different number of rows (from 1 to 6 rows of 10 cylinders per row). IL measured 1 m away from the end of the complete structure. (A) Measurement in the ΓX direction. (B) Measurements in the ΓJ direction. 211

8.18 Experimental measurement of the IL to determine the dependence of the attenuation peaks on the direction of incidence of the wave. Open coloured circles represent the IL for four different directions, 0° , 10° , 20° and 30° . IL measured 1m away from the end of the complete structure (6 rows of 10 cylinders per row). 213

8.19 Effective parameters. (A) Effective bulk modulus. Imaginary part is plotted in red line whereas real part is plotted in blue continuous line. (B) Dispersion relation. (C) Transmission coefficient for a slab of metamaterial with $L_{eff} = 0.66$ m. (D) Measured IL of an array of U-profiles. 217

9.1 Mixed structure proposed. (A) Resulting mixed structure proposed, QOS + balloons. (B) Attenuation spectra obtained for both structures, QOS with and without balloons, at 0° , (C) for the previous structures measured at 30° , and (D) for the mixed structure measured at 0° and 30° 224

9.2 Transversal view of the absorbent SRR. A rigid SRR core is covered by a layer of porous material. 227

9.3 Scattering and eigenvalue problem of a SCAB made of absorbent SRR of $4a \times 4a$ size. Upper panel: Red (Blue) line represents the IL in the ΓX (ΓM) direction of the SCAB made of absorbent SRR. Black line represents the Maekawa's predictions for a rigid wall with the same dimensions. Green dashed line represents the IL in the ΓX direction of a SC made of rigid cylinders. Lower panel: Band structures of the rigid SRR. Blue dashed line represents the Band Structures for the rigid SRR with external radius $r = 0.1$ m, inner radius $r = 0.095$ m and $L = 0.02$ m. Red line represents the band structures for the rigid SRR with external radius $r = 0.14$, inner radius $r = 0.095$ m and $L = 0.02$ m. 229

9.4 Dependence of the IL of a SCAB made of absorbent SRR on the number of rows and on the incidence direction. Blue line, green, cyan and red lines present the IL of the structures made of 1, 2, 3 and 4 rows respectively. Upper panel: IL for the ΓX direction (0°). Lower panel: IL for the ΓM direction (45°). Middel panel: Band structure for the rigid SRR with the same dimensions than the absorbent SRR. Red lines are the band structures for the rigid SRR with $r = 0.14$ m. 232

A.1 Notation used for the addition theorems. 244

B.1 Computational time of the pressure calculation by means of MST. Blue points represent the computational time measure by the computer. Blue line (Red Lie) represents a quadratic (cubic) fit. The residuals of both fits are also plotted in the Figure. 248

C.1 Transversal view of the absorbent scatterer. A rigid core is covered with a layer of porous material. 249

C.2 IL of a finite SC made of absorbent scatterers of size $7a \times 3a$ with $a = 0.015$ m in the direction of incidence ΓX . Blue line represents the results obtained using FEM model and red dashed line represents the IL obtained using MST with absorbent boundary conditions. 253

LIST OF FIGURES

List of Tables

3.1	Directions of incidence, ranges of k , and ranges of phase changes, $k \cdot R_1$ and $k \cdot R_2$, for each of the segments required to traverse the boundary of the irreducible first Brillouin zone for both square and triangular lattices.	70
4.1	Comparative values of the Pareto solutions (PS), generational distance (GD), hyperarea ratio (HR), spacing (SP) and box ratio (BR) metrics for the MOP1 to MOP5 problems between <i>ev-MOGA</i> and ϵ -MOEA algorithm. Bold numbers show the best values obtained for each metric and problem.	94
5.1	Elastic properties of Low Density Polyethylene Foam.	116
5.2	Experimental SC analysed in the work.	116
7.1	AA (Attenuation Area) and average attenuation for the QOSs obtained by means of a simple GA.	149
7.2	Optimization values obtained by independently analysing each of the considered symmetries.	159

Bibliography

- [Abarbanel99] S. Abarbanel, D. Gottlieb, and J. S. Hesthaveny. Well-posed perfectly matched layers for advective acoustics. *J. Compt. Physics*, 154:266, 1999.
- [Altug05a] H. Altug and J. Vuckovic. Experimental demonstration of the slow group velocity of light in two-dimensional coupled photonic crystal microcavity arrays. *Appl. Phys. Lett.* 86 (2005), 86, 2005.
- [Altug05b] H. Altug and J. Vuckovic. Photonic crystal nanocavity array laser. *Opt. Express*, 12:8819–8828, 2005.
- [Altug06] H. Altug, D. Englund, and H. Vuckovic. Ultra-fast photonic crystal nanolasers. *Nat Physics*, 2:484–488, 2006.
- [Anderson98] C.M. Anderson and K.P. Giapis. Larger two-dimensional photonic band gaps. *Phys. Rev. Lett.*, 77:2949, 1998.
- [Back94] T. Back. Selective pressure in evolutionary algorithm: a characterization of sejection mechanisms. *Proceedings of the First IEEE Conference on Evolutionary Computation, IEEE Press, Orlando*, pages 57–62, 1994.
- [Basu03] U. Basu and A.K. Chopra. Perfectly matched layers for time-harmonic elastodynamics of unbounded domains: theory and finite-element implementation. *Perfectly matched layers for time-harmonic elastodynamics of unbounded domains: theory and finite-element implementation*, 33:707–725, 2003.
- [Bayindir00] M. Bayindir, B. Temelkuran, and E. Ozbay. Tight-binding description of the coupled defect modes in three-dimensional photonic crystals. *Phys. Rev. Lett.*, 84:2140, 2000.
- [Becache04] E. Bécache, A.-S. Bonnet-Benn Dhia, and G. Legendre.

BIBLIOGRAPHY

- Perfectly matched layer for the convected helmholtz equation. *SIAM J. Numer. Anal.*, 42:409–433, 2004.
- [Berenguer94] J.P. Berenguer. A perfectly matched layer for the absorption of electromagnetic waves. *J. Compt. Physics*, 114:185, 1994.
- [Boroditsky99] M. Boroditsky, R. Vrijen, T. Krauss, R. Coccioli, R. Bhat, and E. Yablonovitch. Control of spontaneous emission in photonic crystals. *Proceedings of SPIE - The International Society for Optical Engineering*, 3621:190–197, 1999.
- [Brown93] E.R. Brown, C.D. Parker, and E. Yablonovitch. Radiation properties of a planar antenna on a photonic-crystal substrate. *J. Opt. Soc. Am. B*, 10:404, 1993.
- [Caballero01] D. Caballero, J. Sánchez-Dehesa, R. Martínez-Sala, C. Rubio, J. V. Sánchez-Pérez, L. Sanchis, and F. Meseguer. Suzuki phase in two-dimensional sonic crystals. *Phys. Rev. B*, 64:064303, 2001.
- [Caballero99] D. Caballero, J. Sánchez-Dehesa, C. Rubio, R. Martínez-Sala, J.V. Sánchez-Pérez, F. Meseguer, and J. Llinares. Large two-dimensional sonic band gaps. *Phys. Rev. E*, 60:R6316, 1999.
- [Cervera02] F. Cervera, L. Sanchis, J.V. Sánchez-Pérez, R. Martínez-Sala, C. Rubio, and F. Meseguer. Refractive acoustic devices for airborne sound. *Phys. Rev Lett.*, 88(2):023902–4, 2002.
- [Chen01] You-Yu Chen and Zhen Ye. Theoretical analysis of acoustic stop bands in two-dimensional periodic scattering arrays. *Phys. Rev. E*, 64:036616, 2001.
- [Chutinan03] A. Chutinan, S. John, and O. Toader. Diffractionless flow of light in all-optical microchips. *Phys. Rev. Lett.*, 90:123901, 2003.

- [Collino98] F. Collino and P. Monk. The perfectly matched layer in curvilinear coordinates. *SIAM J. Sci. Comput. (USA)*, 19:2061–2090, 1998.
- [Deb07] K. Deb. Current trends in evolutionary multi-objective optimization. *Int. J. Simul. Multidisci. Des. Optim.*, 1:1–8, 2007.
- [Economou93] E.N. Economou and M.M. Sigalas. Classical wave propagation in periodic structures: Cermet versus network topology. *Phys. Rev. B*, 48 (18):13434, 1993.
- [Ehrgott03] Matthias Ehrgott and Dagmar Tenfelde-Podehl. Computation of ideal and nadir values and implications for their use in mcdm methods. *European Journal of Operational Research*, 151:119–139, 2003.
- [Einspruch60] N. Einspruch and R. Truell. Scattering of plane transverse wave by a spherical obstacle in an elastic medium. *J. Appl. Phys.*, 31:806, 1960.
- [Elkady06] I. El-kady, M.M.R. Taha, and M.F. Su. Application of photonic crystals in submicrochips. *Appl. Phys. Lett.*, 88:253109, 2006.
- [Engelen09] R.J.P. Engelen, D. Mori, T. Baba, and L. Kuipers. Sub-wavelengths structure of the evanescent field of an optical bloch wave. *Phys. Rev. Lett.*, 102:023902, 2009.
- [Englund05] D. Englund, D. Fattal, E. Waks, G. Solomon, B. Zhang, T. Nakaoka, Y. Arakawa, Y. Yamamoto, and J. Vuckovic. Controlling the spontaneous emission rate of single quantum dots in a two-dimensional photonic crystal. *Phys. Rev. Lett.*, 95, 2005.
- [Espinosa07] V. Espinosa, V. J. Sánchez-Morcillo, K. Staliunas, I. Pérez-Arjona, and J. Redondo. Subdiffractive propagation of ultrasound in sonic crystals. *Phys. Rev. B*, 76:140302(R),

BIBLIOGRAPHY

- 2007.
- [Fang06] Nicholas Fang, Dongjuan Xi, Jianyi Xu, Muraliddhar Ambati, Werayut Srituravanich, Cheng Sun, and Xiang Zhang. Ultrasonic metamaterials with negative modulus. *Nature Materials*, 5:452–456, 2006.
- [Feng05] L. Feng, X.P. Liu, Y.B. Chen, Z.P. Huang, Y.W. Mao, Y.F. Chen, J.Z. Zi, and Y.Y. Zhu. Negative refraction of acoustic waves in two-dimensional sonic crystals. *Phys. Rev. B*, 72:033108, 2005.
- [Florescu09] M. Florescu, S. Torcuato, and P.J. Steinhardt. Designer disordered materials with large, complete band gaps. *PNAS*, 106:20658, 2009.
- [Garcia00] D. García-Pablos, M. Sigalas, F.R. Montero de Espinosa, M. Torres, M. Kafesaki, and N. García. Theory and experiments on elastic band gaps. *Phys. Rev. Lett.*, 84:4349–4352, 2000.
- [Garcia03] N. Garcia, M. Nieto-Vesperinas, E.V. Poniziovskaya, and M. Torres. Theory for tailoring sonic devices: Diffraction dominates over refraction. *Phys. Rev. E*, 67:036603, 2003.
- [Garcia05] N. Garcia, M. Nieto-Vesperinas, E.V. Poniziovskaya, and M. Torres. Reply to ‘‘comment on theory for tailoring sonic devices: Diffraction dominates over refraction’’. *Phys. Rev. E*, 71:018602, 2005.
- [GarciaVidal97] F. J. García-Vidal, J. M. Pitarke, and J. B. Pendry. Effective medium theory of the optical properties of aligned carbon nanotubes. *Phys. Rev. Lett.*, 78:4289, 1997.
- [Genack91] A.Z. Genack and N. Garcia. Observation of photon localization in a three-dimensional disordered system. *Phys. Rev. Lett.*, 66:2064, 1991.
- [Guenneau04] S. Guenneau and A.B. Movchan. Analysis of elastic band

- structures for oblique incidence. *Arch. Rational Mech. Anal.*, 171:129–150, 2004.
- [Guenneau07] Sébastien Guenneau, Alexander Movchan, Gunnar Pétursson, and S. Anantha Ramakrishna. Acoustic metamaterial for sound focusing and confinement. *New journal of Physics*, 9:399, 2007.
- [Hakanson05a] Andreas Hakansson and José Sánchez Dehesa. Optimal design of microscaled scattering optical elements. *Appl. Phys. Lett.*, 87:193506, 2005.
- [Hakansson04] A. Hakansson, J. Sánchez Dehesa, and L. Sanchis. Acoustic lens design by genetic algorithms. *Phys. Rev. B*, 70:214302, 2004.
- [Hakansson05] A. Hakansson, J. Sánchez-Dehesa, F. Cervera, F. Meseguer, L. Sanchis, and J. Llinares. Comment on “theory of tailoring sonic devices: Diffraction dominates over refraction”. *Phys. Rev. E*, 71:018601, 2005.
- [Hakansson05b] A. Hakansson, F. Cervera, and J. Sánchez-Dehesa. Sound focusing by flat acoustic lenses without negative refraction. *Appl. Phys. Lett.*, 86:054102, 2005.
- [Hakansson05c] Andreas Hakansson, José Sánchez-Dehesa, , and Lorenzo Sanchis. Inverse design of photonic crystal devices. *IEEE Journal on selected areas in communications*, 23(7):1365–1371, 2005.
- [Hakansson06] A. Hakansson, J. Sánchez-Dehesa, and F. Cervera. Experimental realization of sonic demultiplexing devices based on inverse designed scattering acoustic elements. *Appl. Phys. Lett.*, 88:163506, 2006.
- [Harari00] I. Harari, M. Slavutin, and E. Turkel. Analytical and numerical studies of a finite element pml for the helmholtz

BIBLIOGRAPHY

- equation. *J. Computat. Acoust.*, 8:121–137, 2000.
- [Herrero07] J.M. Herrero, X. Blasco, M. Martínez, C. Ramos, and J. Sanchis. Non-linear robust identification of a greenhouse model using multi-objective evolutionary algorithms. *Biosystems Engineering*, 98(3):335 – 346, 2007.
- [Herrero09] J. M. Herrero, S. García-Nieto, X. Blasco, V. Romero-García, J. V. Sánchez-Pérez, and L. M. Garcia-Raffi. Optimization of sonic crystal attenuation properties by ev-moga multiobjective evolutionary algorithm. *Struct. Multidisc. Optim.*, 39:203–215 203–215 203, 2009.
- [Hirsekorn04a] M. Hirsekorn. Small-size sonic crystal with strong attenuation bands in the audible frequency range. *Appl. Phys. Lett.*, 84(3364):3364, 2004.
- [Hirsekorn04b] M. Hirsekorn, P.P. Delsanto, N.K. Batra, and P. Matic. Modelling and simulation of acoustic wave propagation in locally resonant sonic materials. *Ultrasonics*, 42:231, 2004.
- [Hohage03] T. Hohage, F. Schmidt, and L. Zschiedrich. Solving time-harmonic scattering problems based on the pole condition ii: convergence of the pml method. *SIAM J. Math. Anal.*, 35:547–560, 2003.
- [Hsue05] Y.C. Hsue, A.J. Freeman, and B.Y. Gu. Extended plane-wave expansion method in three-dimensional anisotropic photonic crystals. *Phys. Rev B*, 72:195118, 2005.
- [Hu05] Xinhua Hu and C. T. Chan. Two-dimensional sonic crystals with helmholtz resonators. *Phys. Rev. E*, 71:055601, 2005.
- [Ignatowsky14] W. von Ignatowsky. Zur theorie der gitter. *Ann. Phys.*, 44:369, 1914.
- [John87] S. John. Strong localization of photons in certain disordered dielectric superlattices. *Phys. Rev. Lett.*, 58

- (23):2486, 1987.
- [John88] S. John, M.Y. Chou, M.H. Cohen, and C.M. Soukoulis. Density of states for an electron in a correlated gaussian random potential: Theory of the urbach tail. *Phys. Rev. B*, 37:6963, 1988.
- [John91] S. John. Localization of light. *Phys. Today*, 44:32, 1991.
- [Kafesaki00] M. Kafesaki, M.M. Sigalas, and N. Garcia. Frequency modulation in the transmittivity of ewave guides in elastic-wave band-gap materials. *Phys. Rev. Lett.*, 85 (19):4044, 2000.
- [Kafesaki99] M. Kafesaki and E.N. Economou. Multiple scattering theory for three-dimensional periodic acoustic composites. *Phys. Rev. B*, 60(17):11993, 1999.
- [Khelif02] A. Khelif, B. Djafari-Rouhani, J. O. Vasseur, P. A. Deymier, Ph. Lambin, and L. Dobrzynski. Transmittivity through straight and stublike waveguides in a two-dimensional phononic crystal. *Phys. Rev. B*, 65:174308, 2002.
- [Khelif03] A. Khelif, A. Choujaa, B. Djafari-Rouhani, M. Wilm, S. Ballandras, and V. Laude. Trapping and guiding of acoustic waves by defect modes in a full-band-gap ultrasonic crystal. *Phys. Rev. B*, 68:214301, 2003.
- [Khelif04] A. Khelif, M. Wilm, V. Laude, S. Ballandras, and B. Djafari-Rouhani. Guided elastic waves along a rod defect of a two-dimensional phononic crystal. *Phys. Rev. E*, 69:067601, 2004.
- [Kuo04] C.H. Kuo and Z. Ye. Sonic crystals lenses that obey the lensmaker's formula. *J. Phys. D: Appl. Phys.*, 37:2155, 2004.
- [Kushwaha93] M.S. Kushwaha, P. Halevi, L. Dobrzynski, and B. Djafari-Rouhani. Acoustic band structure of periodic elastic com-

BIBLIOGRAPHY

- posites. *Phys. Rev. Lett.*, 71(13):2022–2025, 1993.
- [Kushwaha94] M.S. Kushwaha, P. Halevi, G. Martínez, L. Dobrzynski, and B. Djafari-Rouhani. Theory of acoustic band structure of periodic elastic composites. *Phys. Rev. B*, 49(4):2313–2322, 1994.
- [Kushwaha96] M. S. Kushwaha and P. Halevi. Giant acoustic stop bands in two-dimensional periodic arrays of liquid cylinders. *Appl. Phys. Lett.*, 69(1):31–33, 1996.
- [Kushwaha97] M.S. Kushwaha. Stop-bands for periodic metallic rods: Sculptures that can filter the noise. *Appl. Phys. Lett.*, 70:3218, 1997.
- [Kushwaha97b] M. S. Kushwaha and P. Halevi. Stop bands for cubic arrays of spherical balloons. *J. Acoust. Soc. Am.*, 101:619, 1997.
- [Lassas98] M. Lassas and E. Somersalo. On the existence and convergence of the solution of pml equations. *Computing*, 60:228–241, 1998.
- [Laude09] V. Laude, Y. Achaoui, S. Benchabane, and A. Khelif. Evanescent bloch waves and the complex band structure of phononic crystals. *Phys. Rev. B*, 80:092301, 2009.
- [Li05] Xiaochun Li and Zhengyou Liu. Coupling of cavity modes and guiding modes in two-dimensional phononic crystals. *Solid State Communications*, 133:397–402, 2005.
- [Ling92] Ling Ye, George Cody, Minyao Zhou, Ping Sheng, and Andrew N. Norris. Observation of bending wave localization and quasi mobility edge in two dimensions. *Phys. Rev. Lett.*, 69:3080, 1992.
- [Linton90] C. M. Linton and D. V. Evans. The interaction of waves with arrays of vertical circular cylinders. *Journal of Fluid Mechanics*, 215:549–569, 1990.

- [Lions02] J.L. Lions and J. Méttral and O. Vacus. Well-posed absorbing layer for hyperbolic problems. *Numer. Math.*, 92:535–562, 2002.
- [Liu00] Zhengyou Liu, C. T. Chan, Ping Sheng, A. L. Goertzen, and J. H. Page. Elastic wave scattering by periodic structures of spherical objects: Theory and experiment. *Phys. Rev. B.*, 62:2446, 2000.
- [Liu00a] Z. Liu, X. Zhang, Y. Mao, Y.Y. Zhu, Z. Yang, C.T. Chan, and P.Sheng. Locally resonant sonic materials. *Science*, 289:1734, 2000.
- [Liu99] Q. H. Liu. Perfectly matched layers for elastic waves in cylindrical and spherical coordinates. *J. Acoust. Soc. Am.*, 105:2075–2084, 1999.
- [Lu06] Z. Lu, S. Shi, J. A. Murakowski, G. J. Schneider, C. A. Schuetz, and D. W. Prather. Subdiffractive band-edge solitons in bose-einstein condensates in periodic potentials. *Phys. Rev. E*, 73:065603(R), 2006.
- [Martinez06] R. Martínez-Sala, C. Rubio, L.M. Garcia-Raffi, J.V. Sánchez-Pérez, E.A. Sánchez-Pérez, and J. Llinares. Control of noise by trees arranged like sonic crystals. *Jour. Sound Vib.*, 291:100, 2006.
- [Martinez95] R. Martínez-Sala, J. Sancho, J. V. Sánchez, V. Gómez, J. Llinares, and F. Meseguer. Sound attenuation by sculpture. *Nature*, 378:241, 1995.
- [Martorell90] J. Martorell and N.M. Lawandy. Observation of inhibited spontaneous emission in a periodic dielectric structure. *Phys. Rev. Lett.*, 65:1877, 1990.
- [Meade91] Robert D. Meade, Karl D. Brommer, Andrew M. Rappe, and J. D. Joannopoulos. Photonic bound states in periodic dielectric materials. *Phys. Rev. B*, 44:13772, 1991.

BIBLIOGRAPHY

- [Meade92] D.M. Meade, K.D. Brommer, A.M. Rappe, and J.D. Joannopoulos. Existence of a photonic band gap in two dimensions. *Appl. Phys. Lett.*, 61 (4):495, 1992.
- [Meade94] R.D. Meade, A. Devenyi, J.D. Joannopoulos, O.L. Alerhard, D.A. Smith, and K. Kash. Novel applications of photonic band gap materials: Low-loss bends and high q cavities. *J. Appl. Phys.*, 75:4753, 1994.
- [Mei03] J. Mei, Z. Liu, J. Shi, and D. Tian. Theory for elastic wave scattering by a two-dimensional periodical array of cylinders. *Phys. Rev. B*, 67:245107, 2003.
- [Mishra05] S. Mishra, K. Deb, and M. Mohan. Evaluating the ϵ -domination based multi-objective evolutionary algorithm for a quick computation of pareto-optimal solutions. *Evolutionary computation*, 13(4):501–526, 2005.
- [Movchan04] A.B. Movchan and Guenneau. Split-ring resonators and localized modes. *Phys. Rev B*, 70:125116, 2004.
- [Navon04] I.M. Navon, B. Neta, and M.Y. Hussaini. A perfectly matched layer approach to the linearized shallow water equations models. *Monthly Weather Review*, 132:1369–1378, 2004.
- [Pendry96] J. B. Pendry, A. J. Holden, W. J. Stewart, and I. Youngs. Extremely low frequency plasmons in metallic mesostructures. *Phys. Rev. Lett.*, 76(25):4773–4776, 1996.
- [Pendry99] J.B. Pendry, A.J. Holden, W.J. Stewart, and I. Youngs. Magnetism from conductors, and enhanced non-linear phenomena. *IEEE Trans. Microw. Theory Tech.*, 47:2975, 1999.
- [Pennec04] Y. Pennec, B. Djafari-Rouhani, J. O. Vasseur, A. Khelif, and P. A. Deymier. Tunable filtering and demultiplexing in phononic crystals with hollow cylinders. *Phys. Rev. E*,

- 69:046608, 2004.
- [Perez07] I. Pérez-Arjona, V. J. Sánchez-Morcillo, J. Redondo, V. Espinosa, and K. Staliunas. Theoretical prediction of the nondiffractive propagation of sonic waves through periodic acoustic media. *Phys. Rev. B*, 75(014304):014304, 2007.
- [Psarobas00] I.E. Psarobas, N. Stefanou, and A. Modinos. Phononic crystals with planar defects. *Phys. Rev. B*, 62:5536, 2000.
- [Qi98] Q. Qi and T.L. Geers. Evaluation of the perfectly matched layer for computational acoustics. *J. Comput. Phys.*, 139:166–183, 1998.
- [Rakich06] P. T. Rakich, M. S. Dahlem, S. Tandon, M. Ibanescu, M. Soljai, G. S. Petrich, J. D. Joannopoulos, L. A. Kolodziejski, and E. P. Ippen. Achieving centimetre-scale supercollimation in a large-area two-dimensional photonic crystal. *Nat. Mat.*, 5:93, 2006.
- [Robertson98] W. M. Robertson and J. F. RudyIII. Measurement of acoustic stop bands in two-dimensional periodic scattering arrays. *J. Acoust. Soc. Am.*, 104(2):694–699, 1998.
- [Romero06] V. Romero-García, E. Fuster, L. M. Garcia-Raffi, E. A. Sánchez-Pérez, M. Sopena, J. Llinares, and J. V. Sánchez-Pérez. Band gap creation using quasiordered structures based on sonic crystals. *Appl. Phys. Lett.*, 88:174104, 2006.
- [Romero08] V. Romero-García, J. V. Sánchez-Pérez, L. M. García-Raffi, J. M. Herrero, S. García-Nieto, and X. Blasco. High optimization process for increasing the attenuation properties of acoustic metamaterials by means of the creation of defects. *Appl. Phys. Lett.*, 93:223502, 2008.
- [Romero09] V. Romero-García, J. V. Sánchez-Pérez, L. M. Garcia-Raffi, J. M. Herrero, S. García-Nieto, and X. Blasco. Hole distribution in phononic crystals: Design and optimization.

BIBLIOGRAPHY

- J. Acoust. Soc. Am.*, 125 (6):3774–3783, 2009.
- [Romero10a] V. Romero-García, J.V. Sánchez-Pérez, S. Casti neira Ibáñez, and L.M. Garcia-Raffi. Evidences of evanescent bloch waves in phononic crystals. *Appl. Phys. Lett.*, 96:124102, 2010.
- [Romero10b] V. Romero-García, J.V. Sánchez-Pérez, and L.M. Garcia-Raffi. Evanescent modes in sonic crystals: Complex dispersion relation and supercell approximation. *J. Appl. Phys.*, 108:044907, 2010.
- [Rubio97] C. Rubio, J.V. Sánchez-Pérez, R. Martínez-Sala, and F. Cervera. Medida de las características de campo libre de una cámara anecoica. *Tecniacústica 1997*, pages 96–98, 1997.
- [Rubio99] C. Rubio, D. Caballero, J. V. Sánchez-Pérez, R. Martínez-Sala, J. Sánchez-Dehesa, F. Meseguer, and F. Cervera. The existence of full gaps and deaf bands in two-dimensional sonic crystals. *Journal of Lightwave Technology*, 17(11):2202–2207, 1999.
- [Ruffa92] A.A. Ruffa. Acoustic wave propagation through periodic bubbly liquids. *J. Acoust. Soc. Am.*, 91:1–6, 1992.
- [Sainidou05] R. Sainidou, N. Stefanou, I.E. Psarobas, and A. Modinos. A layer-multiple-scattering method for phononic crystals and heterostructures of such. *Computer Physics Communications*, 166:197–240, 2005.
- [Sainidou06] R. Sainidou and N. Stefanou. Guided and quasiguided elastic waves in phononic crystal slabs. *Phys. Rev. B*, 73:185301, 2006.
- [Sanchez02] J.V. Sánchez-Pérez, C. Rubio, R. Martínez-Sala, R. Sánchez-Grandia, and V. Gómez. Acoustic barriers based on periodic arrays of scatterers. *Appl. Phys.*

- Lett.*, 81:5240, 2002.
- [Sanchez98] J. V. Sánchez-Pérez, D. Caballero, R. Martínez-Sala, C. Rubio, J. Sánchez-Dehesa, F. Meseguer, J. Linares, and F. Gálvez. Sound attenuation by a two-dimensional array of rigid cylinders. *Phys. Rev. Lett.*, 80(24):5325–5328, 1998.
- [Sanchis01] L. Sanchis, F. Cervera, J. Sánchez-Dehesa, J. V. Sánchez-Pérez, C. Rubio, and R. Martínez-Sala. Reflectance properties of two-dimensional sonic band gap crystals. *Jour. Ac. Soc. Am.*, 109:2598–2605, 2001.
- [Schwartz07] T. Schwartz, G. Bartal, S. Fishman, and M. Segev. Transport and anderson localization in disordered two-dimensional photonic lattices. *Nature*, 446:52, 2007.
- [Shang88] T. Shang and L. Gao. Transportation theory of multiple scattering and its application to seismic coda waves of impulsive source. *Sci. Sin., Ser. B*, 31:1503, 1988.
- [Shen01] M. Shen and W. Cao. Acoustic band-gap engineering using finite-size layered structures of multiple periodicity. *Appl. Phys. Lett.*, 75:3713–3715, 2001.
- [Sheng07] Ping Sheng, Jun Mei, Zhengyou Liu, and Weijia Wen. Dynamic mass density and acoustic metamaterials. *Physica B*, 394:256–261, 2007.
- [Sigalas00] M.M. Sigalas and N. Garcia. Theoretical study of three dimensional elastic band gaps with the finite-difference time-domain method. *J. Appl. Phys.*, 87 (6):3122, 2000.
- [Sigalas05] Mihail Sigalas, Manvir S. Kushwaha, Eleftherios N. Economou, Maria Kafesaki, Ioannis E. Psarobas, and Walter Steurer. Classical vibrational modes in phononic lattices: theory and experiment. *Z. Kristallogr.*, 220:765–809, 2005.
- [Sigalas92] M.M Sigalas and E.N. Economou. Elastic and acoustic

BIBLIOGRAPHY

- wave band structure. *J. Sound Vib.*, 158:377, 1992.
- [Sigalas93] M. Sigalas and E.N. Economou. Band structure of elastic waves in two dimensional systems. *Solid State Commun.*, 86:141, 1993.
- [Sigalas94] M.M. Sigalas, E.N. Economou, and M. Kafesaki. Spectral gaps for electromagnetic and scalar waves: Possible explanation for certain differences. *Phys. Rev. B*, 50:3393, 1994.
- [Sigalas96] M.M. Sigalas and E.N. Economou. Attenuation of multiple-scattered sound. *Eurphys. Lett.*, 36:241, 1996.
- [Sigalas97] M. Sigalas. Elastic wave band gaps and defect states in two-dimensional composites. *J. Acoust. Soc. Am.*, 101:1256, 1997.
- [Sigalas98] M.M. Sigalas. Defect states of acoustic waves in a twodimensional lattice of solid cylinders. *J. Appl. Phys.*, 84:3026, 1998.
- [Soukoulis06a] Costas M. Soukoulis, Maria Kafesaki, and Eleftherios N. Economou. Negative-index materials: New frontiers in optics. *Adv. Mater.*, 18:1941–1952, 2006.
- [Suzuki61] K. Suzuki. X-ray studies on precipitation of metastable centers in mixed crystals NaCl-CdCl_2 . *J. Phys. Soc. Jpn.*, 16:67, 1961.
- [Tanaka07] Yukihiro Tanaka, Takafumi Yano, and Shin ichiro Tamura. Surface guided waves in two-dimensional phononic crystals. *Wave Motion*, 44:501–512, 2007.
- [Torcuato03] S. Torcuato and F.H. Stillinger. Local density fluctuations, hyperuniformity, and order metrics. *Phys. Rev. B*, 63:041113, 2003.
- [Torrent06] Daniel Torrent and José Sánchez-Dehesa. Effective pa-

-
- rameters of clusters of cylinders embedded in a nonviscous fluid or gas. *Phys. Rev. B*, 74:224305, 2006.
- [Torrent06a] D. Torrent, A. Hakansson, F. Cervera, and J. Sánchez-Dehesa. Homogenization of two-dimensional cluster of rigid rods in air. *Phys. Rev. Lett.*, 96:204302, 2006.
- [Torrent07] D. Torrent and J. Sánchez-Dehesa. Acoustic metamaterials for new two-dimensional sonic devices. *New journal of physics*, 9:323, 2007.
- [Tournat04] V. Tournat, V. Pagneux, D. Lafarge, and L. Jaouen. Multiple scattering of acoustic waves and porous absorbing media. *Phys. Rev. E*, 70:026609, 2004.
- [Tregoures02] N. Trégourès, R. Hennino, C. Lacombe, N.M. Shapiro, L. Margerin, M. Campillo, and B.A. van Tiggelen. Multiple scattering of seismic waves. *Ultrasonics*, 40:269, 2002.
- [Twersky51] V. Twersky. Multiple scattering of radiation by an arbitrary configuration of parallel cylinders. *J. Acoust.Soc. Am.*, 24(1):42, 1951.
- [Twersky62] V. Twersky. On scattering of waves by the infinite grating of circular cylinders. *IRE Trans. on Antennas and Propagation*, 10:737, 1962.
- [Umnova06] O. Umnova, K. Attenborough, and C. M. Linton. Effects of porous covering on sound attenuation by periodic arrays of cylinders. *J. Acoust. Soc. Am.*, 119(1), 2006.
- [Vasseur08] J. O. Vasseur, P. A. Deymier, B. Djafari-Rouhani, Y. Pennec, and A-C. Hladky-Hennion. Absolute forbidden bands and waveguiding in two-dimensional phononic crystal plates. *Phys. Rev.B*, 77:085415, 2008.
- [Vasseur97] J. O. Vasseur and P. A. Deymier. Propagation of acoustic waves in periodic and random two-dimensional composite media. *J. Matter. Res.*, 12:2207, 1997.
-

BIBLIOGRAPHY

- [Veselago67] V.G. Veselago. The electrodynamics of substances with simultaneously negative values of ϵ and μ . *Usp. Fiz. Nauk.*, 92:517, 1967.
- [Vlasov05] Y. A. Vlasov, M. O'Boyle, H. F. Hamann, and S. J. McNab. Active control of slow light on a chip with photonic crystal waveguides. *Nature*, 438:65–69, 2005.
- [Wang90] Xue-Hua Wang, Ben-Yuan Gu, Zhi-Yuan Li, and Guo-Zhwn Yang. Large absolute photonic band gaps created by rotating noncircular rods in two-dimensional lattices. *Phys. Rev. B*, 60:11417–11422, 1999.
- [Wang93] X. Wang, X.G. Zhang, Yu Qingliang, and B.N. Harmon. Multiple scattering theory for electromagnetic waves. *Phys. Rev. B*, 47:4161, 1993.
- [Wiersma97] D.S. Wiersma, P. Bartolini, A. Lagendijk, and R. Righini. Localization of light in a disordered medium. *Nature*, 390:671, 1997.
- [Wu01] F.G. Wu, Z.L. Hou, Z.Y. Liu, and Y.Y. Liu. Point defect states in two-dimensional phononic crystals. *Phys. Lett. A*, 292:198, 2001.
- [Wu03] Fugen Wu, Huilin Zhong, Shao Zhong, Zhengyou Liu, and Youyan Liu. Localized states of acoustic waves in three-dimensional periodic composites with point defects. *Eur. Phys. J. B*, 34:265–268, 2003.
- [Wu09a] L.Y. Wu, L.W. Chen, and C.M. Liu. Experimental investigation of the acoustic pressure in cavity of a two dimensional sonic crystal. *Physica B*, 404:1766, 2009.
- [Wu09b] Liang-Yu Wu, Lien-Wen Chen, and Chia-Ming Liu. Acoustic pressure in cavity of variously sized two-dimensional sonic crystal with various filling fraction. *Phys. Lett. A*, 373:1189–1195, 2009.

- [Wu88] R.S. Wu and K. Aki. Introduction: Seismic scattering in three-dimensionally heterogeneous earth. *Pure Appl. Geoph.*, 128:1, 1988.
- [Yablonovitch87] E. Yablonovitch. Inhibited spontaneous emission in solid-state physics and electronics. *Phys. Rev. Lett.*, 58:2059, 1987.
- [Yablonovitch88] E. Yablonovitch, T.J. Gmitter, and R. Bhat. Inhibited and enhanced spontaneous emission from optically thin algaas/gaas double heterostructures. *Phys. Rev. Lett.*, 61:2546, 1988.
- [Yablonovitch89] E. Yablonovitch and T.J. Gmitter. Photonic band structures: The face-centered-cubic case. *Phys. Rev. Lett.*, 63 (18):1950, 1989.
- [Yablonovitch91] E. Yablonovitch. Donor and acceptor modes in photonic band structure. *Phys. Rev. Lett.*, 67:3380, 1991.
- [Yablonovitch93] E. Yablonovitch. Photonic band-gap crystals. *J. Phys. Condens. Matter*, 5:2443, 1993.
- [Yang04] Suxia Yang, J. H. Page, Zhengyou Liu, M. L. Cowan, C.T. Chan, , and Ping Sheng. Focusing of sound in a 3d phononic crystal. *Phys. Rev. Lett.*, 93(2):024301, 2004.
- [Yang08] Tao Yang, Huanyang Chen, Xudong Luo, and Hongru Ma. Superscatterer: Enhancement of scattering with complementary media. *Opt. Expr.*, 16:18545, 2008.
- [Zachary09] C.E. Zachary and S. Torcuato. Hyperuniformity in point patterns and two-phase random heterogeneous media. *arXiv:0910.2172v2*, 2009.
- [Zaviska13] F. Zaviska. Über die beugung elektromagnetischer wellen an parallelen, unendlich langen kreisylindern. *Ann. Phys.*, 40:1023, 1913.

BIBLIOGRAPHY

- [Zeng01] Y.Q. Zeng, J.Q. He, and Q.H. Liu. The application of the perfectly matched layer in numerical modeling of wave propagation in poroelastic media. *Geophysics*, 66:1258–1266, 2001.
- [Zhang04] X. Zhang, Z.Y. Liu, Y.Y. Liu, and F.G. Wu. Defect states in 2d acoustic band-gap materials with bend-shaped linear defects. *Solid State Commun.*, 130:67, 2004.
- [Zhao09] Y.C. Zhao and L.B. Yuan. Characteristics of multi-point defect modes in 2s phononic crystals. *J. Phys. D: Appl. Phys.*, 42:015403, 2009.
- [Zhao09b] Yan-Cheng Zhao, Ya-Bin Wu, and Li-Bo Yuan. Characteristics of the localized modes in 2d phononic crystal with heterostructure point defect. *Phys. Scr.*, 80:065401, 2009.
- [Zhong05] Huilin Zhong, Fugen Wu, Xin Zhang, and Youyan Liu. Localized defect modes of water waves through two-dimensional periodic bottoms with point defects. *Physics Letters A*, 339:478, 2005.
- [alander02] J. Alander. An indexed bibliography of genetic algorithms & pareto and constrained optimization. *Tech Rep, Dpt of Information Technology, University of Vaasa*, 2002.
- [ashcroft76] N. W. Ashcroft and D. N. Mermin. *Solid State Physics*. Holt Rinehart and Winston New York, 1976.
- [back96] T. Back. *Evolutionary Algorithms in Theory and Practice: Evolution Strategies, Evolutionary Programming, Genetic Algorithms*. Oxford University Press, USA, 1996.
- [brillouin46] L. Brillouin. *Waves propagation in periodic structures. Electric Filters and Crystal lattices*. McGraw-Hill Book Company Inc., Dover Publications Inc., 1946.
- [cantupaz95] Erick Cantú-Paz. A survey of parallel genetic algorithms. Technical Report 97003, Illinois Genetic Algorithms Lab-

- oratory., 1997.
- [coello02] C. Coello, D. Veldhuizen, and G. Lamont. *Evolutionary algorithms for solving multi-objective problems*. Kluwer Academic Publishers, 2002.
- [coello04] C. Coello and G. Lamont. *Applications of Multiobjective Evolutionary Algorithms*. World Scientific, 2004.
- [coello05b] C. Coello, G. Toscano, and E. Mezura. Information processing with evolutionary algorithms. in: Granam,duro r, d'anjou a, wang pp (eds) information processing with evolutionary algorithms: from industrial applicationsto academic speculations. *Springer*, pages 213–231, 2005.
- [eshelman91] L. J. Eshelman. *The chc adaptive search algorithm: How to have safe search when engaging in nontraditional genetic recombination*. In Rawlins, G. J. E., editor, *Foundations of Genetic Algorithms-1*. Morgan Kauffman., 1991.
- [fonseca95] C. Fonseca. *Multiobjective genetic algorithms with application to control engineeringproblems*. PhD thesis, Dpt. of Automatic Control and Systems Engineering, University of Sheffield, 1995.
- [gaMatlab] Andrew Chipperfield, Peter Fleming, Hartmut Pohlheim, and Carlos Fonseca. *Genetic Algorithm TOOLBOX For Use with MATLAB*, version 1.2 edition.
- [gere97] J.M. Gere and S.P. Timoshenko. *Mechanics of Materials*. 4th ed. Boston: PWS Publishing Company, 1997.
- [goldberg89] D.E. Goldberg. *Genetic Algorithms in Search, Optimization, and machine Learning*. Addison-Wesley, reading, MA, 1989.
- [herrero06] Juan Manuel Herrero. *Non-linear robust identification using evolutionary algorithms*. PhD thesis, Universidad Politécnicade Valencia, Valencia, Spain, 2006.

BIBLIOGRAPHY

- [holland75] J.H. Holland. *Adaptation in natural and Artificial systems*. University of Michigan Press, Ann Arbor, MI, 1975; (MIT Press, Cambridge, MA, 1992), 1975.
- [ihlenburg98] F. Ihlenburg. *Finite Element Analysis of Acoustic Scattering*. Springer Verlag New York Inc, 1998.
- [joannopoulos08] John D. Joannopoulos, Steven G. Johnson, Joshua N. Winn, and Ronert D. Meade. *Photonic Crystals. Molding the Flow of Light*. Princeton University press, 2008.
- [kittel04] Charles Kittel. *Introduction to Solid State Physics*. Wiley; 8 edition (November 11, 2004), 2004.
- [kohn54] W. Kohn and N. Rostoker. Solution of the schrodinger equation in periodic lattices with an application to metallic lithium. *Physical Review*, 94:1111, 1954.
- [korryng47] J. Korryng. On th calculation of the energy of a bloch wave in a metal. *Physica*, XIII:392, 1947.
- [kosevich05] Arnold M. Kosevich. *The crystal lattice; phonons, solitons, dislocations, superlattices*. Wiley-VCH, 2005.
- [laumanns02] M. Laumanns, L. Thiele, K. Deb, and E. Zitzler. Combining convergence and diversity in evolutionary multi-objective optimization. *Evolutionary computation*, 10(3):263–282, 2002.
- [linton01] C.M. Linton and P.McIver. *Handbook of Mathematical Techniques for wave/structure interactions*. CRC Press, 2001.
- [marion00] Jerry B. Marion. *Classical Dynamics of Particles and Systems*. Academic Press, New York and London, 2000.
- [martin06] P.A. Martin. *Multiple Scattering. Interaction of Time-Harmonic Waves with N Obstacles*. Cambirdge University Press, UK, 2006.

- [mechel08] F.P. Mechel. *Formulas of acoustics*. Springer Verlag New York Inc, 2008.
- [michalewicz92] Z. Michalewicz. *Genetic Algorithms + Data Structures = Evolutionary Programs*. Springer-Verlag, 1992.
- [miettinen98] K. Miettinen. *Nonlinear Multiobjective Optimization*. Kluwer Academic Publishers, Boston, 1998.
- [mills07] Nigel J. Mills. *Polymer foams handbook: engineering and biomechanics applications and design guide*. Elsevier, 2007.
- [soukoulis01] C.M Soukoulis, editor. *Photonic Crystals and Light Localization in the 21st Century*. Kluwer Academic Publishers, 2001.
- [soukoulis93] C.M. Soukoulis, editor. *Photonic band gap and localization*. Plenum Press (New York), 1993.
- [voltera65] E Voltera and E.C. Zachmanoglou. *Dynamisc of vibrations*. Columbus, Charles E. Merrill Books, Inc., 1965.
- [zitzler99] E. Zitzler. *Evolutionary algorithms for multiobjective optimization: Methods and applications*. PhD thesis, Swiss Federal Institute of Technology, Zurich, 1999.